School of Physics and Astronomy

Numerical Modelling Of Black-Hole-Binary Mergers

Sebastian Khan

Submitted for the degree of Doctor of Philosophy
School of Physics and Astronomy
Cardiff University

July 1, 2016

Supervisor: Prof Mark Hannam
External examiner: Dr Jonathan Gair
Internal examiner: Prof Bangalore Sathyaprakash
Chair: Dr Peter Hargrave
Date of viva: 16/06/16

Summary of thesis

The beginning of gravitational wave astronomy started on September 14$^{\text{th}}$ 2015 [13]. The *event*, GW150914, was so loud that the distinct morphological features indicative of the merger of two inspiraling black holes was difficult to deny.

The estimation of source parameters and parameterised tests of general relativity in the strong field regime require the use of gravitational waveform models that predict the inspiral, merger and ringdown of binary black holes according to general relativity. This thesis is focused on providing the gravitational wave community with an accurate model for the gravitational wave signal emitted by coalescing, non-precessing binary black holes covering the inspiral, merger and ringdown.

The solutions to the Einstein equations for the late inspiral, merger and ringdown of binary black holes can only be obtained by using numerical relativity. However, the computational cost of a single simulation is on the order of weeks to months and prohibits a dense sampling of the parameter space. Our method is founded on the *phenomenological* modelling program, which was specifically designed to directly incorporate results from numerical relativity and analytic approximations to construct global models across the parameter space for gravitational wave searches.

We have refined the phenomenological method and developed a new waveform model, `IMRPhenomD`, which is suitable not only for gravitational wave searches but is also sufficiently accurate to be in used to estimate the parameters of gravitational wave candidate events without incurring large systematic uncertainties due to waveform modelling errors. Subsequent to the work presented here our waveform model was also extended to include the effects of precession, which was used in the analysis of advanced LIGO data during its first observing run (2015-2016), including the analysis of GW150914.

We evaluate the current state of the field of waveform modelling by performing numerous comparisons between leading inspiral, merger and ringdown waveform models and find that independently developed models are largely in agreement. This builds confidence in our models when we use them outside of their respective calibration regions. However, there are still large regions of parameter space where the models are in disagreement and we highlight these regions as urgent targets for new numerical relativity simulations.

Co-authored papers

Parts of this thesis are results of collaborative work. S. Khan is either the lead author or has contributed significantly to the work.

- Chapter 2 presents new mass-ratio 1:4 numerical relativity simulations that were used in Refs. [106] and [100]. S. Khan computed the mass-ratio 1:4 simulations and developed the preliminary phenomenological waveform model that is also discussed. This is unpublished work that ultimately lead to the model presented in Chapter 3.
- Chapter 3 is based off Refs. [106] and [100], in collaboration with Sascha Husa, Mark Hannam, Frank Ohme, Michael Pürrer, Xisco Jiménez Forteza and Alejandro Bohé. S. Khan is the lead author on [106] and second author on [100].
- Chapter 4 presents several analyses testing the agreement between leading waveform models. This is currently unpublished work. S. Khan is the lead investigator.

Declaration of authorship

- Declaration:
  This work has not previously been accepted in substance for any degree and is not concurrently submitted in candidature for any degree.

  Signed: ..... (candidate) Date: .....

- Statement 1:
  This thesis is being submitted in partial fulfillment of the requirements for the degree of Doctor of Philosophy (PhD).

  Signed: ..... (candidate) Date: .....

- Statement 2:
  This thesis is the result of my own independent work/investigation, except where otherwise stated. Other sources are acknowledged by explicit references.

  Signed: ..... (candidate) Date: .....

- Statement 3
  I hereby give consent for my thesis, if accepted, to be available for photocopying and for inter-library loan, and for the title and summary to be made available to outside organisations.

  Signed: ..... (candidate) Date: .....

Acknowledgements

I would like to acknowledge my funding agency the Science and Technology Facilities Council who have supported by PhD studies since 2012.

For the sake of brevity I must limit the number of acknowledgements. I ask for forgiveness from anyone that I do not mention here and extend my thanks to all of my friends over the years.

I have to thank my family: Mum, Dad, Jim and Ella. You have and will always be there for me and have always supported me in everything that I've done. I couldn't ask for a better family and I dedicate this thesis to all of you, especially Dad.

A huge thank you to my supervisor, mentor and friend Mark Hannam. You have been very patient with me and have always offered sound advice. It has been a pleasure to be your student. To the entire gravitational physics group, both past and present, thank you for making my time here extremely enjoyable and a joy to come into the office. I extend my gratitude to all of you as I have learned so much you all.

To my fellow post-graduates, both past and present, and in particular to Andrew Williamson, Scott Balfour and Mat Allen who started their PhDs at the same time. I wish you all the best of luck in your vivas and for the future. And another thank you to Mat Allen for hosting numerous board games nights and especially the ones when we play Battlestar Galactica!

To my friends of old: David Sullivan, Tom Wilson and Simon Olivari I wish you all the best of luck on completing your PhDs. To Tom Hughes, Michael Dubec, Jo Kelly, Howard, TJ, the rest of my friends from studying undergraduate physics and to my oldest friends including Steve, Vic and Spoon. Thank you for all the laughs and for all the friendship over the years.

A big thank you to Tom Hall and Luke Berry for the countless games of AOE and Civ V, and countless viewings of MacGruber, Napoleon Dynamite and Predator. You guys never fail to make me laugh! Wololo. Thank you to Tom Adams for countless hours of Factorio together and for making me laugh non-stop.

I am grateful have been a part of the LIGO Scientific Collaboration over the past 4 years and to have been involved in our first detection of gravitational waves from merging black holes. It was been an incredibly exciting time and I count myself especially lucky to have been a part of it all. To all my friends I've made throughout my PhD whether it be at the university, in the office or at a conference meeting meeting like minded individuals who love to talk about physics. Thank you all for you friendship: Prayush Kumar, Alex Nielsen, Tito, Ian Harry, Duncan Macleod, Carl Haster, Juan Calderon Bustillo, Xisco Jimenez-Forteza and the many others I fail to mention.

A slightly unusual acknowledgement next but I also have to thank the Yogscast.

They have never failed to put a smile on my face and I grateful for all the content they put out, which has kept me entertained and helped me unwind throughout my whole PhD and especially during my writing up period. I salute you. I am Dave! Yognau(gh)t.

And finally, thank you to Sarah 'Eevee' Roberts. You never fail to put a smile on my face or make me laugh, thank you for being extremely patient and supportive during my writing up period. You have been absolutely vital to me and I love you with all my heart.

Contents

Glossary xiv

Preface xvii

1 Introduction 1
- 1.1 Gravitational Waves . . . 1
  - 1.1.1 Quadrupole Approximation . . . 5
  - 1.1.2 Strain Decomposition . . . 9
- 1.2 Gravitational Wave Interferometers . . . 10
  - 1.2.1 Interferometer Response to Gravitational Waves . . . 12
- 1.3 Sources . . . 14
  - 1.3.1 Binary Black Holes . . . 15
  - 1.3.2 The Three Stages - Inspiral, Merger and Ringdown . . . 17
  - 1.3.3 Precessing Binary Black Holes . . . 19
  - 1.3.4 Non-Precessing Binary Black Holes . . . 21
- 1.4 Numerical Relativity . . . 24
- 1.5 IMR Waveform Models . . . 28
  - 1.5.1 Phenomenological Models . . . 29
  - 1.5.2 Effective-One-Body Models . . . 31
- 1.6 Data analysis . . . 32
  - 1.6.1 Matched Filter . . . 32
  - 1.6.2 Measures of closeness . . . 34

2 Modelling Numerical Relativity 36
- 2.1 Introduction . . . 36
- 2.2 Binary Black Hole Simulations With The BAM Code . . . 37
  - 2.2.1 Gravitational Waves In Numerical Relativity . . . 38
- 2.3 Simulations of aligned-spin, mass-ratio 1:4 Binary Black Holes . . . 39
  - 2.3.1 Convergence - Dominant Harmonic . . . 40
  - 2.3.2 The anatomy of mass-ratio 1:4 systems: Dominant Harmonic 44
- 2.4 Introduction To Phenomenological Modelling . . . 53
- 2.5 Preliminary Aligned-Spin Model: `PhenomC+` (2014) . . . 56
  - 2.5.1 Summary of differences between `PhenomC` and `PhenomC+` . . . 57
  - 2.5.2 Model Validation . . . 61
- 2.6 Concluding Remarks . . . 66

3 IMRPhenomD: An Aligned Spin Model For The Advanced Detector Era 67
- 3.1 Introduction . . . 67

3.2 Preliminaries . . . 70
3.2.1 Outline of the model . . . 70
3.2.2 Matches . . . 72
3.3 Numerical-Relativity Waveforms . . . 73
3.4 Choice of inspiral approximant . . . 77
3.5 Model of the NR regime (Region II) . . . 79
3.5.1 From IMRPhenomC to IMRPhenomD . . . 79
3.5.2 Phase . . . 82
3.5.3 Amplitude . . . 86
3.6 Inspiral model (Region I) . . . 89
3.6.1 Phase . . . 91
3.6.2 Amplitude . . . 92
3.7 Mapping the phenomenological coefficients to physical parameters . . . 93
3.8 Full inspiral-merger-ringdown (IMR) waveforms . . . 93
3.9 Model Validation . . . 94
3.9.1 Mismatches . . . 95
3.9.2 The effective spin approximation . . . 97
3.9.3 Calibration Set of waveforms . . . 100
3.10 Model vs Model Comparisons . . . 101
3.11 Summary and discussion . . . 105

4 Applications: Model Comparisons and Systematic Errors 109
4.1 Introduction . . . 109
4.2 Model Comparisons: Faithfulness . . . 110
4.2.1 Results . . . 111
4.2.2 Summary . . . 114
4.3 Template Bank Simulations . . . 117
4.3.1 Method . . . 117
4.3.2 Results . . . 118
4.3.3 Split Template Bank . . . 122
4.3.4 Summary . . . 122
4.4 Waveform Model Systematic Errors: BAM:7 Case study . . . 125
4.4.1 Method . . . 125
4.4.2 Results . . . 127
4.4.3 Summary . . . 131

5 Conclusions 133

Appendices 137

A Chapter 3 Appendix 138
A.1 Time-domain conversion . . . 138
A.2 PN coefficients . . . 141
A.3 Phenomenological Coefficients . . . 143

Bibliography 147

List of Figures

1 Data from around the time of GW150914 depicted in a time-frequency representation. . . . xviii
2 Time-series strain data from the LIGO-Hanford (red) and LIGO-Livingstron (green) observatories from around the time of GW150914. xviii

1.1 Illustration of the physical effect of a gravitational wave (GW) as it passes through perpendicular to a ring of test particles. . . . 4
1.2 Illustration of a simple "chirp" waveform computed using the leading order quadrupole term. . . . 9
1.3 A simplified schematic of the advanced LIGO detectors. . . . 11
1.4 An illustration of how the detector frame is related to the radiation frame. . . . 15
1.5 Coordinate system attached to a generic (precessing) binary black hole (BBH) system. . . . 16
1.6 Illustration of the relationship between the source frame and the radiation frame. . . . 17
1.7 Gravitational waveform from a mass ratio 1:4 BBH with aligned-spins $\boldsymbol{\chi}_i \cdot \hat{\mathbf{L}} = 0.75$ $(i = 1, 2)$. . . . 18
1.8 The effect of precession on the gravitational waveform (h_+) as predicted by the precessing effective-one-body (EOB) model `SEOBNRv3` [136]. . . . 20
1.9 Coordinate system attached to a non-precessing BBH systems. . . . 21
1.10 Comparison between time and frequency domain representation of the GW strain. . . . 22
1.11 Prediction of the observed gravitational waveform including contributions beyond the leading order. . . . 24
1.12 Geometrical representation of the 3+1 decomposition. . . . 25
1.13 An illustration of how two slices at $t = 0$ and $t = dt$ are related to each other in the 3+1 split. . . . 27

2.1 Results of the phase convergence test for the `BAM:4` non-spinning system. 42
2.2 Results of the amplitude convergence test for the `BAM:4` non-spinning system. . . . 43
2.3 Time domain representation of the inspiral, merger and ringdown of a non-spinning, mass-ratio 1:4 BBH system (`BAM:4`). . . . 45
2.4 Phase of time domain gravitational waveform from `BAM:4`. . . . 46
2.5 Frequency of time domain gravitational waveform from `BAM:4`. . . . 47
2.6 Amplitude of time domain gravitational waveform of all cases in Table 2.1, . . . 48
2.7 Phase of time domain gravitational waveform of all cases in Table 2.1 49

2.8 Frequency of time domain gravitational waveform of all cases in Table 2.1. . . . 50
2.9 Amplitude of Fourier domain gravitational waveform for BAM:4. . . . 51
2.10 Phase of the Fourier domain strain for BAM:4. . . . 52
2.11 Frequency derivative of Fourier domain phase for BAM:4. . . . 53
2.12 Amplitude of Fourier domain gravitational waveform of all cases in Table 2.1. . . . 54
2.13 Phase of Fourier domain strain for all cases in Table 2.1. . . . 55
2.14 Frequency derivative of the Phase of Fourier domain gravitational waveform of all cases in Table 2.1. . . . 56
2.15 The Fourier domain amplitude $|\tilde{h}|$ as a function of geometric frequency Mf for a mass-ratio 1:5 case with aligned-effective-spin $\chi_{\rm eff} = -0.42$ computed using SEOBNRv1_ROM. . . . 58
2.16 The match between IMRPhenomC (orange), IMRPhenomC+TF2 (blue) and IMRPhenomC+EOB (black) against the non-spinning 1:18 BAM simulation. . . . 62
2.17 The match between IMRPhenomC (orange), IMRPhenomC+TF2 (blue) and IMRPhenomC+EOB (black) against the 1:18, $(\chi_1, \chi_2) = (-0.8, 0)$ BAM simulation. . . . 63
2.18 The match between IMRPhenomC+TF2 (blue) and IMRPhenomC+EOB (black) against a SEOBNRv1_ROM waveform with mass-ratio 1:5 and aligned-effective-spin $\chi_{\rm eff} = -0.42$. . . . 64
2.19 Comparison between three models: (i) IMRPhenomC, (ii) IMRPhenomC+TF2 (Using TaylorF2 as the inspiral approximant) and (iii) IMRPhenomC+EOB (Using SEOBNRv1_ROM as the inspiral approximant) against SEOBNRv1_ROM evaluated across the parameter space. . . . 65

3.1 Parameter space over which IMRPhenomC, IMRPhenomD and SEOBRNv2 are calibrated to. . . . 74
3.2 Mismatch error due to numerical resolution. . . . 75
3.3 Mismatch errors due to finite-radius waveform extraction. . . . 76
3.4 Fourier domain amplitude and phase derivative illustrating how they are organised in IMRPhenomD. . . . 80
3.5 Phase derivative $\phi'(f)$ for the $q = 1$, $\chi_1 = \chi_2 = -0.95$ configuration. 81
3.6 Fourier domain amplitude for the $q = 4$, $\chi_1 = \chi_2 = -0.75$ configuration. 82
3.7 Examples of the merger-ringdown (Region IIb) model . . . 84
3.8 Examples of the intermediate (Region IIa) model . . . 85
3.9 Hybrid Fourier domain amplitude for three equal mass cases $q = 1$, $\chi_1 = \chi_2 = 0.98$, $\chi_1 = \chi_2 = 0$ and $\chi_1 = \chi_2 = -0.95$. . . . 87
3.10 Hybrid and model Fourier-domain amplitude for three equal-mass configurations, $\chi_1 = \chi_2 = 0.98$, $\chi_1 = \chi_2 = 0$ and $\chi_1 = \chi_2 = -0.95$. . 89
3.11 The same quantities as in Fig. 3.10, but now for three $q = 18$ configurations, $\chi_1 = 0.4, \chi_2 = 0$, $\chi_1 = \chi_2 = 0$ and $\chi_1 = -0.8, \chi_2 = 0$. . . . 90
3.12 Examples of the inspiral (Region I) model . . . 92
3.13 Phase coefficients for region I and II. . . . 95
3.14 Amplitude coefficients for region I and IIb. . . . 95
3.15 Intermediate (Region IIb) amplitude coefficient. . . . 96
3.16 Mismatches of the IMRPhenomD model against all 48 available hybrid waveforms. . . . 98

3.17 Mismatch between a $q = 8$, $\chi_1 = 0.8$, $\chi_2 = 0$ SEOBv2+NR hybrid, and the IMRPhenomD model. We see that the mismatch exceeds our 1% threshold everywhere. However, the fitting factor is everywhere better than 99%, with negligible parameter biases (see text). 100
3.18 Four sets of calibration waveforms. Set 1 (48 waveforms) is indicated in red, Set 2 (25 waveforms) in green, Set 3 (19 waveforms, used for the final IMRPhenomD model) in orange, and Set 4 (12 waveforms) in blue. 101
3.19 Mismatch comparisons between the SEOBNRv2_ROM model, and three versions of IMRPhenomD. Left: the final IMRPhenomD model. Middle: SEOBNRv2_ROM is used for the inspiral part of IMRPhenomD, i.e., up to $Mf = 0.018$. Right: TaylorF2 is used for the inspiral part of IMRPhenomD. See text for discussion. 103
3.20 Mismatch of IMRPhenomD (solid) or SEOBNRv2_ROM (dashed) against cases A10 – $q = 4, \chi_{\rm eff} = 0.75$ (orange), A15 – $q = 8, \chi_{\rm eff} = 0.85$ (green) and B17 – $q = 2, \chi_{\rm eff} = 0.75$ (black). The mismatch was calculated as described in Sec. 3.3 using the aLIGO zdethp noise curve. 106

4.1 Cumulative distributions of the match from the faithsim analysis. . . 112
4.2 Faithfulness calculations comparing IMRPhenomB/C/D with SEOBNRv2_ROM for the $(\eta, \hat{\chi})$ slice. 115
4.3 aithfulness calculations comparing IMRPhenomB/C/D with SEOBNRv2_ROM for the (m_1, m_2) slice. 116
4.4 Results from template bank simulations. Both runs use SEOBNRv2_ROM as the templates and the effectualness of the bank is determined by injecting SEOBNRv2_ROM (Run 1) and IMRPhenomD (Run 2) signals. . . 120
4.5 Results of template bank simulations Run 1 and 2 showing the $(\eta, \hat{\chi})$ plane. 121
4.6 Cumulative distributions of the fitting factor including Run 3. 123
4.7 Template bank simulation results for Run 3, showing the $(\eta, \hat{\chi})$ plane. 124
4.8 Posterior probability density functions for component masses (top panel) and the $(\chi_{\rm eff}, \eta)$ plane (bottom panel). 130

A.1 Time-domain IMRPhenomD waveforms (solid, light blue online) and numerical relativity (NR) waveforms (dashed, red online) for corners of the parameter space used for calibration. We plot the plus polarization h_+ normalized by the extraction radius, and the binary's parameters are indicated by the mass ratio $q = m_1/m_2$ and the two spin parameters χ_1, χ_2. 140
A.2 Time-domain representation of the IMRPhenomD model outside its calibration region, here for mass ratio 50 and spin parameters of $\chi_1 = \chi_2 = 0.99$. 141

List of Tables

2.1 Configurations of the mass-ratio 1:4 BBH systems simulated with BAM. 39
2.2 Numerical grid configurations for the three base grids used. 40
2.3 Summary of the estimated error assoiciated with the BAM runs where multiple resolutions were available. 43

3.1 Hybrid waveform configurations used to calibrate the IMRPhenomD model. 77
3.2 Locations of the collocation points, f_1, f_2, f_3, and the corresponding values of the amplitude $A(f)$ and its derivative $A'(f)$. 88
3.3 Additional waveforms used to verify the model, but *not* used in its calibration. 97
3.4 Comparison of models constructed with different sets of calibration waveforms. 102

4.1 Summary of IMR models used in this chapter along with their respective calibration regions. 110
4.2 Results from the faithsim analysis. 111
4.3 Results from template bank simulations. Both runs use SEOBNRv2_ROM as the templates and the effectualness of the bank is determined by injecting SEOBNRv2_ROM (Run 1) and IMRPhenomD (Run 2) signals. Also tabulated is the minimum recovered FF and the percentage of injections that were recovered with a FF $< 97\%$. While Run 1 demonstrates that the bank is effectualness to itself it cannot be said to be effectual to IMRPhenomD. For an overview across the parameter space see Figure 4.5. 119
4.4 Results from the third template bank simulation. This run is identical to Run 2 except that the high spin ($\chi_{\rm eff} > 0.7$) templates are generated with IMRPhenomD. 122
4.5 Injection parameters for parameter estimation analysis. 127
4.6 Parameter estimation results for BAM:7 injection. 129

A.1 Coefficient values for linear in $\chi_{\rm PN}$ and $\chi_{\rm PN}$ independent terms for the mapping functions given in Eq. (3.28). These values are calculated under the parametrisation (η, $\chi_{\rm PN}$). 144
A.2 Coefficient values for quadratic in $\chi_{\rm PN}$ terms for the mapping functions given in Eq. (3.28). These values are calculated under the parametrisation (η, $\chi_{\rm PN}$) 144
A.3 Coefficient values for cubic in $\chi_{\rm PN}$ terms for the mapping functions given in Eq. (3.28). These values are calculated under the parametrisation (η, $\chi_{\rm PN}$) 145

Glossary

ADM Arnowitt-Deser-Misner.

AdV Advanced Virgo.

aLIGO Advanced Laser Interferometer Gravitational-wave Observatory.

AMR adaptive mesh refinement.

ASD amplitude spectral density.

BAM bifunctional adaptive mesh.

BBH binary black hole.

BH black hole.

BSSN Baumgarte-Shapiro-Shibata-Nakamura.

CBC compact binary coalescence.

EOB effective-one-body.

FF fitting factor.

GR general relativity.

GW gravitational wave.

IMR inspiral-merger-ringdown.

ISCO inner-most stable circular orbit.

LIGO Laser Interferometer Gravitational-wave Observatory.

LSC LIGO Scientific Collaboration.

NR numerical relativity.

PN post-Newtonian.

PSD power spectral density.

QNM quasi normal mode.

ROM reduced-order model.

ROQ reduced-order quadrature.

SNR signal-to-noise ratio.

SpEC spectral Einstein code.

SXS simulating extreme spacetimes.

We are at the very beginning of time for the human race. It is not unreasonable that we grapple with problems. But there are tens of thousands of years in the future. Our responsibility is to do what we can, learn what we can, improve the solutions, and pass them on.

Richard Feynman

Preface
Detection

One hundred years ago, Albert Einstein presented his general theory of relativity [78]. It was built upon the principles of Special Relativity [77] that the speed of light is the same for all inertial observers and that in inertial reference frames the laws of physics should be the same. The classical Newtonian notion of gravity was replaced with a geometric interpretation of the Universe where space and time are married together to form the space-time fabric. Such a fabric which is perfectly flat when no matter or energy is present, becomes distorted and *curved* when there is matter or energy. It is the curvature of space-time that we perceive as the force of Gravity. In 1916 Einstein found the weak-field solutions to general relativity (GR) had wave-like solutions [79, 80], gravitational waves (GWs).

GR has stood proud for one hundred years, naturally explaining many of the astrophysical phenomena we have found and predicting effects which we can look for such as: the perihelion advance of Mercury, the time-delay of signal around massive bodies (Shapiro time delay), the change in energy of a photon as it passes through gravity gradients (gravitational redshift) and gyroscopic precession.

2015 marked the beginning of gravitational wave astronomy. On September 14^{th} 2015 at 09:50:45 UTC[1] the Laser Interferometer Gravitational-wave Observatory (LIGO) detectors, LIGO-Hanford (H1) and LIGO-Livingston (L1), detected a coincident gravitational wave event (GW150914) with a significance greater that $5.1\,\sigma$ [13]. Figure 1 shows the spectrogram around the time of GW150914. The event was so loud that it is clearly visible above the background. The signal is consistent with a binary black hole merger which most probably originated from the southern hemisphere at a distance of $\sim 410\,\text{Mpc}$ [17]. The peak luminosity for GW150914 was $3.6 \times 10^{56}\text{erg}\,\text{s}^{-1}$ and over the period GW150914 was in band it radiated $3M_{\odot}$ in gravitational radiation.

Not only is this overwhelming evidence for the existence of BHs and GWs, it also indicates that binary black holes (BBHs) form and merge within a Hubble time and that BHs approximately 30 times heavier than the Sun exist. From the first 16 days of LIGO data, the inferred rate of binary black hole mergers is bounded by $2 - 600\,\text{Gpc}^{-3}\,\text{yr}^{-1}$ [12] and the probability of detecting even more BBH signals is yet higher in future observing runs. The measured peak GW strain from GW150914 was 1×10^{-21} [13], which translates into a change in the proper distance between the LIGO mirrors of $\approx 2 \times 10^{-18}\,\text{m}$. That's about a thousandth the size of a proton!

The waveform model presented in this thesis was central to the measurements of GW150914's parameters [17] and in the first ever tests of GR in the strong field, high velocity regime [15]. The results were fully consistent with GR.

[1] GPS time: 1126259462.42

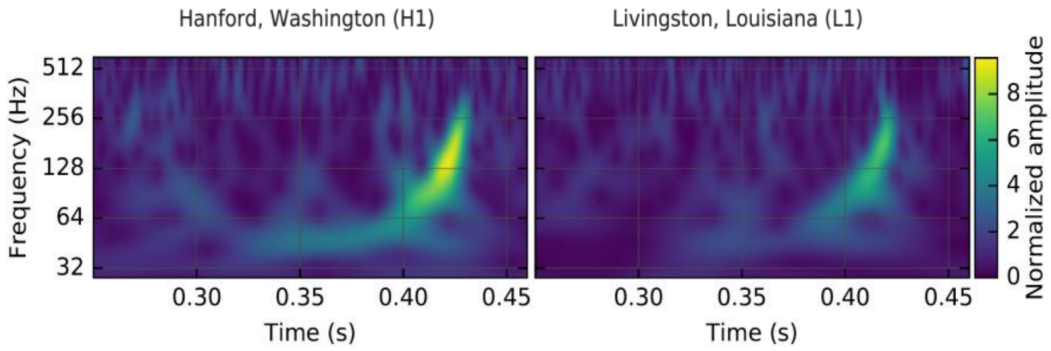

Figure 1: Data from around the time of GW150914 depicted in a time-frequency representation. The characteristic "chirp" morphology is clearly visible above the background. Left: Data from the LIGO-Hanford observatory. Right: Data from the LIGO-Livingston observatory. Adapted from Figure 1 of [13].

We end this brief preface with the time-series strain data from around the time of the event, which has been post-processed to accentuate GW150914 (Figure 2). Overlaid on top is the prediction from the gravitational waveform model presented in this thesis (`IMRPhenomD`) using the Bayesian parameter estimation codes that were used in [17]. The masses used here are $m_1 = 36.65 M_\odot$ and $m_2 = 33.96 M_\odot$; with dimensionless aligned-spins of $\chi_1 = -0.44$ and $\chi_2 = 0.41$.[2] Code from the LIGO Open Science Centre (LOSC) on GW150914 [1] was used to make this plot.

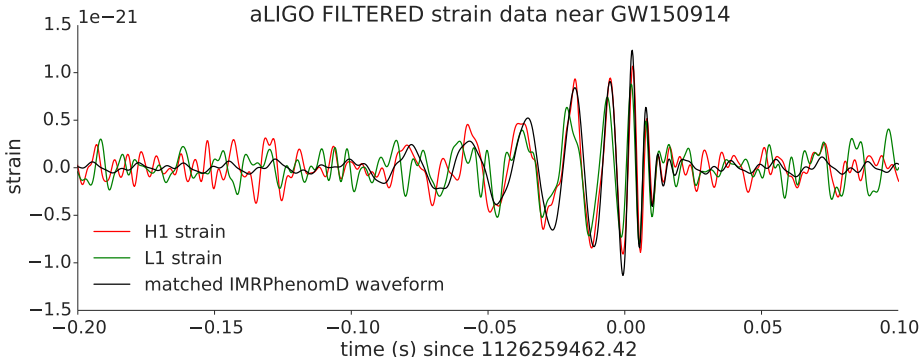

Figure 2: Time-series strain data from the LIGO-Hanford (red) and LIGO-Livingstron (green) observatories from around the time of GW150914. The data has been band-pass filter to accentuate the GW150914. Overlaid on top is the prediction from the gravitational waveform model presented in this thesis (`IMRPhenomD`) using the best-fitting parameters from Bayesian parameter estimation codes that we using in [17]. The masses used here were $m_1 = 36.65\,M_\odot$, $m_2 = 33.96\,M_\odot$ with dimensionless aligned-spins of $\chi_1 = -0.44$ and $\chi_2 = 0.41$.

[2] Values courtesy of a LALInference run by Vivien Raymond [5].

Chapter 1

Introduction

1.1 Gravitational Waves

Gravitational waves are propagating degrees of freedom in General Relativity (GR). Wave solutions to the linearised Einstein equations predicted by Albert Einstein in 1916 [79, 80]. Their physical interpretation was debated for sometime and the Chapel Hill meeting of 1957 is reported to be one where progress was made on recognising their physiciality [154].

The Einstein field equations [78] Eq. (1.1) describe the geometry of space-time and how it reacts to matter and energy. They have been studied for over 100 hundred years and remain a triumph of physics.

$$G_{ab} \equiv R_{ab} - \frac{1}{2} g_{ab} R = \frac{8\pi G}{c^4} T_{ab} \,. \tag{1.1}$$

As John Archibald Wheeler once said

> *"Spacetime tells matter how to move, matter tells spacetime how to curve"* [173].

To access the wave-like solutions to this theory we start from the Einstein field equations Eq. (1.1) and perform linear perturbation theory around a background metric and show that this perturbation obeys a wave equation on top of the background, following the derivation in [122]. Choosing the Minkowski flat space-time metric as our background we add a perturbation with the only constraint being that the components of this perturbation are small, i.e., $|h_{ab}| \ll 1$

$$g_{ab} = \eta_{ab} + h_{ab} \,. \tag{1.2}$$

From Eq. (1.1) we have to express both the Ricci tensor and the Ricci scalar in terms of Eq. (1.2), expand and only keep terms linear in h_{ab}. If the Christoffel symbols are written in terms of the full metric up to linear order as,

$$\Gamma^{\rho}{}_{\mu\nu} = \frac{1}{2} g^{\rho\sigma} \left(\partial_\mu g_{\sigma\nu} + \partial_\nu g_{\sigma\mu} - \partial_\sigma g_{\mu\nu} \right) , \tag{1.3}$$

then substituting Eq. (1.2) into Eq. (1.3) and working to linear order we find

$$\Gamma^{\rho}{}_{\mu\nu} = \frac{1}{2} \eta^{\rho\sigma} \left(\partial_\mu h_{\sigma\nu} + \partial_\nu h_{\sigma\mu} - \partial_\sigma h_{\mu\nu} + \mathcal{O}[h^2] \right) . \tag{1.4}$$

Next we can compute the Ricci tensor, expressed in terms of the Christoffel symbols as

$$R_{\mu\nu} = R^{\alpha}{}_{\mu\alpha\nu} = \partial_\alpha \Gamma^{\alpha}{}_{\mu\nu} - \partial_\nu \Gamma^{\alpha}{}_{\mu\alpha} + \mathcal{O}[\Gamma^2] . \tag{1.5}$$

Again, substituting in our expressions for the metric perturbation into Eq. (1.5) we arrive at the Ricci tensor for the metric perturbation

$$R_{\mu\nu} = \frac{1}{2} \left(\partial_\alpha \partial_\mu h_\nu{}^{\alpha} - \Box h_{\mu\nu} - \partial_\nu \partial_\mu h + \partial_\nu \partial^\alpha h_{\mu\alpha} \right) , \tag{1.6}$$

where the trace of the perturbation is defined as $h = h^{\alpha}{}_{\alpha}$. Finally to construct the Einstein tensor G_{ab} we need an expression for the Ricci scalar, which is given as

$$R = \eta^{\mu\nu} R_{\mu\nu} = \partial_\mu \partial_\nu h^{\mu\nu} - \Box h . \tag{1.7}$$

Finally, we arrive at the linearised Einstein field equations,

$$-\Box h_{\mu\nu} + \partial_\alpha \partial_\mu h_\mu{}^{\alpha} + \partial_\nu \partial^\alpha h_{\mu\alpha} - \partial_\nu \partial^\mu h + \eta_{\mu\nu} \partial_\beta \partial_\alpha h^{\alpha\beta} + \eta_{\mu\nu} \Box h = \frac{16\pi G}{c^4} T_{\mu\nu} . \tag{1.8}$$

The above expression can be greatly simplified with a particular substitution for the metric. The quantity called the *trace-reversed metric perturbation* is given by

$$\bar{h}_{\mu\nu} = h_{\mu\nu} - \frac{1}{2} \eta_{\mu\nu} h , \tag{1.9}$$

with inverse

$$h_{\mu\nu} = \bar{h}_{\mu\nu} - \frac{1}{2} \eta_{\mu\nu} \bar{h} . \tag{1.10}$$

Finally by exploiting the gauge freedom of general relativity (GR) we employ the harmonic gauge condition on $\bar{h}$ i.e.,

$$\partial^\nu \bar{h}_{\mu\nu} = 0 , \tag{1.11}$$

which allows us to write the trace-reversed metric perturbation as a wave equation

$$\Box \bar{h}_{ab} = -\frac{16\pi G}{c^4} T_{ab} . \tag{1.12}$$

Here $\Box = \nabla^2 - \frac{1}{c^2} \frac{\partial^2}{\partial t^2}$ is the flat space-time d'Alembertian. The "coupling constant" $c^4/16\pi G \sim 10^{43}\,\mathrm{N}$ can be loosely interpreted to explain why the amplitude

of GWs are so weak. Because space-time is so "stiff" it takes enormous amounts of energy in order to stretch or vibrate it.

If we consider vacuum spacetimes in the harmonic gauge Eq. (1.12) reduces to the homogeneous wave equation for $\bar{h}$, $\Box\bar{h}_{\mu\nu} = 0$. The tensor $h_{\mu\nu}$ is a symmetric 4×4 matrix and in general has 10 independent components. However, the harmonic gauge condition fixes 4 of those components and an additional 4 components are fixed by residual gauge freedom in the vacuum spacetime. Making use of the gauge freedom we define the *transverse-traceless* (TT) gauge by imposing the following conditions,

$$h^{0\mu} = 0\,, \quad h^{i}{}_{i} = 0\,, \quad \partial^{j}h_{ij} = 0\,, \tag{1.13}$$

where $\mu = 0,1,2,3$ and $i = 1,2,3$. Thus in the TT gauge $h_{\mu\nu} = \bar{h}_{\mu\nu}$ and the only non-zero components of our metric perturbation $h_{\mu\nu}$ are the spatial components. The vacuum equation for the metric perturbation in the TT gauge is thus

$$\Box h_{\mu\nu} = 0\,. \tag{1.14}$$

As Eq. (1.14) is a wave equation we can readily construct plane wave solutions to it. Choosing the direction of propagation to be in the z direction, we find that these solutions propagate at the speed of light and as such solution at the spacetime point (t,z) depend on the retarded time $t_{\rm ret} = t - z/c$. Note that these solutions are free waves; we have not specified what produced them. A simple plane wave solution could be of the form,

$$h^{\rm TT}_{\mu\nu}(t,z) = \begin{bmatrix} 0 & 0 & 0 & 0 \\ 0 & h_+ & h_\times & 0 \\ 0 & h_\times & -h_+ & 0 \\ 0 & 0 & 0 & 0 \end{bmatrix}_{\mu\nu} \cos[\omega(t-z/c)]\,, \tag{1.15}$$

where h_+ and $h_\times$ are the two independent polarisation states of GWs. They are transverse to the direction of propagation and travel at the speed of light. Their names come from their physical effect on matter; this is illustrated over the course of one GW period T in Figure 1.1.

Consider, in flat space-time, a ring of particles with negligible mass. The top panel depicts what happens as a plane GW, with only the h_+ polarisation, travels through perpendicular to the ring. After a quarter of a wavelength $(T/4)$ space-time gets stretched in the vertical direction and simultaneously squashed in the horizontal direction, which changes the proper distance between the particles whilst keeping the area inside the ring preserved. A quarter of a wavelength later $(T/2)$ the particles have been deformed back into a ring. Another quarter of a wavelength

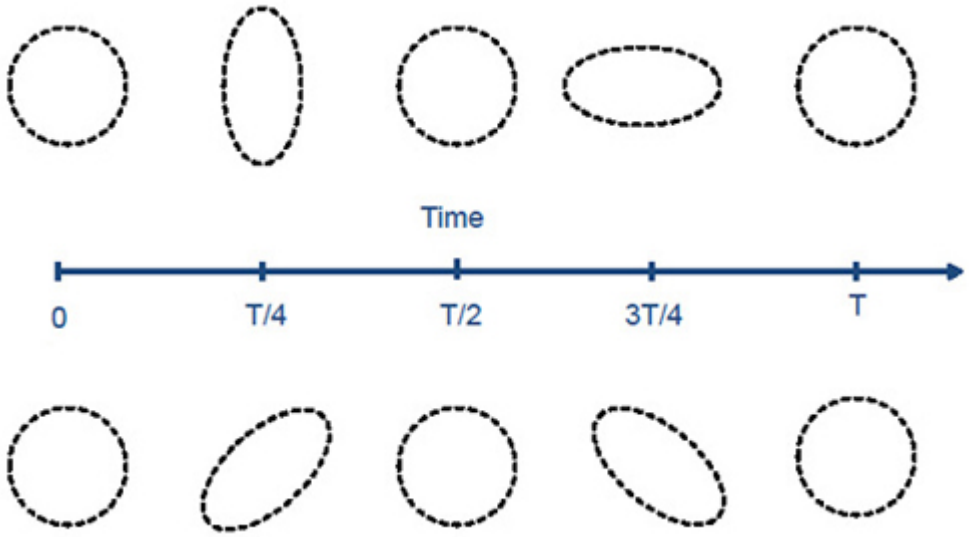

Figure 1.1: Illustration of the physical effect of a GW as it passes through perpendicular to a ring of test particles which are at rest at $T = 0$. The top images contain only the plus polarisation (h_+). After a quarter of a wavelength ($T/4$) space-time gets stretched in the vertical direction and simultaneously squashed in the horizontal direction, which changes the proper distance between the particles whilst keeping the area inside the ring preserved. A quarter of a wavelength later ($T/2$) the particles have been deformed back into a ring. Another quarter of a wavelength later ($3T/4$) the ring is now deformed in the opposite direction, now squashed in the vertical direction and stretched in the horizontal direction. Finally, after another quarter of a wavelength (T) the ring is returned to its original configuration and one wavelength of a GW has passed through it. The bottom images of shows the same situation but when the GW consists of only the $h_\times$ polarisation. The pattern is identical to the h_+ case but simple rotated by 45°. Figure originally published in [4]

later ($3T/4$) the ring is now deformed in the opposite direction, now squashed in the vertical direction and stretched in the horizontal direction. Finally, after another quarter of a wavelength (T) the ring is returned to its original configuration and one wavelength of a GW has passed through it. The bottom panel of Figure 1.1 shows the same situation but when the GW consists of only the $h_\times$ polarisation. The pattern is identical to the h_+ case but simple rotated by 45°.

GWs are a tidal field and in Section 1.2.1 we will see that their measurable effect is to cause a fractional change in proper distance between points, which we characterise by the *strain*, h.[1] The strain is proportional to $\Delta L/L$; in Figure 1.1 the strain is approximatly $h \sim 0.1$.

Strains of this amplitude would only be achievable if you were close to a strong GW source. They are *exceedingly* difficult to produce and even in the case of catastrophic astrophysical systems, which we will derive in the next section, the expected

[1] This is *not* the trace of $h_{\mu\nu}$

strains are approximately of the order 10^{-21} at Earth. GW150914 was recorded to have a peak strain of $h = 10^{-21}$ [13]. This means that the measured change in length of the Advanced Laser Interferometer Gravitational-wave Observatory (aLIGO) interferometers was 2×10^{-18} m - a thousandth the size of a proton!

1.1.1 Quadrupole Approximation

In the previous section we found the free, plane wave solution to the vacuum wave equation for $h_{\mu\nu}$. Now we will use results for the *sourced* wave equation for the trace-reversed metric Eq. (1.12) (because $\bar{h}_{\mu\nu} = h_{\mu\nu}$ can only be true in vacuum). Eq. (1.12) can be solved using Green's functions. The appropriate solution is given by retarded Green's function for the wave equation with outgoing boundary conditions. Solving for the case when we are outside the source in vacuum we can project the equation into the TT gauge with an appropriate projector [122] to get

$$h_{ij}^{TT}(t, \mathbf{x}) = \frac{4G}{c^4} \Lambda_{ijkl}(\hat{\mathbf{n}}) \int d^3x' \frac{1}{|\mathbf{x} - \mathbf{x}'|} T_{kl}\left(t_{\text{ret}}, \mathbf{x}'\right) . \tag{1.16}$$

Here $\hat{\mathbf{n}}$ is the propagation direction and $\Lambda_{ijkl}(\hat{\mathbf{n}})$ is the transverse-traceless projector which projects two-tensors onto the plane transverse to $\hat{\mathbf{n}}$ [122]. $\mathbf{x}'$ is the location of the source element and $\mathbf{x}$ is the location of the observer relative to the centre of the source.

If we further assume that we are very far from the source and that the internal composition of the source is non-relativitstic then we can accurately expand the stress-energy tensor in a multipole expansion. For details see [122] but here we simply quote the leading order quadrupole final result under the above assumptions.

$$[h_{ij}^{TT}(t, \mathbf{x})]_{\text{quad}} = \frac{1}{r} \frac{2G}{c^4} \Lambda_{ijkl}(\hat{\mathbf{n}}) \left(\ddot{M}^{kl}(t_{\text{ret}}) + \text{H.O.Ts} \right) , \tag{1.17}$$

where higher order terms (H.O.Ts) represent the mass and current multipole moments beyond the quadrupole order. The second mass moment is closely related to the moment of inertia and is given by

$$M^{ij}(t) = \int d^3x \, \rho(t, \mathbf{x}) \, x^i x^j . \tag{1.18}$$

The Quadrupole formula Eq. (1.17) shows that GWs are generated by accelerating, non-spherical mass distributions. Eq. (1.17) provides an expression of the gravitational wave with direction of propagation $\hat{\mathbf{n}}$. The angular distribution of gravitational radiation in the quadrupole approximation can be found by acting on Eq. (1.18) with appropriate rotation matrices which can be found in [122]. The angular distributions for the h_+ and $h_\times$ polarisations are given by

$$
\begin{aligned}
h_+(t;\vartheta,\varphi) = \frac{1}{r}\frac{G}{c^4}\Big[&\ddot{M}_{11}(\cos^2\varphi - \sin^2\varphi\cos^2\vartheta) \\
&+ \ddot{M}_{22}(\sin^2\varphi - \cos^2\varphi\cos^2\vartheta) \\
&- \ddot{M}_{33}\sin^2\vartheta \\
&- \ddot{M}_{12}\sin 2\varphi\,(1+\cos^2\vartheta) \\
&+ \ddot{M}_{13}\sin\varphi\sin 2\vartheta \\
&+ \ddot{M}_{23}\cos\varphi\sin 2\vartheta\,\Big]_{t_{\rm ret}}\,,
\end{aligned}
\tag{1.19}
$$

$$
\begin{aligned}
h_\times(t;\vartheta,\varphi) = \frac{1}{r}\frac{G}{c^4}\Big[&(\ddot{M}_{11} - \ddot{M}_{22})\sin 2\varphi\cos\vartheta \\
&+ 2\ddot{M}_{12}\cos 2\varphi\cos\vartheta \\
&- 2\ddot{M}_{13}\cos\varphi\sin\vartheta \\
&+ 2\ddot{M}_{23}\sin\varphi\sin\vartheta\,\Big]_{t_{\rm ret}}\,,
\end{aligned}
\tag{1.20}
$$

where it is understood that the right hand side is evaluated to $t_{\rm ret}$. ϑ and φ are the polar and azimuthal angle respectively.

Binary Toy Model

We can estimate the amplitude of GWs from astrophysical sources using a toy model of a binary system. If we express the system in the centre of mass frame then we can describe a binary system with masses m_1 and m_2 with an equivalent system of a particle of reduced mass $\mu = m_1 m_2/(m_1+m_2)$ orbiting a central mass with mass $M = m_1 + m_2$. The relative coordinate of the binary is $\mathbf{x}_0 = \mathbf{x}_1 - \mathbf{x}_2$. The mass density is then greatly simplified can be expressed as a delta function and we can trivially perform the integral in Eq. (1.18). If we let $\rho(t,\mathbf{x}) = \mu\,\delta^{(3)}(t,\mathbf{x}-\mathbf{x}_0)$ then the second mass moment becomes

$$
M^{ij}(t) = \mu\, x_0^i x_0^j\,. \tag{1.21}
$$

We can model the circular orbit as the parametric set

$$
\begin{aligned}
x_0(t) &= R\cos(\omega t)\,, &(1.22)\\
y_0(t) &= R\sin(\omega t)\,, &(1.23)\\
z_0(t) &= 0\,. &(1.24)
\end{aligned}
$$

Plugging in expressions for the mass distribution (Eq. (1.22), Eq. (1.23) and Eq. (1.24)) into the equation for the second mass moment (Eq. (1.18)), computing the non-zero components to then plug into the expressions for the angular distribution of the GW polarisations (Eq. (1.19) and Eq. (1.20)) and expressing the separation of the two bodies as a function of their orbital frequency through Kepler's

law $\omega^2 = GM/R^2$ we arrive at the gravitational waveform for a conservative binary system,

$$h_+(t;\vartheta,\varphi) = \frac{4}{r}\left(\frac{G\mathcal{M}_c}{c^2}\right)^{5/3}\left(\frac{\pi f_{\rm gw}}{c}\right)^{2/3}\left(\frac{1+\cos^2(\vartheta)}{2}\right)\cos(\Phi(t_{\rm ret})+2\varphi)\,, \tag{1.25}$$

$$h_\times(t;\vartheta,\varphi) = \frac{4}{r}\left(\frac{G\mathcal{M}_c}{c^2}\right)^{5/3}\left(\frac{\pi f_{\rm gw}}{c}\right)^{2/3}\cos(\vartheta)\sin(\Phi(t_{\rm ret})+2\varphi)\,, \tag{1.26}$$

where the GW phase is

$$\Phi(t_{\rm ret}) = 2\pi f_{\rm gw} t_{\rm ret}\,. \tag{1.27}$$

Even from this very simple toy model some very important facts emerge. Firstly the combination of the masses called the *chirp mass* $\mathcal{M}_c = \mu^{3/5}M^{2/5}$ determines the amplitude of the signal. Secondly we also find that the GW frequency is *twice* the orbital frequency i.e., $\omega_{\rm gw} = 2\omega$. The is because the quadrupole moment of the binary is symmetric under rotations of π rad. And finally, the relative amplitude of h_+ and $h_\times$ deserves attention, specifically, when viewed face-on or face-away ($\vartheta = 0$ or π) the waveform is circularly polarised. When viewed edge-on ($\vartheta = \pi/2$) $h_\times$ goes to zero and the waveform is linearly polarised. For other angles the waveform is elliptically polarised, containing varying amounts of h_+ and $h_\times$ as a function of the propagation direction.

So far this toy model describes the conservative motion (circular orbits) of a binary system. As the binary evolves and emits GWs, energy will be lost from the system. Assuming that the energy comes from the potential energy of the orbit we can postulate an *energy-balance equation* of the form,

$$P = -\frac{dE_{\rm orbit}}{dt}\,, \tag{1.28}$$

where P is the average power emitted from the binary at a specific GW frequency. According to Einstein's famous quadrupole formula [80],

$$P = \frac{32}{5}\frac{c^5}{G}\left(\frac{G\,\mathcal{M}_c\,\omega_{\rm gw}}{2c^3}\right)^{10/3}\,, \tag{1.29}$$

and $E_{\rm orbit}$ is the Newtonian orbital binding energy

$$E_{\rm orbit} = -\frac{Gm_1m_2}{2R} = -\left(\frac{G^2\,\mathcal{M}_c^5\,\omega_{\rm gw}^2}{32}\right)^{1/3}\,. \tag{1.30}$$

The resulting change in GW frequency is

$$\dot{\omega}_{\rm gw} = \frac{12}{5}2^{1/3}\left(\frac{G\mathcal{M}_c}{c^3}\right)^{5/3}\omega_{\rm gw}^{11/3}\,. \tag{1.31}$$

The solution of this therefore gives the frequency evolution of the binary. Integrating from $t' = t$ to $t' = t_{\rm coal}$ where $\tau \coloneqq t_{\rm coal} - t$ is defined to be the coalescence time we find the frequency evolution is

$$\omega_{\rm gw}(\tau) = 2\left(\frac{5}{256}\frac{1}{\tau}\right)^{3/8}\left(\frac{G\mathcal{M}_c}{c^3}\right)^{-5/8}. \tag{1.32}$$

The coalescence time is the length of time needed to evolve from angular GW frequency $\omega_{\rm gw}$ until Eq. (1.32) diverges, which in this toy model can be thought of as the "merger". This toy model becomes less accurate as the bodies get closer together, eventually the point particle assumption we have implicitly made will be invalid and finite size effects need to be taken into account to accurately model the dynamics through merger.

The GW phase can be obtained by integrating the GW frequency with respect to time i.e.,

$$\Phi(\tau) = \int_t^{t_{\rm coal}} \omega_{\rm gw}\, dt' \tag{1.33}$$

$$\Phi(\tau) = -2\left(\frac{5G\mathcal{M}_c}{c^3}\right)^{-5/8}\tau^{5/8} + \Phi_0\,. \tag{1.34}$$

Here $\Phi_0 \coloneqq \Phi(\tau = 0)$ is an integration constant which, for inspiral waveforms is typically set to the value of the phase at the coalescence time.

Finally we arrive at an expression for the angular distribution of the gravitational waveform from a simple binary system incorporating the leading order effects of radiation reaction

$$h_+(t;\vartheta,\varphi) = \frac{1}{r}\left(\frac{G\mathcal{M}_c}{c^2}\right)^{5/4}\left(\frac{5}{c\tau}\right)^{1/4}\left(\frac{1+\cos^2(\vartheta)}{2}\right)\cos(\Phi(\tau)+2\varphi)\,, \tag{1.35}$$

$$h_\times(t;\vartheta,\varphi) = \frac{1}{r}\left(\frac{G\mathcal{M}_c}{c^2}\right)^{5/4}\left(\frac{5}{c\tau}\right)^{1/4}\cos(\vartheta)\sin(\Phi(\tau)+2\varphi)\,. \tag{1.36}$$

Figure 1.2 shows the prediced GW using Eq. (1.35) and Eq. (1.36) for parameters similar to those of GW150914.[2]

Whilst we find the amplitude of the strain $|h|(t;\vartheta=0,\varphi=0) \sim 10^{-21}$ to be consistent with the observed GW150914 peak strain $h_{\rm GW150914} = 1\times10^{-21}$ [13] it is rather the frequency evolution to which our search algorithms are most sensitive to. Because the amplitude of GWs is extremely small by the time they reach the Earth advanced data analysis techniques, discussed in Section 1.6, are required to dig out potential signals. The main technique, matched filtering, relies on having accurate models for the gravitational waveform and in particular, an accurate model for the frequency (or equivalently the phase) evolution of the GW. To maximise the

[2] Approximate GW150914 parameters $\mathcal{M}_c = 30M_\odot$ and $d = 400\,\mathrm{Mpc}$

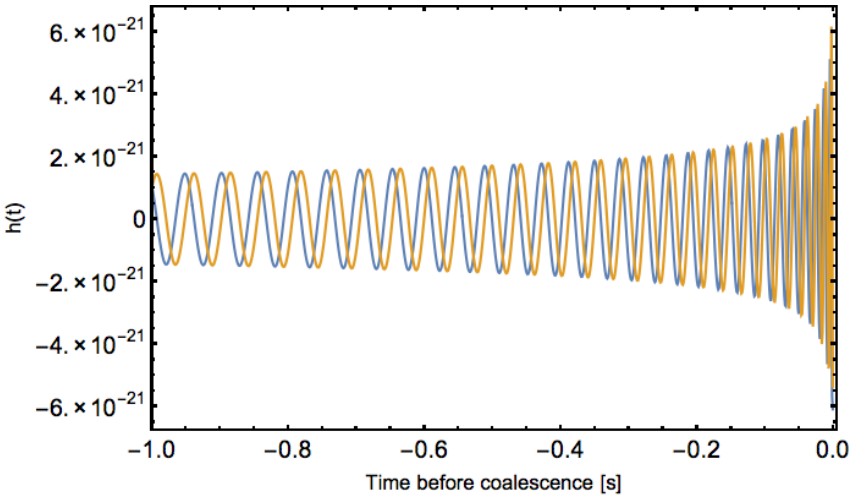

Figure 1.2: Illustration of a simple "chirp" waveform computed using the leading order quadrupole term. h_+ in blue and $h_\times$ in orange. To compare to GW150914 we plot the expected waveform with similar values for $\mathcal{M}_c = 30M_\odot$ and $d = 400\,\mathrm{Mpc}$. Although the peak strain is overestimated the correct order of magnitude is obtained. As the system gets closer to merging this simple approximation becomes inaccurate and higher order terms of full numerical relativity is needed to accurately compute the waveform.

detection probability, waveform models incorporating the dominant physical effects are needed.

The most complete way to compute the gravitational waveform from merging BBHs which incorporates fully general relativistic effects is to simulate them with numerical relativity. Constructing accurate gravitational waveform models which incorporate the results of numerical relativity is the subject of this thesis.

Throughout the rest of this thesis we will use $G = c = 1$ units unless stated otherwise.

1.1.2 Strain Decomposition

In the previous section we derived the GW strain emitted from a coalescing binary system as a function of the direction of propagation given by the spherical polar coordinates (ϑ, φ). When modelling GWs from binaries it is convenient to factor out the angular dependencies into spin-weighted (-2) spherical harmonics where we define the *complex* strain [150] as

$$H = h_+ - ih_\times \tag{1.37}$$

and its decomposition[3] as

[3]The spherical harmonics are defined in a cartesian coordinate system where the $\hat{\mathbf{z}}$ unit vector is identified with the initial direction of unit total angular momentum of the binary $\hat{\mathbf{J}}$.

$$H(t;\vartheta,\varphi) = \sum_{\ell=2}^{\infty}\sum_{m=-\ell}^{\ell} h_{\ell m}(t)\, Y^{-2}_{\ell m}(\vartheta,\varphi)\,. \tag{1.38}$$

The coefficients $h_{\ell m}$ are called the GW harmonics or modes. Due to the quadrupolar nature of GWs the leading order contribution in this decomposition comes from the $\ell = 2$ quadrupole term. In binary systems the dominant mode is $\ell = |m| = 2$ harmonic due to the symmetry of the system. Note that Equations (1.35) and (1.36) are entirely $(\ell, m) = (2, \pm 2)$ modes. The amplitude of sub-dominant (also called higher harmonics/modes) can be increased by increasing the mass-ratio and thereby increasing the asymmetry of the system. As the mass-ratio increases the relative strength of the sub-dominant modes with respect to the dominant mode increases. The strength of the modes also depends on the direction of propagation and viewing binaries with an "edge-on" inclination[4] ($\vartheta = \pi/2$) allows for the maximum effect of the sub-dominant modes on the overall strain.

This decomposition is completely general however, contributions beyond the leading harmonic can only be obtained if the stress-energy tensor used to describe the system contains higher order corrections from higher order mass moments and current moments [108, 34]. Higher order contributions to the full waveform can then occur at frequencies other than twice the orbital frequency.

In the case of precessing binaries (See Section 1.3.3) the orbital plane no longer defines a fixed reference system and when we use a static coordinate system to decompose the GW we find that sub-dominant modes are excited (see [157]),

In the next section we will discuss the instruments built that were able to reach the ground breaking sensitivities required to make the first GW detection.

1.2 Gravitational Wave Interferometers

The successful detection of GWs was achieved by the Laser Interferometer Gravitational-wave Observatory (LIGO) experiment on 14$^{\text{th}}$ September 2015 at 09:50:45 UTC ushering in the era of GW astronomy. The LIGO experiment was proposed in 1989 [76][5] in a collaboration between MIT and Caltech that has grown into the LIGO Scientific Collaboration (LSC). It is comprised of two identical twin laser interferometers, one in Hanford, Washington (H1) and another 3000 km[6] away in Livingston, Louisiana (L1). A greatly simplified schematic of the LIGO interferometers is shown in Figure 1.3. There are a number of other GW interferometers such as Virgo in Pisa, Italy [19], which will be joining the advanced detector network in 2016 as Advanced Virgo (AdV), GEO600 in Hannover, Germany [84], as well as future detectors un-

[4] When describing the observed GW the inclination angle is typically denoted by ι and the azimuthal angle φ is normally absorbed into the definition of the coalescence phase or *reference phase* Φ_0 because we are free to choose coordinates such that $\varphi = 0$.

[5] See [2] for a timeline of the development of LIGO

[6] The light travel time, through the Earth, is thus 10 ms.

der construction such as KAGRA in Japan [33] and the recently approved LIGO detector in India [102]. The prospects for GW astronomy when incorporating future detectors in the network are discussed in more detail in [18].

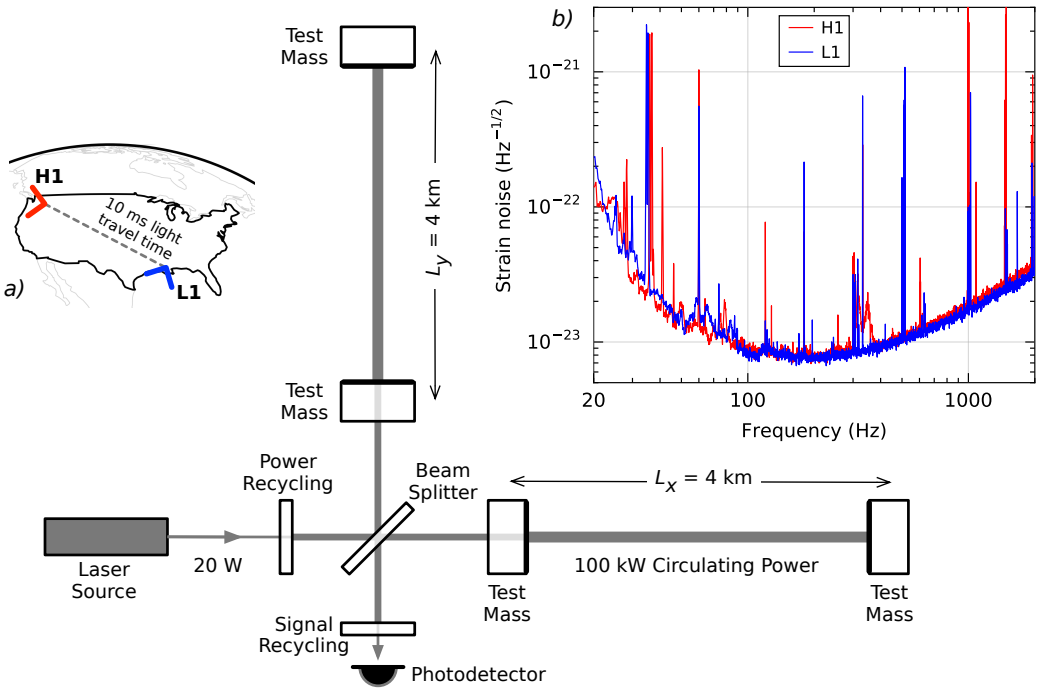

Figure 1.3: A simplified schematic of the advanced LIGO detectors, several modifications to the Michelson interferometer are shown such as power and signal recycling. The photodetector records the differential lengths of the arms. The inset figure a) shows the positions and relative orientation of the LIGO-Hanford and LIGO-Livingston detectors. Figure b) shows the power spectral density (PSD), a characterisation of the noise, of the LIGO detectors near the time of GW150914. Spikes in the PSD include instrument calibration lines, resonant violin modes from mass suspension and the 60 Hz electrical power grid. The noise at low frequencies is dominated by seismic noise, at high frequencies by quantum shot noise as well as thermal noise at the mid frequency range. Figure originally published in [13]

A Michelson interferometer consists of two "arms" almost orthogonal to each other. A laser beam is split evenly down each of the 4km arms (called the x and y arms). At the end of the arms mirrors, suspended by a quadruple pendulum system for seismic isolation, reflect the light that recombines at the beam splitter and is directed towards a photodetector which measures the intensity of the light. When the light recombines at the beam splitter they have acquired a π rad phase shift (because of the beam splitter) and thus when the arms have precisely the same length the laser beam should interfere destructively at the photodetector and no light should be detected. Therefore any change in the lengths of the arms, or equivalently, changes in the light travel time will cause some amount of light to reach the photodetector and thus a measure of the change in length of the arms. We

will see in the next section (Section 1.2.1) exactly how the light travel time changes when a GW is incident and how the detector's response depends on the incoming direction of the GW.

This description about how the LIGO interferometers work is vastly oversimplified and a number of modifications to the simple Michelson interferometer are critical for aLIGO to reach the high sensitivities required for regular detections; for a concise treatment we refer the reader to [62, 11].

1.2.1 Interferometer Response to Gravitational Waves

The signal measured at the photodetector of an interferometer can be expressed as the difference of the measured arm lengths normalised by their expected lengths $\bar{L} = \bar{L}_x = \bar{L}_y$, i.e., $\Delta L/\bar{L} \equiv (L_x - L_y)/\bar{L}$. Thus when the arms are the same length $\Delta L = 0$ as desired. In the following we shall explicitly show the factors of c.

When a GW is incoming from directly over head such that the principal axes of the h_+ polarisation coincide with the arms of the detector, in the TT gauge we can write the line element as

$$ds^2 = -c^2dt^2 + (1 + h_+^{TT})dx^2 + (1 - h_+^{TT})dy^2 + dz^2 \,. \tag{1.39}$$

Here we have dropped the time dependence of the GW by assuming $\lambda_{\rm gw} \gg \bar{L}$ such that the amplitude of the GW is approximately constant over short time intervals. A nice feature of the TT gauge is that the coordinates of freely falling objects are constant. This means that during the passage of a GW the coordinates lines and proper distance in effect get distorted to ensure the coordinate locations are constant. Therefore if our end test masses in our interferometer are in free-fall (or approximately in free-fall) we can use the TT gauge to determine the effect of a GW passing through it, to first order. To determine the path light-like particles take in this spacetime we solve the above line element subject to the constraint $ds^2 = 0$.

If we consider changes in the x arm only first we find

$$\begin{aligned} c^2dt^2 &= (1 + h_+)\, dx^2 \,, \\ c\, dt &= \sqrt{1 + h_+}\, dx \,. \end{aligned}$$

Expanding the RHS to first order and integrating along the arm,

$$\begin{aligned} c\int_{t_0}^{t_1} dt &= \int_0^{\bar{L}_x} \left(1 + \frac{1}{2}h_+\right) dx \,, \\ c\,(t_1 - t_0) &= \bar{L}_x \left(1 + \frac{1}{2}h_+\right) \,, \end{aligned} \tag{1.40}$$

where the time t_0 and t_1 are the times of emission from the laser and the time of arrival at the end mirror (at $x = \bar{L}_x$) respectively. If t_2 is the time at which the

light returns to the point of emission and summing an analogous calculation allows us to write down the expression for the round trip travel time

$$c\,\Delta\tau_x \equiv 2L_x = 2\bar{L}_x + \bar{L}_x h_+ \,. \tag{1.41}$$

Where $\Delta\tau_x \equiv (t_2 - t_0)_x$ is the round trip travel time in the x arm. Note that L_x (without the overbar) denotes the measured proper length and $\bar{L}_x$ denotes the expected length. Performing the same calculation for the y arm we get

$$c\,\Delta\tau_y \equiv 2L_y = 2\bar{L}_y - \bar{L}_y h_+ \,. \tag{1.42}$$

Computing the difference between Eq. (1.41) and Eq. (1.42) and noting that the expected lengths of both arms are equal, i.e., $\bar{L} = \bar{L}_x = \bar{L}_y$ we find

$$\frac{\Delta L}{\bar{L}} \equiv \frac{L_x - L_y}{\bar{L}} = h_+ \,. \tag{1.43}$$

Recall that the variables *with* an overbar denote the expected value in absence of a GW and variables *without* an overbar denote measured quantities – i.e., the *proper length* of the arms. Thus we find that the measured change in the *combined* arm length is directly proportional to the gravitational strain. This was for the special case of a linearly polarised GW directly overhead the detector and optimally orientated with respect to their xy axes. To completely generalise this we first note that we can express the detector's response to a GW as

$$h = \mathbf{D} : \mathbf{h} = D_{ij} h^{ij} \,, \tag{1.44}$$

where D_{ij} is the *detector tensor* which is dependent on the geometry of the detector. For an interferometer with exactly orthonal arms described by the appropriate basis vectors in a cartesian coordinate system $\hat{\mathbf{u}} = (1, 0, 0)$ and $\hat{\mathbf{v}} = (0, 1, 0)$ we have

$$\mathbf{D} = \frac{\hat{\mathbf{u}} \otimes \hat{\mathbf{u}} - \hat{\mathbf{v}} \otimes \hat{\mathbf{v}}}{2} \,. \tag{1.45}$$

Defining the constant *polarisation tensors* $\mathbf{e}_+$ and $\mathbf{e}_\times$ of a GW as

$$\mathbf{e}_+ = \begin{bmatrix} 1 & 0 & 0 \\ 0 & -1 & 0 \\ 0 & 0 & 0 \end{bmatrix} \,, \quad \mathbf{e}_\times = \begin{bmatrix} 0 & 1 & 0 \\ 1 & 0 & 0 \\ 0 & 0 & 0 \end{bmatrix} \tag{1.46}$$

we can write the GW as

$$\mathbf{h} = h_+ \mathbf{e}_+ + h_\times \mathbf{e}_\times \,. \tag{1.47}$$

Now evaluating Eq. (1.44) we get

$$h = \mathbf{D} : (h_+ \mathbf{e}_+ + h_\times \mathbf{e}_\times) = h_+ F'_+ + h_\times F'_\times \,. \tag{1.48}$$

The two new functions we have defined are called the *antenna response* or *antenna pattern* functions. They depend on the sky position where a signal is coming from. The interferometer antenna patterns are functions of the standard spherical polar coordinates (θ, ϕ) and are given by [153]

$$F'_+ = \frac{1}{2}(1+\cos^2\theta)\cos 2\phi \tag{1.49}$$
$$F'_\times = \cos\theta \sin 2\phi\,. \tag{1.50}$$

To completely specify this system we need the final Euler angle. Consider the following and associated Figure 1.4. An interferometer's response to an incident GW depends on the position on the sky where the GW is coming from. We construct the *detector frame* by erecting a cartesian coordinate system where the x^D and y^D axes (with $\{\hat{\mathbf{e}}_x^D, \hat{\mathbf{e}}_y^D\}$ basis vectors) point in the directions of the x and y arms of the interferometer and $\hat{\mathbf{e}}_z^D = \hat{\mathbf{e}}_x^D \times \hat{\mathbf{e}}_y^D$ completes the orthonormal triad. We define the position on the sky where the GW is coming from with standard spherical polar coordinates (θ, ϕ). To describe the incoming GW we construct the *radiation frame*, a cartesian frame located at (θ, ϕ) relative to the detector frame. The z^R axis (with basis vector $\hat{\mathbf{e}}_z^R$) with the wavevector of the GW. The x^R and y^R axes are chosen to coincide with the principal axes of the h_+ polarisation tensor $\mathbf{e}_+$. The final angle needed to relate the radiation frame to the detector frame is the *polarisation angle* ψ, which is the, in-plane angle required to rotate $\hat{\mathbf{e}}_x^R$ into $\hat{\mathbf{e}}_x^D$.[7]

Due to the quadrupole nature of the GW the new F_+ and $F_\times$ are related to the old F'_+ and $F'_\times$ as

$$F_+ = F'_+ \cos 2\psi - F'_\times \sin 2\psi \tag{1.51}$$
$$F_\times = F'_+ \sin 2\psi + F'_\times \cos 2\psi\,. \tag{1.52}$$

The completely generalised interferometer response to a completely arbitray incoming GW is thus

$$h(t;\theta,\phi,\psi) = h_+(t)F_+(\theta,\phi,\psi) + h_\times(t)F_\times(\theta,\phi,\psi)\,. \tag{1.53}$$

The strain h is also a function of source parameters, which are described in Section 1.3.1.

1.3 Sources

In Section 1.1.1 we calculated the expected GW amplitude from a source with parameters similar to GW150914 and found a consistent value of $\sim 10^{-21}$. Only *compact* binary systems, i.e., binaries consisting of combinations of neutron stars and

[7] The polarisation angle could also be defined as the angle needed to rotate the radiation frame into the *source frame*.

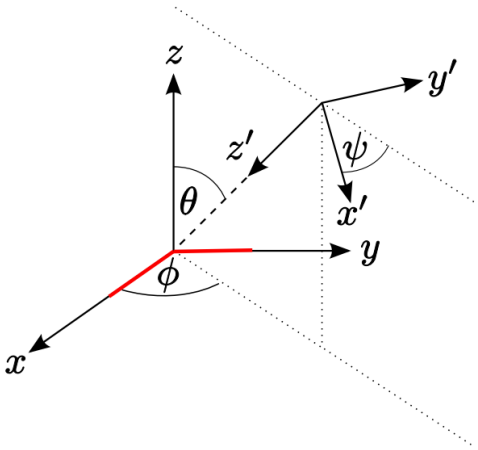

Figure 1.4: An illustration of how the detector frame (x, y, z), with basis vectors $\{\hat{\mathbf{e}}_i^D\}$ is related to the radiation frame (x', y', z'), with basis vectors $\{\hat{\mathbf{e}}_i^R\}$. The angles (θ, ϕ) locate the origin of the radiation frame relative to the detector frame on the sky (sky position) while the polarisation angle ψ describes the relative angle between the x and x' axis. The orientation of x' axis is chosen to coincide with the principal axis of the h_+ polarisation tensor $\mathbf{e}_+$. The red lines illustrate the arms of an interferometer. Figure originally published in [124]

black holes are capable of reaching the low orbital separations and high velocities whilst remaining intact needed to produce GWs in the frequency band of advanced detectors.

There are many potential sources inside the advanced detector's frequency range that we hope to detect such as transient burst events from galactic supernovae, long lasting continuous emission from pulsars and an orchestra of low amplitude signals creating a stochastic GW background. The following discussion will be restricted to BBHs, for a review of expected GW sources see [153].

1.3.1 Binary Black Holes

A BBH system is a gravitationally bound binary where both members are black holes (BHs). We label the primary and secondary BH with 1 and 2 respectively such that the mass-ratio is given by $q \coloneqq m_1/m_2 \in [1, \infty]$ where $m_1 \geq m_2$ and throughout this thesis we will use the notation $m_1 : m_2$ for the mass ratio in the text. Each BH can also possess spin angular momentum $\mathbf{S}_i = \{S_i^x, S_i^y, S_i^z\}$, where the dimensionless spin vector of the i^{th} BH is given by

$$\boldsymbol{\chi}_i \coloneqq \frac{\mathbf{S}_i}{m_i^2}\,. \tag{1.54}$$

Figure 1.5 defines the coordinate system attached to a generic binary system. The magnitude $|\boldsymbol{\chi}_i| \leqslant 1$ is bounded by the Kerr limit and the spins are defined with respect to the orbital angular momentum $\mathbf{L}$. The total angular momentum is then

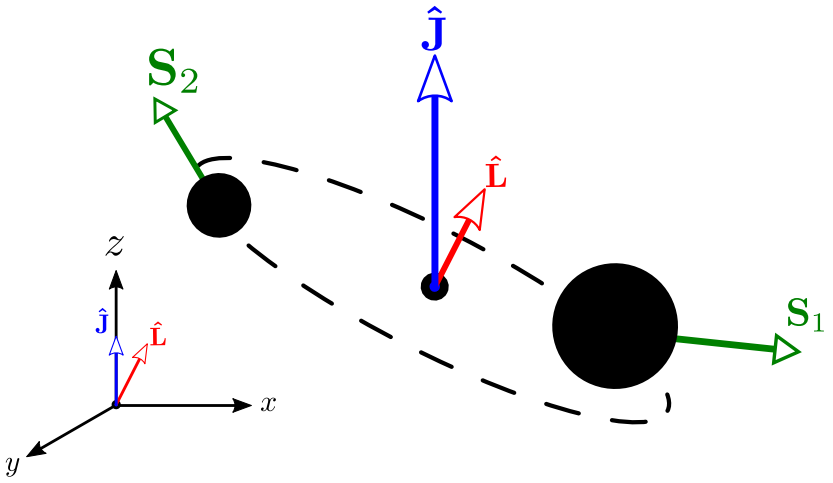

Figure 1.5: Coordinate system attached to a generic (precessing) BBH system. The z axis is aligned with the total angular momentum $\hat{\mathbf{J}}$. The spins are defined with respect to the orbital angular momentum $\hat{\mathbf{L}}$. In generic configurations $\hat{\mathbf{L}}$ and the BH spins $\mathbf{S}_i$ will precess around the approximately fixed direction $\hat{\mathbf{J}}$.

defined as

$$\mathbf{J} = \mathbf{L} + \mathbf{S}_1 + \mathbf{S}_2 \,. \tag{1.55}$$

The interplay between the vectors in the Eq. (1.55) will be key when investigating the effects of spin in BBH systems; see Section 1.3.3.

Assuming this system evolves only through emission of GWs then there are 15 parameters that fully describe these systems. We separate these into 8 *intrinsic* parameters $\boldsymbol{\Xi}$:

$$\boldsymbol{\Xi} = \begin{cases} M & \text{Total Mass} \\ \eta & \text{Symmetric Mass-Ratio} \\ \mathbf{S}_i & \text{Spin angular momentum of } i^{th} \text{ BH} \,, \end{cases} \tag{1.56}$$

which change the dynamics and physical timescales that the system evolves over, and 7 *extrinsic* parameters $\boldsymbol{\Lambda}$:

$$\boldsymbol{\Lambda} = \begin{cases} d_L & \text{Observed (Luminosity) distance} \\ \theta & \text{Sky position - polar angle} \\ \phi & \text{Sky position - azimuthal angle} \\ \psi & \text{Polarisation Angle} \\ \iota & \text{Source Inclination} \\ t_0 & \text{Reference Time} \\ \Phi_0 & \text{Reference Phase} \,. \end{cases} \tag{1.57}$$

Extrinsic parameters affect how the GW is observed such as the sky-location or

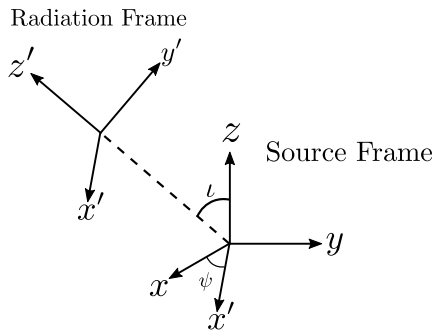

Figure 1.6: Illustration of the relationship between the source frame (x, y, z), with basis vectors $\{\hat{\mathbf{e}}_i^S\}$ and the radiation frame (x', y', z'), with basis vectors $\{\hat{\mathbf{e}}_i^R\}$. ι is the inclination angle and ψ is the polarisation angle between the source frame and the radiation frame.

how far away the source is.

Next we introduce the *source frame* to complete the detector frame – radiation frame – source frame relationship. Figure 1.6 illustrates how the source frame is related to the radiation frame and Figure 1.4 relates the radiation frame to the detector frame. The source frame's $\hat{\mathbf{e}}_z^S$ is defined to lie along the $\hat{\mathbf{J}}$ direction. From the detector's point of view, the angle between the line of sight $\hat{\mathbf{N}} = (\theta, \phi)$ and $\hat{\mathbf{e}}_z^S$ is defined to be the *inclination* angle ι, which is also the angle between $\hat{\mathbf{e}}_z^S$ and $\hat{\mathbf{e}}_z^R$. We define the angle that rotates the $\hat{\mathbf{e}}_x^S$ into $\hat{\mathbf{e}}_x^R$ to be zero implicitly without loss of generality.

As with any binary system the eccentricity of the orbit is also an intrinsic parameter effecting the resulting gravitational waveform. However, in [139] it was shown that the emission of GWs has the effect of efficiently circularising orbits. This implies that binaries formed through *isolated* evolution [38] will have negligible eccentricity by the time they enter the frequency band of advanced detectors. However, through *dynamical capture* scenarios it is possible to form binaries with separations such that the GW frequency is near the advanced detector frequency band and large enough eccentricities that there is not enough time for the binary to circularise. These systems are not expected to be a dominant population in advanced detector searches and we neglect them in all following work.

1.3.2 The Three Stages - Inspiral, Merger and Ringdown

As a compact binary evolves through the emission of gravitational radiation it passes smoothly through three stages called: (i) the inspiral, (ii) the plunge/merger and (iii) the ringdown. Figure 1.7 shows the gravitational waveform from a NR simulation of a mass-ratio 1:4 BBH merger with spins $\boldsymbol{\chi}_i \cdot \hat{\mathbf{L}} = 0.75$ $(i = 1, 2)$.

The Inspiral – During this stage the orbital separation is large and the emission of GWs is small and at low frequencies, here the quadrupole approximation is at its most accurate. Over time the orbital separation will shrink due to energy and

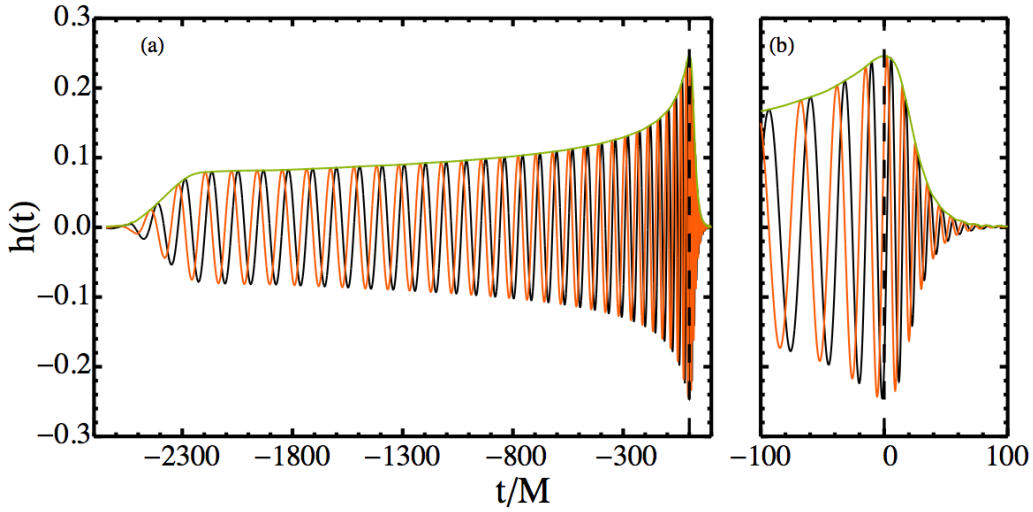

Figure 1.7: Gravitational waveform from a mass ratio 1:4 BBH with aligned-spins $\boldsymbol{\chi}_i \cdot \hat{\mathbf{L}} = 0.75$ $(i = 1, 2)$. The larger the aligned-spin is the higher orbital (as thus gravitational wave) frequencies the system reaches, this is known as the "hang-up" effect. Left panel a): The full length of the NR simulation is shown. The last 15 orbits (30 GW cycles) were simulated, early times of the simulation are considered to be part of the inspiral. The smooth transition from zero near the beginning of the data is an artifact from the fixed frequency integration [149]. Right panel b): A zoom-in around the time of peak GW emission (dashed line at t=0). Around this time the merger takes place. Shortly after t=0 the system enters the ringdown stage.

angular momentum being carried away by GWs increasing the orbital velocity. GW emission increases in amplitude and frequency.

Post-Newtonian (PN) theory [42], a perturbative expansion in the orbital velocity, and EOB theory [51, 52, 67], resummed post-Newtonian (PN), has been very successful in computing the gravitational waveform covering the inspiral regime. However, it is unable to compute the waveform when the orbital velocities are high compared to the speed of light. This condition is violated close to merger.

The Merger – During this stage the orbital velocities are very high[8] and finite-size effects cannot be neglected. NR is the only way to compute solutions to the Einstein equations for BBH mergers. It is during this stage where the GW amplitude, frequency and luminosity reach their peaks.[9] The merger results in a highly distorted and dynamic spacetime, the event horizons during the merger "reach out" and connect at a point, forming a common horizon. For an illustration of how distorted the space-time around merging BHs can get see Figure 2 in Ref [61].

Ringdown – The highly distorted horizon relaxes to its equilibrium state, a Kerr BH [105], by emitting GWs made up of quasi normal modes (QNMs) [109]. QNMs

[8] The peak orbital velocity of GW150914 is estimated to approximately $v/c \sim 0.6$ [13]

[9] The peak luminosity for GW150914 was $3.6 \times 10^{56} \mathrm{erg\,s^{-1}}$ and radiated $3M_\odot$ into gravitational radiation.

are exponentially damped sinusoidal waves. Due to the *no-hair* theorem [101] the frequency spectrum only depends on the final mass M_f and spin a_f. The amplitudes of the various modes can be related to the masses and spins of the coalescing BHs [104, 116].

Remnant Properties – GWs radiate energy, angular momentum and also linear momentum. Emission of linear momentum can impart a recoil velocity or "kick" on the final BH in a direction dependent on the specifics of the merger. NR calculations of these "kicks" found that in extreme cases that demand specific orientations of the spins, the remnant-kick velocity can be as high as $4000\,\mathrm{km\,s^{-1}}$ [49]. This result is particularly interesting as it allows super-massive-black-holes at the centre of galaxies to overcome the escape velocity of its host galaxy. Note that the direction of the spin of the remnant BH can be very different to the orientation of two BHs prior to merger, see for example Ref [57].

1.3.3 Precessing Binary Black Holes

The most general kind of BBH system will contain BHs with spins that have *some* component perpendicular to the orbital angular momentum, i.e., some component of the spin will be *in* the orbital plane. Figure 1.5 illustrates the spin orientation in a generic BBH system.

The spin-orbit interaction and the characterisation of precessing systems is described in detail in [29, 107]. Spin-orbit coupling causes the orbital angular momentum to precess around the near constant direction of the total angular momentum, as a result the orbital plane wobbles. The individual BH spins also precess around this direction. The BH spin vectors and orbital angular momentum also have nutation effects but these are usually a small effect. During precession $\hat{\mathbf{L}}$ is always the direction of prominent GW emission but this is now precessing around $\hat{\mathbf{J}}$, the observed gravitational waveform can become very complicated.

The majority of precessing configurations will evolve through *simple* precession. Here $\hat{\mathbf{J}}$ remains relatively constant throughout the evolution. Another type of precession called *transitional* precession occurs when the orbital angular momentum and the spin angular momentum are almost equal and opposite. As the system evolves the orbital angular momentum decreases while the magnitude of the spin angular momentum remains relatively constant. This can cause the total angular momentum to change sign during the evolution. Systems that are unstable to transitional precession can transition from simple precession of $\hat{\mathbf{L}}$ around $\hat{\mathbf{J}}$ through a transitional precession period where $\mathbf{J}$ loses stability and "tumbles" through space, and later settles back down into a quasi-equilibrium state where simple precession returns around the direction of the new total angular momentum.

The individual BH spins can also evolve in curious ways. It's possible for the BH's polar spin angle to increase over time and given long enough, to point in the

completely opposite direction. Long numerical simulations performed in [117] found close agreement between NR and PN for the spins and suggest this evolution persists over the inspiral until merger.

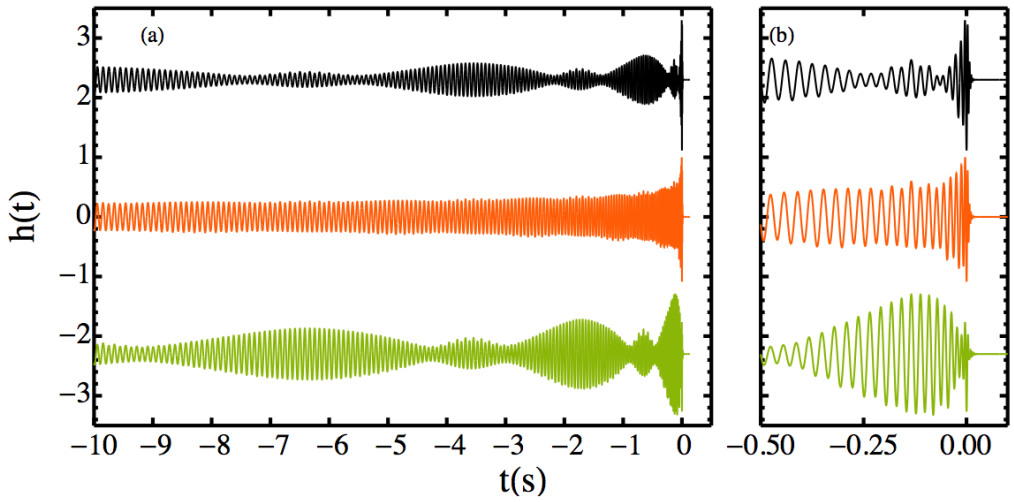

Figure 1.8: The effect of precession on the gravitational waveform (h_+) as predicted by the precessing EOB model `SEOBNRv3` [136]. The waveforms, artificially displaced to allow for ease of comparison, all correspond to a mass-ratio 1:5 BBH with a total mass of $60\,M_\odot$ and equal spins of 0.99 directed *in* the orbital plane at the beginning of the evolution. The left panel shows the waveform from a gravitational wave frequency of 10 Hz through merger and ringdown and the right panel zooms in around the time of merger. The morphology of the waveforms strongly depend on the orientation. `LALSuite` was used to generate these waveforms. To specify the orientation of the source relative to the detector `LAL` uses the convention that the inclination angle ι is the angle between the orbital angular momentum $\hat{\mathbf{L}}$ and the vector $\hat{\mathbf{N}}$ connected to the detector. The inclination angle for the three curves are $\iota = \{0, \pi/4, \pi/2\}$ rad from top to bottom.

Precession introduces modulation in to the amplitude and phase due to the principal axis of radiation emission varying with respect to the observer. Figure 1.8 illustrates the effect of precession on the observed gravitational waveform as predicted by the precessing EOB model `SEOBNRv3` [136]. The waveforms, artificially displaced to allow for ease of comparison, all correspond to a mass-ratio 1:5 BBH with a total mass of $60\,M_\odot$ and equal spins of 0.99 directed *in* the orbital plane at the beginning of the evolution. The left panel shows the waveform from a gravitational wave frequency of 10 Hz through merger and ringdown and the right panel zooms in around the time of merger. The three waveforms correspond to three different inclination angles (here, the inclination angle is the angle between $\hat{\mathbf{L}}$ and the line of sight $\hat{\mathbf{N}}$) $\iota = \{0, \pi/4, \pi/2\}$ rad from top to bottom. Depending on the orientation, varying degrees of modulation is observed.

In terms of a spin-weighted spherical harmonic decomposition that the inertial frame the GW is being decomposed into, this is a physical but not convenient form

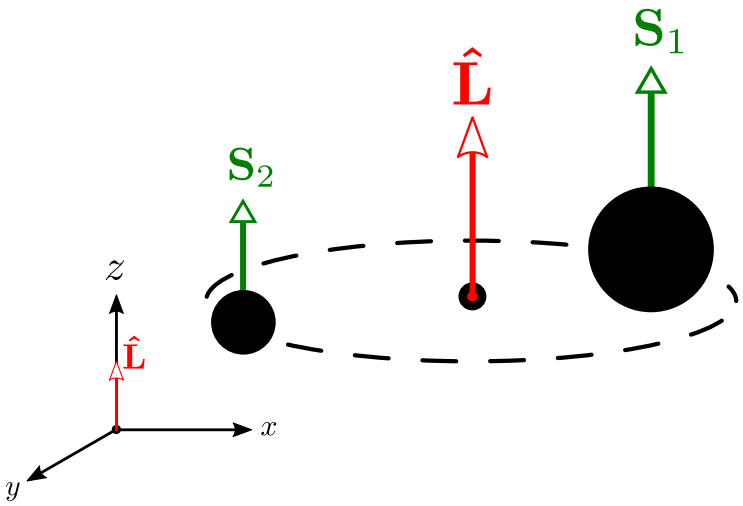

Figure 1.9: Coordinate system attached a non-precessing BBH systems. The z axis is aligned with the orbital angular momentum $\hat{\mathbf{L}}$, which points in the same direction as $\hat{\mathbf{J}}$ in non-precessing systems. The orbital plane in non-precessing systems is fixed and the size and direction of the spins (aligned or anti-aligned with $\hat{\mathbf{L}}$) effect the dynamics through the hang-up effect.

in which to study systematically the phenomenology of precessing systems. In particular sub-dominant modes not present in the non-precessing version of the system are now present. It was found in [157, 158] that a time dependent coordinate transformation can be applied to the binary to align the principal axis of emission with the fixed z axis of the decomposition frame. When a precessing system is transformed into this *quadrupole aligned* frame the hierarchy of the modes are restored and the modulation to the waveform is minimised.

In precessing cases no symmetries exist and this presents the next biggest challenge for waveform modelling. To create an approximate precessing model one method is to model the angles needed to convert a precessing binary into a non-precessing binary and then reverse engineer them. This way a non-precessing waveform can be "twisted" into a precessing waveform. This has been implemented in [91] and [137]. In such a procedure an accurate aligned-spin model is essential. Using the results in this thesis `IMRPhenomP` [91] was upgraded by using as the non-precessing model `IMRPhenomD` [100, 106]. This model `IMRPhenomPv2` was used in the analysis of aLIGO data including GW150914 [17, 15].

1.3.4 Non-Precessing Binary Black Holes

On the way to modelling the generic system, both astrophysically and practically motivated is the study of aligned spin systems. In these systems the spins of the BHs are constrained to lie either parallel or anti-parallel with $\hat{\mathbf{L}}$. If we fix a cartesian coordinate system to aligned spin binaries such that we identify $\hat{\mathbf{z}}$ with $\hat{\mathbf{L}}$ as in Figure 1.9 then the only components of the spins that are non-zero are $\boldsymbol{\chi}_i = \{0, 0, \chi_i^z\}$.

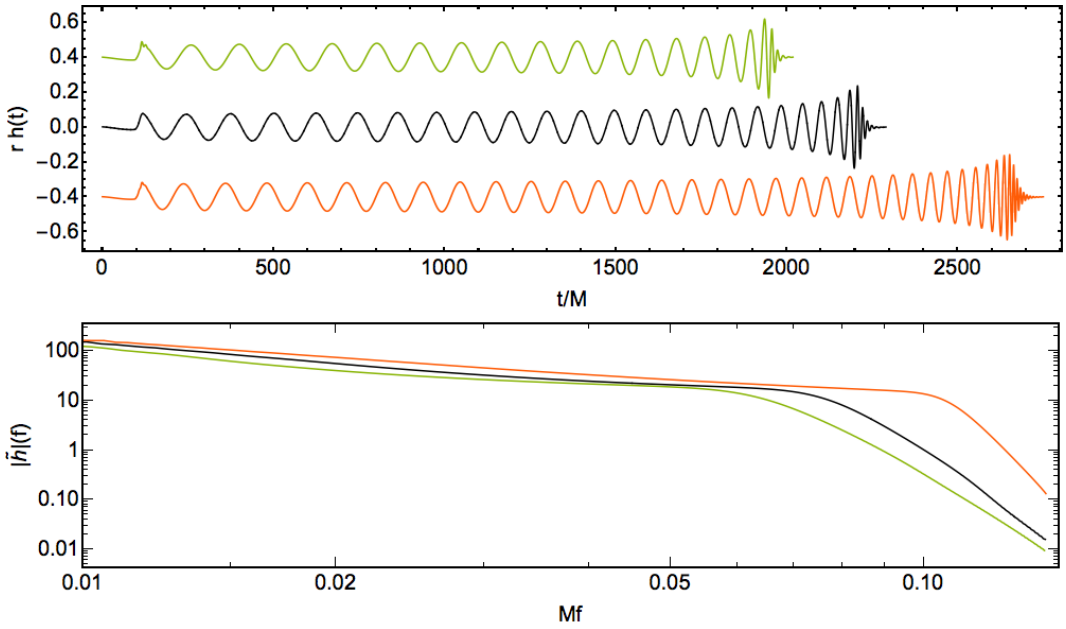

Figure 1.10: Top Panel: Time domain strain calculated using fixed frequency integration [149]. Mass-ratio 1:4 binaries with aligned spins for $(-0.75, -0.75)$ (green), non-spinning (black) and $(+0.75, +0.75)$ (orange). Bottom Panel: Modulus of the Fourier domain strain (i.e., the Fourier domain amplitude) in geometric units (same colour scheme). The orbital hangup effect is apparent from the fact that the high aligned-spin case reaches much higher gravitational wave frequencies (before transitioning to the ringdown) and takes longer to merge.

A special case of non-precessing systems is the non-spinning system where $\boldsymbol{\chi}_1 = \boldsymbol{\chi}_2 = 0$. Non-precessing systems through the merger phase are the most well studied BBH systems. One particularly interesting effect is the orbital hang-up. The component of the spin (anti-) aligned with the $\hat{\mathbf{L}}$ has the effect of (increasing) decreasing the rate of inspiral.[10] To illustrate the hang-up effect Figure 1.10 shows three mass-ratio 1:4 aligned-spin simulations produced with the BAM code (See Section 2.2). The aligned-spin components are $\chi_1^z = \chi_2^z = \{-0.75, 0, +0.75\}$ (green, black and orange respectively). The top panel shows the dominant harmonic in the time domain, which illustrates how the time time to merger is effected. The bottom panel shows the amplitude of the Fourier domain dominant harmonic and illustrates how the maximum frequency before transitioning to the ringdown increases with increasing aligned spin. All three configurations started out with similar separations of order $10M$.

The effects of both aligned-spin components, to first approximation, can be mod-

[10] The intuition behind this is as follows. The Kerr inner-most stable circular orbit (ISCO) as a function of the Kerr spin is further away for retrograde orbits and closer for prograde orbits. By having an ISCO closer to the horizon a particle is able to orbit on circular orbits at smaller radii and thus higher orbital velocity (according to Kepler's 3$^{\text{rd}}$ law.) In the context of BBH and abusing the analogy of the ISCO we can see that a BBH should be able to orbit closer to each other and thus emit GWs at higher frequencies before eventually merging.

elled with a single *effective* spin parameter. This parameter influences the rate of inspiral and is useful for waveform modelling as it allows the parameter space to be reduced by one dimension without having a significant impact on the performance of the model. A natural aligned-spin effective spin parameter comes from taking the 1.5 PN spin-orbit term [20] given by

$$\chi_{\rm PN} = \chi_{\rm eff} - \frac{38}{113}\eta(\chi_1 + \chi_2)\,. \tag{1.58}$$

Here $\chi_{\rm eff}$ is simply a mass-weighted total spin

$$\chi_{\rm eff} = \frac{m_1\chi_1 + m_2\chi_2}{M} \in [-1, 1]\,. \tag{1.59}$$

Although $\chi_{\rm PN}$ is a more accurate parameterisation the first aligned-spin IMR phenomenological models used the $\chi_{\rm eff}$ effective spin parameter [21, 151]. Note that this parameterisation comes from PN theory and as such becomes inaccurate as the binary approaches merger nevertheless, this and similar parameterisations have proven to be adequate when modelling NR.

Whilst a single spin parameterisation does prevent the ability of parameter estimation to uniquely determine the individual BH spins, studies have shown that in the advanced detector era only the spin on the larger BH will be measurable in the best of cases [147].

These systems possess a symmetry about the orbital plane, which simplifies their waveform structure when decomposed into spin-weighted spherical harmonic modes given by the decomposition in Equation 1.38. The symmetry implies the following relationship between modes,

$$h_{\ell\, m} = h^*_{\ell\, -m}\,. \tag{1.60}$$

Furthermore, when decomposed in this way the dominant contribution comes from the ($\ell = 2$, $|m| = 2$) mode further simplifying modelling. In general, for non-precessing systems, higher order $\ell > 2$ modes are excited for systems with higher degrees of asymmetry. Thus the higher the mass-ratio the stronger the sub-dominant modes are with respect to the leading order ($\ell = 2$, $|m| = 2$) mode.

Figure 1.11 illustrates the effect of higher harmonics on the observed gravitational waveform as predicted by the non-spinning, higher mode EOB model `EOBNRv2HM` [134]. The observed GW is computed using $h(t) = h_+ {\rm Cos}(2\psi) + h_\times {\rm Sin}(2\psi)$ with a polarisation angle of $\psi = \pi/3$ (assuming the detector response functions are $F_+ = F_\times = 1$). The waveforms all correspond to a mass-ratio 1:6 BBH with a total mass of 140 $M_\odot$ but at three different inclination angles; face-on $\iota = 0$ (black), intermediate $\pi/4$ (orange) and edge-on $\iota = \pi/2$ (green). The left panel shows the waveform from a gravitational wave frequency of 10 Hz through merger and ringdown and the right panel zooms in around the time of merger. For the face-on case the effect of higher

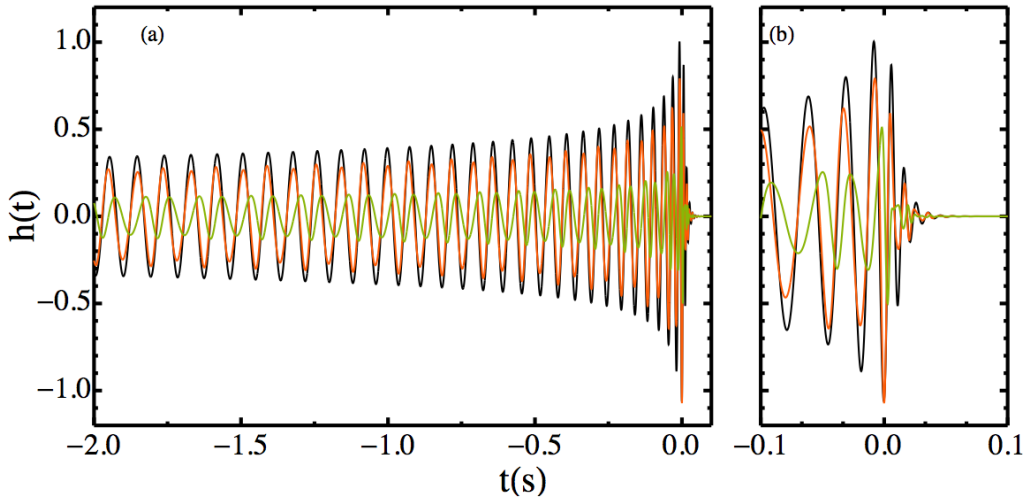

Figure 1.11: Prediction of the *observed* gravitational waveform including contributions beyond the leading order ($\ell = 2$, $|m| = 2$) mode as predicted by the non-spinning, higher mode EOB model `EOBNRv2HM` [134]. The observed GW is computed using $h(t) = h_+ \mathrm{Cos}(2\psi) + h_\times \mathrm{Sin}(2\psi)$ with a polarisation angle of $\psi = \pi/3$ (assuming the detector response functions are $F_+ = F_\times = 1$). The waveforms all correspond to a mass-ratio 1:6 BBH with a total mass of 140 $M_\odot$ but at three different inclination angles; face-on $\iota = 0$ (black), intermediate $\pi/4$ (orange) and edge-on $\iota = \pi/2$ (green). The left panel shows the waveform from a gravitational wave frequency of 10 Hz through merger and ringdown and the right panel zooms in around the time of merger. For the face-on case the effect of higher modes is minimal and there are no amplitude modulations. As the inclination angle increases, the strength of the higher modes relative to the ($\ell = 2$, $|m| = 2$) mode increases. This introduces modulations to the amplitude and also the frequency evolution is slightly different to the face-on case.

modes is minimal and there are no amplitude modulations. As the inclination angle increases, the strength of the higher modes relative to the ($\ell = 2$, $|m| = 2$) mode increases. This introduces modulations to the amplitude and also the frequency evolution is slightly different to the face-on case. For the edge-on case $h_\times$ is zero and only h_+ is observed.

1.4 Numerical Relativity

The Einstein equations are a set of 10 coupled, non-linear, second-order partial differential equations for the metric tensor g_{ab}. Cast in their covariant space-time form as in Eq. (1.1) allows one to find solutions that apply for all of space and for all time simultaneously. Typically this type of approach is only well suited for static and/or highly symmetric systems [160, 105]. To study dynamic, strong-field systems we need to solve the Einstein equations numerically. This is the subject of numerical relativity.

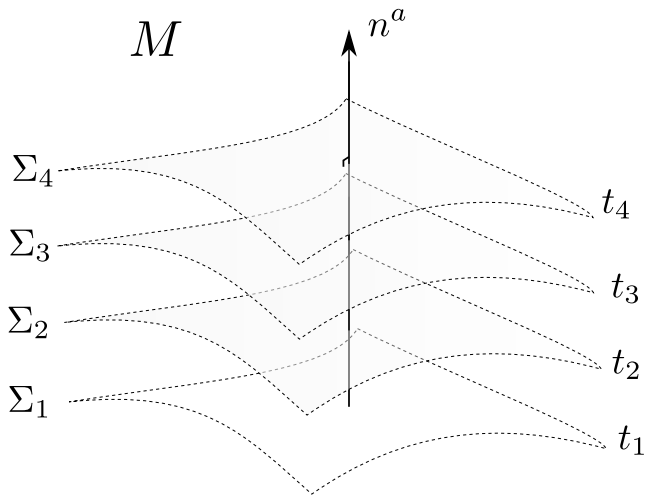

Figure 1.12: Geometrical representation of the 3+1 decomposition. The 4 dimensional space-time manifold M is decomposed into a foliation of 3 dimensional curved space-like hypersurfaces $\{\Sigma\}_t$ parameterised by a scalar field t. Each surface has a constant value of t which represents surfaces of constant coordinate time with the vector $n^a = -g^{ab}\nabla_b t$ being the time-like normal to these slices. Adapted from [37]

To implement the Einstein equations numerically as an initial value problem we first decompose the 4 dimensional space-time, M, into a *foliation* of 3 dimensional curved space-like hypersurfaces $\{\Sigma\}_t$ parameterised by a scalar field t interwoven with a family of time-like curves as illustrated in Figure 1.12. This is known as a 3+1 Arnowitt-Deser-Misner (ADM) decomposition [30, 175, 174]. Each surface has a constant value of t which represents surfaces of constant coordinate time with the vector $n^a = -g^{ab}\nabla_b t$ being the time-like normal to these slices. Each spatial slice has an intrinsic curvature described by the induced spatial metric on it given by,

$$\gamma^{ab} = g^{ab} + n^a n^b \,, \tag{1.61}$$

and an extrinsic curvature that describes how the slice is embedded in the higher dimensional space, which we can express in terms of quantities native to each slice as the gradient of the normal vector to the slice, projected into the slice using the induced spatial metic [37]:

$$K_{ab} = -\gamma_a^c \gamma_b^d \nabla_c n_d \,. \tag{1.62}$$

As the Einstein equations are second order for the metric in the initial value formulation we need to specify the induced spatial metric and its time derivative on a spatial slice to specify the problem. Following York [175], we can specify the time derivative of the metric through the extrinsic curvature as expressed by it's Lie derivative along the flow of the normal vector, this is proportional to the extrinsic curvature expressed as

$$K_{ab} = -\frac{1}{2}\mathcal{L}_{\mathbf{n}}\gamma_{ab}\,. \tag{1.63}$$

Therefore the evolution variables in the initial value formulation are the induced spatial metric and the extrinsic curvature. The spatial metric and the normal to the slice allow us to project 4 dimensional tensors into spatial components in the slice and into temporal components perpendicular to the slice. The 3+1 ADM equations are obtained by projecting the 4 dimensional Einstein equations Equation 1.1 into space-like components in the slice and time-like components normal to the slice. The decomposed system of equations of the 4 dimensional Einstein equations are comprised of the *constraint* equations obtained by spatial projections, and the *evolution* equations obtained by projections normal to the spatial slice. These equations, which are equivalent to the Einstein equations, are now first order in time as opposed to second order as we started out with.

Solving the constraint equations is the speciality of the field of initial data construction. Here the question is, given a physical scenario such as an orbiting binary black hole system, what are the values of (γ_{ab}, K_{ab}) that satisfy the constraint equations. The method of solving the constraint equations can be greatly simplified by performing a conformal transformation [63], but it is still an active area of research to produce highly spinning BBH initial data [118, 119]. Once the constraint equations have been solved we have values for (γ_{ab}, K_{ab}) across the computational domain that we wish to evolve through time using the evolution equations. Note that this system of equations are "constraint satisfying" in the sense that if we supply some initial data at time t then, modulo errors in the numerical implementation, the solution will satisfy the constraint equations for all time.

On the subject of the coordinate freedom in GR each hypersurface is labelled by coordinates that are completely arbitrary and in general freely specified on each spatial slice. To keep track of how the points on a slice Σ_t move to slice Σ_{t+dt} we use the spatial *shift* vector β^i. To traverse an infinitesimal amount of coordinate time from Σ_t to Σ_{t+dt} the elapsed proper-time is given by the lapse function α. Therefore points on a slice Σ_t are related to a subsequent slice Σ_{t+dt} through the 4 vector $t^\mu = \alpha n^\mu + \beta^\mu$ where the normal to these hypersurfaces is n^a as illustrated in Figure 1.13.

Cast in their original ADM form the evolution equations are *ill-posed*, weakly hyperbolic and numerical instabilities quickly arise when attempting to evolve this system [86]. One of the conditions for a stable system is strong hyperbolicity, see Refs [152, 85]. A successful reformulation called the Baumgarte-Shapiro-Shibata-Nakamura (BSSN) formulation [161, 36] introduced intermediate variables to stabilise the system. Another formulation places constraints on the behaviour of the coordinates in such a way that the Einstein equations are a hyperbolic system. This is the generalised harmonic coordinates approach [114].

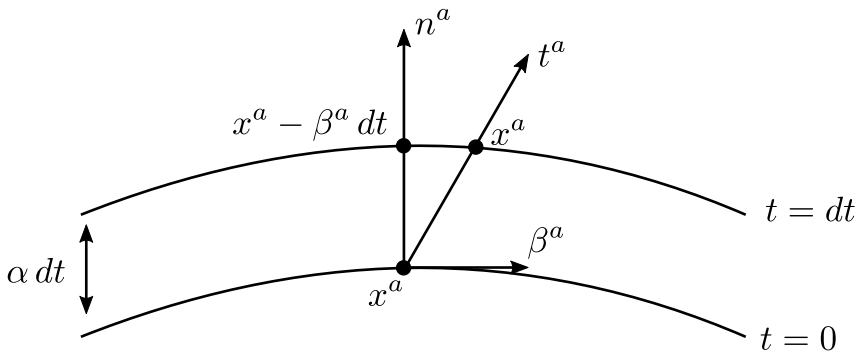

Figure 1.13: An illustration of how two slices $t = 0$ and $t = dt$ are related to each other in the 3+1 split. x^a represents a particular coordinate on the slice. Due to the coordinate freedom each slice has, the coordinate x^a could have a different location on the next slice. The vector $t^a = \alpha n^a + \beta^a$ mark lines of constant coordinates, which gets shifted by the shift vector β^a, where n^a is the vector normal to the slice. The amount of proper time elapsed between the slices is given by $\alpha\, dt$. Adapted from [60].

Evolving BHs numerically presents an interesting problem of how to treat the singularity at the centre of each BH. Currently there are two main methods: (i) punctures [48] and (ii) excision [168]. The puncture method uses singularity avoiding spatial slices such that the grid points that comprise the computational domain do not reach the central singularity but instead are mapped to a fixed "puncture". The puncture approach uses wormhole-like topologies and identifies one asymptotically flat end as the region far away from the BH and compactifies the other, called a puncture, to represent a second asymptotically flat end. In effect, the physical singularity is replaced with a coordinate singularity that can be handled [50]. In the excision method, based on the physical argument that no information can propagate outwards from within the event horizon one "simply" removes the interior of the BHs from the computational domain [96].

The successful computation of a merging BBH system was a long-standing challenge in the field of NR. The breakthrough came in 2005 [142] when the first stable evolution of BBH system was computed using the excision method with generalised harmonic coordinates. Shortly after two groups independently developed the moving puncture [35, 56] approach in the BSSN formulation. The moving puncture method is an improvement on the puncture method with a clever choice of the gauge variables that allow the puncture to move across the computational domain. This along with a well-posed formulation of the system of equations ushered in the era of numerical relativity to start exploring the physics of colliding BHs.

The years since the breakthrough have seen numerous groups explore the compact binary coalescence (CBC) parameter space. In the case of BBH systems; equal-mass simulations with spins approaching the Kerr limit have been performed [155]; spinning high mass-ratios up to 1:18 [100]; a stochastic exploration of the comparable

mass precessing sector has been scouted [127, 3] as well as the impact of eccentricity [97]. Results of NR offer independent comparisons with perturbation theory [49] as well as allow us to explore the highly dynamical space-time around colliding BHs and investigate how their horizons interact. Astrophysically interesting results include calculations of the size of the remnant BH's kick [49]. The main motivation for performing NR simulations though is to extract the gravitational waveform during the final orbits and merger of BBHs.

The NR calculations for this work come from two sources: one from the Cardiff-UIB group using the bifunctional adaptive mesh (BAM) code and the other from the publicly available simulating extreme spacetimes (SXS) catalogue [3] using the spectral Einstein code (SpEC) code [6]. We will mainly describe the NR simulations we (Cardiff-UIB) performed using the BAM code [50, 99] as discussed in Section 2.2.

1.5 IMR Waveform Models

As we have seen the intrinsic parameters of coalescing BBHs imprint a rich phenomenology on the resulting gravitational waveform, for example Figure 1.8. The ultimate goal is to study candidate GW events that have been ranked as highly significant by search pipelines and attempt to extract the parameters of the system by finding regions of parameter space that give the best fit to the data.

Of paramount importance in both the search and parameter estimation of BBH systems with GWs is the modelling of the late-inspiral, merger and ringdown stages. Typically for systems with total mass greater than $12M_{\odot}$ the contribution to the signal-to-noise ratio (SNR) from the merger will be significant and any waveform model used to perform parameter estimation without modelling the merger effects may result in heavily biased parameters. This implies that searches and parameter estimation of BBH signals *need* to use waveform models that predict the full IMR signal. Ideally we would like to directly use NR, as it is after all the full solution to the Einstein equations, to compute waveforms "on-the-fly". Unfortunately, modern day computers are unable to deliver this and the typical timescale for a NR simulation is of the order of weeks or months. For GW searches the typical size of template banks as used in the search of aLIGO data are of the order 10^5 [13] and the typical number of waveform evaluations when estimating parameters in Bayesian inference codes are of the order 10^6 [17]. For these reasons waveform models need to be not only accurate but also very fast to evaluate. The next best thing we can do is to sample the full 7 dimensional intrinsic parameter space of masses and spins and attempt to build a model which, in some sense, interpolates between the NR data sample points and also reliably (to some extent) extrapolates to predict the waveform where no NR simulation exists. In order to validate such models, cross validation between independent models and comparisons to NR data that were not used in the construction of such models is necessary.

In order for the waveforms produced by NR to be utilised by waveform modellers or used directly in GW data analysis [9] they have to be accurate and contain enough GW cycles (extend down to low enough frequencies). There have been a number of studies that attempt to quantify the length and accuracy requirements of NR in data analysis applications [89, 132] by evaluating the accuracy of hybrid PN-NR waveforms. In Ref. [100] and Chapter 3 we will see that we can relax the length requirements for NR waveforms by hybridising NR with an EOB inspiral.

The two main approaches to IMR modelling are called (i) phenomenological and (ii) EOB-NR described in the following section. Recently the methods of reduced order modelling [146, 83, 41] have been applied to the field yielding key results. At the core of these techniques are principal component analyses or singular value decompositions whereby you hope to obtain the desired level of accuracy with a reduced data set thus simplifying the representation. These techniques have mainly been used to develop fast surrogate models of slower waveform models. The reduced-order quadrature (ROQ) method can be applied to speed up the calculation of the likelihood function used in Bayesian parameter estimation [58]. Attempts to estimate the minimum number of NR waveforms needed in order to build an accurate fully precessing model for the advanced detector era has been investigated in [40, 82]. The current hot topic in the field right now is attempting to build accurate – local in parameter space – reduced-order model (ROM)s in the vicinity of GW triggers such as GW150914, using a set of targeted follow-up NR simulations to calibrate them.

1.5.1 Phenomenological Models

It was noted by Ajith in [24] that NR waveforms could be modelled as simple polynomial-like functions whose coefficients could be fitted and mapped to the physical parameter space. The name coined for this was "phenomenological" modelling. It was a method to utilise the results from NR in analysis of GW data by modelling the most prominent features of NR simulations.

This first model, later called `IMRPhenomA` [25], described non-spinning BBH and was calibrated up to mass-ratio 1:4. Natively in the frequency domain and comprised of analytic expressions for the amplitude and phase, this type of model is very attractive for GW searches and parameter estimation.

`IMRPhenomA` allowed for the first time a systematic study of the non-spinning BBH parameter space and the construction of template banks that consisted of the late-inspiral, merger and ringdown [25]. Shortly after, when more aligned-spin NR waveforms became available the phenomenological model was extended towards double aligned-spins from $\chi_1 = \chi_2 = -0.85$ to $\chi_1 = \chi_2 = +0.85$. These aligned-spin models exploited a particular combination of the spins called the effective spin parameter as introduced in Equation 1.59 to model the aligned-spin effects, which

has the effect of reducing the dimensionality of the parameter space by one.

The first aligned-spin phenomenological model `IMRPhenomB` [21] also attempted to incorporate a test-mass limit into the model. Shortly after, a second aligned-spin model called `IMRPhenomC` [151] was developed, which improved upon previous models by using a more realistic amplitude model and by utilising PN information in a novel way. `IMRPhenomC` was designed to reduce to the `TaylorF2` approximant in the low frequency limit. Models of this type are very attractive as they fully incorporate all known PN information into the inspiral part of a full IMR model.

Some of the applications of IMR models are the construction of parameter space metrics as done for `IMRPhenomB` [103]. The metric is of great importance in the field of template bank construction as it allows faster and near optimal placement of templates so as not to over-cover regions of parameter space and thus reduce the computational cost of searches.

Extending phenomenological models into the precessing sector of parameter space has been made possible by the work of [156] with the realisation that the leading order precession effects of the orbital plane can be approximated as a time dependent rotation applied to a *non-precessing* gravitational waveform termed "twisting". This technique was first implemented in `IMRPhenomP` [91] which used `IMRPhenomC` [151] as the underlying non-precessing model. Since then this has been updated to `IMRPhenomPv2` making use of the new aligned-spin model produced in this thesis called `IMRPhenomD` [100, 106]. This IMR precessing BBH waveform model was used in the analysis of aLIGO data and in the analysis of GW150914 including in the first strong field tests of GR [15]. The model has been implemented into the `LALSuite` software library [167] and is currently the most accurate aligned-spin BBH gravitational waveform model in the region of parameter space where we can directly compare to NR results [112]. The construction of `IMRPhenomD` is explained In Chapter 3.

With each new phenomenological model great strides are made in either; extending parameter space coverage, improving the modelling method or incorporating more physical effects. A number of physical effects are still left unmodelled though. The true gravitational waveform will contain higher harmonics, which although they are weaker than the dominant mode, carry additional information about the source. In the exciting case of detecting a high SNR, unequal mass binary system with an edge on inclination where the effects of higher harmonics are strongest current waveform models would be inadequate to extract the maximum amount of information from such an observation. Therefore, one of the next steps for phenomenological models is the incorporation of higher harmonics into the models.

Whilst phenomenological models are an effective single spin model one may argue the need for a full two-spin model. The ability to measure the individual component spins in aLIGO has been investigated by [147] who found that only the spin on the primary BH can be constrained reasonably well but only at high SNRs whereas

the spin of the secondary BH is not constrained well. Their result supports the assumption for a single effective spin model to capture observable aligned spin effects in the advanced detector era.

1.5.2 Effective-One-Body Models

The EOB method [51, 52, 67] has also been used to great success to create highly accurate IMR models. The main driving force behind EOB was to try and squeeze more information out of PN calculations by using Padé resummation techniques. This was achieved by mapping the dynamics of the two-body system onto an effective-one-body description. This mapping simplified the equations and allowed for this resummation to be tractable which did in fact lead to more accurate expressions. The goal of EOB is to push PN calculations almost right the way up until merger, up to the effective light-ring of the system and then attach the well known ringdown waveform from BH perturbation theory. To further help the EOB model, calibration coefficients have been added that are determined by fitting them to NR simulations. Thus NR informed EOB waveform models (EOBNR) were created. The latest of these models are; `EOBNRv2HM` [135] - non-spinning but models up to the $\ell = 5$ multipole; `SEOBNRv2` [166] - dominant harmonic, non-precessing and `SEOBNRv3` [137] - dominant harmonic, precessing; and also recently a non-precessing model from the IHES group [70].

In general EOB models are computationally expensive to compute as they consist of a coupled system of ordinary differential equations, not to mention that they are time domain approximants whereas most GW analyses is performed in the frequency domain, this means that the waveforms produced by the model need to be Fourier transformed as well. To combat this reduced basis methods first introduced in [146] were successfully applied to the `SEOBNRv2` model, called `SEOBNRv2_ROM_DoubleSpin` (`SEOBNRv2_ROM` hereafter). Reduced basis methods such as this have been absolutely crutial to the large scale use of the EOB models in analysis of aLIGO data. The next challenge for this is to apply the ROM techniques to the much larger parameter space of the precessing EOB model, `SEOBNRv3`. Without such a ROM for this approximant the use in aLIGO data will be severely prohibited.

The two dominant waveform modelling techniques, phenom and EOB, both rely on calibrating model parameters to NR. This is one reason why NR is of paramount importance and needs to keep improving its methods to achieve greater accuracies and explore more of the parameter space.

This will be even more important in the long term, when future GW detectors come online such as the Einstein Telescope and eLISA. The accuracy requirements of our models for these detectors will be much higher than advanced detectors models due to the expected high SNRs signals. New techniques will likely need to be developed to construct waveform models accurate enough for such future detectors.

1.6 Data analysis

The only way to observe the merging of isolated BHs is by the GWs that they emit. GW150914 was observed to have a peak strain of $h = 1 \times 10^{-21}$, this signal and all expected signals that advanced detectors will be sensitive to will have strains of about this size. There are two main methods used to search for GWs which are *unmodelled* and *modelled* searches. Unmodelled searches [16] are typically suited to detect transient GW burst events. Methods such as *excess power* are well suited to identify regions in a time-frequency map that statistically differ to expected detector behaviour in the case of a null hypothesis, being no GW is present. This search method has the potential to discover new phenomenon that we haven't thought of. Modelled searches [14, 169] use the method of *matched filtering* [26] to dig deep into the noise and pick out correlations between the data and the expected theoretical signal, called a *template*. Here the noise is assumed to be uncorrelated in frequency but correlated in time. GW150914 was detected first by an *online* unmodelled search [16] and later found in *offline* CBC search pipelines [14]. Both found the event with high significance [13].

1.6.1 Matched Filter

Matched filtering is a data analysis method that is extremely good at finding weak signals in a background of noisy data provided you have a prediction for what your target signal looks like. The techniques used here are also the tools used to define a metric that is commonly used to quantify the agreement between two waveforms, which form the basis for most of the comparisons that we will make in this thesis.

To define the problem we assume that the *real* detector data output $s(t)$ is a continuous stream of data that is a linear combination of background noise $n(t)$ plus a possible GW event $h(t)$.

$$s(t) = n(t) + h(t)\,. \tag{1.64}$$

The basic idea is to multiply the data by a *filter*, which is our prediction of the GW signal. By integrating the data multiplied by our filter over enough time such that the contributions to the integral from the background noise averages to zero, the contribution from the signal should rise above the background.

Under the assumptions of stationary Gaussian noise the noise components are uncorrelated. In this circumstance the statistical properties of the noise are conveniently characterised by its (single-sided) power spectral density (PSD) defined through the time averaged Fourier domain representation of the noise.

$$\langle \tilde{n}^*(f)\tilde{n}(f')\rangle = \frac{1}{2}\delta(f - f')S_n(f)\,. \tag{1.65}$$

With the Fourier transform defined as

$$\tilde{n}(f) = \int_{-\infty}^{\infty} n(t) e^{2\pi i f t} df \,. \tag{1.66}$$

It turns out that the optimal filter to use is proportional to the true signal with a factor of the power spectral density (PSD), this motivates the definition of a noise-weighted inner product [122]

$$(A|B) = 4\,\mathrm{Re} \int_0^{\infty} \frac{\tilde{A}^*(f)\tilde{B}(f)}{S_n(f)} df = 4\,\mathrm{Re} \int_0^{\infty} \frac{\tilde{A}^*(f)}{\sqrt{S_n(f)}} \frac{\tilde{B}(f)}{\sqrt{S_n(f)}} df \,, \tag{1.67}$$

where the last equality is to demonstrate that the inner-product can also be viewed as the integral between the data and the template that have both been whitened by the amplitude spectral density (ASD) (ASD $= \sqrt{\mathrm{PSD}}$). The detector's sensitivity is frequency dependent, the weighted inner product takes this into account and gives more weight to sensitive frequencies.

In the idealised case where we filtered the detector data with the true waveform we would recover the optimal SNR ρ_{opt} defined as:

$$\rho_{\mathrm{opt}} = (h|h)^{1/2} \,. \tag{1.68}$$

In matched filter based searches we do not have access to the true waveform h, instead we use waveform models to generate *templates* g to search through the data. Template banks are a collection of intrinsic parameter values that you are searching over placed in an near-optimal way to reduce the computational cost of searching over intrinsic parameters. Template banks for full IMR waveforms that incorporate aligned-spin effects have been successfully implemented in searches in advanced detector data [59] and an attempt at a precessing template bank is documented in [93].

The *matched-filter* SNR ρ_{mf} is given by

$$\rho_{\mathrm{mf}} = \frac{(g|s)}{(g|g)^{1/2}} = (\hat{g}|s) \tag{1.69}$$

Where $\sigma_g = (g|g)^{1/2}$ is the norm of the template and $\hat{g} = g/(g|g)^{1/2}$ is the normalised waveform. In the case where the template is exactly the true waveform, the optimal SNR is obtained. The matched-filter SNR can be used as a detection statistic and a threshold placed at ρ_0 such that events that have $\rho_{\mathrm{mf}} \geq \rho_0$ are promoted to *triggers* else they are discarded. GW triggers are retained for further scrutiny such as signal consistency tests like the χ^2 veto [26]. Because the template used in the definition of ρ_{mf} is normalised this effectively maximises over the amplitude. Templates are typically computed at a fiducial distance, say 1 Mpc, such that an estimate of the distance can be computed from ρ_{mf}. Geometrically the ρ_{mf} is just the projection of the data onto the unit vector template direction. Note that when

$g = h$ in Eq. (1.69) then the optimum SNR is recovered, $\rho_{\rm mf} = \rho_{\rm opt}$.

1.6.2 Measures of closeness

Of course we don't have access to the *true* waveform. We *hope* that our theoretical predictions for the GW waveform will be close to the *true* waveform.

The field of waveform modelling is about developing models that accurately predict the gravitational waveform for various sources. We estimate the error between the two waveforms, h_1 and h_2 by computing the *match* (also called the *faithfulness*). The *match*[11] is the noise-weighted inner product between two normalised waveforms, maximised over the extrinsic parameters of time (t_0) and phase (ϕ_0) shifts

$$\mathrm{M}\left[h_1, h_2\right] = \max_{t_0,\phi_0} \left(\hat{h}_1 | \hat{h}_2(t_0, \phi_0)\right) \in [0, 1]\,. \tag{1.70}$$

Typically, we say a waveform model ($h_{\rm m}$) is *faithful* to NR ($h_{\rm NR}$) if it has $\mathrm{M}[h_{\rm m}, h_{\rm NR}] \geqslant 99\%$. Geometrically we can interpret the match as simply the cosine of the angle between two unit vectors $\hat{h}_1$ and $\hat{h}_2$, where unit vectors are defined as ($\hat{h} = h/\sqrt{(h|h)}$). The match is useful because it corresponds to the fractional loss in $\rho_{\rm opt}$ from modelling errors, from this we define the recovered SNR as,

$$\rho_{\rm rec} = \mathrm{M}\left[h_1, h_2\right] \rho_{\rm opt}\,. \tag{1.71}$$

At the cost of introducing biases in intrinsic parameters one can calculate the match optimised over intrinsic parameters called the *fitting factor* (FF) [28],

$$\mathrm{FF}\left[h_1, h_2\right] = \max_{\boldsymbol{\Xi}} \mathrm{M}\left[h_1, h_2(\boldsymbol{\Xi})\right]\,. \tag{1.72}$$

To determine the effectiveness of a waveform model or template bank at detecting GWs, the fitting factor (FF) is the relevant quantity. This is why the FF is sometimes called the *effectualness*. For parameter estimation the relevant quantity is the match, which places a lower bound on the FF of a waveform model.

There are two contributions to the FF: (i) the effectualness ($\mathcal{E}$) of the waveform model to the true signal and (ii) the minimum match (MM) of the template bank. Template banks are constructed such that no two templates in the bank have a match less than the MM. Assuming a Universe with sources distributed uniformly in volume then the detection event rate is reduced by a factor of FF^3. To ensure that no more than 10% of signals will be missed in a matched-filter search template banks must have a minimum FF = 96.5%.[12] Assuming that the matches are high (equivalently the mismatches are small) then the two contributions to the FF can be approximately expressed by simply adding them together $\mathrm{FF} \approx \mathcal{E} + \mathrm{MM}$ [54].

[11] We define the *mismatch* simply as $\mathcal{M} := 1 - \mathrm{M}$, which will be used sometimes to quote results instead of the match.

[12] $1 - 0.965^3 = 0.1$

Therefore, if we require FF $\geqslant$ 96.5% along with a typical value for the template bank minimum match of MM = 97% then this implies that the templates in the bank have to have an effectualness to the true waveform of $\mathcal{E} = 99.5\%$.

Recent waveform models, including the one presented in Chapter 3, have been constructed to achieve *matches* of at least, and in many cases much better than 99% to NR waveforms. Noting that the match is a lower bound on $\mathcal{E}$ it is assumed that, by allowing for parameter variations, the waveform model can achieve the required effectualness for detection. By enforcing waveform models to not only be effectual ($\mathcal{E} = 99.5\%$) for detection purposes but also faithful (M = 99%) then we can also use them in Bayesian parameter estimation analyses of GW candidates with (hopefully) small systematic biases on the results.

Chapter 2

Modelling Numerical Relativity

2.1 Introduction

In this chapter we will present new NR simulations of aligned-spin, mass-ratio 1:4 BBHs to illustrate the methods used to simulate them and extract the GW signal. We will analyse the anatomy of the merger signal in the time and frequency domain, which will guide us when proposing new ansätze to accurately model both the amplitude and phase of the GW to later build a new phenomenological model, presented in Chapter 3. We will then proceed to define the phenomenological modelling method in a semi-formal way and motivate the development of a new phenomenological model by constructing a preliminary model based on the methods introduced in [151] applied to NR waveforms up to mass-ratios 1:18 and show that these techniques may not be adequate to build an accurate model.

The goal is to build accurate models to predict the gravitational waveform as a function of the intrinsic parameter space. The intrinsic parameter space, as mentioned in Section. 1.3.1, has 8 dimensions, the BH component masses and their spin components. In BBH spacetimes this is actually reduced to 7 dimensions where the component masses are combined into the mass-ratio q or symmetric mass-ratio η and the total mass can be set to a constant (typically 1) without loss of generality. To obtain physical quantities at desired total masses M one simply scales the quantity by the appropriate weighting factor[1].

Guided by astrophysical and practical arguments we restrict ourselves to the aligned-spin parameter space (3 dimensions) knowing that we have a procedure to approximate fully generic precessing systems by applying a time dependent rotation to the waveform [157, 158].

[1] To convert from mass to time we define the weighting factor $w \coloneqq GM/c^3$. To convert times from geometric code units t/M to physical units we multiply by w. To convert frequencies from geometric code units $M\,f$ we multiply by w^{-1}.

2.2 Binary Black Hole Simulations With The BAM Code

To compute the dynamics of merging BBHs and extract the gravitational waveform we use the NR code BAM. The BAM code [50, 99] solves the Einstein evolution equations using the BSSN [161, 36] formulation of the $3+1$ decomposed Einstein field equations (See Section. 1.4). The BSSN equations are integrated with a fourth order finite-difference Runge-Kutta time integrator, with a fixed time step along with a sixth order accurate finite difference algorithm based on the method-of-lines for spatial derivatives. The χ variation of the moving-puncture method is used where a new conformal factor is defined as $\chi = \psi^{-4}$, which is finite at the puncture. The lapse and shift gauge functions are evolved using the $1+\text{Log}$ slicing condition and the Gamma driver shift condition respectively. Conformally flat puncture initial data [64, 47, 45] are calculated using the pseudospectral elliptic solver described in [27] and the apparent horizons are tracked with the `AHmod` code [113].

In BAM the computational domain is represented as a nested set of cartesian cubic boxes. There are L levels of mesh-refinment indexed from $[0, 1, ..., L-1]$ where $\text{Lev} = 0$ is the coarsest level and $\text{Lev} = L-1$ is the finest. On level ℓ in any direction there are N_ℓ grid points making N_ℓ^3 grid points on level ℓ. The resolution is determined by the number of grid points on the coarsest level N_0 and the number of mesh-refinement levels used. Moving from a lower (coarser) level to a higher (finer) level halves the grid spacing, doubling the resolution. Therefore the grid spacing on any level ℓ is given by $\Delta_\ell = \Delta_0/N_\ell = \Delta_0/2^\ell$. Each puncture is at the centre of a refinement box, which is large enough to enclose the apparent horizon, the box tracks the motion of the puncture. Close to merger, when the two boxes containing each puncture would meet the domain is re-grided to enclose both horizons and the subsequent common horizon. The whole scheme can be referred to as a "moving-boxes-in-boxes" method. In the case of equal-mass BHs the same resolution around each BH is needed. However, for unequal-mass BHs more resolution is needed around the secondary BH because its horizon size is smaller. In these cases extra levels of refinement can be put around the secondary BH.

The size of the BHs are of $O(M)$ where M is the total mass ($M = m_1 + m_2$). They are typically placed at a separation of $O(10M)$ which then take $O(1000M)$ to merge and their GW signal is extracted $O(100M)$ away. The typical wavelength of the GWs during merger is also on the order of $O(10M)$ however, to resolve the higher modes, which have higher frequencies a higher spatial resolution is needed in the wave extraction zone. To resolve these various length scales BAM uses adaptive mesh refinement (AMR) techniques on a 3D cartesian grid to accurately resolve regions of interest and track to motions of the punctures throughout the evolution.

Due to imperfect boundary conditions at the edge of the computational domain unphysical reflections can propagate inwards from the boundary. These should not affect the dynamics of the interior domain as long as the outer boundary is placed

far enough away that it is only causally connected to the wave extraction zone *after* the waves have propagated through it.

2.2.1 Gravitational Waves In Numerical Relativity

The GWs are extracted at finite radius (typically $O(100M)$) using the Newman-Penrose scalar Ψ_4 [130, 138]. In an appropriate null-tetrad Ψ_4 measures the outgoing gravitational radiation encoded in the Weyl tensor and far away from the source we find the following relationship to the metric perturbation,

$$\Psi_4 = \ddot{h}_+ - i\ddot{h}_\times \,. \tag{2.1}$$

In the BAM code Ψ_4 is computed on a 3D cartesian grid that is interpolated onto spheres for a range of extraction radii $r_{\rm ex}$. This data is then decomposed into spin-weighted (-2) spherical-harmonics. The user specifies how many extraction radii to use and how far to place them, but a typical range of radii are $\{50, 60, 70, 80, 90, 100\}M$. Many extraction radii are used so that the finite extraction data can be extrapolated. Methods such as Cauchy characteristic extraction [148] or using hyperboloidal slices [170] can be used to compute Ψ_4 at future null-infinity ($\mathscr{I}^+$).

To compute the strain from Ψ_4 one needs to compute two time integrals of Eq. (2.1)

$$H = h_+ - ih_\times = \int_{t_0}^{t_1} dt' \mathcal{N} = \int_{t_0}^{t_1} dt' \int_{t_0'}^{t_1'} dt'' \Psi_4 \,. \tag{2.2}$$

Where $\mathcal{N}$ is the Bondi News function. A naive time integration of Ψ_4 can introduce a non-linear drift due to underresolved numerical error and higher frequency noise gets aliased to lower frequencies. A very effective method to perform the double time integral is in the Fourier domain with the method of *fixed-frequency integration* described in [149]. In the Fourier domain integration is performed via division and to suppress underresolved errors frequencies lower than f_0 are labeled with f_0. f_0 is chosen to be an estimate of the lowest GW frequency in the data.

Because we will mainly be working with the Fourier domain representation of GWs I define the Fourier domain strain as $\tilde{h}(f)$ through the Fourier domain $\tilde{\Psi}_4$,

$$\tilde{\Psi}_4(f) \equiv \mathrm{FT}\left[\Psi_4\right] = \int_{t_0}^{t_1} \Psi_4(t) e^{2\pi i f t} df \,, \tag{2.3}$$

as

$$\tilde{h}(f) = \frac{\tilde{\Psi}_4}{4\pi^2 f^2} \,, \tag{2.4}$$

via fixed-frequency integration.

SimName	q	χ_1	χ_2	e (10^{-3})	M_f/M	a_f	$N\|_C$
BAM:1	4	-0.75	-0.75	3.0	0.984(8)	0.049(9)	$\{80,96,112\}\|_{0.25}, 80\|_{\{0.35,0.5\}}$
BAM:2	4	-0.50	-0.50	4.1	0.983	0.193	$96\|_{0.25}$
BAM:3	4	-0.25	-0.25	1.6	0.981(0)	0.33(3)	$\{80,96,112\}\|_{0.25}$
BAM:4	4	0.00	0.00	1.4	0.978(0)	0.47(1)	$\{80,96,112\}\|_{0.25}, 80\|_{\{0.35,0.5\}}$
BAM:5	4	0.25	0.25	4.6	0.974	0.606	$96\|_{0.25}$
BAM:6	4	0.50	0.50	5.4	0.9674(6)	0.736(6)	$\{80,96\}\|_{0.25}$
BAM:7	4	0.75	0.75	1.0	0.956(1)	0.86(1)	$\{80,96,112\}\|_{0.25}, 80\|_{\{0.35,0.5\}}$

Table 2.1: Configurations of the mass-ratio 1:4 BBH systems simulated with BAM. Eccentricity was estimated from the orbital frequency following Ref. [144]. The precision of the final mass and spin was calculated by comparing results from multiple resolutions where available. N is the number of grid points on the coarsest level and C is the Courant factor used represented as $N|_C$. All configurations extracted Ψ_4 on spheres of coordinate radii $R_{ex} \in \{50, 60, 70, 80, 90, 100\}M$.

2.3 Simulations of aligned-spin, mass-ratio 1:4 Binary Black Holes

Our group explored the BBH parameter space by performing a suite of simulations with the BAM code including non-precessing simulations with mass-ratio 1:18 [100], the highest mass-ratio with enough orbits to be utilised in waveform models. Also included in this set were non-precessing mass-ratio 1:8 and 1:4 configurations with large spin magnitudes. I performed the mass-ratio 1:4 simulations and will discuss them in some detail.

These mass-ratio 1:4 runs are BBH systems where the spin on each BH are equal and aligned with the orbital angular momentum. These "double" aligned-spin systems take values from -0.75 to +0.75 in steps of 0.25. It is possible to simulate systems with higher spin values, however, with conformally flat initial data there are non-negligible amounts of unphysical "junk radiation" that restricts the spins we can place on the BHs to the Bowen-York limit $\chi \sim 0.93$ [45]. However, with non-conformally flat initial data, simulations with spins up to $\chi \sim 0.99$ have been performed [118]. Further simulations placed at higher spin values will be invaluable indeed at any mass-ratio. With restrictions on computational resources we chose a few cases from this study to perform at multiple resolutions to estimate the error of the runs. The configurations of these runs and information about the number of mesh-refinement levels used, resolution and outer boundary placement for each base grid configuration can be found in Table 2.2.[2] Conformally flat initial data were constructed using the pseudo-spectral solver in [27] and we performed the iterative eccentricity reduction procedure explained in [144] to estimate initial BH momenta to obtain orbits with $e \sim 10^{-3}$ after 1 to 3 iterations. We compute up to the

[2]Note: The 112pt `BAM:7` simulation has the same resolution as the 96pt simulation, i.e., $h_{\min}/m_1 = 4.3 \times 10^{-3}$ and therefore does not constitute a convergence series.

N	$(l1_A/l1_B : l2)$	$h_{\rm min}/m_1$	$h_{\rm max}/M$	x_i/M
80	13/11:6	5.2×10^{-3}	42.5988	2556
96	13/11:6	4.3×10^{-3}	35.4987	2556
112	13/11:6	3.7×10^{-3}	30.4277	2556

Table 2.2: Numerical grid configurations for the three base grids used. $l1_A/l1_B$ are the number of mesh-refinement levels around the smaller and larger horizon respectively. $l2$ is the finest non-moving refinement level. $h_{\rm min}/m_1$ is the resolution around the small horizon, $h_{\rm max}/M$ is the resolution on the finest level and x_i/M is the location of the outer boundary. Note: The 112pt `BAM:7` simulation has the same resolution as the 96pt simulation, i.e., $h_{\rm min}/m_1 = 4.3 \times 10^{-3}$, which also places the outer boundary further away at $x_i/M = 2982$. Due to this the `BAM:7` data does not permit a convergence series analysis.

$\ell = 5$ multipole for the extracted GWs, extracted at $R_{ex} = \{50, 60, 70, 80, 90, 100\}M$. From the simulations we also calculate the mass and spin of the final BH following [90]. To compute the final mass we use a simple conservation of energy argument. From the initial ADM mass M_{ADM} we subtract an estimate of the radiated energy at spatial infinity. We compute the radiated energy at each R_{ex} and then fit the expected $1/r$ dependence to estimate the value at infinity. The final spin is estimated using BH perturbation theory results [39]. This method requires measurements of the final mass and the ringdown frequency, which we estimate from the frequency of the GW. The ringdown frequency is often noisy due to under resolving the ringdown portion of the waveform, however computing the mean value of the ringdown portion of the GW frequency can give robust results. We average the ringdown frequency over a $50M$ interval defined by $t_{\rm peak} + [20, 70]M$ where $t_{\rm peak}$ is the time $|h_{22}|$ is maximum.

2.3.1 Convergence - Dominant Harmonic

Convergence tests are a way to estimate the accuracy of numerical calculations. In finite difference codes the error in a numerical solution is proportional to the order of the finite difference stencil used. In the limit that the grid spacing, Δ, goes to zero we obtain the continuum limit where theoretically a numerical solution and an analytic solution converge. To estimate if a numerical solution is convergent requires three results, $\{X_1, X_2, X_3\}$,[3] from three different resolutions, $\Delta_1 > \Delta_2 > \Delta_3$, each represented by a power series as

$$X_i = X_A + e_n \Delta_i^n \,, \quad i = \{1, 2, 3\} \,. \tag{2.5}$$

Here, the unknown analytic solution is X_A, the finite difference order is n and e_n is the order$-n$ error. From this we form the following ratio

[3] In the next section these will be either the phase ϕ or the amplitude A.

$$\mathcal{C}|_n = \frac{X_1 - X_2}{X_2 - X_3} = \frac{1 - (\Delta_2/\Delta_1)^n}{(\Delta_2/\Delta_1)^n - (\Delta_3/\Delta_1)^n} = \frac{1 - (N_1/N_2)^n}{(N_1/N_2)^n - (N_1/N_3)^n}\,, \tag{2.6}$$

where to get the final equality we convert from numerical resolution to number of grid points assuming the relationship $\Delta_i = D/N_i$, where D is the size of the computational domain. Here $\mathcal{C}|_n$ is the convergence scale factor for an order$-n$ finite difference scheme. Hence, if we combine results as in Eq. (2.6) and we find that the results are consistent with the expected convergence scale factor $\mathcal{C}|_n$ then we say the results are in the *convergent regime*; the error in our numerical approximation is converging to the continuum solution at the expected rate. If we are in the convergent regime then we can apply Richardson extrapolation to compute an improved error estimate. If results are not displaying their expected convergence scale factor then either the implementation of the equations is incorrect or the simulation was not run with enough resolution to be in the convergent regime.

Of the 7 cases in the 1:4 series, four simulations have multiple resolutions with which to perform a convergence test and estimate the numerical error. As an example we take the `BAM:4` run to illustrate the results of the convergence test. The `BAM:4` case was performed for $N = 80, 96, 112$ grid points. We derive the amplitude and phase for each grid configuration, i.e., $A_{\{80,96,112\}}$ and $\phi_{\{80,96,112\}}$ and compute the differences: $80 - 96$ and $96 - 112$ which for the phase we denote as $\Delta\phi_1 \coloneqq \phi_{80} - \phi_{96}$ and $\Delta\phi_2 \coloneqq \phi_{96} - \phi_{112}$ and similarly for the amplitude. For these grid configurations and for the expected 6^{th} order convergence the errors should differ by a scale factor of $\mathcal{C}|_6 = 3.29$.

Figure 2.1 shows the results of the phase convergence test for `BAM:4` (showing times after junk radiation). In blue is $\Delta\phi_1$ and in orange is $\Delta\phi_2 \times \mathcal{C}|_6$ where the expected convergence scale factor is $\mathcal{C}|_6 = 3.29$. Evidence for convergence can be seen during the final $\sim 500\,M$ of the data albeit at an unexpected convergence order. Without observing clean convergence we cannot use Richardson extrapolation to get an estimate of the numerical error however, we do observe that our error estimate does decrease with increasing resolution.

Ideally we would like to perform convergence tests by comparing grids that differ by a factor or 2, due to computation costs our simulations differ only by a factor of ~ 1.2. This results in a convergence scale factor $\mathcal{C}$ that only weakly depends on the finite difference order. This makes it difficult to conclusively determine the scale factor that best describes the data. To illustrate this, in the right panel of Figure 2.1 we also scale the 80pt-96pt data by $\mathcal{C}|_5 = 2.77$ (dashed, green) and by $\mathcal{C}|_7 = 3.91$ (dotted, red). While the data clearly doesn't support $\mathcal{C}|_5$ there is better agreement for $\mathcal{C}|_7$ near merger ($t/M \sim 2200$). This erroneous agreement suggests that our results are not in the convergent regime.

We define the integrated phase difference between two waveforms h_1 and h_2 with

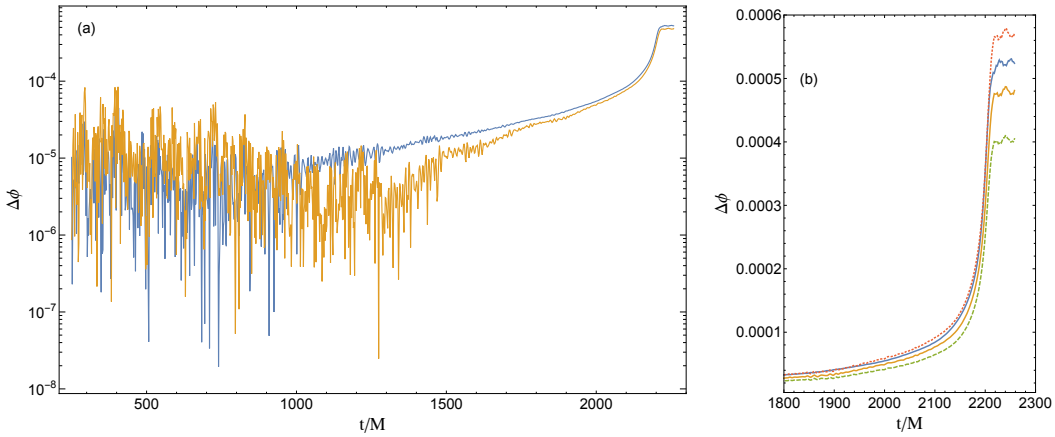

Figure 2.1: Results of the phase convergence test for the `BAM:4` non-spinning system. $\Delta\phi_1$ corresponding to the grid difference 80pt-96pt is in blue and $\Delta\phi_2$ for the grid difference 96pt-112pt is in orange. A convergence scale factor of $\mathcal{C}|_6 = 3.29$ is applied to 80pt-96pt curve (orange). For comparison, in (b), we also scale the 80pt-96pt data by $\mathcal{C}|_5 = 2.77$ (dashed, green) and by $\mathcal{C}|_7 = 3.91$ (dotted, red). Clean 6^{th} order convergence is not observed however, we observe that the error estimate does decrease with increasing resolution.

phases ϕ_1 and ϕ_2 respectively as

$$\Delta\phi = \frac{1}{t_2 - t_1} \int_{t_1}^{t_2} (\phi_1(t) - \phi_2(t))\, dt\,. \tag{2.7}$$

To quantify the error in a waveform we compute Eq. (2.7) for the two highest resolution simulations and quote this as the error estimate.

To estimate the amplitude error we follow [90] and express the amplitude as a function of the phase to remove the need to perform a time and phase shift to the data. Figure 2.2 shows a convergence test for `BAM:4`. The blue curve corresponds to the relative amplitude difference (in percentage) between the 80pt and 96pt configurations and the orange curve corresponds to the 96pt and 112pt configurations multiplied by the expected convergence scale factor $\mathcal{C}|_6 = 3.29$. The data appears to be much cleaner that the phase difference plot (Figure 2.1) however, clean 6^{th} order convergence is still not observed. The (unscaled) relative amplitude error between the 96pt and 112pt configurations is shown as the orange dashed line. We estimate the amplitude error as the maximum amplitude error over the course of the simulation (after junk time). For this case (`BAM:4`) the maximum amplitude error is 3.4%.

The results of the estimates of the errors for the amplitude and phase for the cases where multiple resolutions were available i.e., `BAM:{1,3,4,7}` are shown in Table 2.3. We estimate that the non-spinning case is the most accurate with an

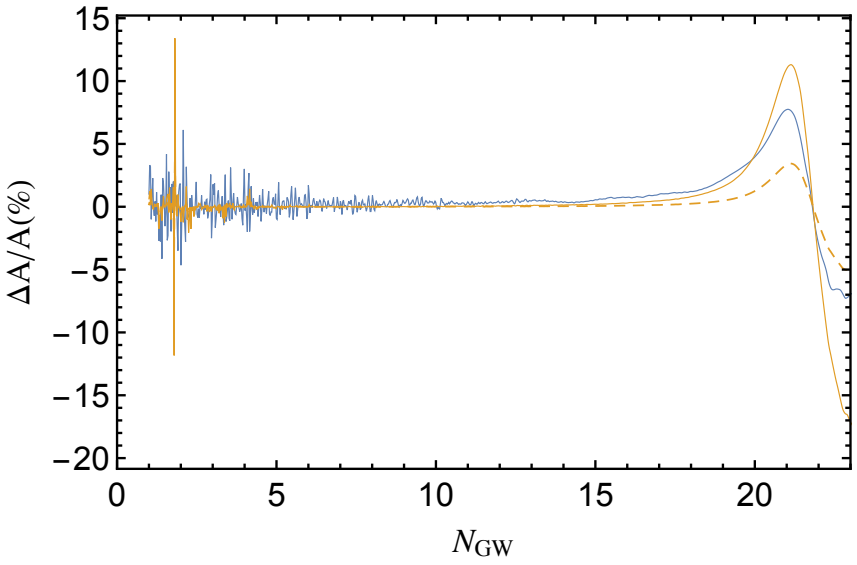

Figure 2.2: Results of the amplitude convergence test, expressed as a function of the number of gravitational wave cycles, for the `BAM:4`, non-spinning configuration. 80pt-96pt (Blue), 96pt-112pt (Orange). A convergence scale factor of $\mathcal{C}|_6 = 3.29$ is applied to 80pt-96pt curve. Although the amplitude data is cleaner than the phase data in Figure 2.1 clean 6^{th} order convergence is not observed. The estimate of the amplitude error does decrease with increasing resolution though. The orange dashed line corresponds to the *unscaled* 96pt-112pt configuration, which shows the maximum amplitude error of 3.4%.

SimName	q	χ_1	χ_2	$\Delta\phi$ (rad)	Max$[\Delta A/A]$%
BAM:1	4	-0.75	-0.75	0.06	17.0
BAM:3	4	-0.25	-0.25	0.03	5.7
BAM:4	4	0.00	0.00	0.018	3.4
BAM:7	4	0.75	0.75	0.17	15.2

Table 2.3: Summary of the estimated error assoiciated with the `BAM` runs where multiple resolutions were available. $\Delta\phi$ is computed over the interval $[t_1, t_{\rm peak}]$ where t_1 = time after junk and $t_{\rm peak}$ is the time where $|h_{22}|$ is maximum. Max$[\Delta A/A]$ is the maximum relative amplitude error. For all cases we estimate the error by comparing the two highest resolution simulations.

estimated phase error of 0.018 rad. The simulations with the largest amplitude and phase errors are the configurations with $|\chi| = 0.75$. The largest phase error occurs for the `BAM:7` case ($\chi = 0.75$) with an estimated phase error of 0.17 rad and an estimated 15.2% maximum amplitude error.[4]

BAM uses a moving boxes-in-boxes method to track the BH apparent horizons across the computational domain. When setting up the numerical grid we require

[4] As mentioned previously, the `BAM:7` runs do not have the correct relative resolutions to perform a standard convergence analysis however, we still attempt to estimate the amplitude and phase error in the same way as the other cases. Because of this the meaning of the error estimates is different.

the apparent horizon to be contained within one of these moving boxes. Whilst all of the simulations presented here fulfill this criteria it may be the case that for the high spin cases $|\chi| = 0.75$ the size of the boxes is suboptimal resulting in higher inaccuracies during the evolution.

The sixth-order convergence of the BAM code has been demonstrated in [99], our results show that these simulations do not have sufficient numerical resolution to be in the convergent regime. That being said for the use in GW data analysis applications a more useful metric to quantify the accuracy of a simulation is the *match* (See Eq. (1.70)). In Chapter 3 we estimate the error in the same BAM simulations by computing the match between different resolutions and different extraction radii and find that these simulations differ by a mismatch smaller than the accuracy requirement of waveform models and hence are sufficient to be used to construct a model.

2.3.2 The anatomy of mass-ratio 1:4 systems: Dominant Harmonic

Prior to the work in [100, 106], the ansätze used to model the Fourier domain amplitude and phase have been heavily influenced by PN and BH perturbation theory [25, 21, 151]. The set of waveforms in Table 2.1 represents an interesting slice through the BBH parameter space and allows us to systematically study the effect of the aligned spins on a mass-ratio 1:4 system. In this section we shall explore the anatomy of this suite of mass-ratio 1:4 waveforms in both their time and frequency domain representation to gain important intuition into their behaviour. The intuition we will gain here will guide us when we develop improved ansätze for the amplitude and phase, which capture the functional dependence more accurately than previous phenomenological models.

Time Domain

We first examine the mass-ratio 1:4, non-spinning system (`BAM:4`) as our fiducial example of what the waveform looks like decomposed into its amplitude and phase before studying how these functions behave depending on the spin of the BHs.

The left panel of Figure 2.3 shows h_+, $h_\times$ and the amplitude A (dominant harmonic only) for the `BAM:4` case, where in the right panel we show a zoom-in around the time of peak amplitude (black dashed line), near the time of merger. The time domain data was computed using the fixed-frequency integration method [149] and the Ψ_4 time series was windowed with the Planck taper function [125] to minimise Gibbs oscillations.[5] This simulation has about 20 useable GW cycles.

In practice, it is much more convenient to work directly with the amplitude and phase representation and construct h_+ and $h_\times$ from them rather than model them

[5] The first $500M$ and the interval $t_{\rm peak} + [100, 150]M$ are windowed. $t_{\rm peak}$ is the time when $|h_{22}|$ is maximum.

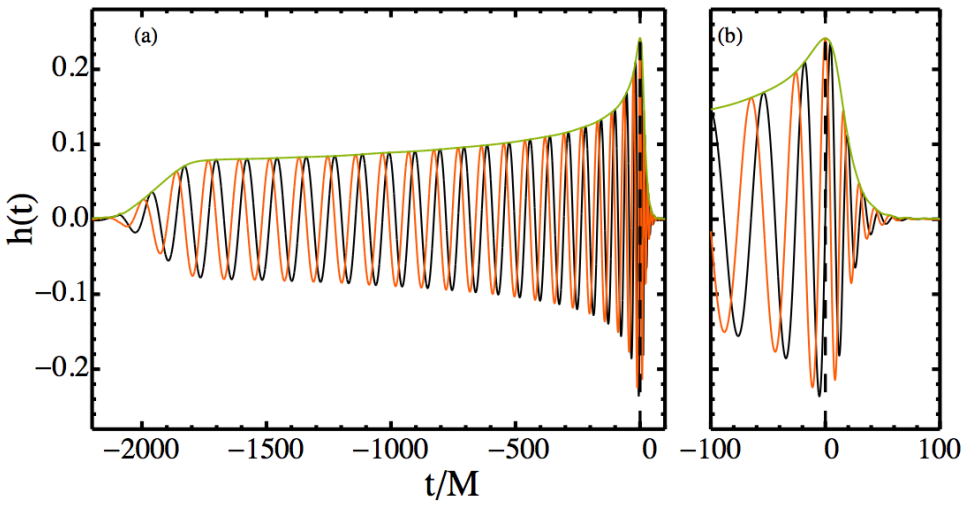

Figure 2.3: Time domain representation of the inspiral, merger and ringdown of a non-spinning, mass-ratio 1:4 BBH system (`BAM:4`). Shown is h_+ (black), $h_\times$ (orange) and $|h|$ (green) as a function of code units, shifted such that the peak of $|h|$ occurs at $t = 0$. Left Panel (a): Complete NR waveform, the gradual increase at early times ($\sim -2000M$) is due to the tapering used during the fixed-frequency integration method. Right Panel (b): Zoom in around merger.

directly. Using the complex strain defined in Eq. (1.37) the amplitude and phase of h given by

$$A(t) = \sqrt{h_+^2 + h_\times^2}\,, \tag{2.8}$$

$$\phi(t) = \mathrm{Arg}[h]\,. \tag{2.9}$$

Figure 2.4 shows the GW phase of the dominant harmonic, shifted in time such that the time the amplitude is maximum occurs at $t = 0$. While this function may look "simplistic" and "uninteresting" it has encoded in it the physical parameters of the binary, its mass-ratio and spins. The efficiency of GW searches and the accuracy and precision of parameter estimation calculations rely on waveform models that predict the phase as accurately as possible. The GW phase increases (monotonically for non-precessing systems) over time, encoding the number of orbits, and has a slight "bend" near the time of merger, which then transitions into a linear function some amount of time after $t = 0$. We can make these observations more precise by computing the GW frequency, i.e., the time derivative, $d\phi/dt = \dot{\phi} = 2\pi f$.

The GW frequency for Ψ_4 (orange) and strain (black) is shown in Figure 2.5. The differences between the frequency computed from Ψ_4 and from the strain is quite dramatic at early times (left panel). The fixed-frequency-integration method performs well at cleaning up this part of the signal. Turning towards late time behaviour, a slight difference between the two frequencies can been seen shortly after the peak amplitude is reached (right panel, black dashed line) but both settle down

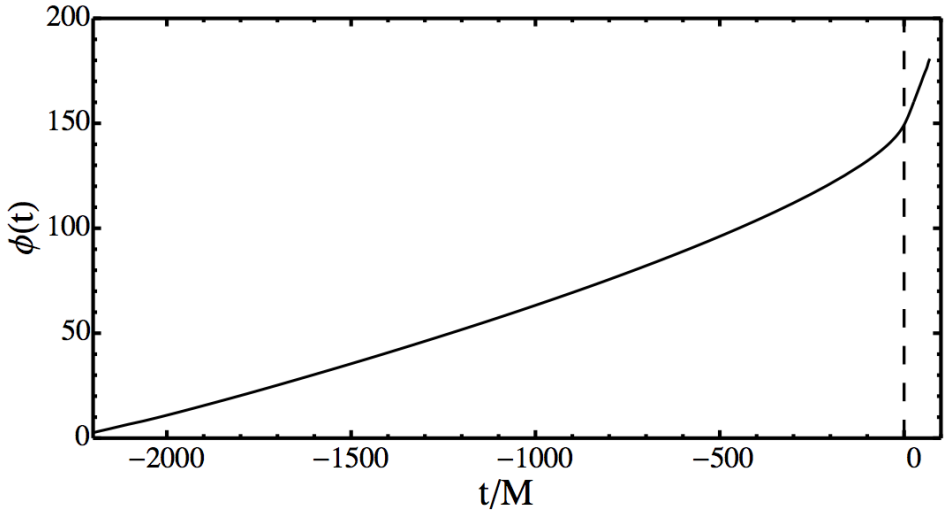

Figure 2.4: Phase of time domain gravitational waveform from `BAM:4`, shifted such that the peak of $|h|$ occurs at $t = 0$ (vertical dashed black line).

to the ringdown frequency. Ψ_4 is often used to estimate the ringdown frequency as it does not suffer from large oscillations (a result of the strain conversion). The GW frequency is an initially slowly increasing function of time, which undergoes a rapid increase close to merger, before reaching the ringdown frequency (the blue dashed line). Physically we know this corresponds to the long slow inspiral at early times followed by the very rapid final orbits/plunge before settling down to a Kerr BH through ringdown radiation. It is interesting to note that the ringdown frequency is reached approximately $20M$ after the time of peak amplitude. We can think of the merger as a *transition* from one regime (the inspiral) to another (the ringdown).

Now that we have examined, briefly, the non-spinning system let us now look at how these various representations of the waveform change as a function of aligned-spin.

Figure 2.6 plots the amplitude for the simulations in Table 2.1. Going from bottom to top the curves correspond to `BAM:1...7`. The shortest and longest simulations were `BAM:1` and `BAM:7` respectively, which correspond to the lowest and highest values of effective spin. Noticeable eccentricity is visible for `BAM:2`, `BAM:6` and just barely for `BAM:5`, which agree with the eccentricity estimates in Table 2.1. A very clear hierarchy is found. The lowest values of effective spin (`BAM:1`) have the smallest amplitude throughout the evolution and as the effective spin increases to the maximum, in this data set `BAM:7`, the amplitude increases. Interestingly the peak of the gravitational waveform gets broader and the rate of increase of amplitude gets smaller. This can be explained through the orbital hang-up effect, this effective repulsive force allows BHs to orbit closer and reach higher velocities and hence frequencies and amplitudes. The impact of this on the ringdown stage is that higher ringdown frequencies are reached.

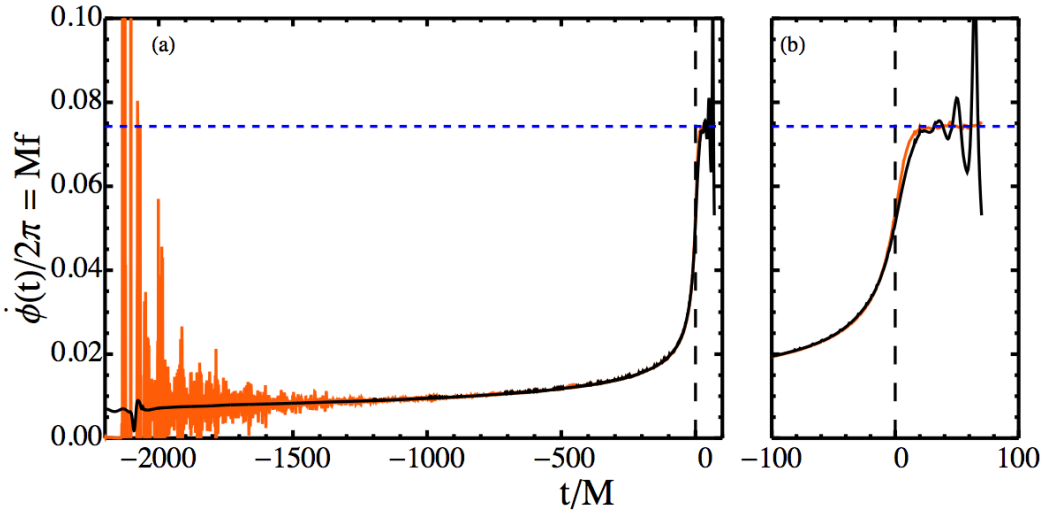

Figure 2.5: Frequency of time domain gravitational waveform from `BAM:4`, shifted such that the peak of $|h|$ occurs at $t = 0$ (vertical dashed black line). The horizontal blue line is the computed ringdown frequency. Left Panel (a): Full time range. Right Panel (b): Zoom in around merger. In black is the frequency as computed from strain and in orange is the frequency as computed using Ψ_4. The early time behaviour is much cleaner for the strain than for Ψ_4 although the late time behaviour during the ringdown is much cleaner for Ψ_4. For this reason the calculation of the ringdown frequency is performed using Ψ_4.

The phase of each case aligned, arbitrarily, such that $\phi(0) = 100$ is shown in Figure 2.7. This time from top to bottom (left panel) the curves correspond to `BAM:1...7`. The effect of increasing the system's effective spin is most noticeable by comparing `BAM:1` (top, black) with `BAM:7` (bottom, purple). A clear non-linear behaviour or "bending" is visible by eye, which increases through the merger and reaches the expected linear function during the ringdown. The change in the gradient as the phases pass through $t = 0$ is greater for the increasing anti-aligned systems. This can be seen in Figure 2.8, which plots the phase derivative, i.e., the frequency. Note the wiggles at $t \sim 100M$ is numerical noise.

In Figure 2.8 the GW frequency is shown. From bottom to top the curves correspond to `BAM:1...7`. As the effective spin increases, for a given time preceding the peak amplitude, a higher GW frequency is achieved, as expected from the hang-up effect. Once again, the time of peak amplitude lies somewhere between the inspiral regime and the onset of the ringdown stage. The rate of increase of frequency actually decreases with higher values of effective spin. Again, this can be explained through the hang-up effect, very anti-aligned systems merge faster and hence changes from its "inspiraling" frequency to its ringdown frequency faster, whereas aligned systems "stay" at a given frequency for longer.

The main time domain waveform models come from PN and EOB methods. EOB has been very successful in producing waveform models that predict the inspiral,

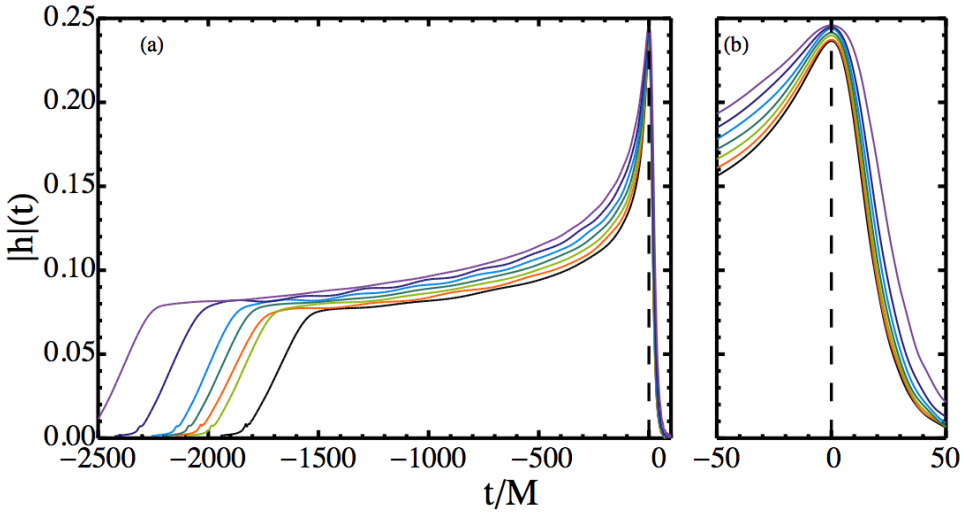

Figure 2.6: Amplitude of time domain gravitational waveform of all cases in Table 2.1, shifted such that the peak of $|h|$ occurs at $t = 0$ (vertical black dashed line). From the bottom (black) curve to the top (purple) curve corresponds to `BAM:1...7`, i.e., from the lowest to the highest values of $\chi_{\rm eff}$. Left Panel (a): Full time range. Right Panel (b): Zoom in around merger.

merger and ringdown. It has been able to do this by speeding up the convergence of PN results through Padè resummations and by calibrating free parameters in the EOB model to reproduce NR data. NR data is crucial in computing exactly how the GW frequency transitions from its final stages into the ringdown, i.e., how steep is the function around the time of peak amplitude.

Frequency Domain

We now turn our attention to the frequency domain representation of GWs. We are in some sense more comfortable with examining data in the time domain because we can apply our intuition most easily here.

However, there are a number of physical properties of BBH systems that allow us to port of some of our intuition from the time domain. In the case of non-precessing BBHs we can associate low frequencies with early times and high frequencies with late times due to the monotonicity of the signal. Monotonicity is lost in precessing and eccentric systems so this is only approximately true in these systems. Nevertheless, we can apply similar techniques as we did in the time domain to categorise the Fourier domain waveform. This is very useful because the majority of GW data analysis is performed in the Fourier domain.

The Fourier domain strain $\tilde{h}(f)$ is computed from the $\tilde{\Psi}_4(f)$ data through two frequency divisions defined in Eq. (2.4). The $\Psi_4(t)$ data is windowed with the Planck taper function to reduce Gibbs oscillations and zero padded to increase frequency resolution.

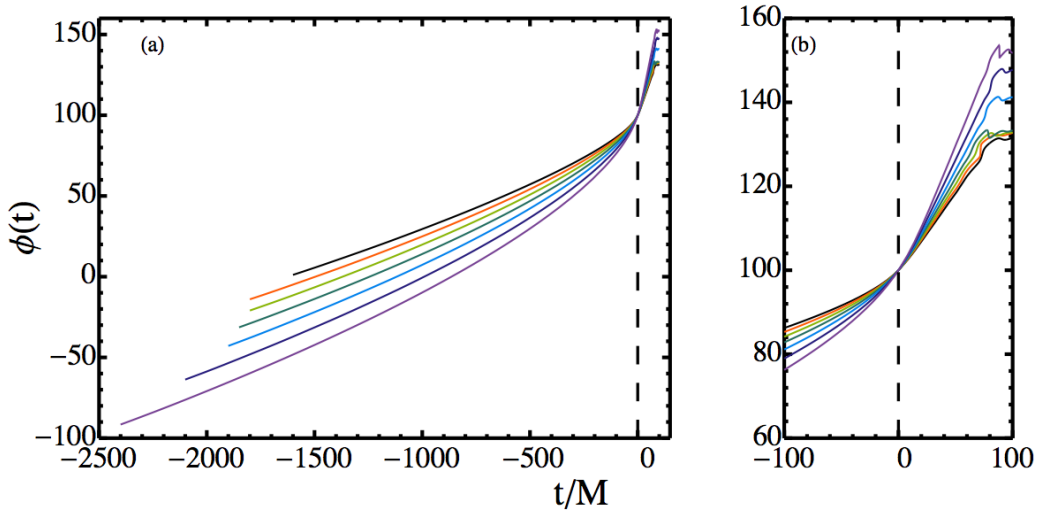

Figure 2.7: Phase of time domain gravitational waveform of all cases in Table 2.1, shifted such that the peak of $|h|$ occurs at $t = 0$ (vertical black dashed line). Left Panel (a): Full time range. From the top (black) curve to the bottom (purple) curve corresponds to `BAM:1...7`, i.e., from the lowest to the highest values of $\chi_{\rm eff}$. Right Panel (b): Zoom in around merger.

The Fourier domain amplitude and phase is defined the analogous way to the time domain as

$$\tilde{A}(f) = |\tilde{h}| = \sqrt{\mathrm{Re}[\tilde{h}]^2 + \mathrm{Im}[\tilde{h}]^2}\,, \tag{2.10}$$

$$\tilde{\phi}(f) = \mathrm{Arg}[\tilde{h}]\,. \tag{2.11}$$

The Fourier domain $(\ell, m) = (2, 2)$ amplitude of the 1:4, non-spinning simulation (`BAM:4`) is shown in Figure 2.9 as a function of the dimensionless, geometric Fourier frequency Mf. At frequencies $Mf \lesssim 0.01$ and $Mf \gtrsim 0.1$ the spectrum contains artefacts from the Fourier Transform. The black dashed line is the calculated ringdown frequency $f_{\rm RD}$ which occurs at the approximate location of the "knee" where the spectrum starts to decay *exponentially*. The ringdown frequency marks the highest *physical* frequency achieved by the BBH system but the Fourier domain spectrum clearly contains higher *Fourier* frequencies that are needed to accurately represent the signal in the Fourier domain.

Precisely determining the true end of the Fourier domain signal is difficult because, as we have seen there is power beyond the ringdown frequency. To estimate the end of the Fourier domain signal we look for frequencies beyond the ringdown frequency where the amplitude starts to get noisy. This typically occurs when $|\tilde{h}|$ has decreased by a few orders of magnitude. The low frequency follows a $f^{-7/6}$ power law predicted from PN theory however, higher order terms are needed to accurately capture the spectrum. When the ringdown is preceded by the inspiral then the ringdown is not simply the Fourier transform of the time domain ringdown from

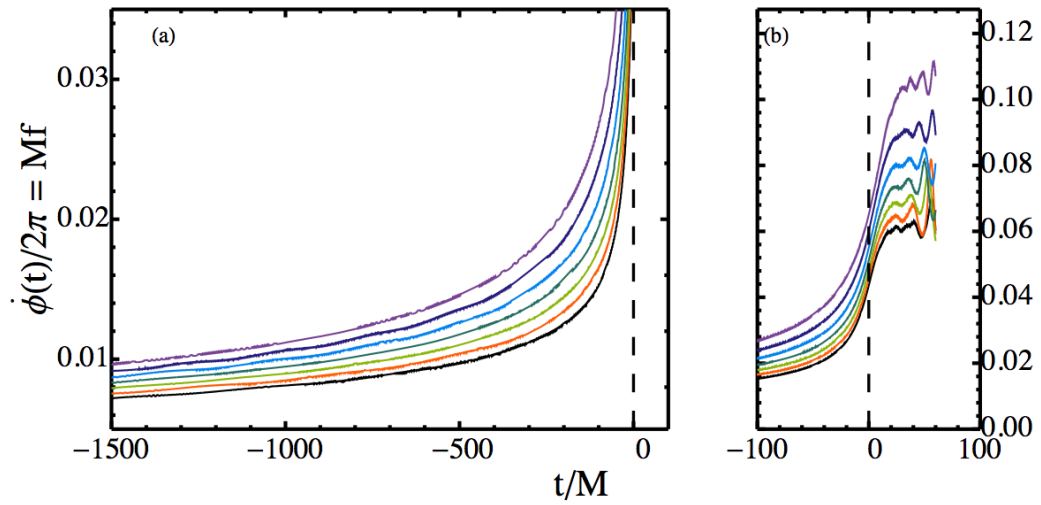

Figure 2.8: Frequency of time domain gravitational waveform of all cases in Table 2.1, shifted such that the peak of $|h|$ occurs at $t = 0$ (vertical black dashed line). Left panel (a): Shows $1500M$ prior to peak amplitude up to a frequency $Mf = 0.035$. Right panel (b): Zoom in around the time of peak amplitude. Over approximately the last $\sim 500M$ of the evolution the GW frequency increases by nearly an order of magnitude to arrive at the ringdown frequency. From the bottom (black) curve to the top (purple) curve corresponds to `BAM:1...7`, i.e., from the lowest to the highest values of $\chi_{\rm eff}$.

black hole perturbation theory.

In the Fourier domain the GW phase is defined up to a linear function corresponding to a phase ϕ_0 and a time t_0 shift such that

$$\tilde{\phi}_{\rm NEW}(f) = \tilde{\phi}_{\rm OLD}(f) + 2\pi f t_0 + \phi_0 \,. \tag{2.12}$$

The time-domain phase also possess a similar ambiguity. In the Fourier domain we may fit and subtract off a linear function over a common frequency range to compare the Fourier domain phases for multiple configurations. In Figure 2.10 we show the Fourier domain phase with a linear function, fit over the frequency interval $[Mf_1, Mf_2] = [0.01, 0.1]$, which is then subtracted from the data. This procedure also highlights interesting features difficult to distinguish without this data processing step.

The behaviour of the phase in the Fourier domain is quite different to that in the time domain, in particular the phase is not monotonic, even for non-precessing systems. Again the black dashed line marks the physical ringdown frequency of the final black hole. For frequencies higher than $f_{\rm RD}$ the phase seems to level off to a linear function.

From BH perturbation theory we known that a perturbed Kerr BH loses its perturbations by emitting a spectrum of Quasi-normal modes (QNMs), usually called ringdown radiation. The ringdown is an exponentially damped sinusoid with a fixed

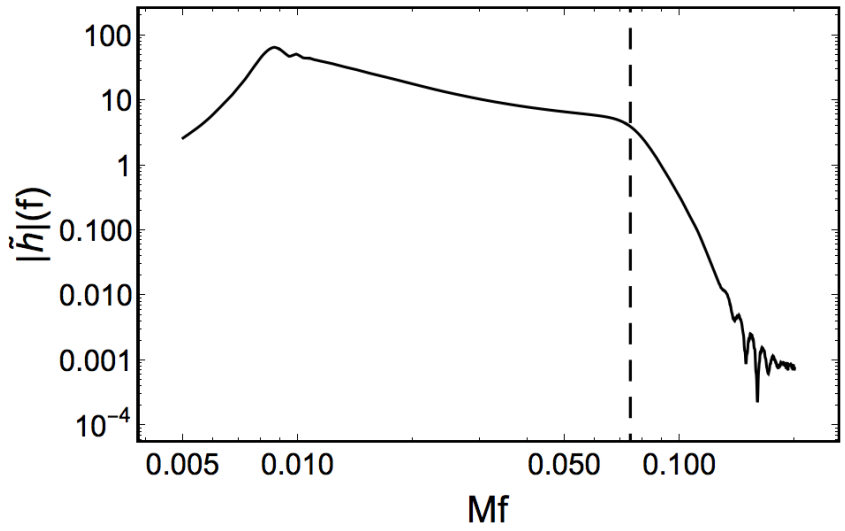

Figure 2.9: Amplitude of Fourier domain gravitational waveform for `BAM:4` on a log-log scale. The vertical dashed line is the ringdown frequency, which is the highest physical frequency. The Fourier domain representation of the signal contains higher frequencies. The spectrum contains artefacts from the Fourier transform at frequencies $Mf \lesssim 0.01$ and $Mf \gtrsim 0.1$. The low frequency follows a $f^{-7/6}$ power law predicted from PN theory however, higher order terms are needed to accurately capture the spectrum and the ringdown is not simply the Fourier transform of the time domain ringdown from black hole perturbation theory.

frequency and damping time determined by the mass and spin of the final Kerr BH. The amplitude is determined by the nature of the perturbation. The Fourier transform of an exponentially decaying signal is a Lorentzian, whose phase is simply linear. This fact has guided previous phenomenological models [25, 21, 151] in how to model the ringdown portion of the Fourier domain amplitude and phase. These results, though invaluable, are not *directly* applicable to the BBH case because the merger cannot be said to be a small perturbation. As such the ringdown waveform is preceded by the inspiral and merger signal. The effect of including the full IMR signal in the Fourier transform is to change the high frequency behaviour from a Lorentzian to an exponential decay and to also deviate the phase around the $f_{\rm RD}$ from a linear function. To explicitly show this deviation in the phase Figure 2.11 shows the frequency derivative of the Fourier domain phase $d\tilde{\phi}/df$. The black dashed line marks the highest physical frequency $f_{\rm RD}$. For frequencies $f < f_{\rm RD}$ we see a similar behaviour to the phase, this is because if you differentiate a power law you get a power law. The right panel is a zoom in around $f_{\rm RD}$. A characteristic "bump" is observed, which seems to have a minima very close to $f_{\rm RD}$. It remains to be seen if the minima corresponds exactly to $f_{\rm RD}$ or if this feature has a physical interpretation. This observation has motivated the final form of the `IMRPhenomD` model.

As before we now examine how these functions change due to the amount of effective spin. In Figure 2.12 we show $\tilde{A}$ for all cases in Table 2.1. From bottom to

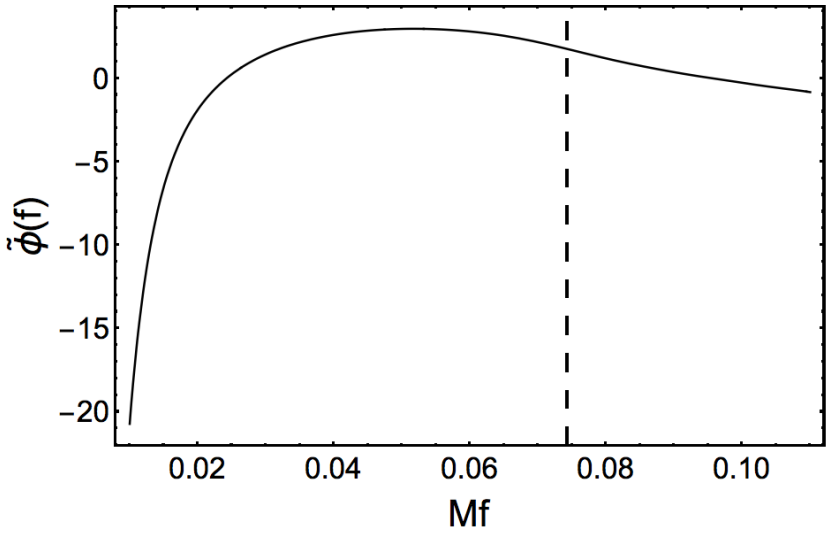

Figure 2.10: Phase of the Fourier domain strain for `BAM:4`. A linear function ($af + b$) has been fitted and subtracted from the data, over the interval $[Mf_1, Mf_2] = [0.01, 0.1]$, to accentuate the features. The Fourier domain phase is quite different to the time domain strain as it is not monotonic even for non-precessing systems.

top the curves correspond to `BAM:1...7`.

In the frequency domain the hang-up effect manifests itself in the amplitude. As the effective spin increases; the location of the "knee" (which is close to $f_{\rm RD}$) moves towards higher frequencies and the inspiral is able to follow a $f^{-7/6}$ trend for longer, which can be interpreted as inspiralling longer due to the hang-up effect. The "post knee" high frequency fall off gets steeper with increasing spin, so steep that the Lorentzian approximation, that was used in previous phenomenological models [25, 21, 151] is really unsuitable to model this region, in Chapter 3 we will see that this rapid fall off can be modelled accurately by a Lorentzian function multiplied by an exponential decay.

In Figure 2.13 we show the Fourier domain phase for all cases with a linear function, fit over the frequency interval $[Mf_1, Mf_2] = [0.01, 0.1]$, which is then subtracted from each data set. With increasing spin (going from the black curve to the purple curve) the phase becomes more curved. Whilst physically this could be a result of the hang-up effect it is difficult to pin down exactly the meaning of this in the Fourier domain also due to the phase and time shift ambiguity. For now we view this simply as a feature of the data that we want to model.

The frequency derivative of $\tilde{\phi}(f)$ for this data set is shown in Figure 2.14. We see that the "bump" is common to all data sets and we find that the minima are all close to the calculated $f_{\rm RD}$. The overall shape is also quite similar, which suggests that the functional dependence on the effective spin, on this part of the phase, is relatively weak, for the range of spins considered here.

Finally, to completely remove the ambiguity from the phase we could take another frequency derivative although the data is not always accurate enough to do

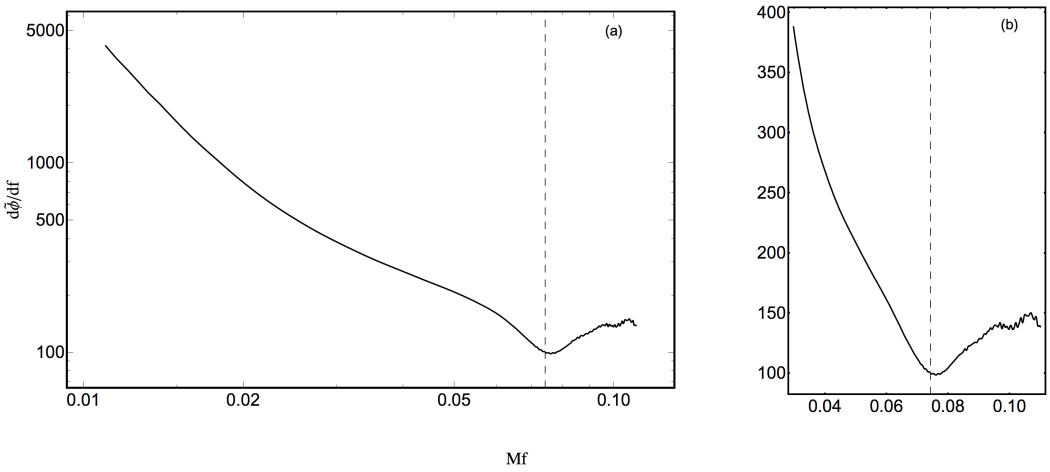

Figure 2.11: Frequency derivative of Fourier domain phase for `BAM:4`. The low frequencies has the form of an increasing power series with initially negative powers. Near merger ($f_{\rm RD}$ is marked by the vertical black dashed line) the trend is interrupted by a Lorentzian "bump" that has a minima very close to $f_{\rm RD}$. Whilst the data is noisy at $Mf \gtrsim 0.1$ we expect the function to level off to a constant. Left Panel (a): Full frequency range (log scale). Right Panel (b): Zoom in around $f_{\rm RD}$ (linear scale).

this and without sufficient amounts of smoothing before taking the derivative then the result is dominated by noise. An example of the second frequency derivative of $\tilde{\phi}$ is shown in Figure 18 from [100].

2.4 Introduction To Phenomenological Modelling

In a broad context modelling is a technique to formalise the description of a physical process typically with physical quantities. Models are built first to reproduce current observations or data and if a model is successful in this then it can be used to *predict* the outcome of future observations. The accuracy of those predictions however, can sometimes be unclear and so it becomes increasingly important to push the boundaries of experiments, to gather new data with which to test the predictions of a model. When new reliable data is presented that contradicts a model, the model should then be revised to take into account the new information and hopefully the overall performance of the model will be improved. This process will then start over and repeat.

Modelling the gravitational waveform is performed at the top level by solving the Einstein equations numerically, this is therefore our most accurate prediction for the dynamics of two BHs colliding and for the GWs they emit. NR is thus our most accurate waveform model. However, due to the large number of intrinsic parameters of BBH systems and the requirement from data analysis techniques that require access to a waveform from anywhere in this large dimensional space on a very short

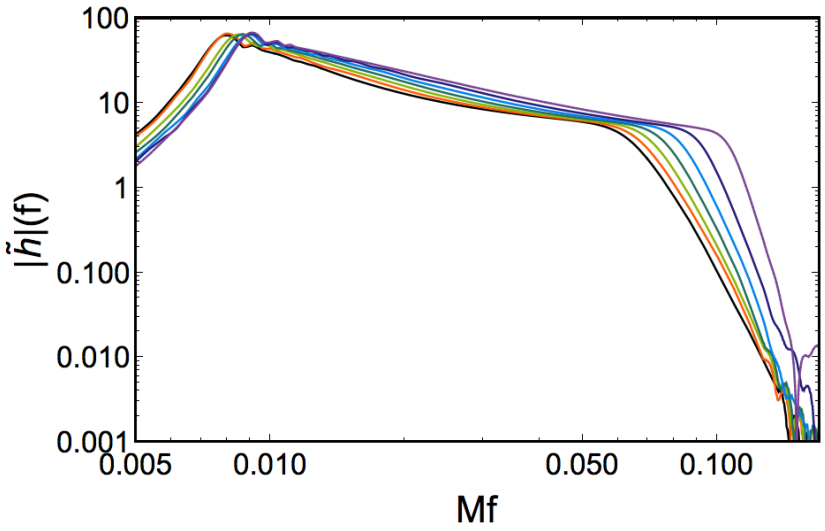

Figure 2.12: Amplitude of Fourier domain gravitational waveform of all cases in Table 2.1. From the bottom (black) curve to the top (purple) curve corresponds to `BAM:1...7`, i.e., from the lowest to the highest values of $\chi_{\rm eff}$. The orbital hang-up effect manifests itself in the amplitude. For lower values of $\chi_{\rm eff}$ the inspiral amplitude changes from the $f^{-7/6}$ power law to a shallower power law also resulting in shallower ringdown slopes.

time scale, NR cannot be used in its raw form. The computations are simply too time consuming.

One approach to incorporate the results from our most accurate predictions of GR for BBH mergers is called the *phenomenological* modelling method. The basic principles were first laid out in [25] and are summarised below.

The main goal is to develop a model (a parameterised set of functions) to predict the gravitational waveform for BBHs. When building a model we have complete freedom over everything that goes into it and about how to access the information stored in the model. The most natural way to access the information stored inside a model is to parameterise it by the *physical* parameters of the system which we denote as $\boldsymbol{\Xi}$, where in this thesis we are focussing on modelling aligned-spin BBHs parameterised by an effective spin parameter χ and their symmetric-mass-ratio, therefore, $\boldsymbol{\Xi} = \{\eta, \chi\}$. The data we are trying to model, denoted by $\mathcal{D}$ will be the frequency domain gravitaitonal strain $\tilde{h}$ decomposed into its amplitude and phase such that $\mathcal{D} = \{\tilde{A}, \tilde{\phi}\}$. These are two scalar functions of frequency, since we are working in the frequency domain. As discussed in Section. 2.3.2 and as noted in [25] these functions, $\mathcal{D}$, appear to be relatively simple functions, there are no jumps or discontinuities, and can be modelled or *fit* by relatively simple polynomial-like functions or as we shall refer to them from now on as *ansätze*. These ansätze are only implicitly functions of $\boldsymbol{\Xi}$. In general, they are functions of a number of *phenomenological coefficients* represented here by $\boldsymbol{\alpha} = \{\alpha_1, \alpha_2, ..., \alpha_n\}$. The ansätz will be represented by $\mathcal{A}(f; \boldsymbol{\alpha})$. The functional form of the ansatz is motivated by

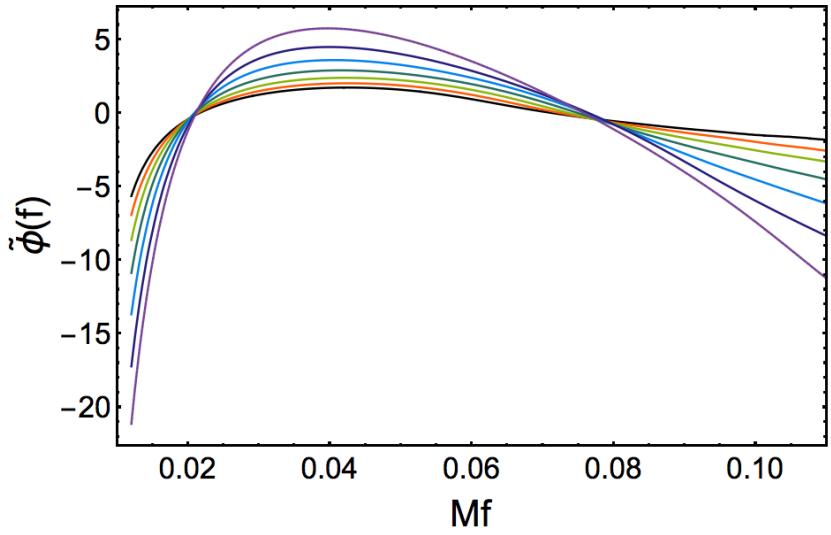

Figure 2.13: Phase of Fourier domain strain for all cases in Table 2.1. From the black curve to the purple curve corresponds to `BAM:1...7`, i.e., from the lowest to the highest values of $\chi_{\rm eff}$. Due to the phase and time shift ambiguity it is difficult to compare the intrinsic phase functions.

the properties of the data, see Section. 2.3.2 and also by the expected behaviour of the data from other sources such as PN or BH perturbation theory. The accuracy of a particular ansatz at representing a particular member of the data set can be described in terms of its residuals $\mathcal{R} = \mathcal{D}(f;\eta,\chi) - \mathcal{A}(f;\boldsymbol{\alpha})$.

Once a sufficiently accurate ansatz is found one needs to find a mapping from the higher dimensional space of phenomenological coefficients to the space of physical parameters. This is done via a *mapping function* $\Gamma : \boldsymbol{\alpha} \to \boldsymbol{\Xi}$. This mapping is constructed by expressing the phenomenological coefficients as a function of the physical parameters, $\boldsymbol{\alpha}(\boldsymbol{\Xi})$.

Note that just like our input data set where we only know the functions $\mathcal{D}$ at discrete points in parameter space from NR we *only* know the mapping function Γ at discrete points in parameter space. In order to complete the description of the model we need to *approximate* this mapping across the parameter space. This is achieved again by a fit across the parameter space where there is another choice of ansätze to make. In general, for each phenomenological coefficient there is a separate mapping ansätze, but it is usually taken to be homogenous across coefficients. Typically this is taken to be some polynomial-like function, although in [100, 106] we used a rational function ansatz to model the radiated energy.

Generally, the behaviour of the mapping function on the *interior* of the calibration region of parameter space should follow the trend of the data and not suffer from artifacts due to overfitting. It should effectively act as an *interpolant* between calibration points. On the *exterior* of the calibration region the mapping function acts as an *extrapolant*, and depending on the functional form of the ansatz these functions could very well deviate from the expected trend of the data. It is therefore

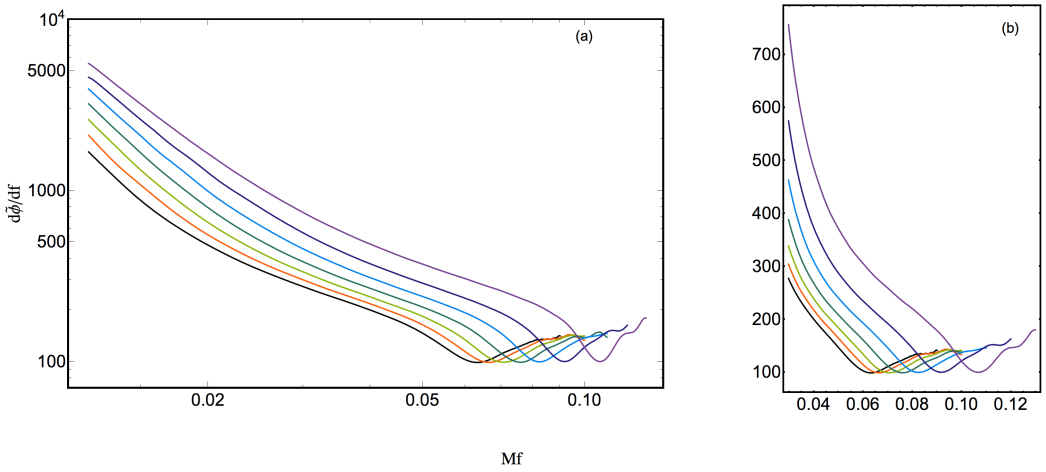

Figure 2.14: Frequency derivative of the Phase of Fourier domain gravitational waveform of all cases in Table 2.1. Left Panel (a): full frequency range (log scale). Right Panel (b): zoom in around $f_{\rm RD}$ (linear scale). From the bottom (black) curve to the top (purple) curve corresponds to `BAM:1...7`, i.e., from the lowest to the highest values of $\chi_{\rm eff}$. The data appears to depend weakly on $\chi_{\rm eff}$ except shifted to higher frequencies and the Lorentzian "bump" becomes more pronounced due to the hang-up effect.

in these *exterior* regions where a well constructed model could predict erroneous waveforms and should be treated with trepidation. Models should then be tested with all available and reliable data both in the interior and exterior to assess the validity of the model and identify regions of parameter space where the model excels and also where it underperforms or fails. Regions of imperfection can be assessed in future models when more data becomes available.

Note that when constructing a model it is very useful to assess the residuals function $\mathcal{R}$ however, for GW data analysis purposes the figure of merit is the *match* (see Section. 1.6.2). As such in the next section where we outline a preliminary BBH waveform model we will assess its accuracy by computing the match.

2.5 Preliminary Aligned-Spin Model: `PhenomC+` (2014)

In 2014 a wealth of new NR data was available, both from within our Cariff-UIB collaboration and publicly available from the SXS collaboration [127, 3]. Whilst some of the observations made in the previous section are new and interesting it remains to be seen how big of an impact they will make in terms of the accuracy of a model. As a first attempt at a new model we use a similar method that was used to construct the previous phenomenological model `IMRPhenomC` [151], with a few modifications, and apply it to a larger catalogue of NR waveforms. The full set of waveforms is given in Table 3.1. We added a few modifications which we will detail below in order to get a working model. The results partially motivated the

development of novel techniques needed to develop the IMRPhenomD model [100, 106] described in Chapter 3.

Due to various reasons such as computational cost and theoretical limits NR waveforms are of finite length and typically have quite high starting frequencies. For use in data analysis purposes waveforms need to be long enough such that their starting frequency is near the low frequency cut off for the detectors, which for advanced detectors (at design sensitivity) will be 10 Hz. A common method to extend NR waveforms is to *hybridise* them to a PN inspiral approximant. In this preliminary model, unlike previous phenomenological models, we do not do this. The reason is because we would like to develop a method to build waveform models that does not rely on any of the ambiguities associated with the hybridisation process. Instead we effectively assume that we have an inspiral approximant that is accurate enough to be used up to the starting frequency of the model. Such a model would be calibrated only to the results from NR and as such we denote this as a *merger-ringdown* model. In the Chapter 3 we present the IMRPhenomD model which *does* use hybrids but in a way so as to keep the hybridisation ambiguities separate from the merger-ringdown model.

This preliminary model now gains additional flexability. The choice of inspiral approximant can, in theory, change. This model is now *modular*. And indeed as we shall see it has allowed us to easily investigate what are the effects of choosing different inspiral prescriptions. In particular we find that the TaylorF2 PN approximant is *not* accurate enough down to the starting frequency of the merger-ringdown model but EOB based models are.

We decompose the Fourier domain strain $\tilde{h}(f)$ into its amplitude $\tilde{A}$ and phase $\tilde{\phi}$ and model each separately. Throughout the following discussion we refer to the new preliminary model as IMRPhenomC+.

2.5.1 Summary of differences between PhenomC and PhenomC+

IMRPhenomC used a set of 22 aligned-spin waveforms, covering mass-ratios from 1:1 to 1:4 and spins ranging from $[-0.85, +0.85]$, see Figure 3.1, hybridised in the frequency domain to TaylorF2. The hybridisation frequency depends on the starting frequency of the NR data, the authors use $\sim 0.1 M f_{\rm RD}$ to roughly trace the start of the NR data. For an equal-mass, non-spinning waveform $0.1 M f_{\rm RD} \sim 0.008$. Therefore, IMRPhenomC considers everything above a frequency of $0.1 M f_{\rm RD}$ part of the NR data. Below frequencies of $0.1 M f_{\rm RD}$ the waveform model reduces to the TaylorF2 approximant.

IMRPhenomC+ used a set of 19 aligned-spin waveform, covering mass-ratios from 1:1 to 1:18 and spins ranging from $[-0.95, 0.98]$, see Table 3.1 and Figure 3.1. As mentioned previously we do not hybridise these waveforms but instead chose to build a merger-ringdown model calibrated only to NR data. Because of this condition the

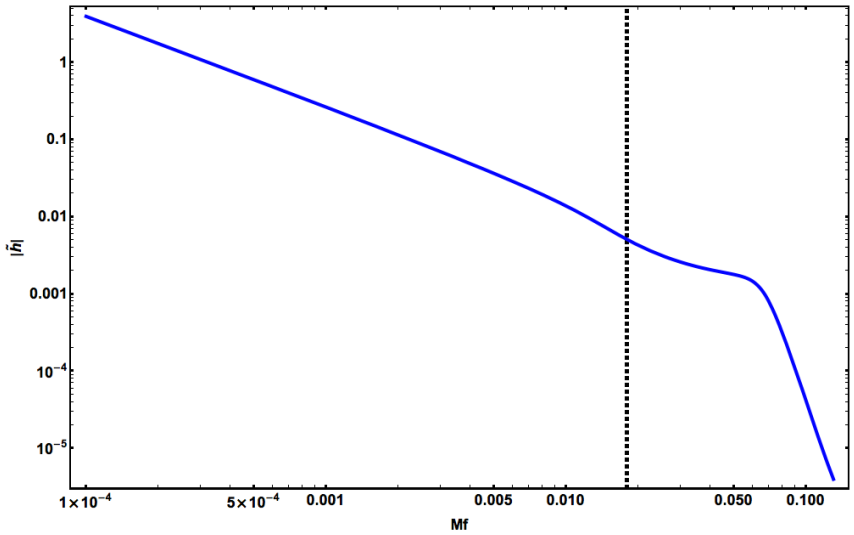

Figure 2.15: The Fourier domain amplitude $|\tilde{h}|$ as a function of geometric frequency Mf for a mass-ratio 1:5 case with aligned-effective-spin $\chi_{\rm eff} = -0.42$ computed using `SEOBNRv1_ROM`. The vertical dashed line at $Mf = 0.018$ marks the boundary between the inspiral and the merger-ringdown model.

merger-ringdown model has a low frequency cut off that is given by the highest common Fourier domain GW frequency which for these cases is $Mf = 0.018$. Below this frequency we attach an analytic inspiral approximant. This then sets the requirement for the inspiral approximant. The inspiral approximant has to be "indistinguishable" from NR up to this starting frequency of $Mf = 0.018$. The criteria for indistinguishability is somewhat arbitrary, here all we demand is that by using a given inspiral approximant joined to our merger-ringdown model then the minimum mismatch over a range of masses if greater than our conservative threshold of 97% or our more strict threshold of 99%.

Phase

Merger-Ringdown - The merger region, defined over the frequency interval $[Mf_1, Mf_2] = [0.018, f_{\rm RD}]$ is fit using the following ansatz from [151]

$$\phi_M(f) = \frac{1}{\eta}\left(\alpha_1 f^{-5/3} + \alpha_2 f^{-1} + \alpha_3 f^{-1/3} + \alpha_4 + \alpha_5 f^{2/3} + \alpha_6 f\right) . \tag{2.13}$$

The specific powers chosen are a subset of the known PN orders in the `TaylorF2` equations. The phase has the form of a power series that turns around meaning that both negative and positive powers are needed to model it.

The ringdown is defined as the region $f \geqslant f_{\rm RD}$. We again follow the same prescription as in `IMRPhenomC` and model the ringdown phase as a linear function

$$\phi_{RD}(f) = \beta_1 + \beta_2 f \,. \tag{2.14}$$

The ringdown coefficients β_1 and β_2 are determined by demanding $C(1)$ continuity at $f = f_{\rm RD}$ and are therefore not free parameters that have to be fit. But we note that the *actual* behaviour of the ringdown resulting from a BBH merger is actually more complicated, see Figure 2.14. Implementation of a more accurate ansatz for this region will come in Chapter 3.

Inspiral - We take advantage of the modularity of `IMRPhenomC+`. At the time, a ROM of the `SEOBNRv1` [164] called `SEOBNRv1_ROM` [143] was available. This provided a fast Fourier domain surrogate model for `SEOBNRv1`. We chose to compare the standard approach using `TaylorF2` against using `SEOBNRv1_ROM` as our inspiral approximant. The inspiral model is simply attached to the merger-ringdown model via $C(1)$ continuity in the phase.

Note that in `IMRPhenomC` the α_4 and α_6 coefficients were *not* fixed by enforcing continuity of any kind. This resulted in the transition between the inspiral and the merger models to develop a "drift" between these regions in some parts of the parameter space. In `IMRPhenomC+` and future models this issue has be resolved by demanding $C(1)$ continuity between the inspiral and the merger models. This effectively simplifies the model by removing two free parameters, in this case the α_4 and α_6 are fixed by matching the phase and the phase derivative of the inspiral and merger models at the point $Mf = 0.018$.

Note that any ROM has a fixed lower frequency cut off which the phenomenological model inherits if a ROM is used as the inspiral approximant. This lower frequency cut off is not present if PN is used as the inspiral approximant.

To map the phenomenological phase coefficients α_i $i \in \{1, 2, 3, 4, 5, 6\}$ to the space of physical parameters $\{\eta, \chi\}$, where χ is the effective spin parameter in Eq. (1.59), we use the following *mapping* function

$$\alpha_k = \sum_{i=0}^{3} \sum_{j=0}^{3} \xi_k^{(ij)} \eta^i \chi^j \,. \tag{2.15}$$

A criticism of this mapping function is the number of terms which gets somewhat reduced in the final model in Chapter 3.

The full IMR phase is composed of three functions, smoothly transitioned from one to other depending on the frequency being evaluated. The transition functions for this preliminary model were chosen to be the same as that in `IMRPhenomC` i.e., tanh windows of width d centred at f_0 defined as

$$w^{\pm}_{f_0} = \frac{1}{2}\left[1 \pm \tanh\left(\frac{4(f - f_0)}{d}\right)\right] \,. \tag{2.16}$$

The full IMR phase is given by

$$\phi_{\texttt{PhenomC+}}(f) = \phi_{Ins}(f) w^{-}_{f_1} + w^{+}_{f_1} \phi_M w^{-}_{f_2} + w^{+}_{f_2} \phi_{RD} \,, \tag{2.17}$$

where ϕ_{Ins} is either the `TaylorF2` approximant or `SEOBNRv1_ROM` the transition frequencies are $(f_1, f_2) = (0.018, f_{\rm RD})$ and with width $d = 0.005$.

Amplitude

Likewise with the amplitude model we follow closely the method described to construct `IMRPhenomC` [151]. Primarily due to the fact that the amplitude is less important to model accurately the amplitude model is somewhat simpler than the phase model. It consists of two regions which have a boundary near $f_{\rm RD}$.

Ringdown - For frequencies larger than $f_{\rm RD}$ we fit the following function with two free coefficients (δ_1, δ_2)

$$\tilde{A}_{RD}(f) = \delta_1 \mathcal{L}(f, f_{\rm RD}, \delta_2 Q) f^{-7/6} \,, \tag{2.18}$$

where $\mathcal{L}(f, f_0, \sigma) \coloneqq \sigma^2/((f - f_0)^2 + \sigma^2/4)$ and Q is the quality factor of the remnant BH. This is a Lorentzian centred around the ringdown frequency, of width $\delta_2 Q$, amplitude δ_1, weighted by $f^{-7/6}$ to try and model the steep fall off observed in Figure 2.12, however, it is not enough and instead an exponential weight is more appropriate, see Chapter 3.

Inspiral - For frequencies less than $f_{\rm RD}$ our ansatz to model the amplitude covering frequencies up to $f_{\rm RD}$ is

$$\tilde{A}_{Ins}(f) = \tilde{A}_{PN}(f) + \gamma_1 f^{5/6} + \gamma_2 f^{-1/7} \,. \tag{2.19}$$

Unlike the phase where we chose to either use PN or EOB as the inspiral phase, for the amplitude we simply choose to use PN.

In `IMRPhenomC` [151] the authors propose modelling this region with a simple extension of one additional term $\gamma_1 f^{5/6}$ to the PN `TaylorF2` amplitude function, which is fixed by fitting to the data. Our data set explores a larger portion of the parameter space and we found that an additional free parameter $\gamma_2 f^{-1/7}$ was needed to more accurately model the data. A qualitatively new effect seen in Figure 2.12, for systems with large anti-aligned spins and unequal masses, which were not in the calibration set for `IMRPhenomC`, the amplitude develops a "dip" at frequencies at $Mf \sim 0.02$. This effect appears to be most prominent for larger mass-ratios and larger anti-aligned spins. Even the addition of an extra parameter was not enough to accurate model this behaviour and, as we shall see in Chapter 3 more sophisticated methods are needed to model this feature.

To map the phenomenological amplitude coefficients $\Gamma_k = \{\gamma_1, \gamma_2, \delta_1, \delta_2\}$ to the space of physical parameters $\{\eta, \chi\}$, we use the proposed ansatz in [151] namely

$$\Gamma_k = \sum_{i+j\in 1,2} \xi_k^{(ij)} \eta^i \chi^j \,. \tag{2.20}$$

The full IMR amplitude is composed of two functions joined via a tanh window at $f_1 = 0.98 f_{\rm RD}$ with width $d = 0.015$ as in [151] given by

$$A_{\texttt{PhenomC+}}(f) = A_{Ins}(f) w^-_{f_1} + w^+_{f_1} A_{RD} \,. \tag{2.21}$$

To summarise the key differences between `IMRPhenomC` and `IMRPhenomC+` are:

- The `IMRPhenomC+` calibration set covers a wider area of the $\{\eta, \chi\}$ parameter space. Up to mass-ratios 1:18 and spins $[-0.95, +0.98]$.
- No hybrids were constructed to build `IMRPhenomC+`.
- `IMRPhenomC+` is modular in the sense that the inspiral, defined as frequencies below $Mf = 0.018$ is purely PN or EOB. And frequencies above $Mf = 0.018$ are purely NR. Each part of the model can be "upgraded" separately and recombined to produce a (hopefully better) new model.
- The same ansatz is used to model the merger phase but over a much smaller frequency interval. By reducing the interval over which you fit a function, you generally expect to obtain smaller residuals.
- By construction, `IMRPhenomC+` fixed the α_4 and α_6 coefficients in the phase, which represent a phase and time shift, according to the values needed to make the connection to the inspiral phase $\phi_{Ins}(f)$ $C(1)$ continuous at $Mf = 0.018$.
- `IMRPhenomC+` can use either `TaylorF2` or `SEOBNRv1_ROM` as its inspiral approximant for the phase. For the amplitude both models will reduce to `TaylorF2` in the limit of low frequency.

2.5.2 Model Validation

To assess the accuracy of `IMRPhenomC+` and to compare against the performance of `IMPRhenomC` we compute the match Eq. (1.70) against each waveform used in the calibration, for a range of masses. In general the performance of both models in the low mass-ratio range, up to 1:4, is very good however, for high spin magnitudes and high mass-ratios then even `IMRPhenomC+`, which was calibrated to these systems, shows sub-optimal behaviour. For this preliminary model we only show a few representative cases.

In Figure 2.16 we show the match of the non-spinning mass-ratio 1:18 case against three models: (i) `IMRPhenomC`, (ii) `IMRPhenomC+TF2` (Using `TaylorF2` as the inspiral approximant) and (iii) `IMRPhenomC+EOB` (Using `SEOBNRv1_ROM` as the inspiral approximant). The match was computed using the `AdvLIGOZeroDethp` PSD with a

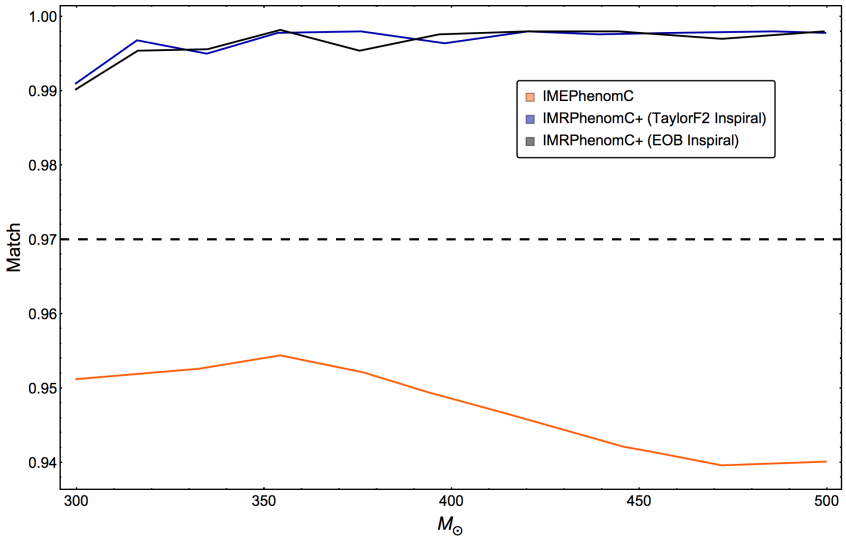

Figure 2.16: The match between `IMRPhenomC` (orange), `IMRPhenomC+TF2` (blue) and `IMRPhenomC+EOB` (black) against the non-spinning 1:18 BAM simulation. Matches were computed using the `AdvLIGOZeroDethp` PSD with a lower frequency cut off of 10 Hz. The mass range is chosen such that the NR waveform had a lower frequency of 10 Hz. Unsurprisingly `IMRPhenomC` underperforms as this is far outside its calibration range. Essentially from recalibration alone, irregardless of inspiral approximant, both variants of `IMRPhenomC+` perform better than 99%, which fulfils our accuracy criteria.

low frequency cutoff of 10 Hz. The masses where chosen such that the NR waveform's lowest frequency was at least 10 Hz. The horizontal dashed line marks the 97% match below which $\sim 10\%$ of signals would be lost in a search due to modelling errors. `IMRPhenomC` (orange) underperforms here, this is not surprising considering this case is far outside of its calibration region. This plot demonstrates the value of recalibrating waveform models to improve their accuracy. Both variants of the `IMRPhenomC+` models have matches greater than 99%.

In Figure 2.17 we show the same calculation as in Figure 2.16 but this time against the mass-ratio 1:18, $(\chi_1, \chi_2) = (-0.8, 0)$ NR waveform. Here it is evident that even though `IMRPhenomC+` was calibrated to this case the model doesn't perform well for this case. As it turns out the reason for this is because the mapping function for this case does not predict the phenomenological coefficients accurately enough. The difference at smaller masses illustrates the benefit of using EOB over PN as the inspiral approximant for this case. Interestingly `IMRPhenomC` outperforms `IMRPhenomC+` at very high masses. However, due to the rapidly changing value of the match this is likely serendipitous as we would expect the results from a robust model to not depend heavily on small changes in the total mass as is observed in this case.

In Figure 2.18 we show the match of the same three models but this time against a mass-ratio 1:5 case with aligned-effective-spin $\chi_{\rm eff} = -0.42$ computed

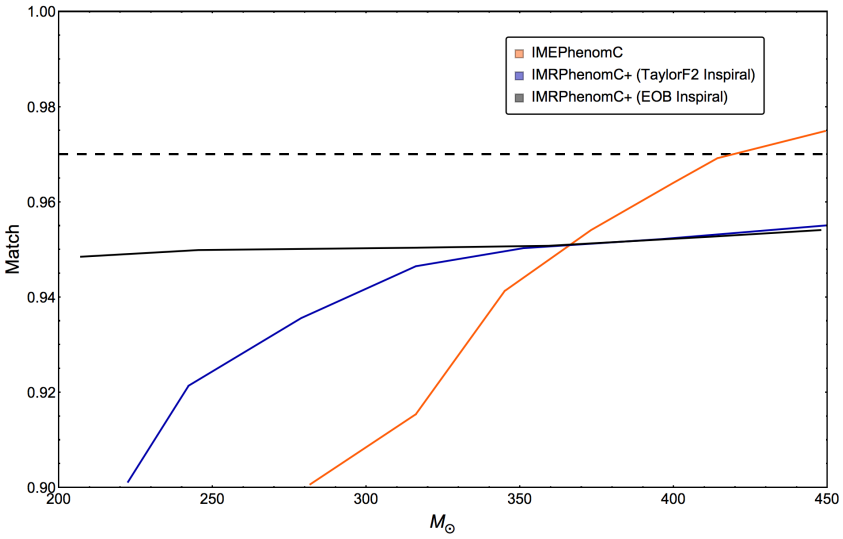

Figure 2.17: The match between `IMRPhenomC` (orange), `IMRPhenomC+TF2` (blue) and `IMRPhenomC+EOB` (black) against the 1:18, $(\chi_1, \chi_2) = (-0.8, 0)$ BAM simulation. Matches were computed using the `AdvLIGOZeroDethp` PSD with a lower frequency cut off of 10 Hz. The mass range is chosen such that the NR waveform had a lower frequency of 10 Hz. Even though this waveform was used in the calibration of `IMRPhenomC+` the model underperforms because the mapping function does not predict the phenomenological coefficients accurately enough.

using `SEOBNRv1_ROM`. This is to test the performance of our new proposed modular method. Since `IMRPhenomC+EOB` should reduce to `SEOBNRv1_ROM` at low frequencies the match should tend to unity for low masses, which is observed and the match stays above 99% for all masses considered. For the other two models that reduce to `TaylorF2` at low frequencies, the difference between inspiral approximants causes a huge drop in the match at low masses beginning at approximately the mass where the boundary bewteen the inspiral and the merger-ringdown model ($Mf = 0.018$) is in the detector's most sensitive frequency band. However at high masses, when only the merger is in band, both `TaylorF2` models perform well, highlighting the accuracy of the merger-ringdown in both models.

Finally, we test how these models perform across the parameter space. In the absence of NR waveforms at arbitrary points in the parameter space we can compare against another waveform model to evaluate the performance across the parameter space. By comparing two models constructed from different methods we can gain confidence in the accuracy of our models, particularly in regions where one or both models are extrapolating.

In Figure 2.19 we show comparisons between three models: (a) `IMRPhenomC`, (b) `IMRPhenomC+TF2` (Using `TaylorF2` as the inspiral approximant) and (c) `IMRPhenomC+EOB` (Using `SEOBNRv1_ROM` as the inspiral approximant) all against the full `SEOBNRv1_ROM` evaluated across the mass-ratio interval $[1, 20]$. The effective spin interval is restricted to $[-1, 0.6]$ due to limitations of `SEOBNRv1_ROM`. Shown is the minimum

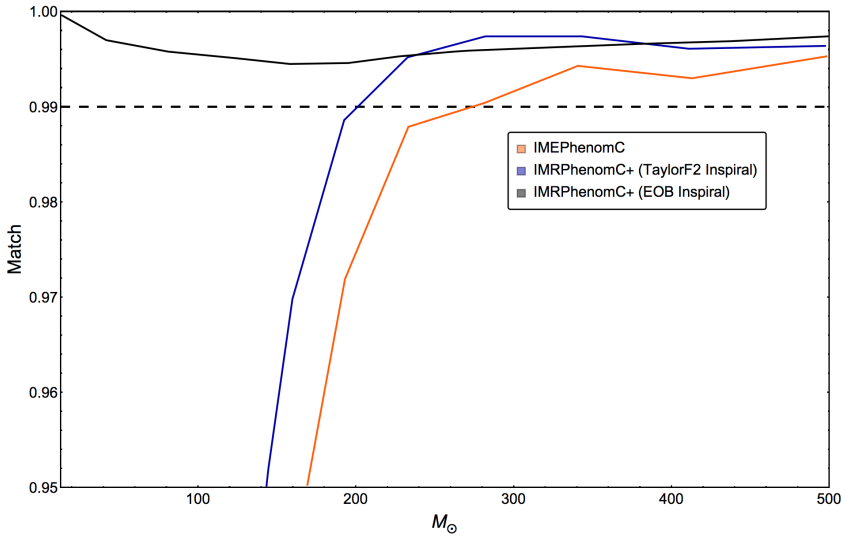

Figure 2.18: The match between IMRPhenomC+TF2 (blue) and IMRPhenomC+EOB (black) against a SEOBNRv1_ROM waveform with mass-ratio 1:5 and aligned-effective-spin $\chi_{\rm eff} = -0.42$. Matches were computed using the AdvLIGOZeroDethp PSD with a lower frequency cut off of 10 Hz. This demonstrates the effectiveness of our new modular approach to IMR modelling as the IMRPhenomC+EOB model has matches $> 99.4\%$ for all masses considered whereas the IMRPhenomC+TF2 model only agree at high masses where there merger-ringdown models are the same. The poor match at low masses is due to the disagreement between TaylorF2 and SEOBNRv1_ROM. Interestingly, this is a case where the extrapolation of IMRPhenomC performs very well, for high masses.

match computed over the total mass interval $[150, 500]M_\odot$ using the AdvLIGOZeroDethp PSD with a lower frequency cut off of 10 Hz.

Figure 2.19a shows the agreement between IMRPhenomC and SEOBNRv1_ROM. The two models agree quite well in the calibration region of IMRPhenomC (up to mass-ratio 1:4) however, exterior to the calibration region the match drops quickly. Large regions of the parameter space have matches < 0.72 indicated by the grey circles. Ordinarily, without a model that has been calibrated to NR waveforms in these regions we wouldn't be able to say confidently which model is accurate or if both models are inaccurate. Fortunately, we have just developed IMRPhenomC+ and we can use this to investigate how this model agrees with SEOBNRv1_ROM; the results are shown in Figure 2.19b (IMRPhenomC+TF2) and Figure 2.19c (IMRPhenomC+EOB). We see high levels of agreement across nearly the entire parameter space considered, with the major exception of a pocket of poor matches in the lower right region. The reason for poor match was due to a bug in the SEOBNRv1 code that SEOBNRv1_ROM inherited [143]. Also the strange pattern of varying match is not present in IMRPhenomC+, which suggests that this model is behaving more smoothly across the parameter space. The fact that these two independent models are agreeing to such a high level and across such a large portion of the parameter space is a sign that both models are performing extremely well.

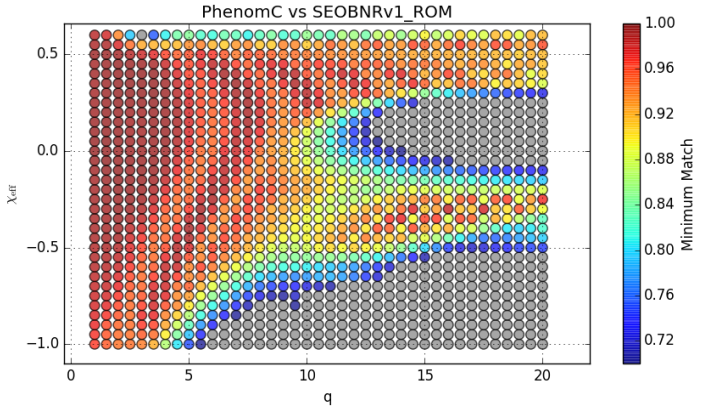

(a)

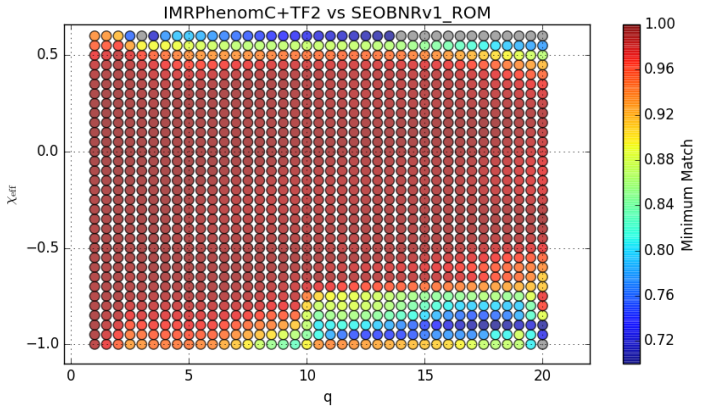

(b)

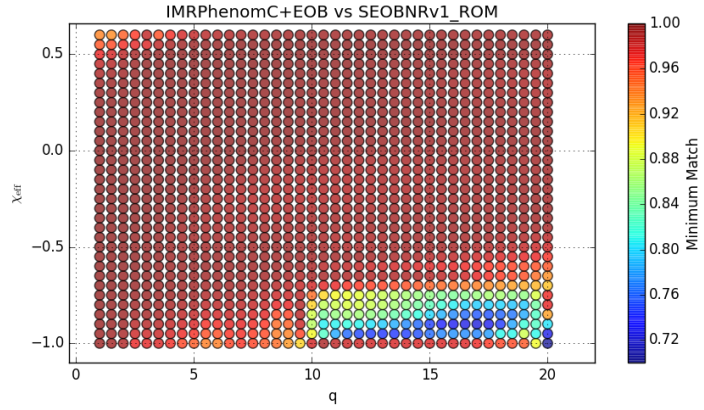

(c)

Figure 2.19: Comparison between three models: (i) `IMRPhenomC`, (ii) `IMRPhenomC+TF2` (Using `TaylorF2` as the inspiral approximant) and (iii) `IMRPhenomC+EOB` (Using `SEOBNRv1_ROM` as the inspiral approximant) against `SEOBNRv1_ROM` evaluated across the mass-ratio interval $[1, 20]$. The effective spin interval is restricted to $[-1, 0.6]$ due to limitations of `SEOBNRv1_ROM`. Shown is the minimum match computed over the total mass interval $[150, 500]M_{\odot}$ using the `AdvLIGOZeroDethp` PSD with a lower frequency cut off of 10 Hz. The loss in match in the lower right region of (b) and (c) was due to a bug in the `SEOBNRv1` code which `SEOBNRv1_ROM` inherited.

2.6 Concluding Remarks

In the previous section we took an in-depth look at the functional form of the amplitude and phase in both the time and frequency domain. We made a number of new observations by looking at the data in new ways, for example studying the frequency derivative of the Fourier domain phase that has revealed new "features" in the data, which allows us to motivate specific ansatz̈e, discussed in Chapter 3.

We presented a preliminary model `IMRPhenomC+` calibrated to a new dataset of NR waveforms by implementing the `IMRPhenomC` modelling method with some modifications. We found that `IMRPhenomC+` is a vast improvement over `IMRPhenomC` but failed to accurately reproduce all the input calibration waveforms to the standard of $> 97\%$ match we desire or even the more strict requirement of $> 99\%$. However, even without meeting this criteria the agreement with an independent model `SEOBNRv1_ROM` was found to be extremely good for high masses placing confidence in *both* modelling efforts. It is especially interesting that `SEOBNRv1_ROM` agrees so well with `IMRPhenomC+` in the high mass-ratio region where the `SEOBNRv1` model was calibrated only up to a non-spinning mass-ratio 1:8 SpEC waveform.

In the next chapter we present the complete construction of `IMRPhenomD` [100, 106], which employs some of the modifications introduced to build `IMRPhenomC+` as well as expanding on some of these concepts and improving them further. We also use the knowledge gained in Section. 2.3.2 to guide us into developing new ansätze that represent the data more accurately.

Chapter 3

IMRPhenomD: An Aligned Spin Model For The Advanced Detector Era

This chapter is based on the Refs. [106] and [100], in collaboration with Sascha Husa, Mark Hannam, Frank Ohme, Michael Pürrer, Xisco Jiménez Forteza and Alejandro Bohé.

3.1 Introduction

Observations and measurements of BBHs rely on accurate theoretical models of their GW signal. Although especially loud signals, such as GW150914, can be found by non matched-filter based burst searches, inference about the physical parameters of GW candidates can only be performed with parameterised gravitational waveform models. The construction of such models is an active research topic [87] and the focus of this thesis.

To date most effort has focussed on binaries where the spin of each BH is either zero, or aligned with the binary's orbital angular momentum. In these configurations the orbital plane and spin directions remain fixed, and the resulting GW signal is far simpler than in generic (precessing) configurations (see Chapter 1.3). Recent work has suggested that aligned-spin models may allow detection of most (even precessing) binaries [20, 94, 66], and also that approximate yet accurate generic models can be constructed based on an underlying aligned-spin model [158].

Aligned-spin models that include the two BHs' inspiral, their merger and the ringdown of the final BH, are based on a combination of analytic PN and EOB methods to describe the inspiral, and the calibration of phenomenological merger-ringdown models to NR simulations. The two classes of models are the *phenomenological* ("Phenom") models [24, 23, 20, 151], which began as phenomenological treatments of both the inspiral and merger-ringdown, and EOB models [53, 55, 72, 73, 68,

133, 176, 134, 164, 75, 136, 166, 69, 128], which have used successively more sophisticated versions of the EOB approach to describe the inspiral all the way to merger, followed by the smooth connection of a ringdown portion; NR waveforms are used to calibrate unknown EOB coefficients and free parameters in the merger-ringdown.

The original motivation of the Phenom approach was to produce an approximate and efficient waveform family suitable for GW searches (the models are written as closed-form analytic expressions in the frequency domain), and indeed this practical approach allowed the construction of the first aligned-spin model, often referred to as "`IMRPhenomB`" [20]. Although some aspects of the model were made more accurate in the succeeding "`IMRPhenomC`" model [151], the Phenom approach is still regarded by many as approximate, and in particular not suitable for parameter estimation. This perception has been reinforced by the limited region of parameter space over which the aligned-spin `IMRPhenomC` model was calibrated — up to binary mass ratios of only 1:4 (spinning up to 1:3), and BH spins of only $\chi \sim 0.75$ (0.85 for equal-mass systems). In this chapter (and a companion article Ref. [100]), we show that the phenomenological approach is capable of describing BBH waveforms with a high degree of physical fidelity, well within the requirements of aLIGO and AdV, and we construct a model that is calibrated to the largest region of parameter space to date — up to mass ratios of 1:18, and spins up to $\chi \sim 0.85$ (0.98 for equal-mass systems). This constitutes the main purpose of this chapter, to present our new "`IMRPhenomD`" model, and demonstrate its accuracy.

In contrast, the most recent EOB-NR (`SEOBNRv2`) [166] model is calibrated to NR waveforms up to mass ratio 1:8, and spins up to $\chi \sim 0.5$. It has been shown to be extremely accurate within its calibration region, and it also appears to produce physically reasonable waveforms over the full range of BH spins, and up to much higher mass ratios [110]. In this work, however, we find that the `SEOBNRv2` model may not accurately describe the merger-ringdown regime for high spins $\chi \gtrsim 0.7$. This finding motivates a second purpose of this chapter: to make clear that the accuracy of *any* merger-ringdown model, Phenom, EOB-NR, or otherwise, is only as good as its NR calibration region. The model may give physically plausible results, but its accuracy cannot be guaranteed until it has been checked against fully general relativistic NR calculations, and its accuracy may well be poor until it has been calibrated to those simulations. This seemingly obvious observation bears emphasising. It also motivates efforts to quantify the accuracy of PN and EOB calculations increasingly far back into the inspiral [163, 110].

Another important contribution of the Phenom programme has been to isolate which combinations of physical binary parameters will be measurable in GW observations. For example, the previous aligned-spin Phenom models [20, 151] exploited the observation that the dominant spin effect on the GW phase is due to a weighted combination of the individual BH spins, and the models depend on only two physical parameters, the symmetric mass ratio and this single effective spin parameter. The

identification of a simple combination of the in-plane spin components in generic binaries [159] in turn led to a simple extension of `IMRPhenomC` to produce a generic-binary model, PhenomP [91].

A corollary of this parameter-space reduction is that individual spins are expected to be difficult to measure from GW observations, even if we have a two-spin model to hand. Based on previous studies [20, 145], and in particular a recent study that illustrates in detail the difficulty of measuring individual spins with an aligned-spin model [147], we also use an effective reduced spin parameter in certain parts of the `IMRPhenomD` model. We will nonetheless pursue the extension of the Phenom approach to two spins in future work.

An additional feature of the `IMRPhenomD` model is its modularity. The separate inspiral and merger-ringdown parts of the model are connected by the requirement of continuity in the phase and amplitude. This simple construction makes it straightforward to improve and change either part of the model independently. We can make use of this feature to compare versions with alternative choices for the inspiral part of the model.

In Ref. [100] we discussed in detail the numerical simulations we have used, and in particular presented studies of the accuracy of the new NR waveforms that we have produced. In Chapter 2 we analysed the mass-ratio 1:4 subset of the new BAM simulations. In this chapter we re-visit these waveforms, but from the point of view of GW applications, and assess their accuracy in terms of their noise-weighted inner product (match) defined in Chapter 1.6.2.

In Secs. 3.5 and 3.6 we give details of the procedure we use to construct our models of the signal phase and amplitude, over three frequency regions, with more details provided in Ref. [100]. In Sec. 3.9 we assess the final complete model's accuracy by calculating matches against both the waveforms used for calibration, and an additional set of waveforms that were *not* used for calibration. We discuss the accuracy of our single-reduced-spin approximation, and our choice for the minimal set of waveforms necessary for an accurate model. In Sec. 3.10 we compare against the `SEOBNRv2` model, illustrating the high-spin, unequal-mass region where we find disagreement between the two models; this is outside the calibration region of `SEOBNRv2`. In Appendix A.1 we revisit the agreement between our new model and the original NR data by transforming `IMRPhenomD` to the time domain, and in Appendix A.2 and A.3 we list the PN inspiral coefficients and calibrated phenomenological coefficients used in our model.

3.2 Preliminaries

3.2.1 Outline of the model

We describe a BBH system by the following parameters. The masses are m_1 and m_2, where we choose $m_1 > m_2$, and the total mass is $M = m_1 + m_2$. The mass ratio of the binary is denoted $q = m_1/m_2 \geq 1$, and the symmetric mass ratio is $\eta = m_1 m_2/M^2$. The BH spin angular momenta are $\mathbf{S}_1$ and $\mathbf{S}_2$ which we assume to be parallel to the direction of the orbital angular momentum, $\hat{\mathbf{L}}$. In this work we restrict ourselves to aligned-spin (non-precessing) systems, and so are only concerned with the dimensionless spin parameters defined as

$$\chi_i = \frac{\mathbf{S}_i \cdot \hat{\mathbf{L}}}{m_i^2}, \tag{3.1}$$

with $\chi_i \in [-1, 1]$. In this work the phenomenological coefficients are parameterised by η and $\chi_{\rm PN}$. $\chi_{\rm PN}$, defined by Eq. (1.58), is the leading-order spin effect on the binary's phasing [65, 141, 20] and we have seen evidence in previous work that this is in general a better parameter to use also in IMR models [145]. On some plots we use a normalised $\chi_{\rm PN}$ such that its range is from -1 to 1 for all mass ratios,

$$\hat{\chi} = \frac{\chi_{\rm PN}}{1 - 76\eta/113}\,. \tag{3.2}$$

The final BH is completely parameterised by the final mass M_f and spin a_f, and for this reason the final mass and spin estimates that we use (see [100]), are parameterised by a different spin combination, $S_1 + S_2$. Finally, our inspiral model is based on the standard frequency-domain PN approximant, "`TaylorF2`" [71, 31], and this is parameterised by *both* spins, χ_1 and χ_2. The final result is a model that depends on both spins χ_1 and χ_2, but the calibration to hybrid EOB+NR waveforms is parameterised by different combinations of χ_1 and χ_2 for the inspiral, merger and ringdown parts of the model. Most of the hybrid waveforms are for equal-spin $\hat{\chi} = \chi_1 = \chi_2$ systems, so we can guarantee our model's accuracy only for these configurations. However, as we discuss in Sec. 3.9.2, the $\hat{\chi}$ approximation is extremely accurate for most regions of parameter space, and in those where it is not (higher mass ratios and high parallel spins), the inaccuracy is unlikely to have any influence on GW astronomy applications with aLIGO or AdV.

The `IMRPhenomD` model provides expressions for the dominant $\ell = 2, |m| = 2$ spin-weighted spherical-harmonic modes of the GW signal. The full signal as a function of the physical parameters $\Xi \in (M, \eta, \chi_1, \chi_2)$ and the angular distribution

(θ, ϕ) with respect to the orbital angular momentum of the binary, is given by,

$$\tilde{h}(f;\Xi,\theta,\phi) = \tilde{h}_+(f;\Xi,\theta,\phi) - i\tilde{h}_\times(f;\Xi,\theta,\phi) \tag{3.3}$$

$$= \sum_{m=-2,2} \tilde{h}_{2m}(f;\Xi)\ {}^{-2}Y_{2m}(\theta,\phi), \tag{3.4}$$

where $\tilde{h}_{2,-2}(f) = \tilde{h}^*_{2,2}(-f)$ expresses the equatorial symmetry of non-precessing systems. We express $\tilde{h}_{22}(f)$ in terms of the signal amplitude and phase by

$$\tilde{h}_{22}(f;\Xi) = A(f;\Xi)e^{-i\phi(f;\Xi)}, \tag{3.5}$$

and it is models of $A(f;\Xi)$ and $\phi(f;\Xi)$ that we provide. Note also that the total mass M provides an overall scale for our waveforms, so the physical parameters over which the model has been explicitly constructed are η, χ_1 and χ_2 (with the spins treated in combinations as described above).

As ingredients in our model construction, we use hybrid waveforms, where the early inspiral is described by the un-calibrated SEOBv2 model (see [100], and Sec. 3.4 below), and the late inspiral and merger-ringdown by NR waveforms. The mass and spin of the final BH, M_f and a_f, which are key parts of the merger-ringdown model, are provided by fits to NR data. The details of the hybrid construction, and of the final mass and final spin fits, are given in [100].

We model separately three frequency regimes of the waveform. The first region covers the inspiral, up to the frequency $Mf = 0.018$. Here the information is predominantly from the analytical EOB inspiral waveforms, although there is some information at higher frequencies from the early parts of the longer NR waveforms; the frequency at which each hybrid switches to an NR waveform is provided in Tab. 3.1. The second two regions are informed purely from NR data. We note that in principle one could also construct the individual inspiral and merger-ringdown models separately from PN or EOB models (for the inspiral) and NR data (for the merger-ringdown), without constructing any hybrid waveforms. In this work we chose to use hybrid waveforms, because they allow us to use the maximum NR information (which influences to some extent our inspiral model), and allows for a consistent choice of calibration points in parameter space for both the inspiral and merger-ringdown.

The resulting model is modular: we are free to use a different inspiral model, or a different merger-ringdown model, as we wish. This introduces a flexibility that was not present in previous models. If in the future we have access to a more accurate inspiral model (EOB, PN, or otherwise), or more accurate merger-ringdown model (e.g., calibrated to waveforms over a larger region of parameter space), then we can easily replace that part of the model without any additional tuning. The model calculates appropriate time- and phase-shifts (a linear correction to the frequency-domain phase) to ensure that the phase connects smoothly between the inspiral and

merger-ringdown. The amplitude model of the the intermediate region between inspiral and merger-ringdown is also constructed such that the function is continuous.

3.2.2 Matches

To assess the accuracy of our model and generally quantify the (dis)agreement between two waveforms h_1 and h_2 (real-valued in the time domain), we use the standard inner product weighted by the power spectral density of the detector $S_n(f)$ defined in Chapter 1.6.2. In practice the limits of the inner product are taken over the finite frequency interval $[f_{\rm min}, f_{\rm max}]$ given by

$$(h_1|h_2) = 4\,\mathrm{Re}\int_{f_{\rm min}}^{f_{\rm max}} \frac{\tilde{h}_1^*(f)\,\tilde{h}_2(f)}{S_n(f)}\,df. \tag{3.6}$$

The *match* (M), defined by Eq. (1.70) in Chapter 1.6.2, between two waveforms is defined as the inner product between *normalised* waveforms $\hat{h} = h/\sqrt{(h|h)}$, maximised over relative time and phase shifts between the two waveforms. A time- and phase-shift has no significance for the physical fidelity of an aligned-spin waveform — they correspond, respectively, to a change in the merger time of the binary, and of the initial phase of the binary, i.e., an overall rotation.

Results will be quoted in terms of the *mismatch* $\mathcal{M}$, defined as,

$$\mathcal{M}\left[h_1, h_2\right] = 1 - \mathrm{M}\left[h_1, h_2\right]. \tag{3.7}$$

We use two noise spectra in this chapter: the "early aLIGO" spectrum, which approximates the detector response during the first observing run, September 2015 - January 2016, and the "zero-detuned high-power" (zdethp) spectrum, which is the design goal of aLIGO that is anticipated by 2019-20 [8][1]. Calculations with the early aLIGO curve use a lower cutoff frequency of $f_{\rm min} = 30\,\mathrm{Hz}$, and zdethp calculations are carried out with $f_{\rm min} = 10\,\mathrm{Hz}$. In both cases, we use $f_{\rm max} = 8000\,\mathrm{Hz}$ which is greater than the highest frequencies contained in the signals we are considering.

In various steps of the model construction in this chapter, we are interested in analyzing the agreement of waveform sections that are only defined over a certain frequency range. (A good example are NR waveforms that are typically too short to fill the entire aLIGO frequency band.) In these cases, one could reduce the integration limits in Eq. (3.6) to the frequency range defined by the waveform sections, but the resulting matches would be difficult to interpret as they have no direct application in GW searches. Here instead, we ask the question "What influence does the difference in a certain part of the signal have on the full waveform, assuming all other parts are perfectly modeled?" We address this question by aligning the signal

[1] It is worth noting that the predicted "early aLIGO" noise curve used in this work agrees well with the actual noise curve of the LIGO detectors during their first observing run (O1). The biggest disagreement occurs at high frequencies (> 300 Hz) where the O1 noise curve is more sensitive by a factor of a few.

parts that we wish to compare as if they were hybridized with a common model of the remaining signal and set the phase difference for this particular alignment to zero over all frequencies that are not covered by the waveform sections we consider. To construct the full integrand in Eq. (3.6), we additionally need a model of the amplitude, which we take from our final `IMRPhenomD` model, although this particular choice is far less important than the phase disagreement we wish to quantify. We can then use a standard algorithm to calculate the mismatch between both signals, and due to their simple form in the frequency domain, time and phase shifts will be properly taken into account across the entire signal. More details and a full discussion of this approach is given in [132].

3.3 Numerical-Relativity Waveforms

We calibrated the `IMRPhenomD` model with publicly available NR waveforms from the Simulating Extreme Spacetimes (SXS) collaboration [3], and a set of new simulations produced with the BAM code [50, 99]. Details of the new BAM simulations and their numerical accuracy are presented in Ref. [100]. Here we summarize the 19 NR waveforms that we used to calibrate the model. The additional waveforms that were used to further test its accuracy are discussed in Section 3.9.1.

Our two main goals are to extend the parameter-space coverage of aligned-spin phenomenological models to higher mass ratios, and to improve the overall accuracy to well within the requirements of GW detection and parameter estimation with Advanced LIGO and Virgo; in practice we consider a mismatch error of less than 1% to be sufficient. The first goal dictated our choice of new NR simulations.

The previous aligned-spin phenomenological models, `IMRPhenomB` [20] and `IMRPhenomC` [151], were constructed from waveforms up to mass ratios of 1:4, and (equal) spins up to ± 0.75 (with ± 0.85 for equal-mass binaries), although spinning-binary waveforms were used only up to mass-ratio 1:3. The authors found in constructing those models that it was sufficient to use only four or five NR waveforms in each direction of parameter space. This suggests that we can construct a model across the entire $(\eta, \hat{\chi})$ parameter space with only 30 waveforms.

Five aligned-spin waveforms equally spaced in η would be placed at $\eta = (0.25, 0.20, 0.15, 0.10, 0.05, 0)$[2]. (In the current model we do not include extreme-mass-ratio $\eta \to 0$ waveforms, e.g., Refs. [92, 165], but we plan to use these to complete our parameter-space mapping in future work). We focus on simulations at mass ratios $q = 1, 4, 8, 18$, which correspond to $\eta \approx (0.25, 0.16, 0.10, 0.05)$; we find that waveforms at $\eta \approx 0.2$ are not necessary to produce an accurate model, although the model is tested against waveforms at $q = 2, 3$ ($\eta = 0.222, 0.1875$).

We produced new waveforms with the BAM code up to mass ratio 1:18, and for a

[2]Here $\eta = 0$ represents extreme-mass-ratio limit systems. In practice these have values of symmetric-mass-ratio of order $\mathcal{O}(\eta) = 10^{-3}$, corresponding to mass-ratio $\sim$ 1:1000.

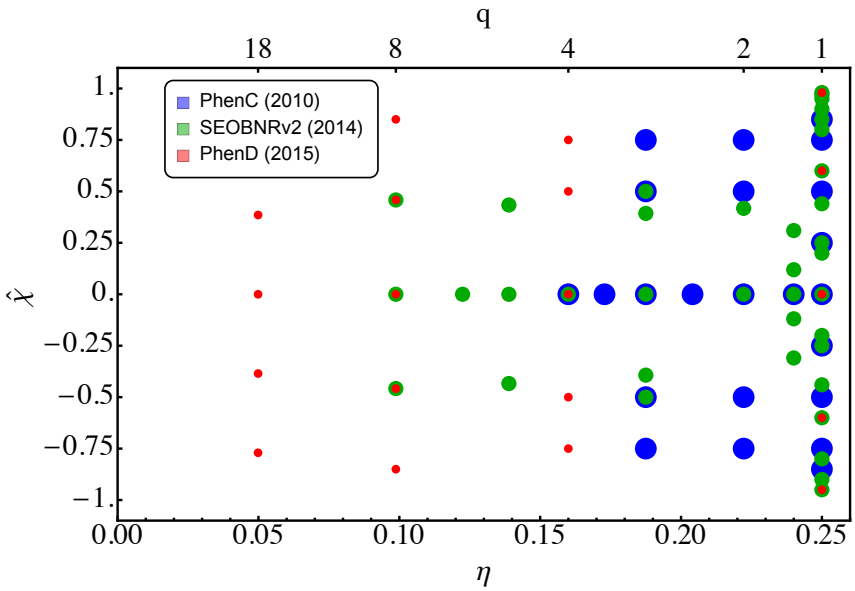

Figure 3.1: Parameter space over which the `IMRPhenomD` (red) model has been calibrated. The locations in parameter space of the calibration waveforms are indicated by red points. Also shown are the calibration points for the `SEOBNRv2` (green) and `IMRPhenomC` (blue) models.

range of spins. At lower mass ratios we have also used publicly available waveforms, which were produced by the SXS collaboration using the Spectral Einstein Code (SpEC). In particular, their catalogue provides waveforms for equal-mass binaries with high BH spins of -0.95 and $+0.98$. The parameter space coverage of NR waveforms used in previous models, and in our new model, are shown in Fig. 3.1, and the details of the waveforms that we used are summarized in Tab. 3.1. We tested the model against an extended set of waveforms, and this is described in more detail in Sec. 3.9 and Tab. 3.3.

The accuracy of the new 1:4 BAM simulations was discussed in Chapter 2 and the others are discussed in Ref. [100]. In this work we are interested in constructing accurate waveform models for GW astronomy with aLIGO and AdV. In that context, an important accuracy measure is the mismatch between the waveforms with respect to the aLIGO noise spectrum. We calculate the mismatch between the numerical waveforms following the procedure outlined in Sec. 3.2.2; in particular, we take into account the inspiral signal power, allowing us to calculate mismatches for low-mass systems, and reliably infer the (typically larger) mismatches in these systems due to any errors in the merger-ringdown waveforms. This procedure tends to estimate larger mismatches than integrating Eq. (3.6) over only the frequency range of the NR waveforms, as in, e.g., Ref. [98], and is a more conservative estimate of the mismatch error in the NR waveforms.

We consider the effect of two sources of error on the mismatch: the errors due to

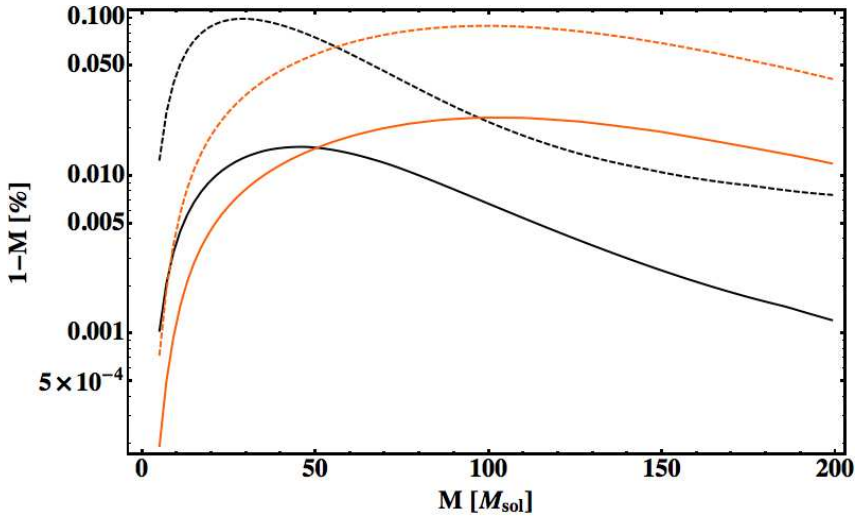

Figure 3.2: Mismatch error due to numerical resolution, for the $q = 4$, $\chi_1 = \chi_2 = \hat{\chi} = 0.75$ (black lines) and non-spinnning $q = 18$ simulations (orange lines). The solid black line shows the mismatch between waveform $q = 4$ 112- and 96-point simuations, and the dashed black line shows the mismatch between the 112- and 80-point simulations. For the $q = 18$ configuration, the solid orange line shows the mismatch between the 144- and 120-point simulations, and the dashed orange line shows the mismatch between the 144- and 96-point simulations (see text).

(1) finite numerical resolution, and (2) finite waveform extraction radius. In all cases we have found the overall mismatch error from these sources to be $< 0.5\%$. Here we focus on two configurations, $q = 4$, $\chi_1 = \chi_2 = \hat{\chi} = 0.75$ (A10), and nonspinning $q = 18$ (A18).

Fig. 3.2 shows the mismatch error due to numerical resolution. In the $q = 4$ configuration, the reference simulation uses a base grid size of 112^3 points, with the finest grid spacing being $h_{\rm min} = M/230$. Comparisons are made against a simulation with the same resolution but a base grid size of 96^3 points, and an 80^3 simulation with the resolution scaled to give the same physical grid sizes as in the 96^3 simulation. The solid black line shows the mismatch between the 112-point and 96-point simulations, i.e., simulations where only the physical grid sizes were changed. This change introduces a mismatch error of at most $\sim 0.01\%$. The dashed black line shows the mismatch between the 112-point and 80-point simulations, i.e., both the physical grid sizes and the numerical resolution have been reduced. Here the mismatch difference is at most $\sim 0.1\%$.

The orange lines show the mismatch between the $q = 18$ waveforms, with grid sizes of 96^3, 120^3 and 144^3 points. These three simulations constitute a convergence series, and we have shown in Ref. [100] that they exhibit evidence of sixth-order convergence. The solid orange line shows the mismatch between the 144^3 and 120^3 simulations, and the dashed orange line shows the mismatch between the 144^3 and 96^3 simulations. The higher mismatches at high mass, compared to the $q = 4$ configuration, suggests that the merger-ringdown errors are larger in this case, although

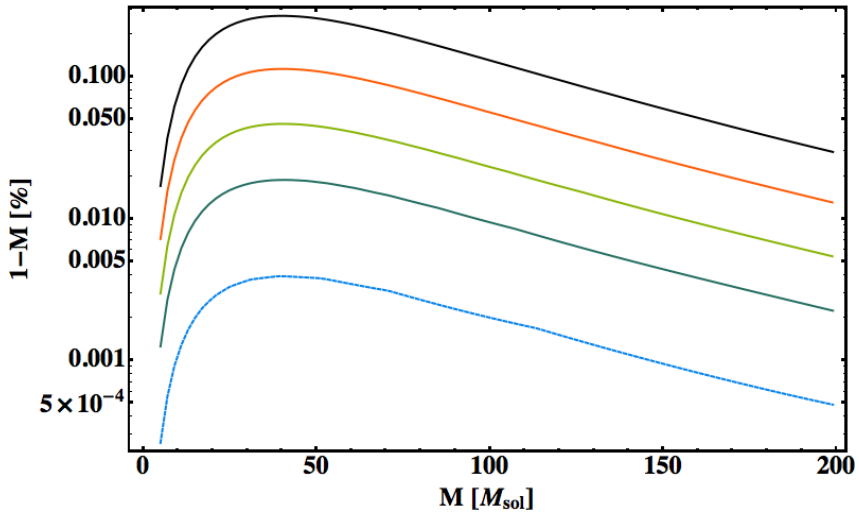

Figure 3.3: Mismatch errors due to finite-radius waveform extraction for the 120-point simulations of the same $q = 4$ case as in Fig. 3.2. Mismatches are between the $R_{ex} = 100\,M$ waveform and those extracted at $R_{ex} = \{50, 60, 70, 80, 90\}\,M$ (from top to bottom).

their effect on the mismatches at lower masses is comparable. We again conclude that the waveforms are accurate to well within our 1% criterion.

Although the convergence of our simulations is in general unclear, we typically find that our 80-point simulations are not in the convergence regime, and are much less accurate than higher-resolution simulations. We therefore expect that if the mismatch between the 112-point and 80-point simulations is no larger than 0.1%, then the mismatch between the 96- or 112-point simulations and the continuum limit will be lower than this; it will certainly be lower than the 1% accuracy requirement that we place on our model.

Fig. 3.3 shows the mismatch between waveforms extracted at different radii. The waveforms were extracted at $R_{ex} = \{50, 60, 70, 80, 90, 100\}\,M$, and the mismatch calculations are performed against the $R_{ex} = 100\,M$ waveforms. We expect the error to fall of as $\sim 1/R_{ex}$, and in general we observe this for our simulations, but only for $R_{ex} \gtrsim 60\,M$. Since even the $R_{ex} = 50\,M$ waveform has a mismatch of only $\sim 0.3\%$ with the $R_{ex} = 100\,M$ waveform, and assuming a $1/R_{ex}$ fall-off in waveform extraction error, we expect that the contribution of this error to the $R_{ex} = 100\,M$ waveforms is less than 0.1%.

Based on this analysis, we conclude that our simulations are well within the accuracy requirements to construct a waveform model with an overall mismatch error of $\lesssim 1\%$.

#	Code/ID	q	η	χ_1	χ_2	$\hat{\chi}$	M_f	a_f	$Mf_{\rm RD}$	$Mf_{\rm hyb}$	$N_{\rm GW,NR}$
A1	SXS:BBH:0156	1.	0.25	-0.95	-0.95	-0.95	0.9681	0.3757	0.0713	0.00522	22
A2	SXS:BBH:0151	1.	0.25	-0.6	-0.6	-0.6	0.9638	0.4942	0.0764	0.00517	26
A3	SXS:BBH:0001	1.	0.25	0.	0.	0.	0.9516	0.6865	0.0881	0.00398	54
A4	SXS:BBH:0152	1.	0.25	0.6	0.6	0.6	0.9269	0.8578	0.1083	0.00501	42
A5	SXS:BBH:0172	1.	0.25	0.98	0.98	0.98	0.8892	0.9470	0.1328	0.00497	48
A6	BAM	4.	0.16	-0.75	-0.75	-0.75	0.9846	0.0494	0.0614	0.00713	15
A7	BAM	4.	0.16	-0.5	-0.5	-0.5	0.9831	0.1935	0.0649	0.00716	18
A8	SXS:BBH:0167	4.	0.16	0.	0.	0.	0.9779	0.4715	0.0743	0.00665	28
A9	BAM	4.	0.16	0.5	0.5	0.5	0.9674	0.7377	0.0906	0.00811	26
A10	BAM	4.	0.16	0.75	0.75	0.75	0.9573	0.8628	0.1054	0.00818	30
A11	BAM	8.	0.099	-0.85	-0.85	-0.85	0.9898	-0.3200	0.0546	0.00918	8
A12	SXS:BBH:0064	8.	0.099	-0.5	0.	-0.458	0.9923	-0.0526	0.0589	0.00632	36
A13	SXS:BBH:0063	8.	0.099	0.	0.	0.	0.9894	0.3067	0.0677	0.00623	49
A14	SXS:BBH:0065	8.	0.099	0.5	0.	0.458	0.9846	0.6574	0.0838	0.00615	66
A15	BAM	8.	0.099	0.85	0.85	0.85	0.9746	0.8948	0.1087	0.01580	15
A16	BAM	18.	0.05	-0.8	0.	-0.77	0.9966	-0.5311	0.0514	0.01035	14
A17	BAM	18.	0.05	-0.4	0.	-0.385	0.9966	-0.1877	0.0563	0.01283	15
A18	BAM	18.	0.05	0.	0.	0.	0.9959	0.1633	0.0633	0.01284	13
A19	BAM	18.	0.05	0.4	0.	0.385	0.9943	0.5046	0.0745	0.00916	23

Table 3.1: Hybrid waveform configurations used to calibrate the `IMRPhenomD` model. For each configuration we list both the mass ratio q and symmetric mass ratio η, along with the spins χ_1 and χ_2 and the reduced-spin combination, $\hat{\chi}$, which follows from Eq. (3.2). The final BH has mass M_f and dimensionless spin a_f, and the ringdown signal has frequency $Mf_{\rm RD}$. The frequency $Mf_{\rm hyb}$ marks the midpoint of the transition region between SEOBv2 inspiral and NR data. The approximate number of NR GW cycles in each hybrid is given by $N_{\rm GW,NR}$.

3.4 Choice of inspiral approximant

The early, gradual inspiral of compact binaries and the GWs they emit can be accurately modeled by expanding the energy and flux of the system into a PN series. Depending on how the underlying equations are formulated and solved, there is a variety of PN approximants, each consistent with the others when truncated at the same expansion order. However, as every approximant is formulated with different, mostly implicit, assumptions of how higher order terms are treated, the GW signals they predict can differ considerably, especially towards higher mass ratios, increased spin magnitudes and for increasing orbital frequencies [88, 54, 90, 132, 120, 121, 131]. There are sophisticated methods that aim to improve the convergence and accuracy of PN-based approximants, and one of the most successful approaches is the mapping to an EOB system [51, 52, 67].

In the construction of a complete waveform model we face the following two issues. First, we need to pick one approximant that, to our current knowledge, models the inspiral most accurately. Second, this inspiral description has to be complemented by NR-based information about the merger and ringdown. We briefly

summarize our strategy to address both issues below and give references to the following sections that describe our reasoning in more detail.

Recent studies have indicated that among the family of non-precessing inspiral approximants, the EOB approximant by Taracchini et al. [166] shows the most consistent agreement with NR simulations within the calibration range of the model [163, 110]. In [100], we have performed an independent consistency test between inspiral approximants and our set of NR data and confirmed this conclusion. (Note that the most recently calibrated version of a non-precessing EOB model [128] has not yet been included in any of these tests.) Hence, we used the Taracchini et al. model (dubbed `SEOBNRv2` in the publicly available LIGO software library [167]) as our target inspiral approximant, albeit in its original, uncalibrated form that does not include NR fitted corrections (we refer to this form as as SEOBv2). Specifically, this involves calculating the `SEOBNRv2` waveforms with all of the NR calibration terms set to zero, to provide an "uncalibrated" SEOBv2 calculation of the inspiral waveform.

We do so because our goal is to explore an alternative modeling approach that is independent of previous NR-informed EOB tuning. In particular, we performed dedicated NR simulations outside the calibration range of `SEOBNRv2`, and instead of inheriting higher-order corrections that were fitted in a smaller parameter space region, we prefer to use the uncalibrated EOB model purely in the inspiral regime and hybridize it with NR data of the merger and ringdown.

We are naturally limited by the lengths of the NR waveforms, which are different for every simulation. Previous studies of NR waveform length requirements have suggested that PN inspiral waveforms up to 5-10 orbits before merger are sufficiently accurate for detection purposes [89, 132]; many more orbits are needed to fulfil more stringent accuracy requirements [120, 121, 74, 46], especially in the high-mass-ratio and high-spin regime that we are covering. Many of our NR waveforms are too short to allow that. However, previous studies estimated the accuracy of PN approximants based on the differences between *all* available approximants at 3.5PN order (with highest spin corrections at 2.5PN order at that time). One might argue that the EOB approach is more accurate, and therefore comparisons between PN waveforms exaggerate the uncertainty in our best current models. On the other hand, without fully general-relativistic results to compare to, one might be sceptical of good agreements between alternative EOB waveforms that are very similar by construction.

Nevertheless, given that we can join EOB with our NR data in a much more robust manner than any of the PN approximants (see Sec. II of [100] for our full analysis), we trust that they provide a reasonably accurate description of the inspiral up to the point where NR data take over. At what frequency this switch from EOB to NR happens depends on the length of the individual NR simulations. We note that the lowest common starting frequency of our NR waveforms is $Mf \sim 0.018$,

and this is where we begin our phenomenological merger-ringdown model. Note, however, that our hybridization procedure ensures that the maximum amount of NR information is used in every point of the parameter space to inform both the inspiral and merger-ringdown part of our model.

3.5 Model of the NR regime (Region II)

We model separately three frequency regions of the waveforms. These are indicated in Fig. 3.4. *Region I* is defined to be the portion of the hybrid that contains the optimal blend of NR and SEOBv2 data, *Region II* is the portion of the hybrid that contains purely NR data and corresponds to frequencies $Mf \geq 0.018$. This region is further sub-divided into two regions, *Regions IIa* and *IIb*. These divisions correspond to the *intermediate* and *merger-ringdown* models for both the amplitude and phase.

The figures indicate both the frequency ranges over which the three parts are connected, but also the ranges that are used to calibrate the model's coefficients to the hybrid data. These regions are in general slightly larger than those used when piecing together the final model.

We will refer to other features of these figures in the forthcoming sections.

3.5.1 From `IMRPhenomC` to `IMRPhenomD`

The merger-ringdown portion of the phase was modelled in `IMRPhenomC` [151] using the ansatz,

$$\begin{aligned}\psi^{22}_{\rm PM}(f) = \frac{1}{\eta}\Big(&\alpha_1 f^{-5/3} + \alpha_2 f^{-1} \\ &+\alpha_3 f^{-1/3} + \alpha_4 + \alpha_5 f^{2/3} + \alpha_6 f\Big)\,.\end{aligned} \tag{3.8}$$

The phase was fit over the frequency range $[0.1, 1]f_{\rm RD}$. The reference phase and time of the fit are given by the coefficients α_4 and α_6. At the ringdown frequency $f_{\rm RD}$ the phase was smoothly connected to a linear function, $\psi^{22}_{\rm RD}(f) = \beta_1 + \beta_2 f$, using a tanh transition function.

We now aim to model the merger-ringdown phase of the NR waveforms only from $Mf = 0.018$, to ensure that we include only NR information in this part of the model. Fig. 3.5 shows the derivative of the frequency-domain phase for the configuration $q = 1$, $\chi_1 = \chi_2 = -0.95$. The dashed line shows a fit to the phase using the procedure described above; beyond the ringdown frequency $Mf_{\rm RD} = 0.071$ the derivative of the phase is constant, and in this example the transition is only piecewise continuous. We see that, while Eq. (3.8) is able to accurately reproduce the phase up to the ringdown frequency, the linear approximation at higher frequencies

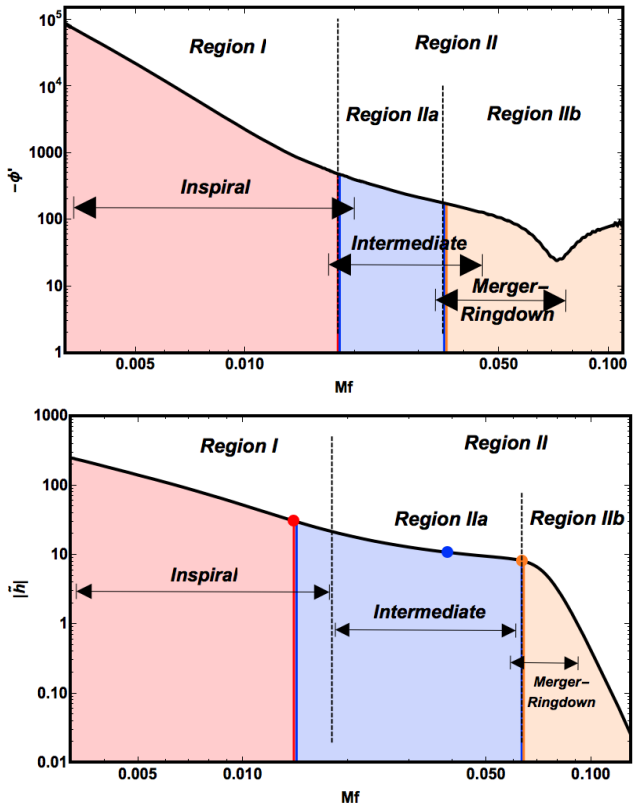

Figure 3.4: Phase derivative $-\phi'(f) \equiv -\partial\phi(f)/\partial f$ (upper panel) and amplitude (lower panel) for the $q = 1$, $\chi_1 = \chi_2 = -0.95$ configuration. The frequency ranges that were used in the fits for each section are shown as black double-ended arrows. For reference, the frequency $Mf = 0.018$ is marked with a black dashed line. Shaded regions illustrate the boundaries between the different regions when constructing the full IMR waveform. The ringdown frequency for this case is $Mf = 0.071$.

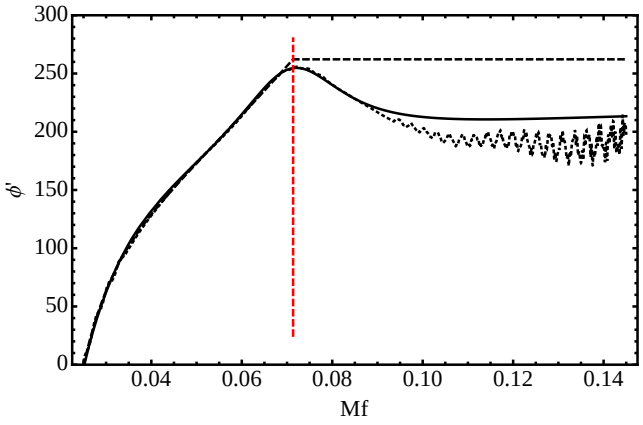

Figure 3.5: Phase derivative $\phi'(f)$ for the $q = 1$, $\chi_1 = \chi_2 = -0.95$ configuration. The numerical data (dotted) show a distinctive extremum at the ringdown frequency, $Mf_{\rm RD} = 0.071$, indicated by a vertical dashed line. A fit that follows an approach similar to that used for `IMRPhenomC` (dashed) is only a crude approximation to the phase for $f > f_{\rm RD}$, whereas the approach used for the `IMRPhenomD` model (solid) accurately models the phase into the ringdown.

is crude.

The solid line in Fig. 3.5 shows a fit to the phase following the procedure we use to construct `IMRPhenomD`, which was motivated in detail in [100], Chapter 2, and is also described in Sec. 3.5.2 below. This accurately reproduces the main features of the phase derivative in the vicinity of the ringdown frequency. There is some disagreement at higher frequencies, but we note that the accuracy of the NR data typically degrades at these frequencies, and the true behaviour of $\phi'(f)$ is not clear.

The `IMRPhenomC` amplitude model consists of two pieces; an inspiral ($f < f_{\rm RD}$) modelled with the ansatz of $A_{\rm TF2} + \gamma_1 f^{5/6}$ and a ringdown ($f > f_{\rm RD}$) modelled by a modified Lorentzian. The two pieces were joined together smoothly by a Tanh window function near $f_{\rm RD}$. For the calibration set of `IMRPhenomC` this ansatz performed reasonably well however, our expanded calibration set for `IMRPhenomD` contains higher mass-ratios and higher anti-aligned spins whose Fourier domain amplitude is sufficiently different that the `IMRPhenomC` ansatz is unable to capture these features. For an illustration of how $\chi_{\rm eff}$ changes the functional form of the Fourier domain amplitude for mass-ratio 1:4 binaries see Figure 2.12. Figure 3.6 shows the Fourier domain amplitude for the $q = 4$, $\chi_1 = \chi_2 = -0.75$ configuration. The numerical data (black), the prediction from `IMRPhenomC` (red) and the final `IMRPhenomD` model (blue, dashed) all agree at very low frequencies however, `IMRPhenomC` quickly deviates from NR. `IMRPhenomC` is unable to predict the noticeable "dip" near $Mf \sim 0.01$ or the high frequency ringdown falloff. To accurately model these new features we introduced an "intermediate" region between the inspiral and ringdown of the amplitude with the capability to model a wider range of functional forms, our method is described in detail in Section 3.5.3. The ring-

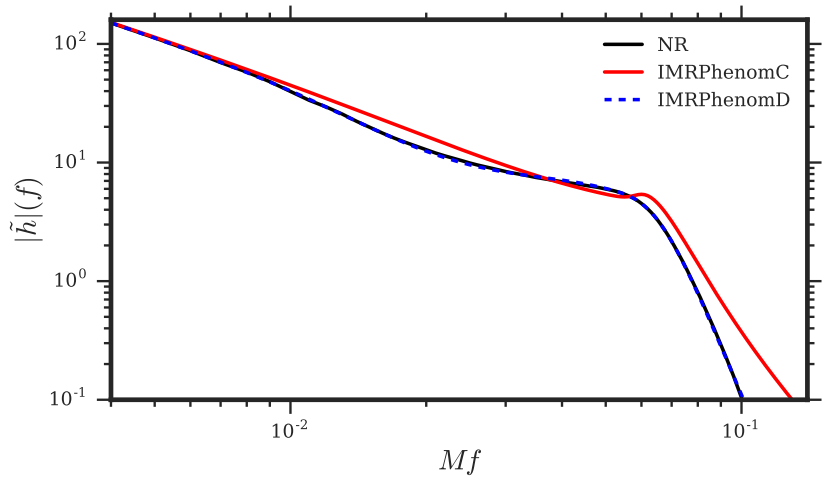

Figure 3.6: Fourier domain amplitude for the $q = 4$, $\chi_1 = \chi_2 = -0.75$ configuration. The numerical data (black), the prediction from `IMRPhenomC` (red) and the final `IMRPhenomD` model (blue, dashed) all agree at very low frequencies however, `IMRPhenomC` quickly deviates from NR. `IMRPhenomC` is unable to predict the noticeable "dip" near $Mf \sim 0.01$ or the high frequency ringdown falloff. The qualitatively different function form exhibited in this waveform is unable to be captured by the `IMRPhenomC` ansatz and motivated the method adopted by `IMRPhenomD`, described in Section 3.5.3.

down also shows a steeper falloff during the ringdown ($Mf \sim 0.08$) that is not captured by the `IMRPhenomC` ansatz. We improve the ringdown model by modifying the Lorentzian ansatz by a decaying exponential, which accurately captures the observed behaviour. Our ringdown model is described in Section 3.5.3.

In the next section we describe the methodology used to produce models of the phase and amplitude for the late inspiral, merger and ringdown parts of the waveform, i.e., those frequencies for which we have NR data. These we have denoted Region II; see Fig. 3.4. We assume that we have a valid inspiral approximant that we can join to our NR-based Region II model to construct a full IMR waveform model. The construction of a suitable inspiral model (Region I) is given in Sec. 3.6.

Our current construction requires that the starting frequency of the Region II model must be consistent for all waveforms. This imposes the constraint that the starting frequency of the NR-based Region II model is the lowest common GW frequency for which we have NR data, $Mf \sim 0.018$. This is purely based on the available NR data and could in principle be pushed towards lower frequencies given longer waveforms.

3.5.2 Phase

To produce a robust model there are two key requirements: (1) the ansatz must fit the data well, i.e., the fits have small residuals to the data, and (2) the choice of

ansatz should ideally be chosen to in such a way that the coefficients vary smoothly across the parameter space, to enable an accurate parameter-space fit in the final model.

We find that a simple approach is to split Region II into an intermediate (Region IIa) and merger-ringdown (Region IIb) part, and model them separately, as shown in Fig. 3.4.

The detailed features of the phase through Region II are most apparent when we consider the derivative of the phase, $\partial\phi/\partial f \equiv \phi'(f)$. For this reason we first model ϕ', and then integrate the resulting expression to produce the final phase model. We also note that the overall $1/\eta$ dependence in the inspiral, Eq. (3.24), also holds for the merger and ringdown, and so all of our primary fits are to $\eta\phi'$.

Region IIb - merger-ringdown

An example of the derivative of the phase, ϕ' is shown in Fig. 3.4 for a binary with $q = 1$, $\chi_1 = \chi_2 = -0.95$. As described in [100], we propose the following ansatz to model this functional form,

$$\eta\,\phi'_{\rm MR} = \alpha_1 + \alpha_2 f^{-2} + \alpha_3 f^{-1/4} + \frac{a}{b^2 + (f - f_0)^2}. \tag{3.9}$$

The last term models the 'dip' in Fig. 3.4. The location of the minimum is given by f_0, while a is the overall amplitude of the dip and b is the width. We find that the frequency location of the dip is very close to the final BH's ringdown frequency, $f_{\rm RD}$ (they agree within our uncertainty in calculating $f_{\rm RD}$), and that the ringdown damping frequency $f_{\rm damp}$ is a good approximation to our best fit of the width. These quantities are calculated from our final mass and spin fits. For these reasons the ansatz that we use in practice is,

$$\eta\,\phi'_{\rm MR} = \alpha_1 + \alpha_2 f^{-2} + \alpha_3 f^{-1/4} + \frac{\alpha_4 f_{\rm damp}}{f_{\rm damp}^2 + (f - \alpha_5 f_{\rm RD})^2}. \tag{3.10}$$

We find that the parameter α_5 is in the range $[0.98, 1.04]$. The power law terms account for the overall trend of the data, and its behaviour at lower frequencies. The constant term translates into a time shift in the overall phase, which will be determined by the continuity requirements of the final IMR phase; see Sec. 3.8. The phase derivative data are fit to Eq. (3.10) over the frequency range $[0.45, 1.15]\, f_{\rm RD}$. The upper frequency $1.15 f_{\rm RD}$ approximates the highest frequency for which we have clean NR data. This fitting window was chosen to have some overlap between the intermediate phase model, as indicated in Fig. 3.4.

The merger-ringdown phase is given by the integral of Eq. (3.10),

$$\phi_{\rm MR} = \frac{1}{\eta}\left\{\alpha_0 + \alpha_1 f - \alpha_2 f^{-1} + \frac{4}{3}\alpha_3 f^{3/4} + \alpha_4 \tan^{-1}\left(\frac{f-\alpha_5 f_{\rm RD}}{f_{\rm damp}}\right)\right\} . \tag{3.11}$$

For the full IMR phase we use the above fit for frequencies larger than $0.5\, f_{\rm RD}$. At lower frequencies we find that $\eta\,\phi'$ is fit better by $\sim 1/f$ and we model this region (IIa) separately.

The phase offset that appears as a constant of integration α_0, and the time-shift term α_1, will both be determined in the final model by requiring a smooth connection with the phase from Region IIa.

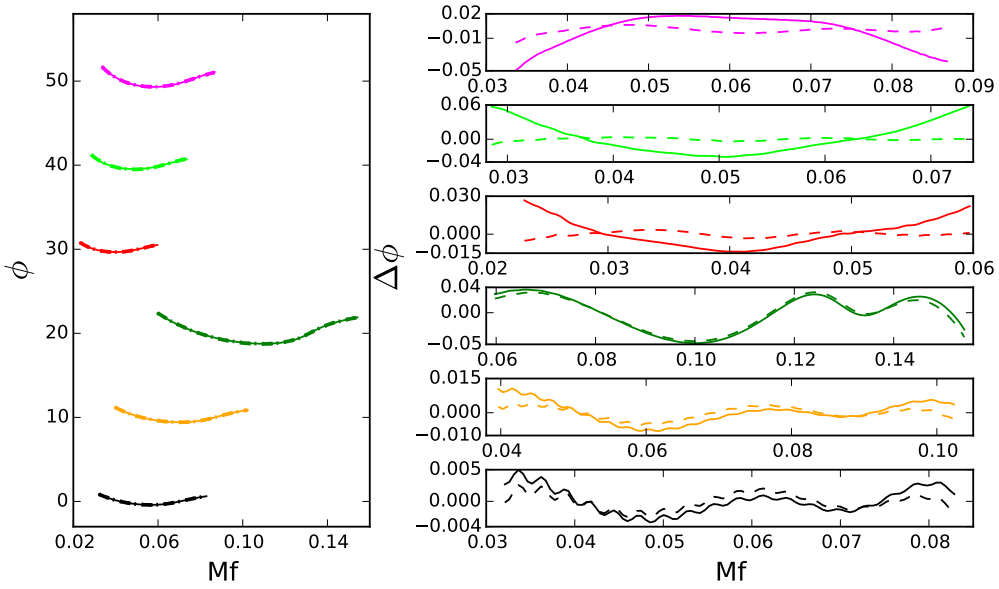

Figure 3.7: Examples of the merger-ringdown (Region IIb) model for three $q = 18$ configurations where the spin on the large BH is $\chi_1 = \{+0.4, 0, -0.8\}$ and three equal-spin $q = 1$ configurations ($\chi_{1,2} = +0.98, 0, -0.95$). The configurations are ordered top to bottom in the figure. The left panel shows the hybrid data, best-fit and final-model predictions over Region IIb. The right panel shows the difference between the hybrid data and the best-fit (dashed line) and between the hybrid data and the final model (solid line).

Examples of the results are shown in Fig. 3.7 for six configurations at the edges of our calibration parameter space. These are equal-spin $q = 1$ waveforms with spins $\hat{\chi} = \{-0.95, 0, 0.98\}$ and $q = 18$ waveforms with spins on the larger BH of $\chi_1 = \{-0.8, 0, 0.4\}$ (the second BH has no spin). In addition to demonstrating that both the ansatz and the final model capture the data well, the figure also illustrates the large differences in the frequency range of the merger-rigndown at different points

in the parameter space.

Region IIa - intermediate

To bridge the gap between the lowest common frequency of the NR data and the Region IIb merger-ringdown model, i.e., over the frequency range $Mf \in [0.018, 0.5 f_{\rm RD}]$, we use the following ansatz,

$$\eta\, \phi'_{\rm Int} = \beta_1 + \beta_2 f^{-1} + \beta_3 f^{-4}\,. \tag{3.12}$$

The behaviour of the data over this frequency range is predominately proportional to $1/f$. This is not sufficient at higher mass ratios and high anti-aligned spins, where $f_{\rm RD}$ can be approximately half that of the equal mass non-spinning case. We find that the additional f^{-4} term fits the data well across the entire parameter space. The intermediate (Region IIa) ansatz is used over the frequency interval $[0.018, 0.5 f_{\rm RD}]$, but we found that the best results were obtained if the data were fit over $[0.017, 0.75 f_{\rm RD}]$.

Once again the phase is obtained by integrating Eq. (3.12),

$$\phi_{\rm Int} = \frac{1}{\eta}\left(\beta_0 + \beta_1 f + \beta_2\, {\rm Log}(f) - \frac{\beta_3}{3} f^{-3}\right)\,. \tag{3.13}$$

As in Region IIb, the phase-shift due to the constant of integration β_0, and the time-shift term β_1, will be fixed by requiring a smooth connection to the Region I phase. The results for the corner cases are shown in Fig. 3.8.

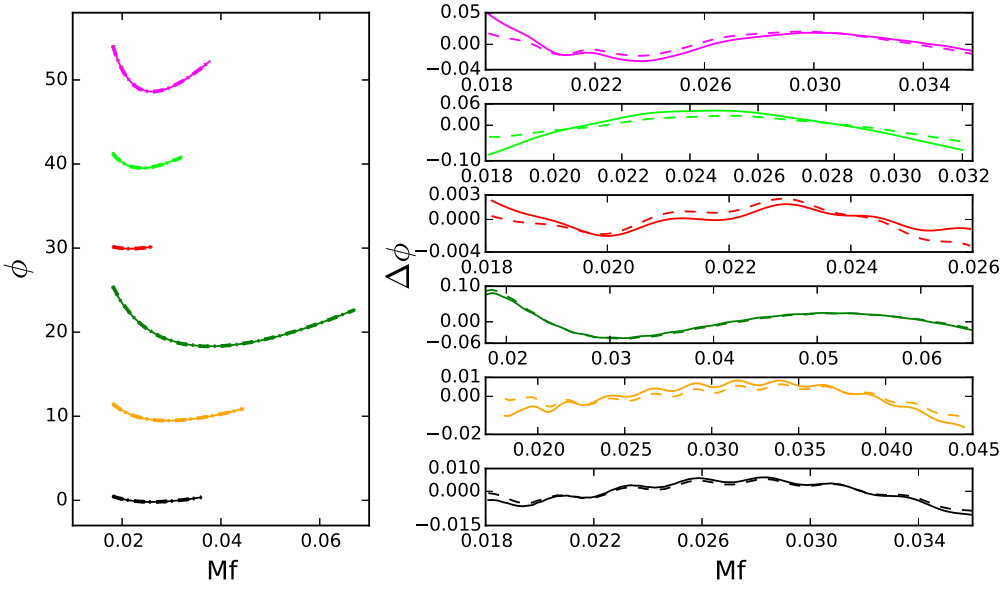

Figure 3.8: The same configurations and layout as in Fig. 3.7, but now showing phase over the intermediate region (IIa).

This completes the modelling of the phase over the frequencies for which we have NR data, Region II. We will now consider the signal amplitude over the same region, before moving on to the inspiral, Region I.

3.5.3 Amplitude

When we perform the fits to the amplitude across Region I and Region II, we first factor out the leading order PN $f^{-7/6}$ behaviour. The resulting data tend to unity as the frequency tends to zero, and as with the use of the phase derivative, allows us to identify and model detailed features of the amplitude behaviour; see Fig. 3.9, which shows both amplitude for PN inspiral waveforms, and for the full hybrids.

The normalisation is given by,

$$\lim_{f\to 0}\left[f^{7/6}\,A_{\rm PN}(f)\right] \to \sqrt{\frac{2\,\eta}{3\,\pi^{1/3}}}, \tag{3.14}$$

and our normalisation factor is therefore,

$$A_0 \equiv \sqrt{\frac{2\,\eta}{3\,\pi^{1/3}}} f^{-7/6}. \tag{3.15}$$

Region IIb - merger-ringdown

In all previous phenomenological models [24, 20, 151], the ringdown amplitude has been modelled with a Lorentzian function, which is the Fourier transform of the (two-sided) exponential decay function. The Fourier transform of the full IMR data instead exhibit an exponential decay, as discussed in [100]. The amplitude in Region IIb is fit over the frequency range $Mf \in [1/1.15, 1.2]\, f_{\rm RD}$ using the following ansatz,

$$\frac{A_{\rm MR}}{A_0} = \gamma_1 \frac{\gamma_3 f_{\rm damp}}{(f-f_{\rm RD})^2 + (\gamma_3 f_{\rm damp})^2} e^{-\frac{\gamma_2 (f-f_{\rm RD})}{\gamma_3 f_{\rm damp}}}. \tag{3.16}$$

The coefficient $\gamma_1 \in [0.0024, 0.0169]$ determines the overall amplitude of the ringdown. We expect that the frequency width and location of the amplitude peak can be inferred from the remnant BH parameters, which motivates the appearance of the ringdown damping frequency $f_{\rm damp}$ in Eq. (3.16). In practice we find that the width is increased by the factor $\gamma_3 \in [1.25, 1.36]$, and the decay rate $1/(f_{\rm damp}\gamma_3)$ is modified by the factor $\gamma_2 \in [0.54, 1.0339]$.

If we used only the Lorentzian part of Eq. (3.16), the amplitude peak would be located at $f_{\rm RD}$. With the additional exponential factor, the peak is located at

$$f_{\rm peak} = \left| f_{\rm RD} + \frac{f_{\rm damp}\gamma_3\left(\sqrt{1-\gamma_2^2}-1\right)}{\gamma_2} \right|. \tag{3.17}$$

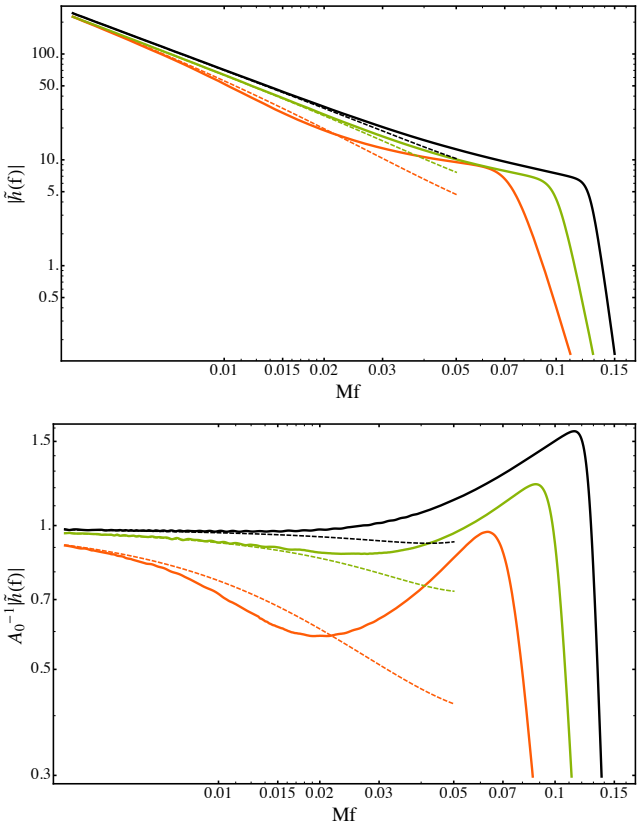

Figure 3.9: Hybrid Fourier domain amplitude for three equal mass cases $q = 1$, $\chi_1 = \chi_2 = 0.98$, $\chi_1 = \chi_2 = 0$ and $\chi_1 = \chi_2 = -0.95$, indicated by black, orange and green lines respectively. The PN prediction is shown as dashed lines. The top panel shows the full Fourier domain amplitude, while the bottom panel shows the Fourier domain amplitude but rescaled by A_0^{-1}, Eq. (3.15).

Region IIa - intermediate

We now consider the intermediate region (IIa) between the end of the inspiral region (I) and the start of the merger-ringdown region (IIb).

Fig. 3.9 shows the `TaylorF2` inspiral amplitude in comparison to the amplitude in the hybrid data. In some cases, we see that we can model the intermediate (Region IIa) amplitude by simply smoothly connecting regions I and IIb. For example, we could fit the four coefficients of a third-order polynomial by matching the value of the amplitude and its derivative at the end of the Region I (nominally $Mf = 0.018$) and at the beginning of Region IIb, $f_{\rm peak}$.

In other cases, however, we see that the rescaled amplitude will have a minimum in the intermediate region, and a naive connection of the inspiral and merger-ringdown regions would not in general locate this minimum correctly.

For this reason, we model the intermediate amplitude with a fourth-order polynomial. Four of the coefficients are fixed (as above), by matching the value and derivative of the amplitude at the endpoints of our intermediate fit. The lower fre-

Collocation Point (Mf)	Value	Derivative
$f_1 = 0.014$	$v_1 = A_{\rm Ins}(f_1)$	$d_1 = A'_{\rm Ins}(f_1)$
$f_2 = (f_1 + f_3)/2$	$v_2 = A_{\rm Hyb}(f_2)$	
$f_3 = f_{\rm peak}$	$v_3 = A_{\rm MR}(f_3)$	$d_3 = A'_{\rm MR}(f_3)$

Table 3.2: Locations of the collocation points, f_1, f_2, f_3, and the corresponding values of the amplitude $A(f)$ and its derivative $A'(f)$. All information comes from either the inspiral or merger-ringdown models, except for the value v_2, which is read off the input waveform data.

quency is chosen as $Mf_1 = 0.014$, i.e., slightly before the end of the inspiral at $Mf = 0.018$, and the upper frequency is $f_3 = f_{\rm peak}$. The fifth coefficient is determined by the value of amplitude of the NR waveform at the frequency mid-way between the two, $f_2 = (f_1 + f_3)/2$.

In practice, the amplitude values and derivatives at the endpoints are given by the models for Region I and Region IIB. The only additional piece of information that needs to be modelled from the NR data is the value of the amplitude at f_2. We find that this can be accurately modelled across the parameter space by a polynomial ansatz in $(\eta, \hat{\chi})$, as will be described in Sec. 3.7.

This collocation method is similar to that used in spectral methods. Given an ansatz with n free coefficients we require n pieces of information from the data to constrain the ansatz and solve the system. In this case we use the value of the function at three points, and the derivative at two points. The intermediate ansatz is given by

$$A_{\rm Int} = A_0 \left(\delta_0 + \delta_1 f + \delta_2 f^2 + \delta_3 f^3 + \delta_4 f^4\right), \tag{3.18}$$

and the δ_i coefficients are the solution to the system of equations,

$$A_{\rm Int}(f_1) = v_1, \tag{3.19}$$
$$A_{\rm Int}(f_2) = v_2, \tag{3.20}$$
$$A_{\rm Int}(f_3) = v_3, \tag{3.21}$$
$$A'_{\rm Int}(f_1) = d_1, \tag{3.22}$$
$$A'_{\rm Int}(f_3) = d_3. \tag{3.23}$$

The frequencies and values are given in Tab. 3.2.

The results of our amplitude model are shown in Figs. 3.10 and 3.11, which show the same equal-mass and $q = 18$ cases as in Fig. 3.7. The left panels show the full signal amplitude, while the right panels show the amplitude scaled by the $f^{7/6}$ factor, Eq. 3.15.

The scaled plots indicate that the weakest part of the model is that which describes the intermediate Region IIa amplitude. This is because the minimum that we see in the scaled figures (those in the right panels) is captured only through the

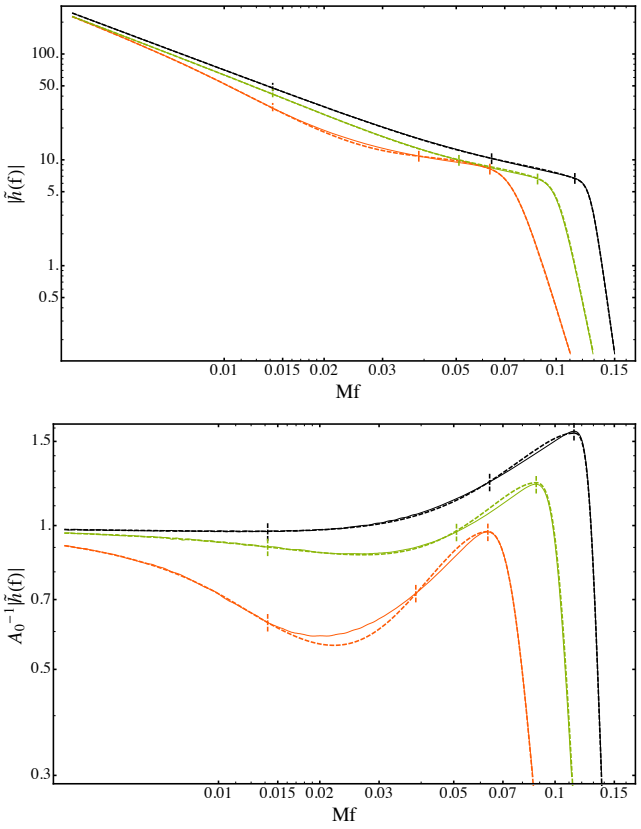

Figure 3.10: Hybrid and model Fourier-domain amplitude for three equal-mass configurations, $\chi_1 = \chi_2 = 0.98$, $\chi_1 = \chi_2 = 0$ and $\chi_1 = \chi_2 = -0.95$, indicated by black, orange and green lines respectively. The hybrid data are shown by solid lines, and the `IMRPhenomD` model by dashed lines. The top panel shows the full Fourier-domain amplitude, while the bottom panel shows the Fourier-domain amplitude but rescaled by A_0^{-1}, Eq. (3.15). The short vertical dashed lines mark the three frequency points in Tab (3.2), while the lines at lower and higher frequency coincide with the transition points between regions I and IIa and between regions IIa and IIb respectively.

value of the amplitude at the frequency in the middle of Region IIa. If we were in addition to model the frequency at which the minimum occurs, and prescribe the amplitude value there, the model may perform better. We could also, of course, add further collocation points. However, we can see from the full unscaled amplitude (the top panels) that the amplitude is nonetheless very accurately represented, and in addition, small variations in the amplitude play a far smaller role in GW applications (both searches and parameter estimation) than the GW phase.

3.6 Inspiral model (Region I)

We now turn our attention to modelling Region I, i.e., the inspiral portion of the waveform, below the frequency $Mf = 0.018$; see Fig. 3.4.

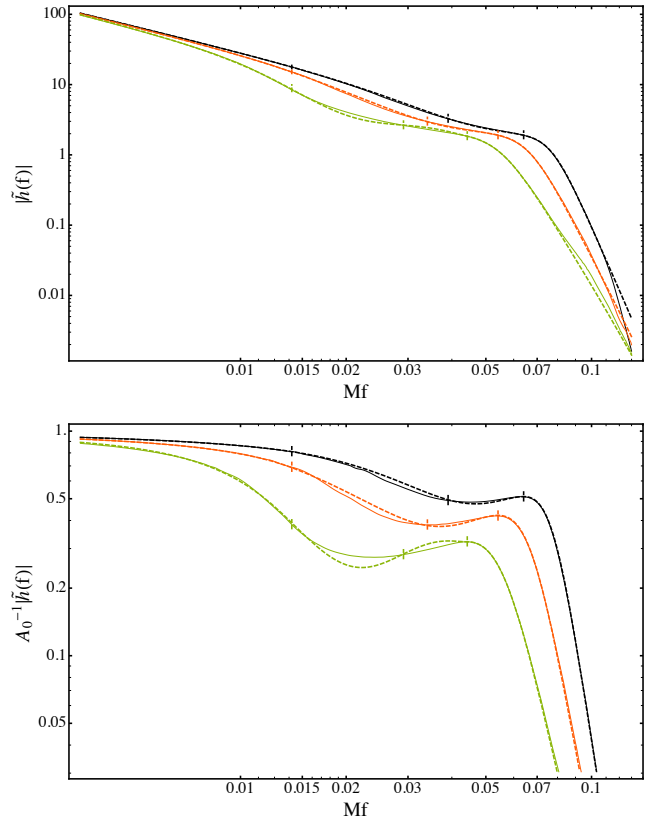

Figure 3.11: The same quantities as in Fig. 3.10, but now for three $q = 18$ configurations, $\chi_1 = 0.4, \chi_2 = 0$, $\chi_1 = \chi_2 = 0$ and $\chi_1 = -0.8, \chi_2 = 0$.

The non-spinning [24] and the first aligned-spin [20] phenomenological models used a PN-like ansatz for the inspiral phase, calibrated against PN+NR hybrids. In the `IMRPhenomC` model [151], the `TaylorF2` phase was used for the equivalent of Region I; in that model the inspiral region ended at $0.1 f_{\rm RD}$. For the parameter space covered by our new model, this would corresponds to frequencies between $Mf \sim 0.005$ and $Mf \sim 0.012$.

In [100] we presented evidence that the uncalibrated SEOBv2 model is currently the inspiral approximant that is most consistent with NR data for the inspiral. In this section we construct a frequency domain model of the SEOBv2 inspiral, up to $Mf = 0.018$, using our SEOBv2+NR hybrids. As discussed previously, we expect that the SEOBv2 model is sufficiently accurate up to this frequency, and very likely to higher frequencies, allowing us to match to our merger-ringdown model at significantly higher frequencies than was considered reasonable with the `TaylorF2` approximant used for `IMRPhenomC`.

Note that it is possible, in principle, to cover the parameter space with an arbitrarily high density of SEOBv2 waveforms, and use those to calibrate an inspiral model. In this chapter, however, we use hybrid SEOBv2+NR waveforms and therefore calibrate the inspiral model to the same points in parameter space as used for

the Region II merger-ringdown models.

3.6.1 Phase

The inspiral portion $Mf \in [0.0035, 0.018]$ of the hybrids can be accurately modelled with an ansatz consisting of the known `TaylorF2` terms for the phase, augmented with the next four higher order PN terms, with their coefficients fit to the SEOBv2+NR hybrid data. We find that these higher order terms are enough to capture the EOB and NR data over this frequency range to a very high level of accuracy.

The full `TaylorF2` phase is,

$$\begin{aligned}\phi_{\rm TF2} &= 2\pi f t_c - \varphi_c - \pi/4 \\ &\quad + \frac{3}{128\,\eta}(\pi f M)^{-5/3}\sum_{i=0}^{7}\varphi_i(\Xi)(\pi f M)^{i/3},\end{aligned} \tag{3.24}$$

where $\varphi_i(\Xi)$ are the PN expansion coefficients that are functions of the intrinsic binary parameters. Explicit expressions are given in Appendix A.2. We incorporate spin-independent corrections up to 3.5PN order ($i = 7$) [54, 42], linear spin-orbit corrections up to 3.5PN order [43] and quadratic spin corrections up to 2PN order [140, 32, 126]. In re-expanding the PN energy and flux to obtain the `TaylorF2` phase, we drop all quadratic and higher-order spin corrections beyond 2PN order as they would constitute incomplete terms in our description. We note that we also constructed a full model that incorporated recently calculated higher-order terms, specifically quadratic spin terms at 3PN order [44] and cubic spin terms at 3.5PN order [123], but we found no significant difference between both constructions.

Equation Eq. (3.24) includes both spins, χ_1 and χ_2, while our fit for the coefficients of additional terms will be parameterised only by $\chi_{\rm PN}$. This means that the final phase expression will incorporate some effects from the spins of each BH, but, although the model is sufficiently accurate for use in GW astronomy applications across a wide range of the two-spin parameter space, it should not be considered an accurate representation of two-spin effects. We expect the model to be more than sufficient for searching for BH binaries with any BH spins within the calibration parameter space, or for estimation of the parameters $(M, \eta, \chi_{\rm PN})$, but we *do not* recommend its use in, for example, theoretical studies of detailed double-spin effects in binaries.

The phase ansatz is given by,

$$\begin{aligned}\phi_{\rm Ins} =& \phi_{\rm TF2}(Mf;\Xi) \\ &+ \frac{1}{\eta}\left(\sigma_0 + \sigma_1 f + \frac{3}{4}\sigma_2 f^{4/3} + \frac{3}{5}\sigma_3 f^{5/3} + \frac{1}{2}\sigma_4 f^2\right).\end{aligned} \tag{3.25}$$

Note that to compute the phenomenological coefficients the fit is performed over the frequency range $Mf \in [0.0035, 0.019]$ to achieve an optimal balance between goodness of fit and accuracy in reproducing phenomenological coefficients and to reduce boundary effects at the interface between Region I and Region IIa (i.e., $Mf = 0.018$). In practice the fits were performed over the ϕ' data, as with Region II above. We will see in Sec. 3.9.1 that this model also sufficiently accurately represents SEOBv2+NR hybrids down to much lower frequencies.

The results for the three example $q = 1$ and $q = 18$ configurations are shown in Fig. 3.12. We see that once again our ansatz accurately models the data, and that the Fourier-domain phase error is below 0.15 rad for the entire inspiral for the high-mass ratio configurations, while for the equal-mass configurations the phase error is typically an order of magnitude smaller.

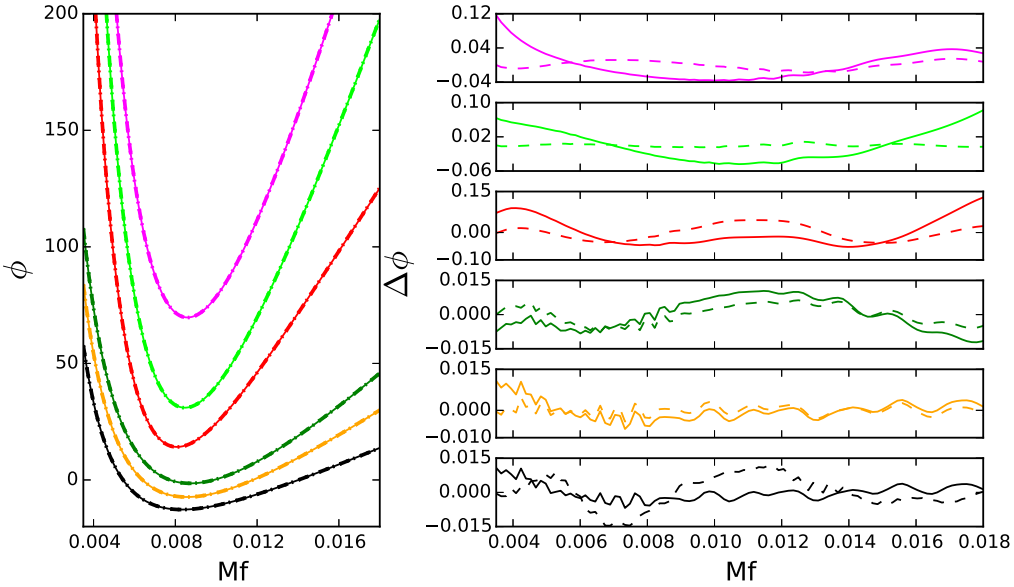

Figure 3.12: The same analysis as in Figs. 3.7 and 3.8, but now for the inspiral model.

3.6.2 Amplitude

Our model of the inspiral amplitude is based on a re-expanded PN amplitude, as discussed in Sec. IV of [100]. The base amplitude is given by,

$$A_{\rm PN}(f) = A_0 \sum_{i=0}^{6} \mathcal{A}_i (\pi f)^{i/3} \,, \tag{3.26}$$

where A_0 is the leading order $f^{-7/6}$ behaviour in Eq. (3.15). The higher order terms that we calibrate are the next natural terms in the PN expansion,

$$A_{\rm Ins} = A_{\rm PN} + A_0 \sum_{i=1}^{3} \rho_i \, f^{(6+i)/3}. \tag{3.27}$$

3.7 Mapping the phenomenological coefficients to physical parameters

Our model has 11 amplitude and 14 phase coefficients. However four of the amplitude coefficients in Region IIa (Sec. 3.5.3) and four of the phase coefficients $(\alpha_0, \alpha_1, \beta_0, \beta_1)$ across Region II (See Sec. 3.8) are constrained analytically; there is only one time and phase-shift freedom for the full waveform. This leaves a total of 17 phenomenological parameters which need to be mapped on to the physical parameter space. We parametrise the phenomenological coefficients by two physical parameters, $(\eta, \chi_{\rm PN})$. Our model is also dependent on the total mass M of the system through a trivial rescaling.

As in previous phenomenological models [24, 20, 151] we map the phenomenological coefficients in terms of polynomials of the physical parameters, up to second order in η and third order in $\chi_{\rm PN}$, although in this work our polynomial ansatz is expanded around $\chi_{\rm PN} = 1$. Note that in the fit across the parameter space we use the unscaled reduced-spin parameter $\chi_{\rm PN}$,

$$\begin{aligned} \Lambda^i = & \lambda^i_{00} + \lambda^i_{10}\eta \\ & + (\chi_{\rm PN} - 1)\left(\lambda^i_{01} + \lambda^i_{11}\eta + \lambda^i_{21}\eta^2\right) \\ & + (\chi_{\rm PN} - 1)^2\left(\lambda^i_{02} + \lambda^i_{12}\eta + \lambda^i_{22}\eta^2\right) \\ & + (\chi_{\rm PN} - 1)^3\left(\lambda^i_{03} + \lambda^i_{13}\eta + \lambda^i_{23}\eta^2\right) , \end{aligned} \tag{3.28}$$

where Λ^i indexes the amplitude and phase coefficients for Regions I, IIa and IIb. Tables A.1, A.2 and A.3 in Appendix A.3 contains the values of all the mapping coefficients for each phenomenological parameter.

3.8 Full IMR waveforms

By construction, all the regions of the amplitude and phase models are joined by $C(1)$-continuous conditions. This ensures the first derivative of the amplitude and phase at the boundary between the various regions, which are used in analytic calculations, are smooth. We assume that this is sufficient and simply join together

the piecewise regions with step functions. Our step function is defined as

$$\theta(f - f_0) = \begin{cases} -1, & f < f_0, \\ 1, & f \geq f_0, \end{cases} \tag{3.29}$$

and,

$$\theta^{\pm}_{f_0} = \frac{1}{2}\left[1 \pm \theta(f - f_0)\right]. \tag{3.30}$$

The full IMR phase is determined up to an arbitrary time- and phase shift. These shifts are absorbed into the constant and linear coefficients of the inspiral part (σ_0, σ_1). The constant and linear coefficients of the Region IIa (α_0, α_1) and IIb models (β_0, β_1) are fixed by the requirement of $C(1)$ continuity.

The full IMR phase is given by the following equation

$$\Phi_{\rm IMR}(f) = \phi_{\rm Ins}(f)\,\theta^{-}_{f_1} + \theta^{+}_{f_1}\,\phi_{\rm Int}(f)\,\theta^{-}_{f_2} + \theta^{+}_{f_2}\,\phi_{\rm MR}(f)\,, \tag{3.31}$$

where $\phi_{\rm Ins}$ is given by Eq. (3.25), $\phi_{\rm Int}$ by Eq. (3.13), and $\phi_{\rm MR}$ by Eq. (3.11), and the transition frequencies are $f_1 = 0.018$ and $f_2 = 0.5 f_{\rm RD}$. As noted previously, when evaluating the known PN part of $\phi_{\rm Ins}$, given in Eq. (3.25), we use the full two spin dependence.

The full IMR amplitude is given by

$$A_{\rm IMR}(f) = A_{\rm Ins}(f)\,\theta^{-}_{f_1} + \theta^{+}_{f_1}\,A_{\rm Int}(f)\,\theta^{-}_{f_2} + \theta^{+}_{f_2}\,A_{\rm MR}(f)\,, \tag{3.32}$$

where $A_{\rm Ins}$ is given by Eq. (3.27), $A_{\rm Int}$ by Eq. (3.18), and $A_{\rm MR}$ by Eq. (3.16), and where the transition frequencies are $f_1 = 0.014$ and $f_2 = f_{\rm peak}$, Eq. (3.17). The amplitude is $C(1)$-continuous by construction. Once again, note that the base inspiral PN amplitude includes both spin contributions.

The phase and amplitude coefficients across the $(\eta, \hat{\chi})$ parameter space are shown in Figs. 3.13, 3.14 and 3.15. We see that in general the coefficients vary smoothly across the parameter space, and are captured well by our fits.

3.9 Model Validation

To evaluate the accuracy of our model we compute the mismatch, defined in Sec. 3.2.2, between the model and a set of hybrid waveforms, including the 19 waveforms used to calibrate the model (Tab. 3.1), and an additional 28 waveforms, listed in Tab. 3.3. The additional SpEC NR waveforms comprise most of the remaining aligned spin simulations in the public SXS catalogue [3]. The remaining NR waveforms were produced with BAM.

In this section we quantify the agreement for each of these waveforms against the `IMRPhenomD` model. We also show (Sec. 3.9.3) that using additional waveforms in the calibration does not significantly change our model, and provide evidence that

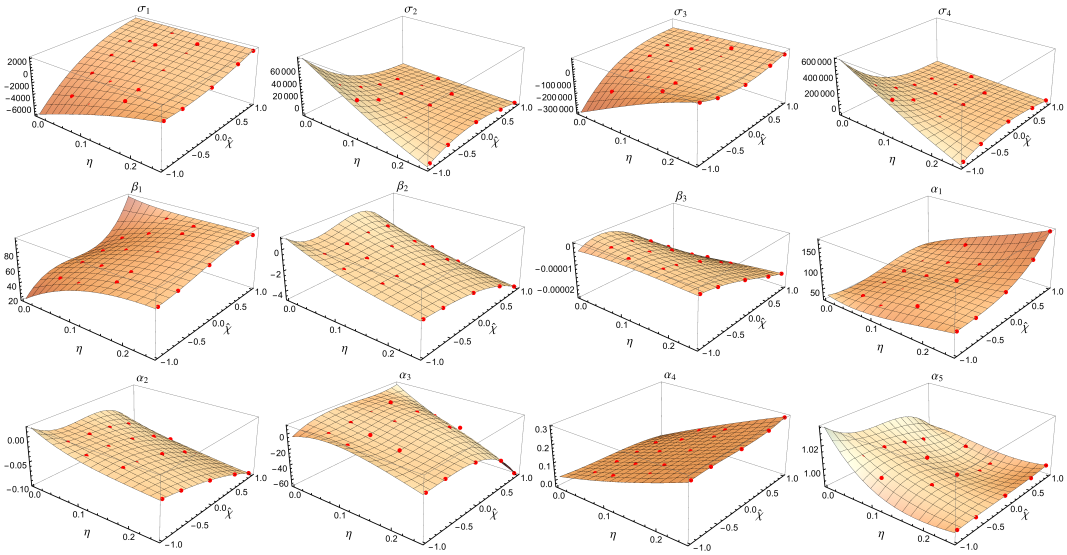

Figure 3.13: Phase coefficients for region I and II. The calibration points and the model, extrapolated to the boundary of the physical parameter space are shown.

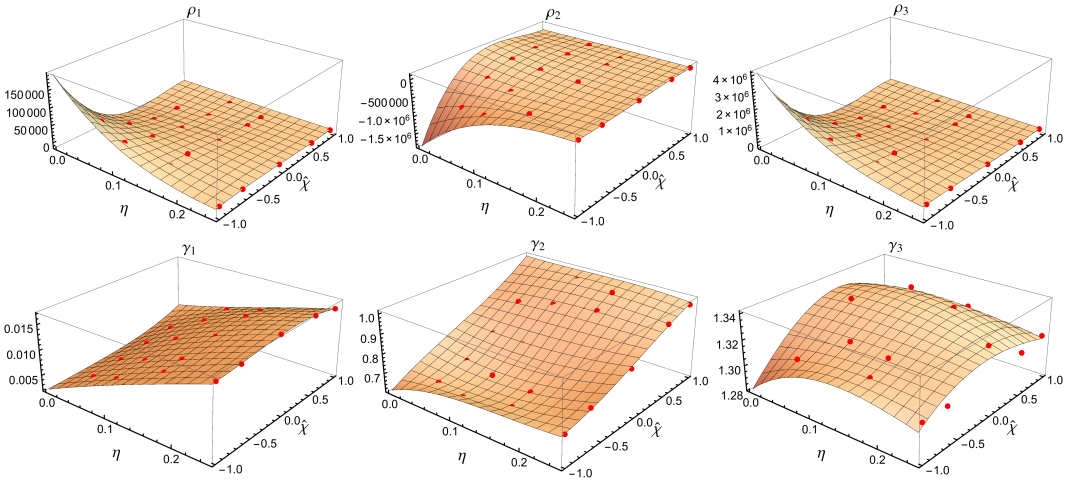

Figure 3.14: Amplitude coefficients for region I and IIb. The calibration points and the model, extrapolated to the boundary of the physical parameter space are shown.

the set of waveforms we have chosen may be close to the minimal set necessary to accurately calibrate our model.

A further, complementary validation based on time-domain transformations is presented in Appendix A.1.

3.9.1 Mismatches

In this section we compute the mismatch between `IMRPhenomD` and all of the hybrid waveforms in Tabs. 3.1 and 3.3.

The model was calibrated to hybrid waveforms with a starting frequency of $Mf = 0.0035$, but the waveforms from many astrophysical compact binaries will

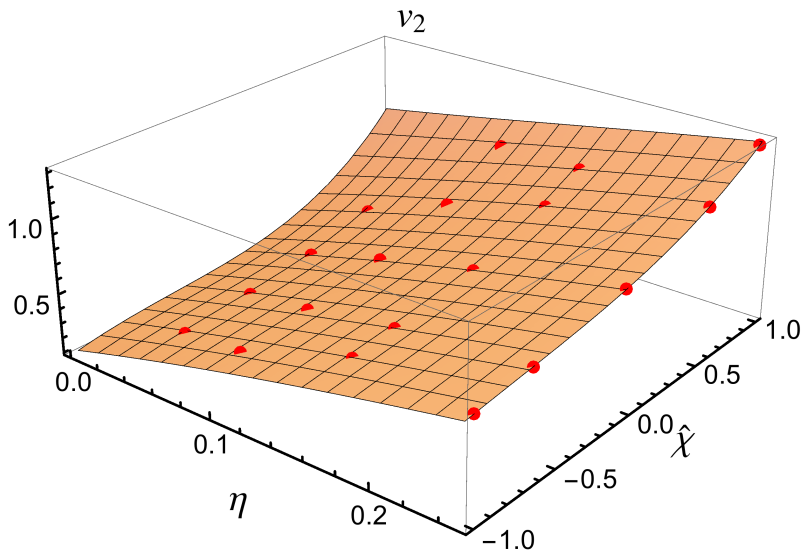

Figure 3.15: Intermediate (Region IIb) amplitude coefficient. The calibration points and the model, extrapolated to the boundary of the physical parameter space are shown.

be detectable by aLIGO and AdV from much lower frequencies. We assume that the minimum mass for one of the compact objects is given by the typical mass of a neutron star i.e., $M_{\rm NS} \sim 1.4 M_\odot$. The total mass of the binary can then be no lower than $M_{\rm min} = (q+1)M_{\rm NS}$ for configurations with mass-ratio q. Our goal is to produce a model that is accurate for binaries that can be detected from 10 Hz down to either $12\,M_\odot$ [54], or $M_{\rm min}$, if this exceeds $12\,M_\odot$, which is the case for systems with $q \gtrsim 8$. At 10 Hz, the waveform frequency of a $12\,M_\odot$ binary is $Mf \approx 0.0006$, and so in this section we compare our model to much longer hybrids that extend down to $Mf = 0.0006$.

The results are presented in Fig. 3.16. The top panel uses the aLIGO design sensitivity zero-detuned, high-laser-power noise curve with $[f_{\rm min}, f_{\rm max}] = [10, 8000]$ Hz [162]. The worst mismatch is for the $\{q, \chi_1, \chi_2\} = \{6, 0, 0\}$ at low masses which tends towards a mismatch of 3% at $12\,M_\odot$. All other mismatches fall below 1% with the majority distributed around 0.1%. In particular, at low masses the mismatch between different options of inspiral approximant will be much larger than the mismatch between `IMRPhenomD` and our hybrid waveforms; the dominant error is in our uncertainty of the true inspiral waveform, and not in our model; this will be made clearer in Sec. 3.10.

The bottom panel in Fig 3.16 shows the same calculation but using the predicted noise curve for early aLIGO science runs [8], with a lower frequency cut-off of 30 Hz. Due to the change in shape of the noise curve and lower frequency cut-off the mismatches improve such that *all* mismatches are comfortably below 1%. This gives a more realistic idea of the performance of our model during the initial science run of the advanced detectors.

#	Code/ID	q	χ_1	χ_2
B1	SXS:BBH:0159	1.	-0.9	-0.9
B2	SXS:BBH:0154	1.	-0.8	-0.8
B3	SXS:BBH:0148	1.	-0.438	-0.438
B4	SXS:BBH:0149	1.	-0.2	-0.2
B5	SXS:BBH:0150	1.	0.2	0.2
B6	SXS:BBH:0170	1.	0.437	0.437
B7	SXS:BBH:0155	1.	0.8	0.8
B8	SXS:BBH:0153	1.	0.85	0.85
B9	SXS:BBH:0160	1.	0.9	0.9
B10	SXS:BBH:0157	1.	0.95	0.95
B11	SXS:BBH:0158	1.	0.97	0.97
B12	SXS:BBH:0014	1.5	-0.5	0.
B13	SXS:BBH:0008	1.5	0.	0.
B14	SXS:BBH:0013	1.5	0.5	0.
B15	SXS:BBH:0169	2.	0.	0.
B16	BAM	2.	0.5	0.5
B17	BAM	2.	0.75	0.75
B18	BAM	3.	-0.5	-0.5
B19	SXS:BBH:0036	3.	-0.5	0.
B20	SXS:BBH:0168	3.	0.	0.
B21	SXS:BBH:0045	3.	0.5	-0.5
B22	SXS:BBH:0031	3.	0.5	0.
B23	SXS:BBH:0047	3.	0.5	0.5
B24	BAM	4.	-0.25	-0.25
B25	BAM	4.	0.25	0.25
B26	SXS:BBH:0060	5.	-0.5	0.
B27	SXS:BBH:0056	5.	0.	0.
B28	SXS:BBH:0166	6.	0.	0.
B29	BAM	10.	0.	0.

Table 3.3: Additional waveforms used to verify the model, but *not* used in its calibration.

In both panels, the highlighted cases are those at the edges of the calibration region of parameter space. We note that the worst mismatches are for high mass ratios and large spins. This suggests the region of parameter space that requires the most improvement in future models — although it is clear that for all of these configurations the model is well within the accuracy requirements for the second-generation detectors.

3.9.2 The effective spin approximation

The phenomenological fits to the waveform phase and amplitude are parameterised by the weighted reduced spin, $\chi_{\rm PN}$, Eq. (1.58). This is an approximation, based on the observation that the dominant spin effect on the inspiral phase is due to this combination of the two spins, χ_1 and χ_2. This approximation is not expected to

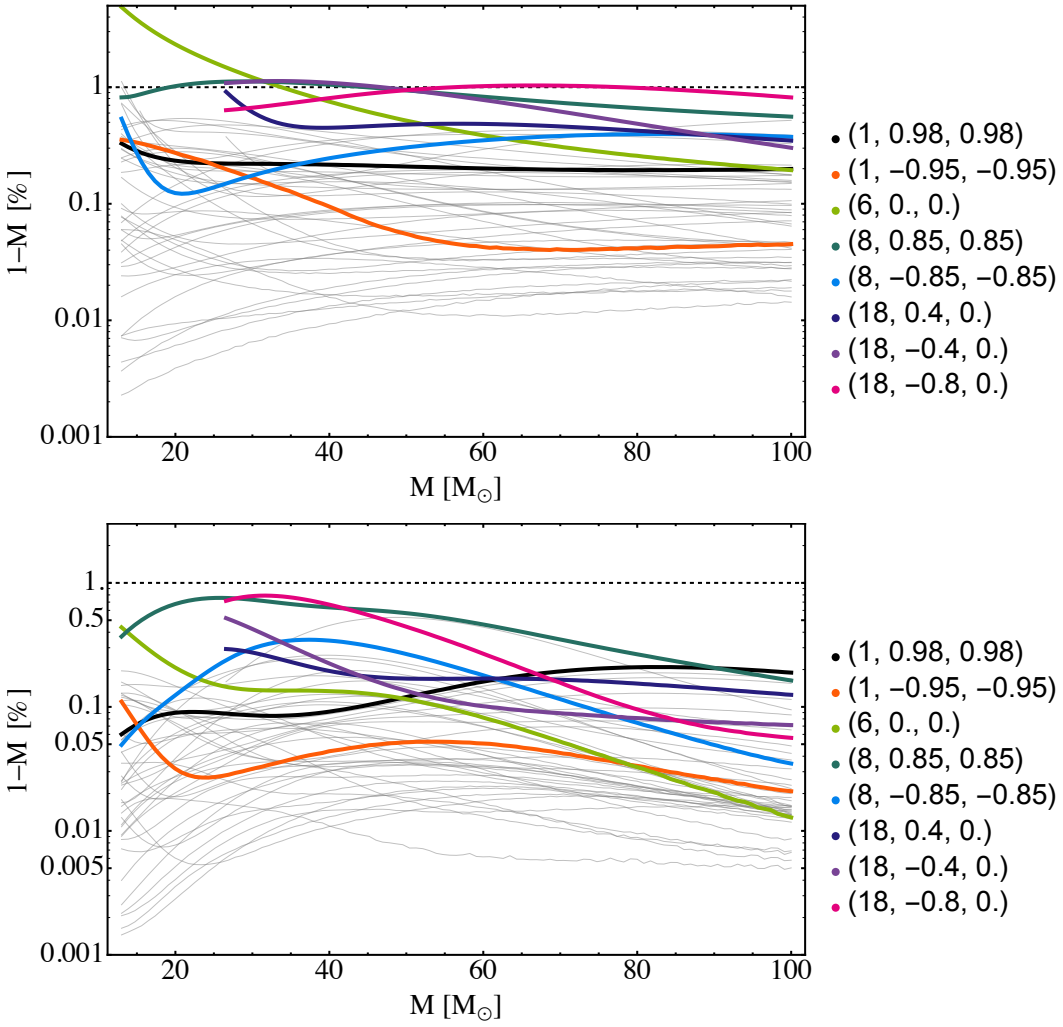

Figure 3.16: Mismatches of the `IMRPhenomD` model against all 48 available hybrid waveforms. The highlighted configurations are those closest to the edge of the $(\eta, \hat{\chi})$ parameter space as well as the case with the worst mismatch $(q, \chi_1, \chi_2) = (6, 0., 0)$. The majority of cases show mismatches well below 1%. Top: Mismatches using the aLIGO design sensitivity noise curve (zdethp) with a lower frequency cut off of 10 Hz. Bottom: Early aLIGO noise curve with a 30 Hz cut off.

be valid through the merger and ringdown; in the ringdown the waveforms will be characterized by the *final spin*. The model was produced using mostly equal-spin $\chi_1 = \chi_2$ waveforms, and in general may not be accurate for systems with unequal spins.

However, we have seen in the previous Sec. 3.9.1 that our model agrees well with all available hybrid waveforms, *including* several with unequal spins. This included only four unequal-spin configurations that were not included in the calibration, and none were high-aligned-spin systems.

We expect that the reduced-spin approximation will perform worst for high mass ratios and high aligned spins. If we consider pure PN inspiral waveforms, we find, for

example, that a system with mass-ratio 1:3 and total mass of $12\,M_{\odot}$, with $\chi_1 = 1$ and $\chi_2 = -1$, that the match against the corresponding reduced-spin waveform (with $\hat{\chi} = 0.655$) is less than 0.8. However, if we consider a configuration where the larger BH has an anti-aligned spin, $\chi_1 = -1, \chi_2 = 1$, then the match with the corresponding reduced-spin waveform ($\hat{\chi} = -0.655$) is much better, 0.955.

This example was only an illustration. The performance of the reduced-spin approximation at low masses does not concern us in the `IMRPhenomD` model, where we use both spins χ_1 and χ_2 to generate the base `TaylorF2` phase. What we wish to know is how well the approximation holds for high-mass systems, where the late inspiral, merger and ringdown dominate the SNR. Those systems are described by our merger-ringdown Region II model, for which the spin dependence is parameterised only with $\chi_{\rm PN}$.

We have produced one high mass-ratio, high-spin NR simulation to compare with, $q = 8$ and $\chi_1 = 0.8$, $\chi_2 = 0$. Fig. 3.17 shows the mismatch between this hybrid waveform and the `IMRPhenomD` model. As we expect in this region of the parameter space, the poor quality of the reduced-spin approximation causes a mismatch that exceeds our 1% threshold for all masses. However, if we calculate *fitting factors* (i.e., minimise the mismatch with respect to the model parameters $(\eta, \chi_{\rm PN})$, as done in a GW search and, effectively, in parameter estimation), then we find deviations from unity of below 1% for all masses. We also find biasses of less than 0.1% in the total mass, less than 3% in the symmetric mass ratio, and less than 0.02 in the reduced spin, $\chi_{\rm PN}$. We expect these biasses to be far less than the statistical uncertainties in these quantities for observations with second-generation detectors, and so we conclude that the reduced-spin approximation will not impose any limit on the science potential of these detectors.

Studies with the `SEOBNRv2` model support this conclusion. Although we do not expect that model to be accurate through the merger-ringdown for high spins, as we will see in Sec. 3.10, it is likely that its qualitative behaviour with respect to parameter variations is approximately correct, and the model allows us to study the behaviour of the reduced-spin approximation over the entire calibration parameter space of our model.

Although the reduced-spin approximation will not limit our ability to measure $\chi_{\rm PN}$, one could argue that it nonetheless prevents any measurement of individual spins. It was argued in previous work [145] that it may be difficult to measure both BH spins even if we have a double-spin model. The study in [147] provides much stronger evidence for this claim. In practice the measurable intrinsic parameters of the binary will be $(M, \eta, \chi_{\rm PN})$, and these are the parameters of our model.

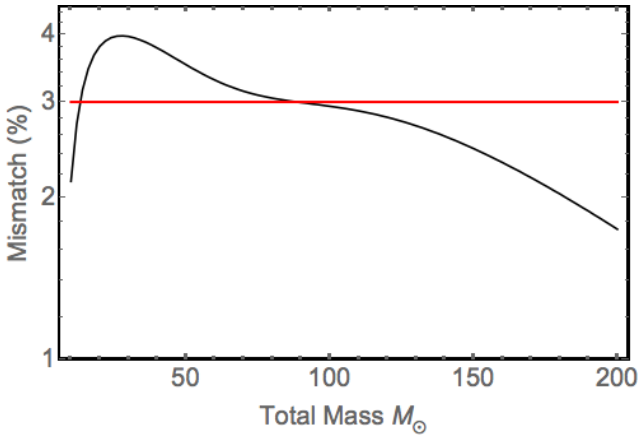

Figure 3.17: Mismatch between a $q = 8$, $\chi_1 = 0.8$, $\chi_2 = 0$ SEOBv2+NR hybrid, and the `IMRPhenomD` model. We see that the mismatch exceeds our 1% threshold everywhere. However, the fitting factor is everywhere better than 99%, with negligible parameter biases (see text).

3.9.3 Calibration Set of waveforms

The construction of previous phenomenological models [24, 23, 20, 151] suggested that if the parameter dependence of the coefficients in our models depend sufficiently smoothly across the parameter space that each coefficient can be presented by a low-order polynomial in each parameter, and therefore we require only 4-5 waveforms for each direction in parameter space. This expectation is borne out in the current model, where we use four values of the mass ratio (1, 4, 8 and 18) and four or five values of the spin at each mass ratio.

In this section we consider versions of the model constructed with more (or less) calibration waveforms. We find that our small set of 19 calibration waveforms is just as accurate as a model that is calibrated against a much larger set of 48 waveforms. To quantify this test we compute the maximum mismatch of four distinct models against all hybrid waveforms used in this chapter, i.e., the 48 waveforms in Tabs. 3.1 and 3.3.

Fig 3.18 indicates four choices of parameter-space coverage. The first set is the largest, and includes all 48 configurations indicated in the figure. The second set includes 25 waveforms, but only at mass ratios 1, 4 8 and 18, and does not include all available spin values at mass ratio 1. The third set consists of the 19 waveforms that we use for our final model. The fourth set is more sparsely sampled in spins, with only three spin values at each mass ratio, and only 12 waveforms in total.

Four models were constructed, each using the same prescription, except for the Set-4 model, for which we used a lower-order fit in the $\chi_{\rm PN}$ direction, since in general we cannot expect to fit four coefficients with only three spin values.

The results are summarised in Tab. 3.4. We calculate the mismatch between each of the models and all 48 hybrids, over the same mass range used in Sec. 3.9.1 using the

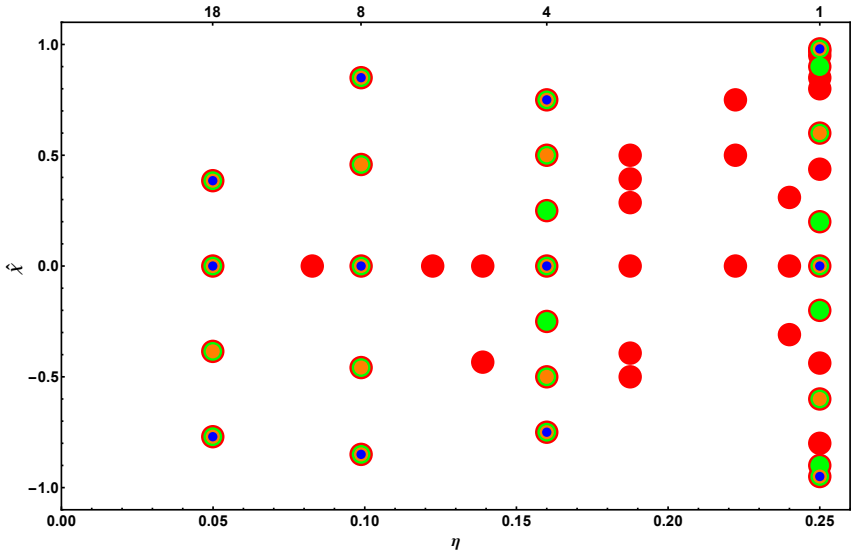

Figure 3.18: Four sets of calibration waveforms. Set 1 (48 waveforms) is indicated in red, Set 2 (25 waveforms) in green, Set 3 (19 waveforms, used for the final `IMRPhenomD` model) in orange, and Set 4 (12 waveforms) in blue.

early aLIGO noise curve with a 30 Hz cut off. For each hybrid we calculate the largest mismatch in that mass range. The table indicates the number of configurations for which we find mismatches larger than 0.1%, 1% and 3% for each model. As we have already seen in Fig. 3.16, the fiducial Set-3 model has mismatches of less than 1% for all configurations. We find that increasing the number of calibration waveforms does not significantly improve the model's performance.

We also see that if we further *reduce* the number of calibration waveforms, as in the Set-4 model, then the accuracy of the model drops significantly. For this model there are now three configuration with mismatches worse than 1%, and one configuration with a mismatch worse than 7%. We therefore conclude that, in the sense of the simple comparison that has been performed here, the Set-3 model represents the optimal choice of calibration waveforms.

3.10 Model vs Model Comparisons

We have demonstrated the high degree of fidelity of `IMRPhenomD` to both the waveforms that were used in calibrating the model and to those that were not. Without further comparisons to NR waveforms we cannot rigorously quantify the accuracy of our, or indeed any, waveform model. However, it is reasonable to assume that if two independent waveform models agree over a portion of the parameter space then we can gain some well-founded confidence in their accuracy.

The computational cost of the `SEOBNRv2` model makes it difficult to make detailed comparisons across the entire parameter space with high resolution in $(\eta, \hat{\chi})$. However, based upon the recent work in Ref. [143], a *reduced order model* (ROM) of

Model	# waveforms	$> 0.1\%$	$> 1\%$	$> 3\%$	$\max \mathcal{M}$ (%)
Set 1	48	19	0	0	0.94
Set 2	25	27	0	0	0.83
Set 3 (*)	19	29	0	0	0.87
Set 4	12	37	3	1	7.82

Table 3.4: Comparison of models constructed with different sets of calibration waveforms. The table shows, for each calibration set (see Fig. 3.18), the number of waveforms (out of 48) for which there is a mismatch $\mathcal{M}$ above 0.1%, 1%, or 3%, over the same mass range used in Sec. 3.9.1 using the early aLIGO noise curve with a 30 Hz cut off. We see that with a small set of 19 waveforms we achieve comparable mismatches to models which used larger sets of calibration waveforms, and that using *less* waveforms significantly degrades the quality of the model. Set 3 is used for the final model.

`SEOBNRv2`, called `SEOBNRv2_ROM`, has been developed [146]. This is a fast, frequency-domain approximation to the `SEOBNRv2` model that has a worst mismatch against `SEOBNRv2` of 1%, but in general mismatches are better than $\sim 0.1\%$. `SEOBNRv2_ROM` is a two spin model which can be used to estimate `SEOBNRv2` waveforms with symmetric mass-ratios $\eta \in [0.01, 0.25]$ and spins $\chi_i \in [-1, 0.99]$. The ROM can be used over the frequency range $Mf \in [0.0001, 0.3]$. Note that the underlying `SEOBNRv2` model was calibrated to NR waveforms up to mass-ratios 1:8 and spins up to 0.5 (except along the equal mass line where spins in the range $[-0.95, 0.98]$ were used). The merger-ringdown parts of the `IMRPhenomD` and `SEOBNRv2` models are almost completely independent of one another with the only common features being that they share some of the same calibration waveforms, i.e., the ones from the public SXS catalogue.

During the following comparison we restrict the computation of the mismatch to the frequencies of the `SEOBNRv2_ROM`, namely $[0.0006, 0.135]$, using the design sensitivity noise curve with a lower frequency cut-off of 10 Hz as in previous sections.

We noted earlier that the `IMRPhenomD` model is modular, and we can use alternative models of either the inspiral or merger-ringdown regions as we wish. In the following comparisons we consider three versions of the model. One is the full `IMRPhenomD` model that we have presented in the previous sections. In comparisons with `SEOBNRv2_ROM` at low masses, the mismatch is dominated by differences between the uncalibrated SEOBv2 model that we used to calibrate the inspiral of `IMRPhenomD`, and the calibrated `SEOBNRv2` model; it is a reflection of a different choice of inspiral approximant, and not the inherent accuracy of either model. For this reason we also perform a second set of comparisons, where we use `SEOBNRv2_ROM` for the inspiral (Region I) part of `IMRPhenomD`; the merger-ringdown (Region II) remains unchanged. This allows us to compare `IMRPhenomD` and `SEOBNRv2_ROM` over only the merger-ringdown, and also illustrates the flexibility of the `IMRPhenomD` model in using alternative inspiral approximants. Finally, we replace the inspiral part of the

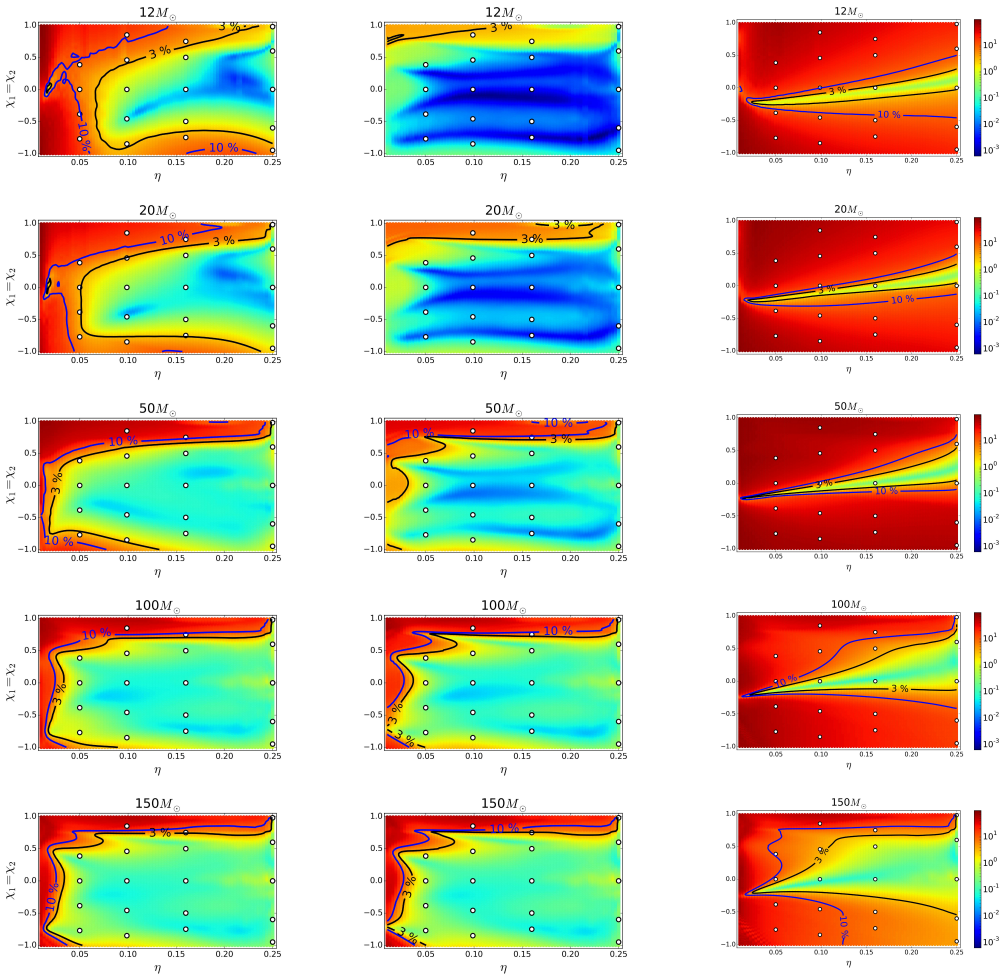

Figure 3.19: Mismatch comparisons between the `SEOBNRv2_ROM` model, and three versions of `IMRPhenomD`. Left: the final `IMRPhenomD` model. Middle: `SEOBNRv2_ROM` is used for the inspiral part of `IMRPhenomD`, i.e., up to $Mf = 0.018$. Right: `TaylorF2` is used for the inspiral part of `IMRPhenomD`. See text for discussion.

`IMRPhenomD` with `TaylorF2`.

The results of our comparions are shown in Fig. 3.19. Each panel shows the mismatch in percentage between the `IMRPhenomD` model and `SEOBNRv2_ROM` (left column) and between [`SEOBNRv2_ROM`-inspiral + `IMRPhenomD`-merger-ringdown] and `SEOBNRv2_ROM` (middle column), and between [`TaylorF2`-inspiral + `IMRPhenomD`-merger-ringdown] and `SEOBNRv2_ROM` (right column). The calculations were performed over mass ratios $[1, 100]$, spins in the range $[-1, 0.99]$ and for the total masses $[12, 20, 50, 100, 150]M_\odot$. Overlaid in white dots are the calibration points of the `IMRPhenomD` model. It is instructive when studying these plots to recall that the common region of parameter space calibration is up to mass-ratios 1:8 ($\eta \sim 0.01$) and spin $[-0.5, 0.5]$, except along the equal mass line where the spins range from $[-0.95, 0.98]$.

We focus first on the low-mass configurations ($M < 50\,M_\odot$). We see that the

agreement between IMRPhenomD and SEOBNRv2_ROM is in general quite poor — some parts of the common calibration region of both models show mismatches greater than 3%, e.g, for anti-aligned spins. This is not necessarily due to the innaccuracy of either model. We have seen in Fig. 3.16 that IMRPhenomD typically has matches of better than 1% against our hybrid waveforms, which demonstrates that the model accurately reproduces the *uncalibrated* SEOBv2 model at low frequencies. Therefore, we expect that the poor mismatches between IMRPhenomD and SEOBNRv2_ROM at low masses are due to differences between SEOBv2 and the calibrated SEOBNRv2 inspiral. This expectation is borne out in the middle column, where the SEOBv2-based IMRPhenomD inspiral is replaced with the SEOBNRv2_ROM inspiral. Now the modified IMRPhenomD and SEOBNRv2_ROM models differ only in their description of the merger-ringdown, and should agree well at very low masses, where the merger-ringdown contributes little SNR. This is what we find: at $12\,M_\odot$ the mismatches are better than 1% for most of the parameter space. The merger-ringdown still has some influence, increasing the mismatches for high-spin and high-mass-ratio systems, but in general the agreement is extremely good.

Although the uncalibrated SEOBv2 and the calibrated SEOBNRv2 inspirals show poor matches at low masses, we note that both are still consistent with our full NR data at higher frequencies, and both are adequate options for an inspiral description, as we discussed in detail in [100], and also in Sec. 3.4 above. The right panel illustrates how the model would change if we instead used TaylorF2 for the inspiral. At the matching frequency with the merger-ringdown model ($Mf = 0.018$) the TaylorF2 phase disagrees (in the sense of the time-shift analysis in [100]) at a level that makes it difficult to smoothly connect them over large regions of the parameter space. This, in addition to the differences between TaylorF2 and SEOBv2(NR) at low frequencies, introduces high mismatches over all but a small strip of parameter space.

As we progress down the table of plots to higher masses, the merger-ringdown contributes more power to the SNR, and the results of the left and middle comparisons agree more. At $150\,M_\odot$, where the contribution from the inspiral (taken here as $Mf < 0.018$) is negligible, we see that the two comparisons are almost identical. The poor agreement between TaylorF2 and our merger-ringdown model at $Mf = 0.018$ continues to lead to large mismatches.

We now focus on the high-mass configurations ($M \geq 50\,M_\odot$), and the left panels that directly compare IMRPhenomD and SEOBNRv2_ROM. It is evident that the region of agreement between the two models follows closely the region of common calibration points. Indeed, it is very encouraging that there is a high level of agreement between these two independent models even up to high mass-ratios of 1:18 and towards large negative spin values.

The positive spin section shows a different behaviour. At high masses (i.e., where the merger and ringdown are in the detector's most sensitive frequency range), there

is a sudden drop in the agreement between the two models at mass-ratios larger than equal mass and spin greater than ~ 0.75.

IMRPhenomD is calibrated to two high-spin unequal-mass cases, $(q, \chi_1, \chi_2) = \{(4, 0.75, 0.75), (8, 0.85, 0.85)\}$, and we have one additional case for verification, $(2, 0.75, 0.75)$. These are the waveforms A10 and A15 from Table 3.1 and B17 from Table 3.3 respectively. As we have already seen, IMRPhenomD has better than 1% mismatch to all theses cases and therefore the poor mismatches are unlikely due to errors in IMRPhenomD. We note that these cases are well outside the calibration region of the SEOBNRv2 model, and we therefore suspect that the accuracy of its description of the merger-ringdown degrades significantly for high spins.

Our results also suggest that, despite the lack of calibration waveforms at high anti-aligned spins, the SEOBNRv2 model remains accurate in that region of parameter space, and the relatively good agreement between the two models even for nearly extreme anti-aligned spins suggests that additional calibration waveforms, while they would be valuable, are less crucial in those cases.

We also observe poor mismatches for very high mass ratios. However, since this is outside the calibration region of both models, we cannot conclude which (if either) is correct.

To illustrate further the disagreement between IMRPhenomD and SEOBNRv2 at unequal masses and high spins, we consider in more detail the three NR configurations that we have available. Fig. 3.20 shows mismatches between pure NR waveforms (*not* the hybrids) for each of these cases, and against the IMRPhenomD and SEOBNRv2 models, using the techniques discussed in Sec. 3.2.2. The mismatch against SEOBNRv2 is above 1% for all masses, and can be as high as 10%. We have reproduced these plots using SEOBNRv2 waveforms generated from the LAL code, and the results are indistinguishable; the poor mismatches cannot be attributed to any errors in the ROM construction.

We therefore conclude that the merger and ringdown are not accurately represented in the SEOBNRv2 model for high spins. This does not detract from the power of the EOBNR approach, but simply illustrates that we should not expect any merger-ringdown model to be accurate outside its region of NR calibration. The same applies to our IMRPhenomD model; we cannot make any statements on its accuracy for spins with $\hat{\chi} \gtrsim 0.85$, other than for equal-mass systems.

3.11 Summary and discussion

In this chapter we have presented a new phenomenological model of the GW signal from the inspiral, merger and ringdown of aligned-spin BH binaries, IMRPhenomD. The new model is calibrated to hybrid EOB+NR waveforms that cover the largest region of parameter space of any aligned-spin model to date — mass ratios up to 1:18

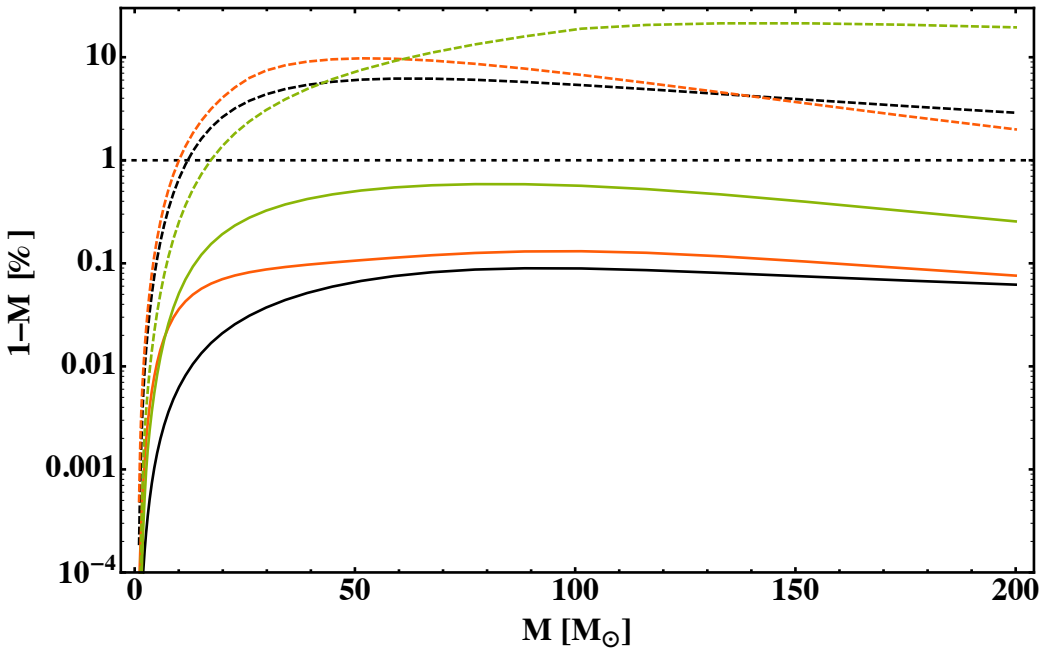

Figure 3.20: Mismatch of `IMRPhenomD` (solid) or `SEOBNRv2_ROM` (dashed) against cases A10 – $q = 4, \chi_{\rm eff} = 0.75$ (orange), A15 – $q = 8, \chi_{\rm eff} = 0.85$ (green) and B17 – $q = 2, \chi_{\rm eff} = 0.75$ (black). The mismatch was calculated as described in Sec. 3.3 using the aLIGO zdethp noise curve.

and spins up to $\chi \sim 0.85$. The inspiral and merger-ringdown are described by three separate models, allowing high accuracy over the full frequency range detectable by aLIGO and AdV, and also making the model modular: the inspiral and merger-ringdown parts can easily be modified or replaced if improved or extended models (e.g., to a yet larger region of parameter space) become available.

The inspiral part of our hybrids consists of *uncalibrated* SEOBv2 waveforms. We have shown in Ref. [100] that the SEOBv2 waveforms are the most consistent with our NR simulations over the full parameter space that we consider, and we choose to use uncalibrated SEOBv2 to produce a model that is fully independent of the NR calibration done to produce `SEOBNRv2`.

The merger-ringdown part of the hybrids (i.e., the NR waveforms) have a common lowest frequency of $Mf \sim 0.018$, and so this is the frequency at which we switch from the inspiral to the merger-ringdown model.

The final model has mismatches against both the 19 calibration hybrids and an additional 29 verification hybrids, of typically better than 1% for all masses. The mismatches are shown in Fig. 3.16, and demonstrate that we have faithfully modelled this region of the aligned-spin parameter space.

The model is parameterised by the binary's symmetric mass ratio, η, and a normalized reduced effective spin parameter, $\chi_{\rm PN}$, defined in Eq. (1.58). A parameterization in terms of a weighted sum of the two BH spins has been used in previous Phe-

nom models [20, 151], and is motivated by the leading-order spin effect on the inspiral phasing [65, 141, 20], and demonstrations of its efficacy for merger-ringdown [145]. In this chapter we show that the reduced-spin approximation becomes inaccurate only for high-spin unequal-mass systems, but in these configurations the parameter errors due to our approximation appear to be smaller than statistical errors in the spin and mass-ratio measurements with aLIGO and AdV. This implies that it will be difficult to measure both BH spins in GW measurements; this was studied in [147].

We have compared the new `IMRPhenomD` model with the state-of-the-art `SEOBNRv2` model, and found that the two models agree well over their common region of calibration, which is mass ratios up to 1:8, and spins up to $\chi \sim 0.5$ (and near-extremal spins for equal-mass systems). At low masses the agreement is not good, but we show that this is due to differences between the calibrated and uncalibrated SEOBv2 inspiral descriptions.

Outside the common calibration region, the two models show significant disagreement, in terms of their mismatch. This is particularly true for high aligned spins. Given that `IMRPhenomD` was calibrated to several high-spin unequal-mass simulations (spins of 0.75 or 0.85), while `SEOBNRv2` was calibrated to spins of no higher than 0.5 for unequal-mass configurations, we conclude that `SEOBNRv2` does not accurately capture the merger and ringdown for these systems. We expect, however, that its performance will become comparable to `IMRPhenomD` when calibrated to additional NR waveforms.

The broader conclusion we draw from these results is that high-aligned-spin systems deserve greater attention in future modelling efforts. The `IMRPhenomD` model was calibrated to only two (unequal-mass) high-aligned-spin binaries, but it is clear that a larger number of NR simulations in this region of parameter space will benefit GW astronomy.

The `IMRPhenomD` model involves 17 coefficients that are mapped across the parameter space with polynomials up to second order in η and up to third order in $\chi_{\rm PN}$. Although the total number of coefficients is similar to the previous `IMRPhenomC` model, the development of a refined ansatz for each frequency region allows us to more accurately model a wider range of features of the waveforms. We have also carefully tuned each ansatz, and our parameter-space fits, to ensure that the model produces physically reasonable results outside the calibration region, and that the waveforms show no pathological features when converted to the time-domain (Appendix A.1). These modifications significantly improve the model beyond previous Phenom models, in addition to increasing the range of calibration and lowering the mismatch error.

In previous work it has been shown that models for generic (precessing) binaries can be produced by "twisting up" an aligned-spin model. The `IMRPhenomP` model exploits that idea, but to date has been based on the `IMRPhenomC` model, which

limits its applicability to mass ratios $q \lesssim 4$. With the advent of `IMRPhenomD`, we will be able to make `IMRPhenomP` valid to much higher mass ratios and higher values of the parallel component of the spin. This simple replacement of `IMRPhenomC` with `IMRPhenomD` is called as `IMRPhenomPv2` in the LIGO-Virgo LAL code and has been used in the analysis of advanced detector data [17] and in tests of strong field GR [15].

Gravitational wave searches and parameter estimation rely on accurate waveform models. In this chapter we have found evidence that the `SEOBNRv2` model does not accurately capture the merger and ringdown for systems with unequal masses and large aligned-effective-spins ($\chi \gtrsim 0.75$). The mismatch for these systems, which is the fractional loss in the optimal SNR, can be as large as 10% whereas `IMRPhenomD` performs better than 1% mismatch for all cases considered. The mismatch, though appropriate for evaluating the accuracy of a model is not the correct metric to measure the ability of a waveform model to detect GWs. The correct quantity to compute is the fitting factor (FF), which is the mismatch optimised over intrinsic parameters of the source (see Section 1.6.2). In the next chapter we perform an extensive systematic comparison between aligned-spin waveform models and we estimate the impact on GW searches and parameter estimation due to waveform modelling errors.

Chapter 4

Applications: Model Comparisons and Systematic Errors

4.1 Introduction

The two main applications that the `IMRPhenomD` model was constructed for are as templates in matched-filter based searches and parameter estimation of GW candidates. In this chapter we explore the accuracy of waveform models that predict the inspiral, merger and ringdown GW signal. We expand on the study performed in Chapter 3.10, which was restricted to `IMRPhenomD` and `SEOBNRv2_ROM` with aligned equal-spin ($\chi_1 = \chi_2$) systems, to include `IMRPhenomB` and `IMRPhenomC` as well as relaxing the equal-spin constraint.

In section 4.2 we compare several aligned-spin IMR models by computing the match or faithfulness, i.e, inner-product maximised over phase and time shifts. The results of this analysis provide information on how accurate a waveform model is when the accuracy of the recovered parameters are important, i.e., in parameter estimation.

We then investigate if a template bank of EOB waveforms is effectual towards an injection set of `IMRPhenomD` signals. We do this because we found that EOB and Phenom agree very well in large regions of the parameter space except for spins higher than 0.75 and unequal mass-ratios. This poses the important question, "Does an EOB search miss a significant fraction of signals from this region?" To try and answer this we simulate a population of `IMRPhenomD` signals and recover them with an EOB template bank in Section 4.3.

Finally, in Section 4.4 we perform full Bayesian parameter estimation of a mass-ratio 1:4 and $\chi_{\rm eff} = 0.75$ NR waveform (`BAM:7`, see Table 2.1)[1]. This is a particularly

[1] See Table 2.3 for error estimates on the phase and amplitude.

Name	Ref	Spins	Calibration Region (q, χ)
`IMRPhenomB`	[20]	Aligned	$q \in [1, 4]$ & $q \to \infty$, $\chi \in [-0.85, 0.85]$
`IMRPhenomC`	[151]	Aligned	$q \in [1, 4]$, $\chi \in [-0.85, 0.85]$
`IMRPhenomD`	[100, 106]	Aligned	$q \in [1, 18]$, $\chi \in [-0.95, 0.98]$
`IMRPhenomPv2`	[91]	Precessing	Inherited from `IMRPhenomD`
`SEOBNRv2`(ROM)	[166]([146])	Aligned	$q \in [1, 8]$ & $q = 1000$, $\chi \in [-0.95, 0.98]$
`SEOBNRv3`	[136]	Precessing	Inherited from `SEOBNRv2`

Table 4.1: Summary of IMR models used in this chapter along with their respective calibration regions. We show `IMRPhenomPv2` and `SEOBNRv3` [136] for completeness but do not use.

interesting configuration as `SEOBRNv2` has a maximum mismatch of $\sim 11\%$ whereas `IMRPhenomD` has a maximum mismatch of $\sim 0.1\%$ to this waveform (see Figure 3.20). Our primary goal is to evaluate the size of the systematic errors in realistic GW parameter estimation that are due to modelling errors.

In this chapter we will evaluate a number of different IMR models, for convenience Table 4.1 summarises the calibration regions of each model used in this chapter with the exception of `IMRPhenomPv2` and `SEOBNRv3` [136], which we note for completeness but do not use. `SEOBNRv3` is a precessing version of the aligned-spin `SEOBNRv2` model but due to the high computational cost to generate a waveform it is difficult to use them in the following studies that require $\mathcal{O}(10^6)$ waveform evaluations. In the co-precessing frame the model contains the $\ell = 2, |m| = \{1, 2\}$ modes however, only $m = 2$ is calibrated to NR.

`IMRPhenomPv2` is a precessing IMR model. It uses PN expressions for the Euler angles describing the transformation from the co-precessing frame to the inertial frame, which encodes the leading order orbital precession on the waveform. This model uses `IMRPhenomD` as its underlying non-precessing model and reduces to this in the non-precessing limit $\chi_p \to 0$. χ_p is the effective precessing spin parameter introduced in Ref [159]. It quantifies the amount of in-plane spin, which drives the precession. Its value is essentially the magnitude of the in-plane spin on the larger BH. In the co-precessing frame the model contains the $\ell = |m| = 2$ mode, however, in the inertial frame, due to the rotations, the other m modes are present.

4.2 Model Comparisons: Faithfulness

In this section we will present results of an analysis designed to determine the amount by which different IMR waveform models agree with each other. A similar study was performed for inspiral-only approximants in [131] and for IMR in [111, 112]. In [111, 112] their goal was to estimate the accuracy of waveform models by comparing to NR simulations. Our goal is similar but, we will compare different waveform models against each other. Whilst we cannot strictly conclude if one model is more

accurate than another we can achieve a broad perspective of the overall agreement between different models over large regions of the parameter space. For example in Figure 3.19 (first column, second row onwards) we see a sudden drop in the agreement between `IMRPhenomD` and `SEOBNRv2_ROM` for high positive spins and for mass-ratios barely higher than equal-mass. This surprising behaviour was only found by comparing against another waveform model. These studies are valuable when deciding which waveform model to use in GW searches, parameter estimation, and parameterised tests of GR, and where they can be trusted.

This "faithfulness" analysis is performed as follows: given a canonical waveform model, which we take here as `SEOBNRv2_ROM`, compute the match Eq. (1.70) against a set of other waveform models; which we take here as {`IMRPhenomB`, `IMRPhenomC`, `IMRPhenomD`}; across the parameter space of interest. The waveforms were generated using `LALSuite` [167] and the computation of the match was done using `pyCBC`'s `faithsim` [7] code.

The parameter space explored was chosen to test all models both inside and outside of their respective calibration regions. We probe the component mass space $(m_1, m_2) \in [6, 300]M_\odot$ and allow total masses in the range $[12, 300]M_\odot$. We do not consider lighter systems as we are focusing on systems where the merger signal contributes significantly to the SNR [54]. The spins are restricted to just under the full spin range to be $[-0.99, 0.99]$ and for each comparison 10^6 samples were taken from each parameter uniformly. Matches were computed using a noise curve similar to that of the advanced detectors first observing run (2015-2016) over the frequency interval $[30, f_{\rm end}]$ Hz, where $f_{\rm end}$ is the end of the waveform.

4.2.1 Results

Figure 4.1 shows the cumulative distribution of the match, which shows the percentage of cases below the corresponding match for each case; `IMRPhenomB` (blue), `IMRPhenomC` (green) and `IMRPhenomD` (red). Figure 4.1a shows the full range of matches and Figure 4.1b shows a zoom-in for matches > 0.95. The improvement of `IMRPhenomD` over the previous phenomenological models is quite dramatic, almost 86% of the cases considered have matches $> 99\%$. This is contrasted against 42% for `IMRPhenomC` and 5% for `IMRPhenomB`, summarised in Table 4.2.

Name	Waveform 1	Waveform 2	Min Match (%)	% < 97%(%)	% < 99%(%)
Run 1	`IMRPhenomB`	`SEOBNRv2_ROM`	12	78	95
Run 2	`IMRPhenomC`	`SEOBNRv2_ROM`	19	21	58
Run 3	`IMRPhenomD`	`SEOBNRv2_ROM`	43	11	14

Table 4.2: Results from the faithsim analysis. The improvement of `IMRPhenomD` over the previous phenomenological models is quite dramatic, almost 86% of the cases considered have matches $> 99\%$. This is contrasted against 42% for `IMRPhenomC` and 5% for `IMRPhenomB`.

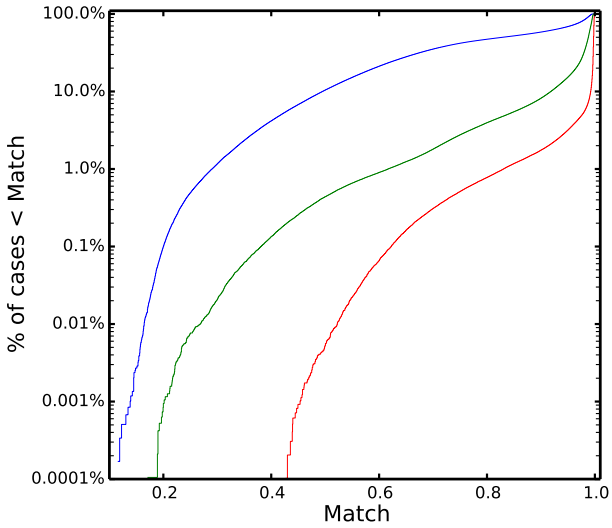

(a)

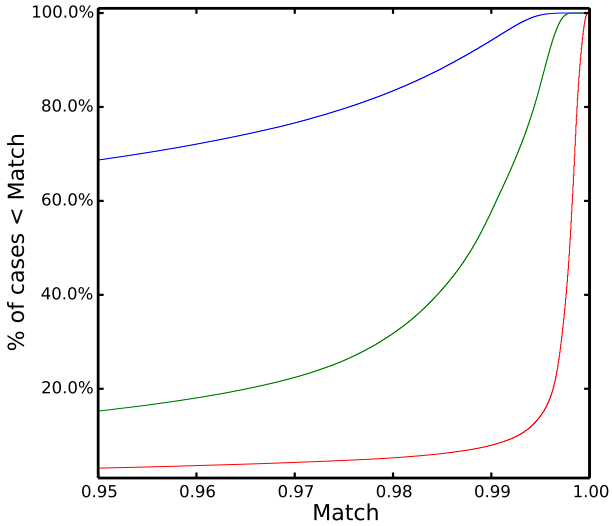

(b)

Figure 4.1: Cumulative distributions of the match for each case `IMRPhenomB` (blue), `IMRPhenomC` (green) and `IMRPhenomD` (red). 4.1a shows the full range of matches and 4.1b shows a zoom-in for matches > 0.95.

To better understand where in the parameter space the various models agree or disagree with each other we plot two different slices through the parameter space. In Figure 4.2 we show the results in terms of their $(\eta, \hat{\chi})$ values and in Figure 4.3 show the results in terms of component masses (m_1, m_2).

We first focus on the $(\eta, \hat{\chi})$ slice Figure 4.2. From the top row to the bottom row shows the results of `IMRPhenomB/C/D` each compared against `SEOBNRv2_ROM` respectively. The left column plots all data points whereas the right column only shows points where the match is less than 0.97. All colour bars show the same range for the match $[0.2, 1]$. Grey points represent configurations where the waveform

failed to generate. Note that whereas IMRPhenomC has regions where waveform generation is restricted[2], our new model IMRPhenomD posses no such restrictions in the region of parameter space. The overlaid white dots mark the calibration points for IMRPhenomD.

The agreement between phenomenological models and SEOBNRv2_ROM has vastly improved over nearly the entire parameter space with the development of our new model IMRPhenomD. The fact that independent modelling methods seem to be converging to a common solution is reassuring.

The results of IMRPhenomB and IMRPhenomC (first two rows) shows some interesting features. The calibration set of these models are the same, i.e., up to mass-ratio 1:4 and aligned-spins in the range $[-0.85, 0.85]$ and indeed this appears to be roughly the region where these models agree with SEOBNRv2_ROM the most. The overall trend however, is quite different between IMRPhenomB and IMRPhenomC. Poor matches for IMRPhenomB seem to be scattered uniformly in this space. Comparing to Figure 4.3b reveals systems with $M \gtrsim 150 M_{\odot}$ have poor matches. IMRPhenomC's results seem to be much more ordered in the sense thet the falloff of the match seems to happen smoothly as your go beyond its calibration region, with the exception of the feature in the lower left corner of the middle row plots (Figures 4.3c and 4.3d). Irregularity of the matches outside of the calibration regions tends to indicate that a model is not extrapolating well.

These comparisons include systems with mass-ratio's up to ∼1:50. IMRPhenomD was calibrated upto mass-ratio 1:18 and SEOBNRv2 was calibrated only up to 1:8 (with also 1:1000 Teukolsky waveforms [165, 166]). Focusing on the bottom right plot we see that the agreement between IMRPhenomD and SEOBNRv2_ROM over the mass-ratio interval [8,50] is remarkable, with matches > 0.97. In this region both models agree beyond their calibration region. The construction of these models is independent, which again is evidence that both models are extrapolating outside their calibration regions reasonably well and can be used in this region of parameter space in analyses [95].

There are three interesting outlying populations of signals visible in the IMRPhenomD results (Figure 4.2f). A number of signals are found with comparable masses and relatively low effective spins ($-0.5 \lesssim \hat{\chi} \lesssim 0.5$). In this region we are typically very confident about the agreement between IMRPhenomD and SEOBNRv2_ROM, which makes these signals curious outliers. Upon further investigation we find these signals have individual spin components which are comparable in magnitude and opposite in direction resulting in a relatively low effective spin.

The second region occurs for very high anti-alined spin and mass-ratios (lower left corner of the plot). As this is one of the regions where both models are extrapolating the most, we assume this to be the cause.

The final region of outliers lies between mass-ratios 8 and 18 with effective spins

[2] IMRPhenomC is restricted to mass-ratio's less than 1:20 and $|\chi| \lesssim 0.9$

between 0.5 and 0.75. Further investigations reveal that these systems contain an aligned spin primary BH and an *anti*-aligned spin secondary BH and that this region extends down to mass-ratios 1:4. These systems have lower matches than other systems in their vicinity due to using a single effective spin approximation. This was explored in more detail in Chapter 3.9.2. Even though the faithfulness is lower than expected we expect the FF to be high with small biases.

The top row plots (`IMRPhenomB`) shows an interesting result for the high mass-ratio ($q \gtrsim 18$) and high aligned-spin ($\hat{\chi} \gtrsim 0.75$) region where the agreement is better than `IMRPhenomD` (Figure 4.2e and 4.2f), `IMRPhenomB` incorporates some information from the extreme mass-ratio limit of PN which could be responsible for this or the agreement could be serendipitous.

Figure 4.2 only conveys part of the information, in particular it excludes information about the total mass, and hence which frequencies contribute most to the match calculation. To regain this, in Figure 4.3 we similarly plot the results in terms of the component masses. The `IMRPhenomB` results (Figures 4.3c and 4.3d) show a qualitatively different behaviour to the $(\eta, \hat{\chi})$ plots (Figures 4.2a and 4.2b). The previous, relatively uniform distribution is replaced with a very clear total mass divide at $\sim 150 M_{\odot}$, below which the matches are relatively good and above which they are very poor. Due to the uniformity in the $(\eta, \hat{\chi})$ plots we can deduce that the poor matches occur for systems with any values of $\hat{\chi}$. It is clear that these high mass systems are skewing the statistics.

The `IMRPhenomC` results (Figures 4.3c and 4.3d) show no sign of the strong deterioration of the match towards high masses which we saw in the `IMRPhenomB` results. The match is distributed much more uniformly than in the counterpart plot $(\eta, \hat{\chi})$ (Figures 4.2c and 4.2d). From this we deduce that the poor matches observed in Figure 4.2f occur at all total masses evenly. The grey region in Figure 4.3d near the equal mass line corresponds to the highly spinning systems and the grey region at the bottom of the plot corresponds to mass-ratios > 20, regions which are prohibited by the `IMRPhenomC` code.

The `IMRPhenomD` results are shown in Figures 4.3e and 4.3f. The agreement with `SEOBNRv2_ROM` is not quite as startling as in Figures 4.2f but from this we do see that the systems with matches $< 97\%$ also seem to be uniformly distributed (with a slight over density for high mass-ratios). This implies that the poor matches at high aligned-spin occur at all total masses considered.

4.2.2 Summary

In this analysis we have investigated how well different waveform models agree with each other by only allowing a relative phase and time shift between waveforms. Because we keep the intrinsic parameters of the waveforms fixed there is little freedom and high values for the match indicate that two waveforms are indeed close to each

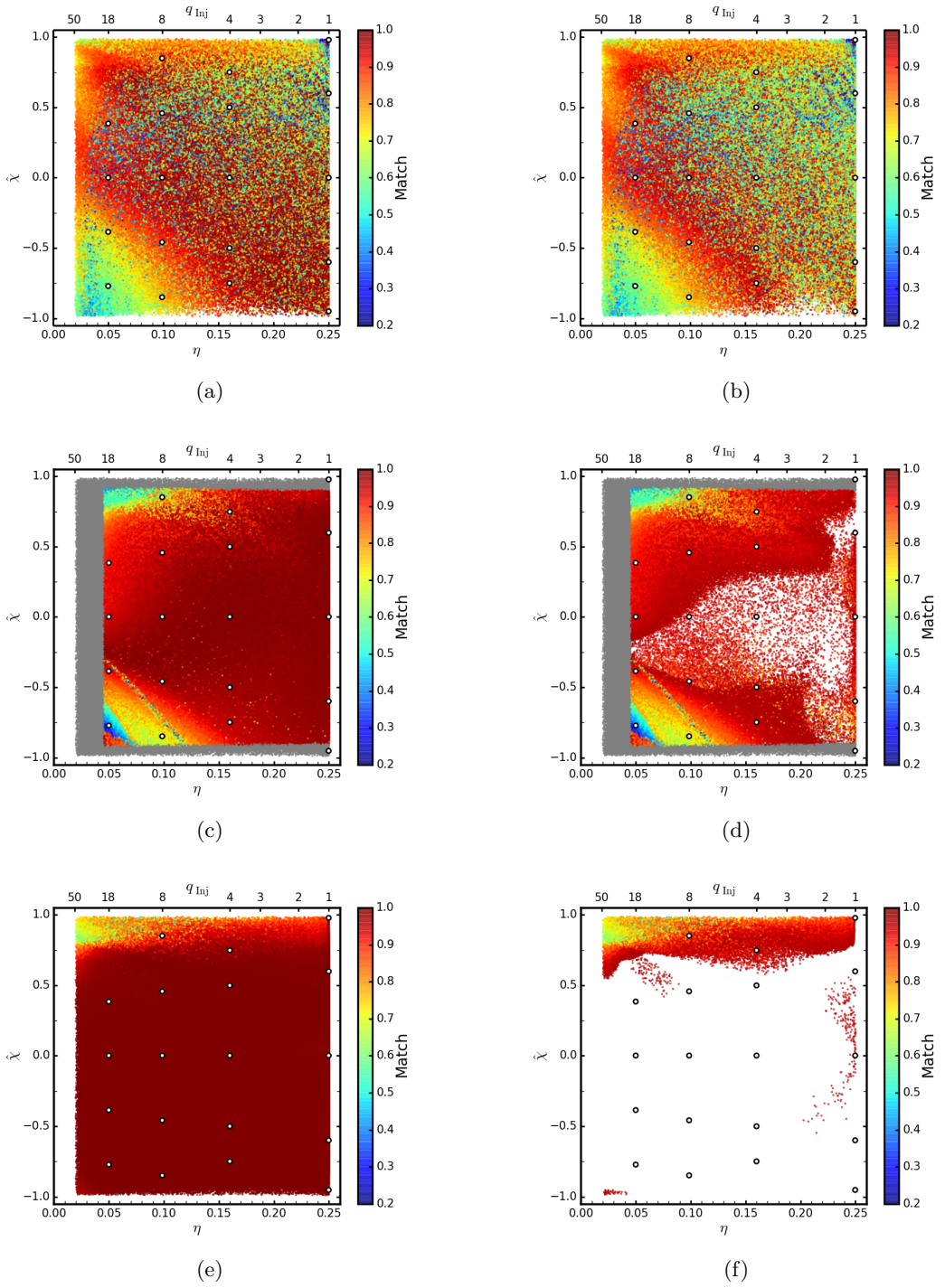

Figure 4.2: Faithfulness calculations comparing IMRPhenomB/C/D with SEOBNRv2_ROM. The x- and y- axes are the symmetric mass-ratio and the effective spin parameter defined by Equation 3.2 repectively and the colour bar shows the match. The top x-axis is the corresponding mass-ratio. Top: PhenomB. Middle: PhenomC. Bottom: PhenomD. Left column shows results for over the whole range of matches. Right column, uses the same colour bar scale but only plots points where the match is less than 0.97. Any grey points represent configurations where the waveform failed to generate. The overlaid white dots mark the calibration points for `IMRPhenomD`.

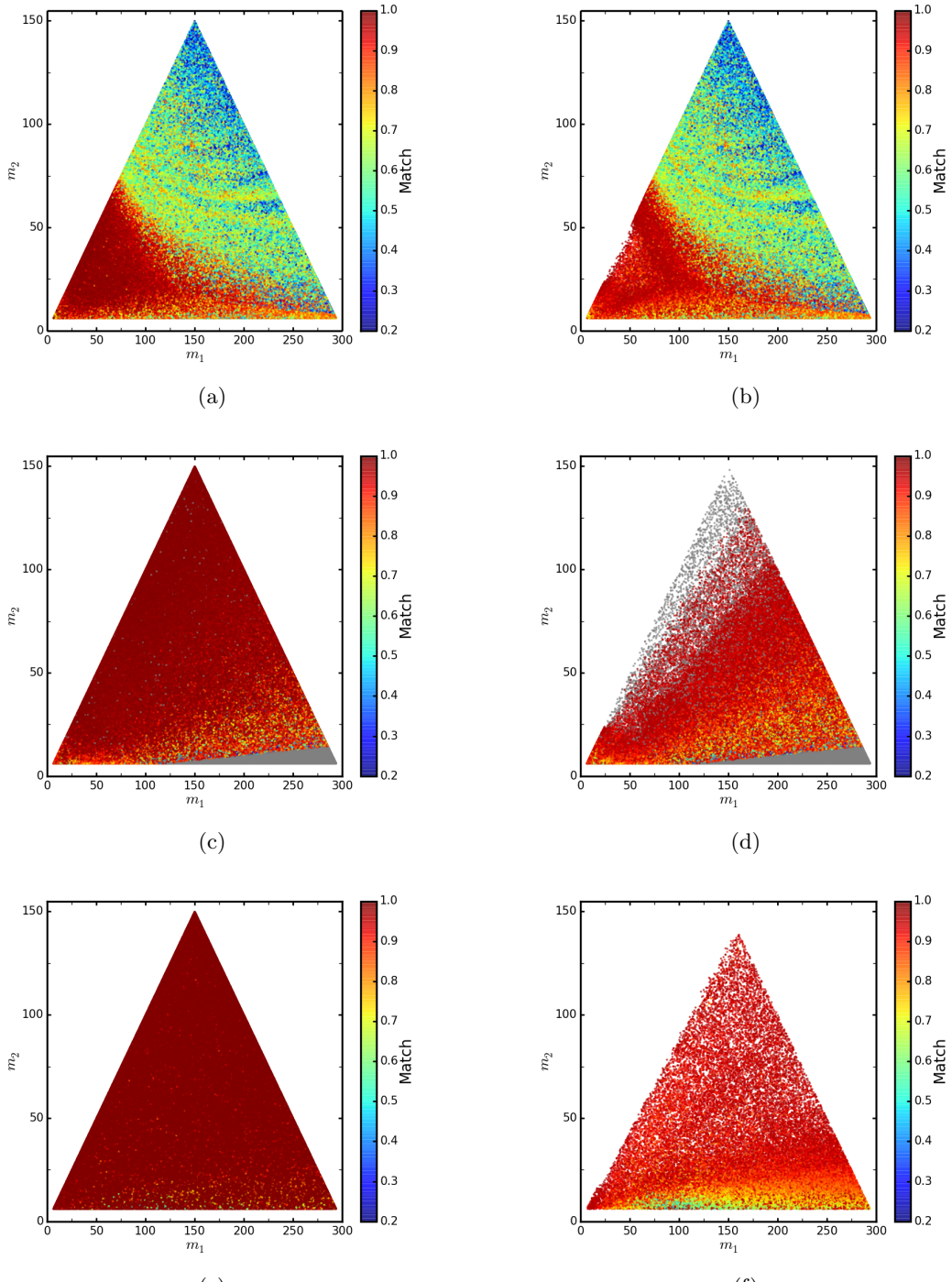

Figure 4.3: Faithfulness calculations comparing IMRPhenomB/C/D with SEOBNRv2_ROM. The x- and y- axes are the primary and secondary masses repectively and the colour bar shows the match. Top: PhenomB. Middle: PhenomC. Bottom: PhenomD. Left column shows results for over the whole range of matches. Right column, uses the same colour bar scale but only plots points where the match is less than 0.97. Any grey points represent configurations where the waveform failed to generate.

other. Our results provide compelling evidence that IMRPhenomD is vastly superior to previous phenomenological models (IMRPhenomB and IMRPhenomC) both in the interior and exterior of their respective calibration regions.

4.3 Template Bank Simulations

The results of comparing IMRPhenomD with SEOBNRv2_ROM shown in Figures 3.19 (left column) and Figure 4.2 (bottom row) as well as the comparison to NR waveforms in Figure 3.20 indicate that the SEOBNRv2 model is being outperformed by IMRPhenomD in the unequal-mass and high aligned-spin ($\chi \gtrsim 0.7$) region of parameter space; similar conclusions were found in [112].

In this section we will investigate if there is a significant loss in detection efficiency in GW searches for BBHs with unequal masses and high aligned-spin. To quantify detection efficiency we will invoke the concept of fitting factors (FF) and use a template bank to estimate the FF (see Section 1.6.2).

A template bank is used to maximise over the intrinsic parameters of CBCs being searched over. It is a list of coordinates in the BBH parameter space built such that the match between nearest neighbours is less than some user defined threshold, usually 97%. This implies that the loss in event rate due to a discrete template bank is no more than 10% (see Chapter 1.6.2). A template bank which recovers any signal (in the parameter space it was designed to cover) with a FF $\geqslant 97\%$ is called *effectual*.

In aLIGO CBC searches the SEOBNRv2_ROM waveform family was used as the search template for the first observing run (O1) [13]. In this section we will use a template bank that is effectual to SEOBNRv2_ROM signals to test if it is also effectual to IMRPhenomD signals.

Because we are not calculating the true FF we cannot accurately quote the resulting parameter biases. However, in Section 4.4 we perform a Bayesian parameter estimation analysis to compute the resulting probability density distribution on parameters when we inject the BAM:7 waveform from Chapter 2 and attempt to recover the parameters of the injection with SEOBNRv2 and IMRPhenomD.

4.3.1 Method

We will use a template bank generated using the method outlined in [59] to build effectual template banks for aligned-spin.BBHs[3] The bank contains 236784 templates and was built to be effectual to the SEOBNRv2_ROM waveform. To test if a template bank is effectual we generate a population of signals with parameters consistent with the range of the bank and use the bank to recover those signals. We use pyCBC's banksim code [7] to evaluate the effectualness of a template bank. The banksim

[3]The template bank was provided by Alex Nielsen, Ian Harry and Collin Capano.

code computes the match between the injected signal and all templates within a $\mathcal{M}_c$ window of $\pm 10\%$ of the injection.[4] The largest match in this window is the recovered FF. Note that this is only approximately the FF because the template bank is discrete.

The parameter space explored tests the full extent of the template bank. The bank contains templates with component masses $(m_1, m_2) \in [1, 49] M_\odot$ restricted to the total mass interval $[12, 50] M_\odot$.[5] The bank covers systems with aligned-spins $(\chi_{1z}, \chi_{2z}) \in [-0.99, 0.99]$. The injection set comprised of $2 \cdot 10^5$ signals whose parameters were drawn from uniform distributions. Matches were computed using a noise curve similar to that of the advanced detectors initial observing run over the frequency interval $[30, f_{\rm end}]$ Hz where $f_{\rm end}$ is the end of the waveform.

We perform two `banksim` runs (See Table 4.3). The first run (Run 1) uses `SEOBNRv2_ROM` as the template *and* signal waveform, which validates the effectualness of the bank to itself. The second run (Run 2) uses `SEOBNRv2_ROM` as the template waveform, and `IMRPhenomD` as the signal waveform. This will test the EOB bank's ability to recover `IMRPhenomD` signals. Specifically we are most interested in the bank's ability to recover unequal mass and high-aligned spin `IMRPhenomD` signals as there is evidence that `SEOBNRv2` less accurate than `IMRPhenomD` here.

4.3.2 Results

The results of Run 1 (blue curve) and Run 2 (green curve) are presented in Figure 4.4 in the form of a cumulative histogram that shows, for each value of the FF, what is the % of injections that were recovered with a FF less than that value. Results are summarised in Table 4.3. We find that the template bank is indeed effectual to `SEOBNRv2_ROM` signals with the worst recovered FF being 96% and only 0.15% of all injections have a recovered FF$<$ 97%. In terms of the recovered SNR of a signal this translates to the majority of injections being recovered with at most a 3% loss in optimal SNR. The same template bank however, cannot be said to be effectual to `IMRPhenomD` signals. The distribution develops a tail towards lower recovered FFs with a minimum FF of 74% with 3.5% of injections with a recovered FF$<$ 97%.

To find out exactly where in the parameter space is causing this tail in the cumulative histogram Figure 4.5 shows the results from the Run 2 injection set with respect to $(\eta, \hat{\chi})$ and the colour bar shows the recovered FF ($\mathrm{FF_{Rec}}$). On the top axis is the corresponding mass-ratio. Figure 4.5a shows all injections and 4.5b only shows injections that were recovered with a FF$\leqslant$ 97% (both use the same colour bar range). First we note, as expected, that the regions of poor fitting factors ($\leqslant$ 97%) roughly follows a similar distribution to the regions of poor match ($\leqslant$ 97%)

[4] This is a tunable parameter.

[5] Note here we only consider total masses up to $50 M_\odot$. This is in contrast to the faithfulness analysis in section 4.2 where we considered total masses up to $300 M_\odot$. However, we are still probing a similar mass-ratio interval of $[1, 49]$.

Name	Template	Signal	Minimum FF (%)	% < 97%(%)
Run 1	SEOBNRv2_ROM	SEOBNRv2_ROM	96	0.15
Run 2	SEOBNRv2_ROM	IMRPhenomD	74	3.5

Table 4.3: Results from template bank simulations. Both runs use SEOBNRv2_ROM as the templates and the effectualness of the bank is determined by injecting SEOBNRv2_ROM (Run 1) and IMRPhenomD (Run 2) signals. Also tabulated is the minimum recovered FF and the percentage of injections that were recovered with a FF $< 97\%$. While Run 1 demonstrates that the bank is effectualness to itself it cannot be said to be effectual to IMRPhenomD. For an overview across the parameter space see Figure 4.5.

in Figure 4.2f. There is a region in the lower left of the plots (high mass-ratio and anti-aligned spins) where the template bank is not recovering IMRPhenomD injections where we would expect both models to agree (see Figure 4.2f). The injections in this region also have total masses $> 20M_{\odot}$ with the majority of them between 40 and $50M_{\odot}$. In general the falloff of the match for high mass systems, compared with low mass systems is gradual, in terms of template bank placement this translates into fewer templates at high masses and this is likely causing an undercoverage of the bank to IMRPhenomD signals. We argue similarly for the low $\hat{\chi}$ region at high mass-ratios and low mass-ratios with $\hat{\chi} \sim -0.25$ too as these are systems with high total masses.

We now turn our attention to the high aligned-spin region. In the high mass-ratio and high aligned-spin region (top left corner of plot) we known that SEOBNRv2_ROM and IMRPhenomD deviate from each other at the level of 70% match (see Figure 4.2, bottom right), similar to the values obtained in the template bank simulations. However, without NR simulations in the region of parameter space we cannot conclude that one more is more accurate than the other.

The region with the mass-ratio interval $[1, 8]$ and $\hat{\chi} \gtrsim 0.7$ is more interesting because in this region IMRPhenomD has been calibrated to NR simulations. There is a population of injections with FF $\leqslant 97\%$ in this region, the majority of which have recovered FF $\sim 95\%$, which is slightly lower than the lowest recovered FF found in Run 1.

Assuming IMRPhenomD is a more accurate approximation to the true waveform in this region then a GW search using a template bank similar to the one used here would be sub-optimal to detect highly (aligned) spinning BBHs, losing about 5% of the optimal SNR corresponding to a loss of $0.95^3 \rightarrow 14\%$ of detectable signals. Whilst this is greater than the typically quoted upper limit of 10% for what is an acceptable lose of signals it is not larger by a significant amount. As a possible solution to this problem we recommend trying to either: (i) increase the number of SEOBNRv2_ROM templates in this region, to (ii) create a dual template bank where the "holes" in the EOB bank are filled with IMRPhenomD using a stochastic template

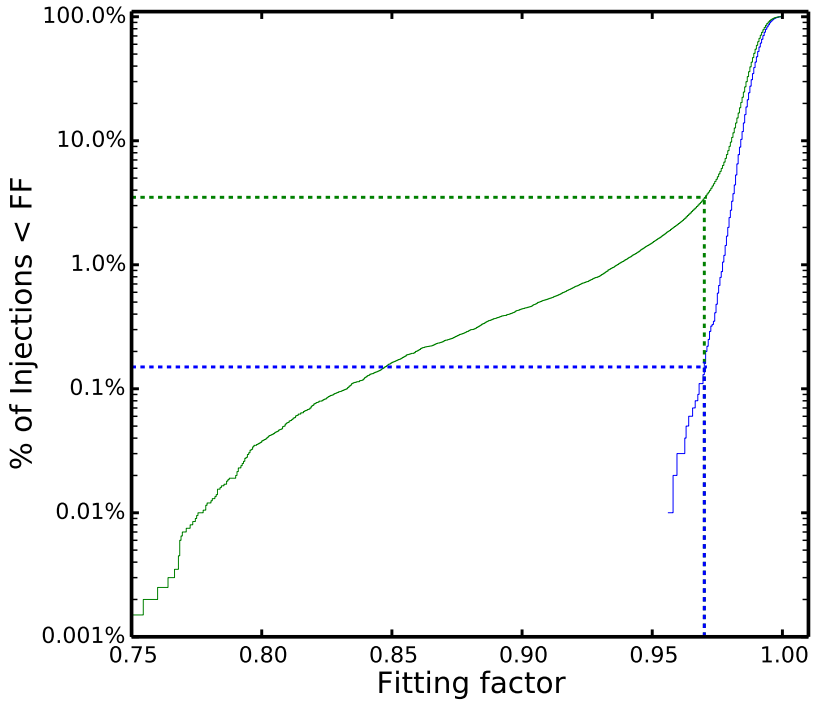

Figure 4.4: Cumulative distributions of the fitting factor. Blue: Run 1 using `SEOBNRv2_ROM` as the signal waveform and `SEOBNRv2_ROM` as templates, the worst recovered FF is 96% and is deemed effectual. Green: Run 2 using `IMRPhenomD` as the signal waveform and `SEOBNRv2_ROM` as templates, the worst recovered FF is 74% with 3.5% of signals recovered with a FF$<$ 97%. These results show that the EOB bank ineffectual towards `IMRPhenomD`.

placement algorithm [22] or (iii) simply generate the high spin templates in the bank with `IMRPhenomD` and the rest of the bank uses `SEOBNRv2`. In Section 4.3.3 we investigate option (iii).

This analysis is idealised in the sense that equal probabilities have been given to all systems, which comes from drawing the parameters from uniform distributions. A more complete analysis could invoke the results from population synthesis models to construct a more physically motivated injection set. This could then be used in either template bank simulations such as the ones performed here or even used as injections for a CBC pipeline such as `pyCBC` in the presence of real detector data to get a more realistic result of how much this difference between `SEOBNRv2_ROM` and `IMRPhenomD` effects GW searches for BBHs with unequal-masses and high aligned-spins.

Although we have restricted ourselves to only consider the effective-spin parameter for unequal-mass systems the effective-spin parameter can be large even if only the larger BH is spinning.

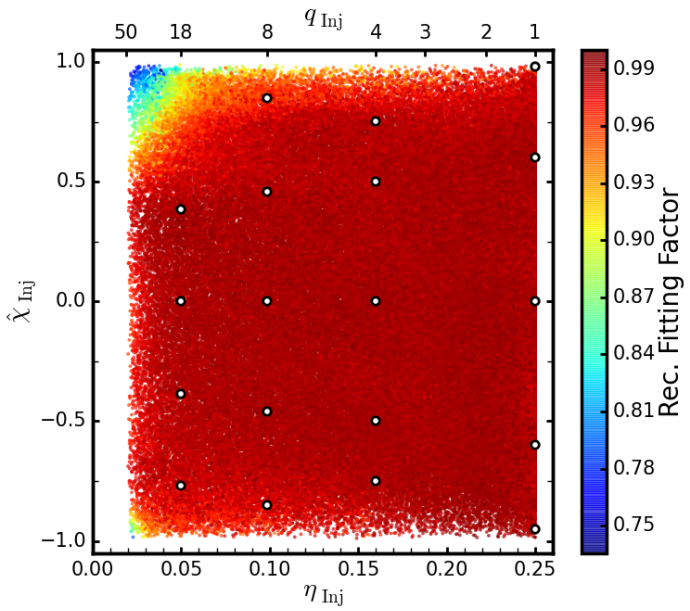

(a)

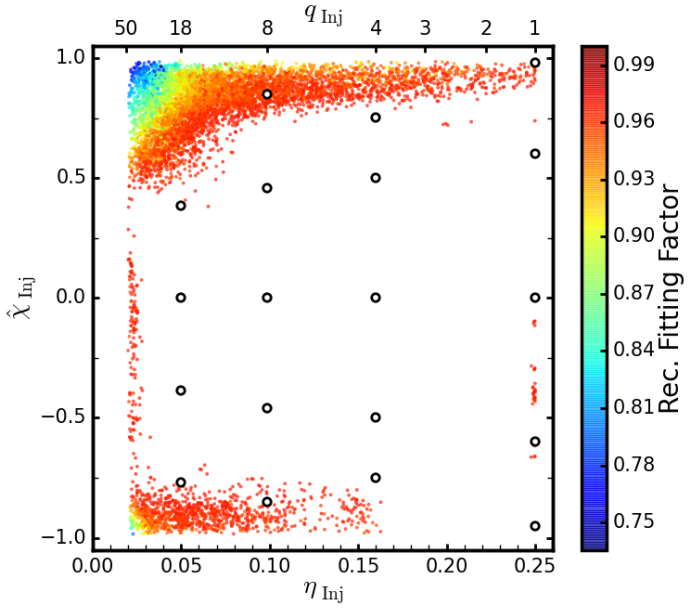

(b)

Figure 4.5: Banksim calculations, injecting `IMRPhenomD` into a `SEOBNRv2_ROM` template bank. The x- and y- axes are the symmetric mass-ratio and the effective spin parameter defined by Equation 3.2 respectively and the colour bar shows the match. The top x-axis is the corresponding mass-ratio. 4.5a: shows results for over the whole range of matches. 4.5b: uses the same colour bar scale but only plots points where the fitting factor is less than 0.97. The overlaid white dots mark the calibration points for `IMRPhenomD`.

Name	Template	Template $\chi_{\rm eff} > 0.7$	Signal	Min FF (%)	% < 97%(%)
Run 3	SEOBNRv2_ROM	IMRPhenomD	IMRPhenomD	80	2.1

Table 4.4: Results from the third template bank simulation. This run is identical to Run 2 except that the high spin ($\chi_{\rm eff} > 0.7$) templates are generated with IMRPhenomD. Both the minimum recovered FF and the percentage of signals recovered with FF< 97% is improved but the bank is still not effectual to IMRPhenomD signals.

4.3.3 Split Template Bank

To investigate our hypothesis if we can improve the effectualness of the EOB bank by replacing high aligned spin EOB templates with IMRPhenomD we perform another template bank simulation, Run 3 (see Table 4.4). We find that enforcing the template bank to use IMRPhenomD as the approximant for $\chi_{\rm eff} > 0.7$ increases the effectualness of the bank towards IMRPhenomD signals but not enough to be effectual towards IMRPhenomD. The recovery of high mass-ratio and high aligned-spin injections improves from a minimum FF of 74% to 80% and the percentage of signals recovered with FF< 97% is improved from 3.5% to 2.1%. Figure 4.6 adds the result from Run 3 to the cumulative distribution, which shows that the split template bank reduces the tail in the distribution by over an order of magnitude at FF= 90%.

Figure 4.7 shows the results from the Run 3 template bank simulation on the two dimensional space $(\eta, \hat{\chi})$ coloured by their recovered FF. Using IMRPhenomD templates for $\chi_{\rm eff} > 0.7$ improves the bank's effectualness to IMRPhenomD, especially in the high mass-ratio, high aligned-spin region (top left) where the minimum FF (as compared with Run 2) is increased from 74% to 80%. The effectualness to the moderate mass-ratio systems $q \sim [1, 8]$ is improved as well but there are still a number of signals recovered with a FF< 97%. We conclude that the bank will need more templates to become effectual to IMRPhenomD signals however, it is likely that a relatively small number of templates will be needed.

4.3.4 Summary

In this section we have used an effectual template bank for SEOBNRv2_ROM to recover a population of IMRPhenomD injected signals with parameters covering the range of the template bank. We find that the EOB bank recovers IMRPhenomD signals over the vast majority of the parameter space tested with the exception of mass-ratios > 4 and effective-spins < -0.74, which we attribute to a lack of templates in this region. The signals with mass-ratios in the interval $[1, 8]$ and effective-spins > 0.75 we find the EOB bank is unable to recover the injections indicating that either there are not enough templates to cover this region *or* the waveform models are sufficiently

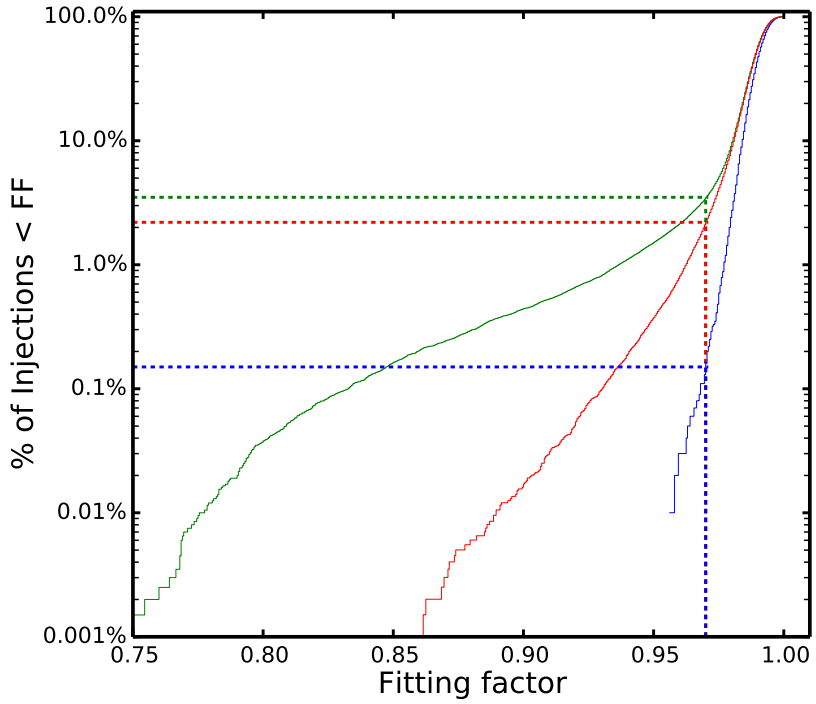

Figure 4.6: Cumulative distributions of the fitting factor. Blue: Run 1, worst FF of 96% Green: Run 2, worst FF of 74%. Red: Run 3, worst FF of 80%. The spit template bank reduces the tail in the distribution by over an order of magnitude at FF= 90% however, the bank is still not effectual to `IMRPhenomD` signals.

different that an EOB template bank would be unable to recover these signals.

We proposed and tested a simple solution to this in Section 4.3.3 where we injected `IMRPhenomD` signals into a bank where templates with $\chi_{\rm eff} > 0.7$ were generated with `IMRPhenomD` and all the others were generated with `SEOBNRv2_ROM`. We found that the performance of the bank does improve towards high spin signals, in particular the minimum recovered FF increases from 74% to 80% and the tail in the recovered FF cumulative distribution is reduced significantly however, the bank is still not effectual. We postulate that adding a relatively small number of `IMRPhenomD` templates to the EOB bank using a stochastic template bank placement algorithm [22] would produce an effectual template bank towards *both* `SEOBNRv2` and `IMRPhenomD`. We note that a similar hybrid bank has already being used in the analysis of O1 data, where the `TaylorF2` inspiral-only approximant was used for systems with a total mass $M \leqslant 4M_{\odot}$.

Nevertheless, the high values for the FF suggest that a matched-filter based search for unequal-mass and high aligned-spin binaries will not suffer a substantial loss in detection efficiency by using `SEOBNRv2_ROM` over `IMRPhenomD` as templates in this region. From this highly idealised analysis we estimate the loss in event rate with unequal-mass and high effective spin to be 14%, slightly larger than the typically quoted acceptable value for searches of 10%. However, we should not settle

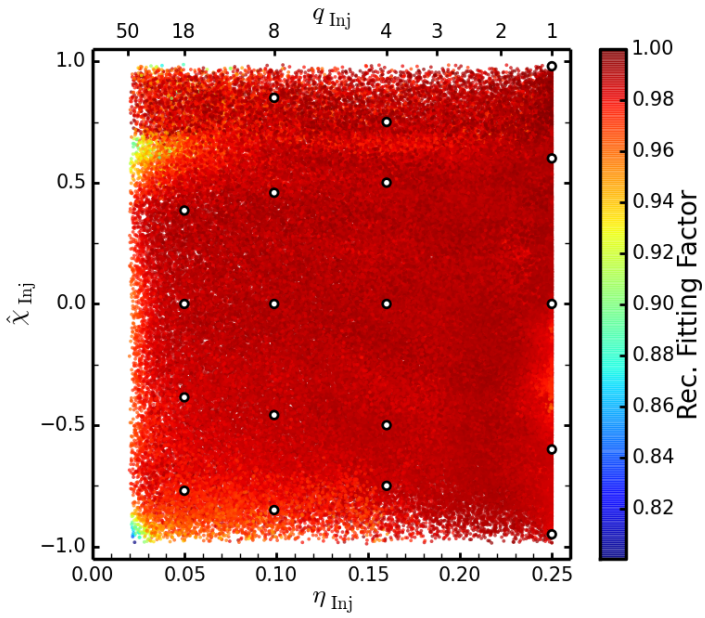

(a)

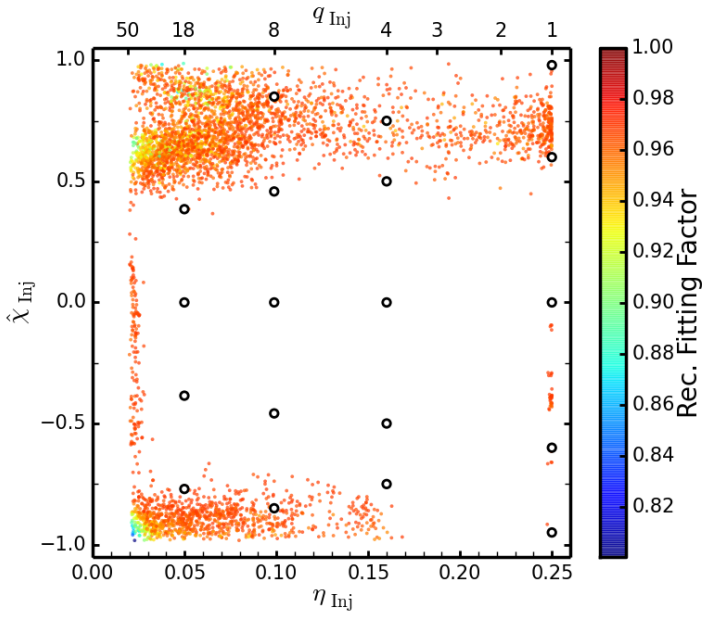

(b)

Figure 4.7: Template bank simulation results for Run 3. Injecting `IMRPhenomD` into a `SEOBNRv2_ROM` template bank that uses `IMRPhenomD` templates for $\chi_{\mathrm{eff}} > 0.7$. The x- and y- axes are the symmetric mass-ratio and the effective spin parameter defined by Equation 3.2 respectively and the colour bar shows the match. The top x-axis is the corresponding mass-ratio. 4.7a: shows results for over the whole range of matches. 4.7b: uses the same colour bar scale but only plots points where the fitting factor is less than 0.97. The overlaid white dots mark the calibration points for `IMRPhenomD`. Using `IMRPhenomD` templates for $\chi_{\mathrm{eff}} > 0.7$ improves the bank's effectualness to `IMRPhenomD`, especially in the high mass-ratio, high aligned-spin region (top left) where the minimum FF (as compared with Run 2) is increased from 74% to 80%.

for this small drop in detection efficiency and improved template banks should be constructed, possibly by investigating the suggestions mentioned above.

4.4 Waveform Model Systematic Errors: BAM:7 Case study

In Chapter 3 we compared IMRPhenomD and SEOBNRv2 not only to each other but also to NR. Figure 3.20 shows the mismatch between unequal mass, high positive spin NR waveforms and both waveform models. We see that for all three cases the maximum mismatch for IMRPhenomD is 0.5% whereas for SEOBNRv2_ROM it is $\sim 11\%$.

In Section 4.3 we investigated the implications of these high mismatches from the SEOBNRv2 model in the context of GW searches and concluded that an EOB template bank is ineffectual to a population of IMRPhenomD signals, specifically when the masses are unequal and the spins are positive and large. However, only marginally ineffectual at the level of 95%, which could be improved by adding more EOB or even IMRPhenomD templates to the regions of poor FF.

We now turn our attention to the estimation of GW signal parameters. In this context there is a stricter requirement on the level of fidelity of waveform models to the true GW signal, it is here were we expect differences between waveform models to manifest themselves as systematic biases in recovered parameters.

4.4.1 Method

In this section we will test the ability of our IMR models to determine the system parameters of a GW signal by performing a full bayesian parameter estimation study. To quantify this we will use the NR waveform BAM:7 described in Section 2.3[6] as our target signal. This is a mass-ratio 1:4 BBH system with aligned-spins $\chi_1 = \chi_2 = 0.75$. It should also be noted that this NR waveform *was* used to calibrate IMRPhenomD. We choose this as our signal waveform because it resides in the region of parameter space where the two most accurate current waveform models (SEOBNRv2 and IMRPhenomD) disagree. We also have estimated the accuracy of this NR waveform, quantified by computing the mismatch between different numerical resolutions, to be no higher than 0.015% (Figure 3.2), which we expect to be sufficiently accurate for GW data analysis studies of advanced detector data.

The parameter space for non-eccentric, non-precessing BBH systems is 11 dimensional. This is far too large to use naive grid-based methods, which is why stochastic sampling methods such as Markov chain Monte Carlo are used to cleverly explore the high dimensional parameter space and home in on regions of high posterior probability. We use the GW parameter estimation library LALInference [172] to sample this large parameter space with the code LALInferenceNest [171],

[6] This simulation is also designated as A10 during the construction of IMRPhenomD in Chapter 3

which implements the nested sampling algorithm to compute posterior probability densities.

In the Bayesian framework $\mathcal{P}(\theta|s)$ is the *posterior* estimate for the model parameters, θ, given the data, s, determined by evaluating the *likelihood* function $\Lambda(s|\theta)$. Through Bayes' theorem,

$$\mathcal{P}(\theta|s) \propto \Lambda(s|\theta)\pi(\theta)\,, \tag{4.1}$$

the posterior is proportional to the likelihood multiplied by the function $\pi(\theta)$, called the *prior*. The proportionality factor is called the *evidence*, which ensures that the right hand side is normalised to unity. As we will be comparing posterior probability density functions and not performing a model selection analysis we can ignore this factor. The likelihood function takes as input the data (injected NR waveform) and the prediction of the data from a model, in this case either from `SEOBNRv2` or `IMRPhenomD`. The values returned are proportional to the probability that the model matches the data. The prior $\pi(\theta)$ encapsulates your current state of knowledge about the parameters, θ. Throughout the calculation parameters that do not match the data well are down-weighted accordingly. The final posterior distribution represents the final state of the prior, which has been driven by the data.

To derive the appropriate form of the likelihood function we start off by assuming that the background detector data are both stationary and Gaussian, following [122]. We can then express the expected probability distribution for this process using our standard inner-product (Eq. (1.67)) as

$$\Lambda(s|\theta) = \exp\left\{-(n|n)/2\right\}\,. \tag{4.2}$$

To arrive at the likelihood function in terms of our model we simply re-write the argument of the inner-product in Eq. (4.2) assuming that the detector data could also contain a GW component as well as the persisting noise component. Rearranging Eq. (1.64) for n and substituting into Eq. (4.2) we get

$$\Lambda(s|\theta) = \exp\left\{-(s-h(\theta)|s-h(\theta))/2\right\}\,, \tag{4.3}$$

where $h(\theta)$ is our prediction for the GW with parameters θ.

In this study we are primarily concerned with the systematic error of waveform models and so we chose to generate frame files[7] in "zero-noise". This means that the time series in the frame file only contains the strain data. If we denote the $s = h_{\rm NR}$ with parameters $(\theta_{\rm NR})$ as the injected NR waveform then Eq. (4.3) reduces to

[7] Gravitational wave frame files (file extension `.gwf`) are standard file formats for GW data, which can be read by LIGO analysis pipelines. We create the frame files using `pyCBC` [7].

case	$m_1\,(M_\odot)$	$m_2\,(M_\odot)$	$q\,(\eta)$	M $(M_\odot)$	χ_{1z}	χ_{2z}	$\chi_{\rm eff}$
BAM:7	64	16	4 (0.16)	80	0.75	0.75	0.75
α	δ	ψ (rad)	$f_{\rm low}$ (Hz)	modes	SNR	ι (rad)	d_L (Mpc)
-1.26157	1.9497	1.42892	24	$\ell \leqslant 5$	25	0	1572

Table 4.5: Injection parameters. Upper table lists the NR configuration name as used in Chapter 2 and the intrinsic parameters for the injection. The lower table lists the extrinsic parameters of the injection. The inclination angle ι is defined to be the angle between $\hat{\mathbf{L}}$ and the line of sight $\mathbf{N}$, the vector connecting the detector to the system. All injections were made with a matched filter network SNR of 25. At $80M_\odot$ the lowest frequency for this NR waveform is ~ 24 Hz.

$$\Lambda(s|\theta) = \exp\left\{-(h_{\rm NR} - h(\theta)|h_{\rm NR} - h(\theta))/2\right\} . \tag{4.4}$$

We use a model for the noise curve when performing overlaps to compute the likelihood function. Again this is to eliminate the ambiguity in the results due to noise realisations. Specifically we use the "zero-detuned high-power" (zdethp) spectrum, which is the design goal of aLIGO that is anticipated by 2019-20 [8] however, we fix the lower cut-off frequency to 30 Hz to mimic the performance of the detectors duing O1. We also use this noise curve to compute the amplitude of the injected waveform for a given SNR.

Table 4.5 shows the source parameters for the injection. We inject the mass-ratio 1:4 system at a total mass of 80 $M_\odot$, for this NR waveform this places the lowest GW frequency at 24 Hz. Due to the high dimensionality of the problem we are unable to do an in-depth study so instead we focus on the most optimistic case in terms of detection and inject our NR waveform with $\iota = 0$, i.e., face-on, as this configuration would have the largest horizon distance for any extrinsic parameter. For this face-on configuration the polarisation angle is irrelevant and the sky position was chosen at random. For comparison with GW150914 we inject our signal at matched filter network SNR[8] of 25 placing the source at a distance of 1572 Mpc. In the injected NR waveform we include all multipoles up to and including $\ell = 5$, however, as the binary is face-on the contribution from the higher modes is small. We choose our prior distribution to be uniform for all parameters, allowing component masses between $[10, 200]\,M_\odot$. We also allow the spins to take any value within the limitations of the model, for `SEOBNRv2` this is $[-0.99, 0.99]$ and for `IMRPhenomD` it's $[-1, 1]$.

4.4.2 Results

Using the `LALInferenceNest` code we obtained marginalised posterior distribution functions with 16000 and 20000 samples for the `SEOBNRv2_ROM` and `IMRPhenomD` runs respectively. Table 4.6 presents the results from both runs.

[8]The network SNR the quadrature sum of the individual detector SNRs, i.e., $\rho_N^2 = \rho_H^2 + \rho_L^2$

To quantify the results we compute median values of the marginalised posteriors for each intrinsic parameter and quote the 1D 90% credible interval (CI) as our uncertainty. In brackets after each result in the table we also quote the percentage bias as well as the N-σ error[9]. The first column shows the true, injected values and the second and third columns show the SEOBNRv2_ROM and IMRPhenomD results respectively. The results for the SEOBNRv2_ROM run show biases of at most $\sim 18\%$ with the most accurate parameter recovered being $\mathcal{M}_c$ with a bias of 1.6%. It is surprising, given the high total mass of the injection that the chirp mass is recovered with more accuracy than the total mass, which was recovered with a bias of 4.6%.

Even though the size of the 90% CI is approximately the same the computed biases from the IMRPhenomD run are much smaller. The maximum bias[10] is 3% with the chirp mass recovered to an accuracy of 0.3% and the total mass to 1.5%.

Whereas the estimates for the component masses from the IMRPhenomD run are within 2% of injected value we see that SEOBNRv2_ROM tends to overestimate the primary mass and underestimate the secondary mass by about 8%. This combines to produce an underestimation of the symmetric mass-ratio of 0.144 opposed to the injected value of 0.16 however, the injected value is not excluded at 90% confidence.

In GW astronomy we do not expect to be able to measure the individual BH spins [147], instead we are sensitive to a combination of the spins, $\chi_{\rm eff}$ (Eq. (1.59)). The effective spin parameter is constrained by the 90% confidence interval to approximately the same degree as the masses. The IMRPhenomD results are symmetrically distributed around the median value, which was estimated to be the injection value to an accuracy of one part in 10^4. The median value for $\chi_{\rm eff}$ from SEOBNRv2_ROM is slightly shifted towards higher values and the injected value lies just within the 90% CI.

We also quote results for the two individual spins. For the SEOBNRv2_ROM results we see that the primary and secondary BH spins are quite similar to that of $\chi_{\rm eff}$, however, the size of 90% CI for the second spin is much larger, which indicates that this spin component is much less constrained than the primary spin, consistent with the study in Ref [147]. On the other hand as IMRPhenomD is a single spin model during the merger-ringdown[11] it predicts that the spin is distributed unevenly between the two BHs. However, the posteriors for the second spin for both SEOBNRv2_ROM and IMRPhenomD and fairly uninformative, represented by the large 90% CIs, only slightly favouring high spins. This is a manifestation of the unfortunate fact that the prospect for determining the spin of the second, smaller BH is small.

If we take the width of the 90% CIs as an indication of the statistical uncertainty

[9] If we denote the absolute bias for parameter X as $\Delta X \equiv X_{\rm rec} - X_{\rm inj}$ then the percentage bias is simply $\Delta X/X_{\rm inj} \times 100$. The N-$\sigma$ uncertainty is calculated as the absolute bias divided by the width of the 90% CI, $X^{90\%}$, multiplied by the appropriate standard deviation weight. For a 90% CI this corresponds to 3.29σ. The N-σ for each parameter is calculated as $3.29 \times \Delta X/X^{90\%}$.

[10] We ignore the individual component spins when quoting the maximum bias as this is an effective single spin model during the merger-ringdown and as such only sensitive to $\chi_{\rm eff}$.

[11] The model is actually a two-spin model during the early inspiral, see Chapter 3

Parameter	Injected Value	SEOBNRv2_ROM	IMRPhenomD
$m_1/M_\odot$	64	$69.09^{+9.89}_{-7.21}$ (8%, 0.98)	$65.3^{+8.15}_{-6.08}$ (2%, 0.3)
$m_2/M_\odot$	16	$14.67^{+1.19}_{-1.19}$ (8.3%, 1.83)	$15.83^{+1.66}_{-1.75}$ (1.1%, 0.16)
$M/M_\odot$	80	$83.69^{+9.05}_{-6.13}$ (4.6%, 0.8)	$81.21^{+6.55}_{-4.98}$ (1.5%, 0.35)
$\mathcal{M}_c/M_\odot$	26.64	$26.22^{+0.93}_{-0.7}$ (1.6%, 0.84)	$26.71^{+0.96}_{-0.92}$ (0.3%, 0.13)
η	0.16	$0.144^{+0.018}_{-0.019}$ (10%, 1.41)	$0.157^{+0.018}_{-0.022}$ (1.9%, 0.24)
q	4	$4.72^{+1.09}_{-0.8}$ (18%, 1.25)	$4.12^{+1.0}_{-0.7}$ (3%, 0.22)
$\chi_{\rm eff}$	0.75	$0.81^{+0.08}_{-0.07}$ (8%, 1.24)	$0.75^{+0.06}_{-0.06}$ (0%, 0.01)
a_1	0.75	$0.82^{+0.08}_{-0.09}$ (9.3%, 1.28)	$0.81^{+0.14}_{-0.11}$ (8%, 0.76)
a_2	0.75	$0.81^{+0.17}_{-0.33}$ (8%, 0.36)	$0.6^{+0.37}_{-0.52}$ (20%, 0.57)

Table 4.6: Parameter estimation results for intrinsic source parameters. The second column shows the injected value and the third and fourth columns show the SEOBNRv2_ROM and IMRPhenomD results respectively. To quantify the results we quote the median value of the 1D marginalised posterior density functions and quantify the uncertainty using the 90% credible interval. In brackets we also quote percentage biases computed using the median values as well as the N-σ error. The source inclination for this injection was $\iota = 0$ (face on)

in the measurement of a parameter and the difference between the true value and the median value as the systematic uncertainty then for all parameters the systematic uncertainty is less than the statistical uncertainty. The exception to this is m_2 for SEOBNRv2_ROM for which the true value lies marginally outside the 90% CI by 0.88%.

Figure 4.8 shows the plane of 1D marginalised posteriors for component masses (top panel) and for the $(\chi_{\rm eff}, \eta)$ plane (bottom panel). The injected value to marked by the yellow star in the plane and by the yellow dashed lines on the 1D marginalised histograms. The results from SEOBNRv2_ROM and IMRPhenomD are shown in red and blue respectively, where contours are the 90% credible regions (CRs) and the red and blue dashed lines on the histograms are the 90% CIs. Whereas IMRPhenomD has histograms that are relatively symmetrical centred about the injected value the SEOBNRv2_ROM results show slightly skewed posteriors shifted away from the injected value. The injected value lies in approximately the centre of the 90% credible region for IMRPhenomD indicating that the systematic errors are smaller than the statistical however, the converse is true for the SEOBNRv2_ROM results where the injected value lies near the edge of the 90% credible region. These results suggest that at higher SNRs the systematic errors for SEOBNRv2_ROM would be larger than the statistical errors for systems similar to the injected one, i.e., mass-ratio 1:4 and aligned-spin of 0.75.

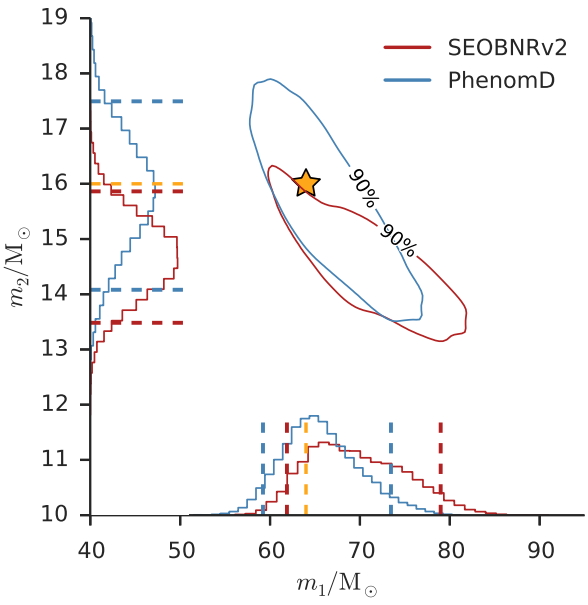

(a)

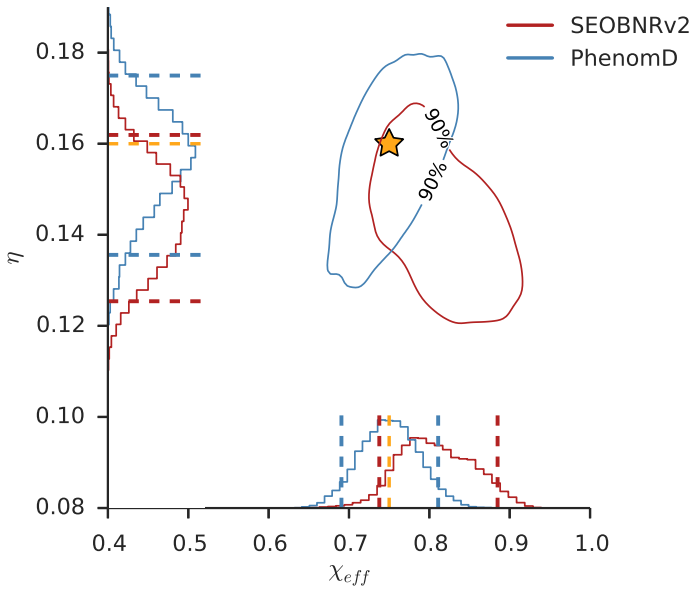

(b)

Figure 4.8: Posterior probability density functions for component masses (top panel) and the $(\chi_{\rm eff}, \eta)$ plane (bottom panel). The histograms are 1D marginalised distributions and the contours mark the 90% credible regions for `SEOBNRv2_ROM` (red) and `IMRPhenomD` (blue). The red and blue dashed lines on the histograms mark the 90% credible intervals and the yellow dashed line and star mark the injected values.

4.4.3 Summary

In this section we have quantified the size of the statistical and systematic uncertainty in the measurements of intrinsic binary parameters using the Bayesian inference code `LALInferenceNest`. Our analysis focused on the `BAM:7`[12] mass-ratio 1:4, high aligned spin ($\chi_{\rm eff} = 0.75$) BBH system because our previous analysis (see Chapter 3) found the typical accuracy requirement for waveform models was violated by the `SEOBNRv2_ROM` model at the level of $\sim 11\%$ whereas `IMRPhenomD` is faithful at the level of 0.5%.

We find that the relatively low match ($\sim 11\%$) does impact the resulting posterior distributions, although perhaps not as much as perhaps one would have thought. For all intrinsic parameters the injected value lies within the 90% CI of the marginalised probability distributions for both `SEOBNRv2_ROM` and `IMRPhenomD`, which indicates that the statistical uncertainty, at this SNR, is greater than the systematic uncertainty from the model. The exception to this is m_2 for `SEOBNRv2_ROM` for which the true value lies marginally outside the 90% CI by 0.88%. As expected, from the known level of faithfulness of the models to the NR waveform, the systematic error[13] is smaller for `IMRPhenomD` than `SEOBNRv2_ROM`, by a factor of 3-6 times.

If we assume that the width of the 90% CI scales inversely with SNR then from our results we can estimate the SNR at which the systematic uncertainty will be larger than the statistical uncertainty. This study injected a signal at SNR=25, for a SNR of twice the size we expect the width of the 90% CI to half. If we further assume that the median values will not change then at SNR=50 the unfaithfulness of `SEOBNRv2_ROM` will cause the systematic errors to be larger than the statistical errors whereas `IMRPhenomD`'s estimate will remain within the predicted 90% CI.

As we have seen for the parameter estimation of GW150914 [17] the models `SEOBNRv2_ROM` and `IMRPhenomPv2`[14] can agree very well with each other in regions of parameter space where both models have been tuned to NR. We emphasise that predicting the effect on parameter estimation due to modelling error is non-trivial and could very well result in larger (or smaller) systematic biases in different parts of the parameter space, for example waveforms that extend to lower frequencies.

In this section we have shown that if a future GW event, with high enough SNR, is in a region of the parameter space where our models do not perform accurately then the systematic uncertainty could be larger than the statistical uncertainty. While for this case `IMRPhenomD` is more faithful than `SEOBNRv2_ROM` to the injected signal the situation could be reversed or in the worst case *both* models could fail to accurately recover the injected parameters. To prepare for the future we must continue to extend waveform models to larger regions of the parameter space, which implies the need for more NR simulations in unexplored regions of the parameter

[12] See Chapter 2
[13] The difference between the median value and the injected value
[14] Note that the underlying model for `IMRPhenomPv2` is `IMRPhenomD`.

space. We must continue to compare our waveform models to the latest NR results as well as to each other. Multiple approaches are valuable to gauge the accuracy of the models. Knowing which waveform models are accurate in which regions of parameter space will be key in helping to draw reliable conclusions from real GW events.

Finally, this study is restricted to aligned-spin injections and parameter recovery with IMRPhenomD and SEOBNRv2_ROM. Future work could extend this to investigate the effect of precession on parameter estimation.

Chapter 5

Conclusions

The beginning of gravitational wave astronomy started on September 14$^{\text{th}}$, 2015 [13]. The *event*, GW150914, was so loud that the distinct morphological features indicative of the merger of two inspiraling black holes was difficult to deny, see Figures 1 and 2. GW astronomy has already provided new astrophysical information from its first observation [10]. The final BH is measured to have a mass of $62\,M_{\odot}$ and a spin of 67% of its maximum possible value. The two merging BHs, with masses $36\,M_{\odot}$ and $29\,M_{\odot}$, along with the final BH, are all individually heavier than any other stellar mass BH inferred from electro-magnetic observations [129, 81]. Unfortunately, the spin measurements of the inspiraling BHs and also evidence for precession are not constrained well. These measurements of BBH system parameters [17] and the first tests of strong field general relativity [15] both used models for the gravitational wave signal from the inspiral, merger and ringdown of binary black hole coalescences derived from this thesis.

The main result of this thesis is the construction of a highly accurate gravitational waveform model (`IMRPhenomD`) to predict the dominant harmonic from the inspiral, merger and ringdown of binary black holes with spin either aligned or anti-aligned with the orbital angular momentum, for a wide range of mass-ratios. Our model improves on previous models by using a set of NR simulations that cover a greater area of parameter space, and more sophisticated modelling methods, which raises the accuracy standard for future phenomenological models. By expanding the calibration set we also push NR codes into unexplored regions of parameter space such as simulating systems with mass-ratios up to 1:18 with aligned-spin during their late-inspiral through merger. Our new model is calibrated to a relatively conservative number of 19 NR waveforms distributed almost evenly throughout our parameter space and was tested against a larger set of 29 NR waveforms. For all cases considered the model is highly accurate with mismatches of at most 1% and many with mismatches of 0.05%, see Figure 3.16, and therefore fulfilling the simple accuracy criteria discussed in Chapter 1.6.2.

In a problem as complicated as this where solutions rely on numerical methods

and many different approximations can be made to find approximate solutions, having a diverse set of techniques to solve the same problem is invaluable to validate our methods. The development of our model allowed us to perform, for the first time, systematic comparisons across large regions of parameter space with the alternative EOB-based model; the results are presented in Chapters 3 and 4. The leading aligned-spin models from the phenomenological[1] and EOB[2] modelling programs were found to agree with each other to a remarkably high degree over a very large portion of the parameter space, even in regions where both models are extrapolated beyond their respective calibration regions. This agreement lent great confidence to the parameter measurements of GW150914. That being said there are still regions of parameter space where the models disagree. This is most noticeable for systems with unequal masses and high aligned-spins ($\chi \gtrsim 0.7$). In this region where we have NR simulations we find `IMRPhenomD` to be the faithful model, however, the EOB model could be recalibrated to NR simulations in this region to (hopefully) improve the accuracy of the model in this region. Results such as this guide the placement of future NR simulations and when they are available both modelling efforts can recalibrate their models to further improve their accuracy, which impacts GW searches and also the analysis of GW candidate events.

The larger than expected mismatch of `SEOBNRv2` towards unequal masses and high aligned-spin systems prompted the study in Chapter 4.3 to determine if the loss in optimal SNR would cause an EOB template bank to not recover `IMRPhenomD` signals above FF = 97%. Using a template bank representative of the one used in the analysis of O1 data we found the template bank to be ineffectual to `IMRPhenomD` in this unequal-masses and high aligned-spins region, though only at the level of FF = 95% corresponding to a loss of detection rate of 14% as opposed to the usually quoted acceptable value of 10%. Our suspicion is that template banks could be improved to become effectual to both `SEOBNRv2` and `IMRPhenomD` with a negligible cost to search sensitivity or computation cost by adding `IMRPhenomD` templates to fill the holes in the EOB bank.

In Chapter 4.4 we investigated the size of the systematic biases of `IMRPhenomD` and `SEOBNRv2` by performing full Bayesian parameter estimation on an injected NR signal. We targeted the unequal-mass, high aligned-spin region and injected the mass-ratio 1:4, $\chi_{\rm eff} = 0.75$ `BAM:7` waveform in to zero-noise. We find that the systematic errors, in this region of parameter space, for `IMRPhenomD` is no more than 3% for intrinsic parameters in contrast to `SEOBNRv2_ROM` where the bias in recovered parameters can be as high as 18% favouring larger mass-ratios and higher BH spins. However, at the injected SNR of 25 both models' posterior probability density functions include the injected value within their 90% CIs albeit for `SEOBNRv2_ROM` this is marginally true. Further more we estimate that the systematic errors for

[1] `IMRPhenomD`
[2] `SEOBNRv2`

`IMRPhenomD` will remain smaller than the statistical errors at SNRs as high as 50 but the same may not be true for `SEOBNRv2_ROM`.

To be useful in GW astronomy applications waveform models have to be computationally efficient to evaluate. As phenomenological models are composed of closed-form analytic expressions, they are typically very fast to evaluate. On the contrary, EOB models require numerical integration of ODEs to compute the waveform, which prohibit their use in typical parameter estimation studies requiring $\mathcal{O}(10^6)$ waveform evaluations per analysis. To reduce the computational cost of waveform models such as EOB models, the techniques of reduced-order-modelling (ROM) have been very successful to create surrogate waveform models in both the time and frequency domain [146, 83], which have allowed them to be utilised in the analysis of advanced detector data. More recently, similar methods have been applied directly to NR waveforms [41], which is opening up a promising new avenue to modelling NR alongside phenomenological and EOB methods. Specifically in the context of parameter estimation, the likelihood calculation can be speeded up significantly by expressing the calculation as a reduced-order-quadrature (ROQ) summation [58]. With the reduced-order quadrature (ROQ) method it will be possible to perform parameter estimation on a significantly shorter timescale.

Inference from GW signals relies on waveform modelling. To extract the maximum information from GW observations we must develop waveform models to accurately predict the GW signal, which incorporate all the physical effects that we think are relevant. Though we hope that the methods presented here will be robust enough to handle future data sets that explore further reaches of the parameter space in reality it is likely to be the case, as we found when going from `IMRPhenomC` to `IMRPhenomD`, that in order to accurately model new regions of the parameter space new techniques will have to be developed. A natural extension of the `IMRPhenomD` model is to include the higher modes of the data set. While we hope that most of our techniques can be applied to higher modes there are known added complexities such as mode-mixing in the $(\ell, m) = (3, 2)$ mode during the ringdown. Directly applying our current methods would not be able to reproduce this feature of the data. Extending the inspiral model to higher modes poses a different challenge. Our inspiral model relies on having an accurate inspiral prescription to construct hybrid waveforms. In Ref. [100] we determined that EOB models were required to construct accurate hybrid waveforms. As there is currently no aligned-spin EOB model for higher modes another strategy would have to be used until such an EOB becomes available.

The first precessing IMR models from the phenomenological [91] and EOB [137] programs have recently been developed. These models are derived from an underlying aligned-spin model where the effect of precession on the waveform is encoded through time or frequency dependent rotations given by PN or EOB calculations. While they both represent breakthroughs in the treatment of precession, they are

limited in terms of their accuracy, validity across the parameter space, physical content and computational cost. These models define the state-of-the-art and are heavily used in the analysis of advanced detector data. However, due to the infancy of these precessing models a complete analysis of their accuracy and of the size of their inherent systematic errors has not been performed. This directly impacts the conclusions we draw from using them in analysis of GW candidate events. Investigating this is of the utmost importance if we wish to confidently answer questions about the astrophysics of compact body formation and evolution such as the existence of a mass-gap [81, 115] or the presence of an "in-plane" spin, which drives the precessional dynamics. Each piece of information we derive from our measurements of GW events is extremely valuable and adds to our understanding of the physical processes in the Universe. It is important that we do not draw biased conclusions due to our lack of understanding the limitations of our own models.

The ultimate goal in the coming years is to improve the accuracy of precessing IMR models. With accurate aligned-spin models developed as strong foundations of precessing models the main focus will be on improving how the precession is included. Currently in the phenomenological precessing model the precession of the orbital plane is modelled by closed-form frequency domain PN expressions. Initial comparisons with NR imply that the accuracy of these expressions do not extend to the entire calibration region of the underlying aligned-spin model. This restricts the precessing model to be useful to only a small subset of the parameter space of the underlying model. A natural extension is to extract these expressions from NR simulations and attempt to improve the accuracy of the PN expressions by calibrating them to NR in an analogous manner to the phenomenological modelling of the amplitude and phase.

The next advanced LIGO observing run (O2) is due to start during Summer 2016. As well as observing for 6 months[3] with an improved sensitivity, the advanced Virgo detector is scheduled to join the network, which will improve the network's ability to localise the source of GW events. During O2 we expect to detect many more BBH signals and hopefully signals from other sources such as binary neutron stars and mixed neutron star-black hole binaries. The simultaneous detection of an electro-magnetic counterpart to a GW event will start the field of multi-messenger astronomy and could be the key to answering the mysterious origins of gamma-ray bursts.

The confidence we place in our conclusions from the data and the astrophysics we shall infer will rely on the fidelity of our waveform models. To accelerate future development of waveform models it is important to strengthen the collaboration between waveform modellers and numerical relativists. The relationship between them drives progress in both areas and together they play a critical role in gravitational wave astronomy.

[3] 50% longer than the initial observing run, O1

Appendices

Appendix A

Chapter 3 Appendix

A.1 Time-domain conversion

Our `IMRPhenomD` model is formulated entirely in the frequency domain, which is a great advantage for performing fast GW searches and parameter estimation studies. However, our construction process started with data in the time domain, and physical signals are smooth functions in *both* the frequency and time domain. Therefore, it is desirable to check how our model transforms from the frequency domain back into the time domain via a straightforward inverse Fourier transformation.

This serves also as an independent, powerful sanity check. The previous PhenomC model [151], for instance, quickly develops a pathological behavior in the time domain once the parameters leave the calibration region, which is a result of steep transitions caused by extrapolating fitting coefficients. We do not find these features for our new `IMRPhenomD` model.

Before applying the inverse Fourier transformation, we multiply our model with a variant of the Planck taper function [125],

$$\mathcal{T}(f) = \begin{cases} 0, & f \leq f_1 \\ \left[\exp\left(\frac{f_2-f_1}{f-f_1} + \frac{f_2-f_1}{f-f_2}\right) + 1\right]^{-1}, & f_1 < f < f_2 \\ 1, & f > f_2 \end{cases},$$

where f_2 is the smallest frequency that we want to represent in the time-domain data (which become infinitively long for $f_2 \to 0$). In order to avoid a sharp transition, which would introduce unphysical oscillations, $\mathcal{T}$ uses an extra cushion, $f \in (f_1, f_2)$, in which the frequency domain amplitude smoothly increases from zero to their correct value. We typically set $f_1 = 0.8 f_2$.

We perform the Fourier transformation numerically, which requires us to define a suitable sampling rate in the time and frequency domain. From our model, we find that the amplitude has dropped several orders of magnitude for frequencies $Mf > 0.25$, so we can choose any sampling with $\Delta t/M < 2$ which in turn is solely

determined by the largest frequency we include in our frequency-domain data.

The frequency-domain sampling, on the other hand, is determined by the total length of the signal in the time domain, which is information we do not have a priori access to. However, in the spirit of the stationary-phase approximation that typically relates the time-domain phase derivative to the frequency ($d\phi(t)/dt \approx 2\pi f$), we approximate

$$\frac{d\phi(f)}{df} = \phi'(f) \approx 2\pi t, \tag{A.1}$$

$$\Rightarrow \quad \Delta f < \frac{1}{t_{\max} - t_1} \approx \frac{\pi}{|\phi'(f_{\max}) - \phi'(f_1)|}. \tag{A.2}$$

In (A.2), we have introduced an extra factor of $1/2$ to account for the negative-frequency content of real-valued signals (just like in the usual sampling theorem), and when choosing Δf we usually apply another factor of $1/2$ as safety margin.

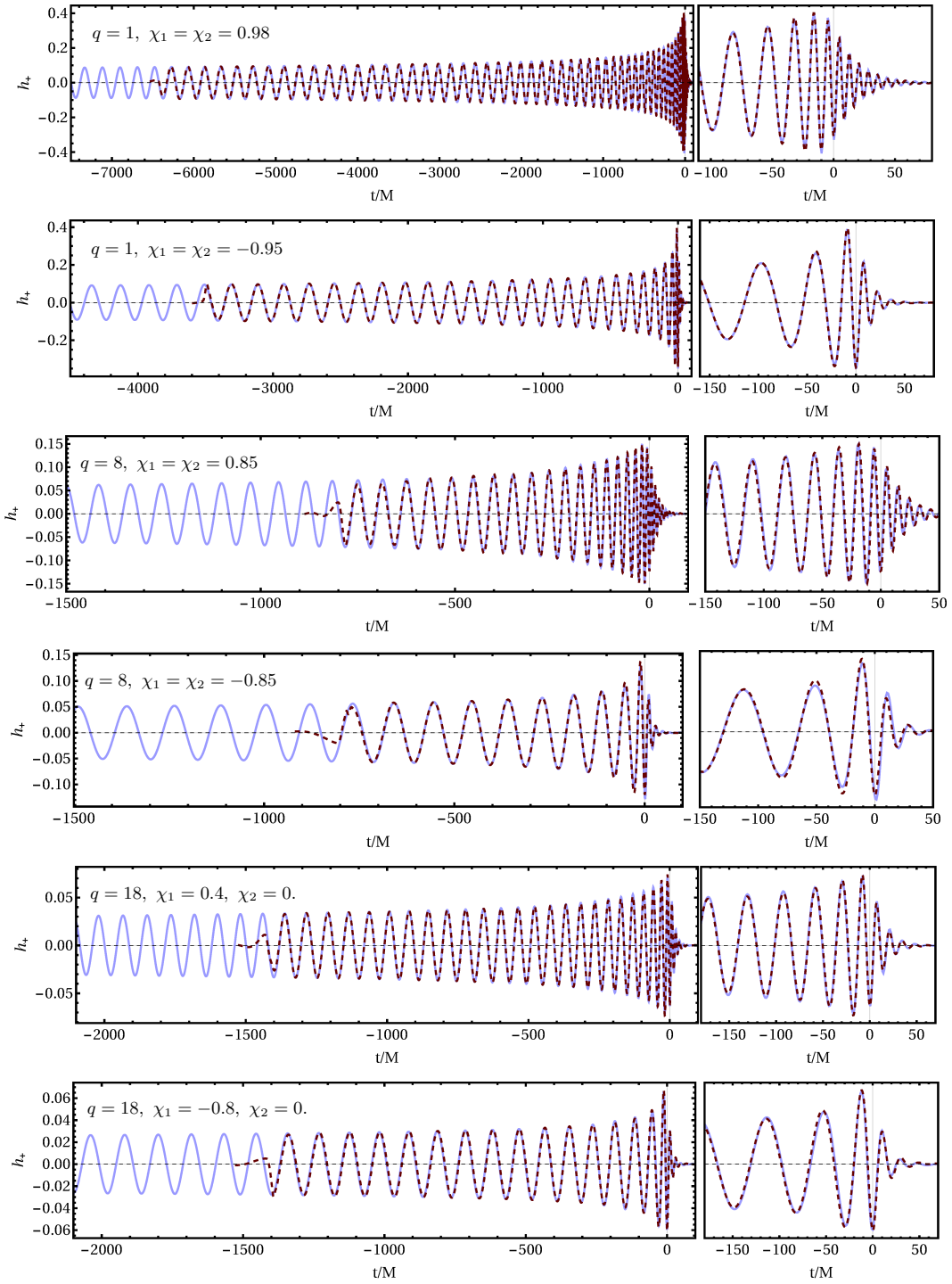

Figure A.1: Time-domain `IMRPhenomD` waveforms (solid, light blue online) and NR waveforms (dashed, red online) for corners of the parameter space used for calibration. We plot the plus polarization h_+ normalized by the extraction radius, and the binary's parameters are indicated by the mass ratio $q = m_1/m_2$ and the two spin parameters χ_1, χ_2.

The time-domain waveforms we obtain this way can be compared to the original NR data, and for corners of the parameter space used for calibration we show the results in Fig. A.1. Note that a small overall time and phase shift was applied to the model, as these parameters are not meant to faithfully capture the arbitrary choices made in the original NR simulations. No other optimization has been applied. The agreement visible in Fig. A.1 throughout the late inspiral, merger and ringdown is remarkable and a strong indication (in additional to the matches presented in Sec. 3.9.1) that our hybridization, fitting and interpolation procedures accurately represent the original data.

In addition to complementing the model validation, we may also use the time-domain representations as a visual sanity check, even outside the model's calibration region. As mentioned above, this proved to be a powerful test of the previous PhenomC model that failed to produce reasonable time-domain waveforms in many parts of the parameter space outside its calibration range. `IMRPhenomD`, however, does not show any pathological behavior outside its calibration region, neither in the time nor frequency domain. We illustrate this fact in Fig. A.2 by showing a case where the model parameters have been extrapolated to mass ratio 50 and near-extremal spins $\chi_1 = \chi_2 = 0.99$. While such a plot is by no means a guarantee that the waveforms are accurate in this regions of the parameter space, it is reassuring that our new model is much more robust in its extrapolation, which will allow GW search algorithms to use our model slightly outside its calibration region, even if we cannot vouch for the level of accuracy there.

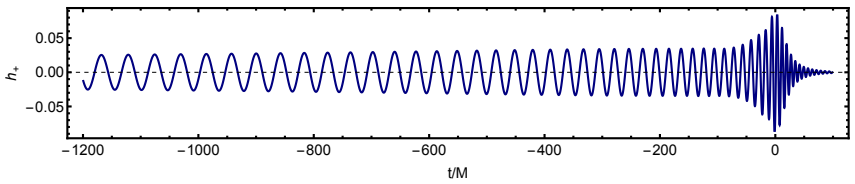

Figure A.2: Time-domain representation of the `IMRPhenomD` model outside its calibration region, here for mass ratio 50 and spin parameters of $\chi_1 = \chi_2 = 0.99$.

A.2 PN coefficients

For the convenience of the reader, we list below the PN coefficients implemented in our model. We incorporated spin-independent corrections up to 3.5PN order ($i = 7$) [54, 42], linear spin-orbit corrections up to 3.5PN order [43] and quadratic spin corrections up to 2PN order [140, 32, 126]. Our re-expansion strategy follows the choices made in the current state of the LIGO software library [167] as discussed in Sec. 3.6.1.

Following (3.24), we express the frequency-domain phase as

$$\phi_{\rm TF2} = 2\pi f t_c - \varphi_c - \pi/4 + \frac{3}{128\,\eta}(\pi f M)^{-5/3}\sum_{i=0}^{7}\varphi_i(\Xi)(\pi f M)^{i/3}.$$

The individual masses and spin parameters, m_i and χ_i $(i = 1, 2)$, are encoded in the following parameter combinations,

$$M = m_1 + m_2, \tag{A.3}$$
$$\eta = m_1\, m_2/M^2, \tag{A.4}$$
$$\delta = (m_1 - m_2)/M, \tag{A.5}$$
$$\chi_s = (\chi_1 + \chi_2)/2, \tag{A.6}$$
$$\chi_a = (\chi_1 - \chi_2)/2. \tag{A.7}$$

The expansion coefficients are then given by

$$\varphi_0 = 1, \tag{A.8}$$
$$\varphi_1 = 0, \tag{A.9}$$
$$\varphi_2 = \frac{3715}{756} + \frac{55\eta}{9}, \tag{A.10}$$
$$\varphi_3 = -16\pi + \frac{113\delta\chi_a}{3} + \left(\frac{113}{3} - \frac{76\eta}{3}\right)\chi_s, \tag{A.11}$$

$$\varphi_4 = \frac{15293365}{508032} + \frac{27145\eta}{504} + \frac{3085\eta^2}{72} + \left(-\frac{405}{8} + 200\eta\right)\chi_a^2 - \frac{405}{4}\delta\chi_a\chi_s + \left(-\frac{405}{8} + \frac{5\eta}{2}\right)\chi_s^2, \tag{A.12}$$

$$\varphi_5 = [1 + \log(\pi M f)]\left[\frac{38645\pi}{756} - \frac{65\pi\eta}{9} + \delta\left(-\frac{732985}{2268} - \frac{140\eta}{9}\right)\chi_a + \left(-\frac{732985}{2268} + \frac{24260\eta}{81} + \frac{340\eta^2}{9}\right)\right. \tag{A.13}$$

$$\varphi_6 = \frac{11583231236531}{4694215680} - \frac{6848\gamma_E}{21} - \frac{640\pi^2}{3} + \left(-\frac{15737765635}{3048192} + \frac{2255\pi^2}{12}\right)\eta + \frac{76055\eta^2}{1728} - \frac{127825\eta^3}{1296} - \frac{6848}{63}\log(64\pi M f) + \frac{2270}{3}\pi\delta\chi_a + \left(\frac{2270\pi}{3} - 520\pi\eta\right)\chi_s, \tag{A.14}$$

$$\varphi_7 = \frac{77096675\pi}{254016} + \frac{378515\pi\eta}{1512} - \frac{74045\pi\eta^2}{756} + \delta\left(-\frac{25150083775}{3048192} + \frac{26804935\eta}{6048} - \frac{1985\eta^2}{48}\right)\chi_a + \left(-\frac{25150083775}{3048192} + \frac{10566655595\eta}{762048} - \frac{1042165\eta^2}{3024} + \frac{5345\eta^3}{36}\right)\chi_s. \tag{A.15}$$

As discussed in Sec. 3.6.2 and Sec. IV in [100], our inspiral amplitude model is based on a re-expanded PN amplitude. The expansion coefficients of Eq. (3.26) are given by

$$\mathcal{A}_0 = 1, \tag{A.16}$$

$$\mathcal{A}_1 = 0, \tag{A.17}$$

$$\mathcal{A}_2 = -\frac{323}{224} + \frac{451\eta}{168}, \tag{A.18}$$

$$\mathcal{A}_3 = \frac{27\delta\chi_a}{8} + \left(\frac{27}{8} - \frac{11\eta}{6}\right)\chi_s, \tag{A.19}$$

$$\mathcal{A}_4 = -\frac{27312085}{8128512} - \frac{1975055\eta}{338688} + \frac{105271\eta^2}{24192} + \left(-\frac{81}{32} + 8\eta\right)\chi_a^2 - \frac{81}{16}\delta\chi_a\chi_s + \left(-\frac{81}{32} + \frac{17\eta}{8}\right)\chi_s^2, \tag{A.20}$$

$$\mathcal{A}_5 = -\frac{85\pi}{64} + \frac{85\pi\eta}{16} + \delta\left(\frac{285197}{16128} - \frac{1579\eta}{4032}\right)\chi_a + \left(\frac{285197}{16128} - \frac{15317\eta}{672} - \frac{2227\eta^2}{1008}\right)\chi_s, \tag{A.21}$$

$$\begin{aligned}\mathcal{A}_6 = &-\frac{177520268561}{8583708672} + \left(\frac{545384828789}{5007163392} - \frac{205\pi^2}{48}\right)\eta - \frac{3248849057\eta^2}{178827264} + \frac{34473079\eta^3}{6386688} \\ &+ \left(\frac{1614569}{64512} - \frac{1873643\eta}{16128} + \frac{2167\eta^2}{42}\right)\chi_a^2 + \left(\frac{31\pi}{12} - \frac{7\pi\eta}{3}\right)\chi_s \\ &+ \left(\frac{1614569}{64512} - \frac{61391\eta}{1344} + \frac{57451\eta^2}{4032}\right)\chi_s^2 \\ &+ \delta\chi_a\left(\frac{31\pi}{12} + \left(\frac{1614569}{32256} - \frac{165961\eta}{2688}\right)\chi_s\right)\end{aligned} \tag{A.22}$$

A.3 Phenomenological Coefficients

The values of the coefficients for the mapping functions given in Eq. (3.28) are shown in Tables A.1, A.2 and A.3. These values are calculated under the parameterisation $(\eta, \chi_{\rm PN})$.

Λ^i	λ_{00}	λ_{10}	λ_{01}	λ_{11}	λ_{21}
ρ_1	3931.9	-17395.8	3132.38	343966.	-1.21626×10^{6}
ρ_2	-40105.5	112253.	23561.7	-3.47618×10^{6}	1.13759×10^{7}
ρ_3	83208.4	-191238.	-210916.	8.71798×10^{6}	-2.69149×10^{7}
v_2	0.814984	2.57476	1.16102	-2.36278	6.77104
γ_1	0.0069274	0.0302047	0.00630802	-0.120741	0.262716
γ_2	1.01034	0.000899312	0.283949	-4.04975	13.2078
γ_3	1.30816	-0.00553773	-0.0678292	-0.668983	3.40315
σ_1	2096.55	1463.75	1312.55	18307.3	-43534.1
σ_2	-10114.1	-44631.	-6541.31	-266959.	686328.
σ_3	22933.7	230960.	14961.1	1.19402×10^{6}	-3.10422×10^{6}
σ_4	-14621.7	-377813.	-9608.68	-1.71089×10^{6}	4.33292×10^{6}
β_1	97.8975	-42.6597	153.484	-1417.06	2752.86
β_2	-3.2827	-9.05138	-12.4154	55.4716	-106.051
β_3	-2.51564×10^{-5}	1.97503×10^{-5}	-1.83707×10^{-5}	2.18863×10^{-5}	8.25024×10^{-5}
α_1	43.3151	638.633	-32.8577	2415.89	-5766.88
α_2	-0.0702021	-0.162698	-0.187251	1.13831	-2.83342
α_3	9.59881	-397.054	16.2021	-1574.83	3600.34
α_4	-0.0298949	1.40221	-0.0735605	0.833701	0.224001
α_5	0.997441	-0.00788445	-0.0590469	1.39587	-4.51663

Table A.1: Coefficient values for linear in $\chi_{\rm PN}$ and $\chi_{\rm PN}$ independent terms for the mapping functions given in Eq. (3.28). These values are calculated under the parametrisation (η, $\chi_{\rm PN}$).

Λ^i	λ_{02}	λ_{12}	λ_{22}
ρ_1	-70698.	1.38391×10^{6}	-3.96628×10^{6}
ρ_2	754313.	-1.30848×10^{7}	3.64446×10^{7}
ρ_3	-1.98898×10^{6}	3.0888×10^{7}	-8.39087×10^{7}
v_2	0.757078	-2.72569	7.11404
γ_1	0.00341518	-0.107793	0.27099
γ_2	0.103963	-7.02506	24.7849
γ_3	-0.0529658	-0.992379	4.82068
σ_1	-833.289	32047.3	-108609.
σ_2	3405.64	-437508.	1.63182×10^{6}
σ_3	-3038.17	1.87203×10^{6}	-7.30915×10^{6}
σ_4	-22366.7	-2.50197×10^{6}	1.02745×10^{7}
β_1	138.741	-1433.66	2857.74
β_2	-11.953	76.807	-155.332
β_3	7.15737×10^{-6}	-5.578×10^{-5}	1.91421×10^{-4}
α_1	-61.8546	2953.97	-8986.29
α_2	-0.17138	1.71975	-4.53972
α_3	27.0924	-1786.48	5152.92
α_4	-0.0552029	0.566719	0.718693
α_5	-0.0558534	1.75166	-5.99021

Table A.2: Coefficient values for quadratic in $\chi_{\rm PN}$ terms for the mapping functions given in Eq. (3.28). These values are calculated under the parametrisation (η, $\chi_{\rm PN}$)

Λ^i	λ_{03}	λ_{13}	λ_{23}
ρ_1	-60017.5	803515.	-2.09171×10^{6}
ρ_2	596227.	-7.42779×10^{6}	1.8929×10^{7}
ρ_3	-1.4535×10^{6}	1.70635×10^{7}	-4.27487×10^{7}
v_2	0.176693	-0.797869	2.11624
γ_1	0.000737419	-0.0274962	0.0733151
γ_2	0.030932	-2.6924	9.60937
γ_3	-0.00613414	-0.384293	1.75618
σ_1	452.251	8353.44	-44531.3
σ_2	-7462.65	-114585.	674402.
σ_3	42738.2	467502.	-3.06485×10^{6}
σ_4	-85360.3	-570025.	4.39684×10^{6}
β_1	41.0251	-423.681	850.359
β_2	-3.41293	25.5724	-54.408
β_3	5.44717×10^{-6}	-3.22061×10^{-5}	7.97402×10^{-5}
α_1	-21.5714	981.216	-3239.57
α_2	-0.0499834	0.606207	-1.68277
α_3	11.1757	-577.8	1808.73
α_4	-0.0155074	0.157503	0.210768
α_5	-0.0179453	0.59651	-2.06089

Table A.3: Coefficient values for cubic in $\chi_{\rm PN}$ terms for the mapping functions given in Eq. (3.28). These values are calculated under the parametrisation (η, $\chi_{\rm PN}$)

Bibliography

[1] https://losc.ligo.org/events/GW150914/.

[2] https://www.ligo.caltech.edu/page/timeline.

[3] http://www.black-holes.org/waveforms.

[4] https://www.learner.org/.

[5] https://ldas-jobs.cgca.uwm.edu/~vivien/offline_pe/G184098/C01/IMRPhenomD_spline/nest/1126259462.39-0/H1L1/posplots.html.

[6] http://www.black-holes.org/SpEC.html.

[7] https://github.com/ligo-cbc/pycbc, 2016.

[8] J. Aasi et al. Prospects for Localization of Gravitational Wave Transients by the Advanced LIGO and Advanced Virgo Observatories. 2013.

[9] J Aasi et al. The ninja-2 project: detecting and characterizing gravitational waveforms modelled using numerical binary black hole simulations. *Classical and Quantum Gravity*, 31(11):115004, 2014. URL http://stacks.iop.org/0264-9381/31/i=11/a=115004.

[10] B. P. Abbott et al. Astrophysical implications of the binary black hole merger gw150914. *The Astrophysical Journal Letters*, 818(2):L22, 2016. URL http://stacks.iop.org/2041-8205/818/i=2/a=L22.

[11] B. P. Abbott et al. Calibration of the Advanced LIGO detectors for the discovery of the binary black-hole merger GW150914. 2016.

[12] B. P. Abbott et al. The Rate of Binary Black Hole Mergers Inferred from Advanced LIGO Observations Surrounding GW150914. 2016.

[13] B. P. Abbott et al. Observation of gravitational waves from a binary black hole merger. *Phys. Rev. Lett.*, 116:061102, Feb 2016. doi: 10.1103/PhysRevLett.116.061102. URL http://link.aps.org/doi/10.1103/PhysRevLett.116.061102.

[14] B. P. Abbott et al. GW150914: First results from the search for binary black hole coalescence with Advanced LIGO. 2016.

[15] B. P. Abbott et al. Tests of general relativity with GW150914. 2016.

[16] B. P. Abbott et al. Observing gravitational-wave transient GW150914 with minimal assumptions. 2016.

[17] B. P. Abbott et al. Properties of the binary black hole merger GW150914. 2016.

[18] Benjamin P. Abbott, others (LIGO Scientific Collaboration, and Virgo Collaboration). Prospects for observing and localizing gravitational-wave transients with advanced ligo and advanced virgo. *Living Rev. Rel.*, 19:1, 2016. doi: 10.1007/lrr-2016-1.

[19] F Acernese et al. Advanced virgo: a second-generation interferometric gravitational wave detector. *Classical and Quantum Gravity*, 32(2):024001, 2015. URL http://stacks.iop.org/0264-9381/32/i=2/a=024001.

[20] P. Ajith. Addressing the spin question in gravitational-wave searches: Waveform templates for inspiralling compact binaries with nonprecessing spins. *Phys. Rev. D*, 84:084037, Oct 2011. doi: 10.1103/PhysRevD.84.084037. URL http://link.aps.org/doi/10.1103/PhysRevD.84.084037.

[21] P. Ajith, M. Hannam, S. Husa, Y. Chen, B. Brügmann, N. Dorband, D. Müller, F. Ohme, D. Pollney, C. Reisswig, L. Santamaría, and J. Seiler. Inspiral-merger-ringdown waveforms for black-hole binaries with nonprecessing spins. *Phys. Rev. Lett.*, 106:241101, Jun 2011. doi: 10.1103/PhysRevLett.106.241101. URL http://link.aps.org/doi/10.1103/PhysRevLett.106.241101.

[22] P. Ajith, N. Fotopoulos, S. Privitera, A. Neunzert, N. Mazumder, and A. J. Weinstein. Effectual template bank for the detection of gravitational waves from inspiralling compact binaries with generic spins. *Phys. Rev. D*, 89:084041, Apr 2014. doi: 10.1103/PhysRevD.89.084041. URL http://link.aps.org/doi/10.1103/PhysRevD.89.084041.

[23] P. Ajith et al. A Template bank for gravitational waveforms from coalescing binary black holes. I. Non-spinning binaries. *Phys. Rev.*, D77:104017, 2008. doi: 10.1103/PhysRevD.79.129901,10.1103/PhysRevD.77.104017. [Erratum: Phys. Rev.D79,129901(2009)].

[24] Parameswaran Ajith et al. Phenomenological template family for black-hole coalescence waveforms. *Class. Quant. Grav.*, 24:S689–S700, 2007. doi: 10.1088/0264-9381/24/19/S31.

[25] Parameswaran Ajith et al. Template bank for gravitational waveforms from coalescing binary black holes: Nonspinning binaries. *Phys. Rev. D*, 77:104017, May 2008. doi: 10.1103/PhysRevD.77.104017. URL http://link.aps.org/doi/10.1103/PhysRevD.77.104017.

[26] Bruce Allen, Warren G. Anderson, Patrick R. Brady, Duncan A. Brown, and Jolien D. E. Creighton. Findchirp: An algorithm for detection of gravitational waves from inspiraling compact binaries. *Phys. Rev. D*, 85:122006, Jun 2012. doi: 10.1103/PhysRevD.85.122006. URL http://link.aps.org/doi/10.1103/PhysRevD.85.122006.

[27] Marcus Ansorg, Bernd Brügmann, and Wolfgang Tichy. Single-domain spectral method for black hole puncture data. *Phys. Rev. D*, 70:064011, Sep 2004. doi: 10.1103/PhysRevD.70.064011. URL http://link.aps.org/doi/10.1103/PhysRevD.70.064011.

[28] Theocharis A. Apostolatos. Search templates for gravitational waves from precessing, inspiraling binaries. *Phys. Rev. D*, 52:605–620, Jul 1995. doi: 10.1103/PhysRevD.52.605. URL http://link.aps.org/doi/10.1103/PhysRevD.52.605.

[29] Theocharis A. Apostolatos, Curt Cutler, Gerald J. Sussman, and Kip S. Thorne. Spin-induced orbital precession and its modulation of the gravitational waveforms from merging binaries. *Phys. Rev. D*, 49:6274–6297, Jun 1994. doi: 10.1103/PhysRevD.49.6274. URL http://link.aps.org/doi/10.1103/PhysRevD.49.6274.

[30] Richard Arnowitt, Stanley Deser, and Charles W. Misner. Republication of: The dynamics of general relativity. *General Relativity and Gravitation*, 40 (9):1997–2027, 2008. ISSN 1572-9532. doi: 10.1007/s10714-008-0661-1. URL http://dx.doi.org/10.1007/s10714-008-0661-1.

[31] K. G. Arun, Bala R. Iyer, B. S. Sathyaprakash, and Pranesh A. Sundararajan. Parameter estimation of inspiralling compact binaries using 3.5 post-Newtonian gravitational wave phasing: The Non-spinning case. *Phys. Rev.*, D71:084008, 2005. doi: 10.1103/PhysRevD.71.084008,10.1103/PhysRevD.72.069903. [Erratum: Phys. Rev.D72,069903(2005)].

[32] K. G. Arun, Alessandra Buonanno, Guillaume Faye, and Evan Ochsner. Higher-order spin effects in the amplitude and phase of gravitational waveforms emitted by inspiraling compact binaries: Ready-to-use gravitational waveforms. *Phys. Rev.*, D79:104023, 2009. doi: 10.1103/PhysRevD.79.104023, 10.1103/PhysRevD.84.049901. [Erratum: Phys. Rev.D84,049901(2011)].

[33] Yoichi Aso, Yuta Michimura, Kentaro Somiya, Masaki Ando, Osamu Miyakawa, Takanori Sekiguchi, Daisuke Tatsumi, and Hiroaki Yamamoto. Interferometer design of the kagra gravitational wave detector. *Phys. Rev. D*, 88:043007, Aug 2013. doi: 10.1103/PhysRevD.88.043007. URL http://link.aps.org/doi/10.1103/PhysRevD.88.043007.

[34] Luca Baiotti, Sebastiano Bernuzzi, Giovanni Corvino, Roberto De Pietri, and Alessandro Nagar. Gravitational-wave extraction from neutron-star oscillations: Comparing linear and nonlinear techniques. *Phys. Rev. D*, 79:024002, Jan 2009. doi: 10.1103/PhysRevD.79.024002. URL http://link.aps.org/doi/10.1103/PhysRevD.79.024002.

[35] John G. Baker, Joan Centrella, Dae-Il Choi, Michael Koppitz, and James van Meter. Gravitational-wave extraction from an inspiraling configuration of merging black holes. *Phys. Rev. Lett.*, 96:111102, Mar 2006. doi: 10.1103/PhysRevLett.96.111102. URL http://link.aps.org/doi/10.1103/PhysRevLett.96.111102.

[36] Thomas W. Baumgarte and Stuart L. Shapiro. Numerical integration of einstein's field equations. *Phys. Rev. D*, 59:024007, Dec 1998. doi: 10.1103/PhysRevD.59.024007. URL http://link.aps.org/doi/10.1103/PhysRevD.59.024007.

[37] T.W. Baumgarte and S.L. Shapiro. *Numerical Relativity: Solving Einstein's Equations on the Computer*. Cambridge University Press, 2010. ISBN 9780521514071. URL https://books.google.co.uk/books?id=dxU1OEinvRUC.

[38] Matthew J. Benacquista and Jonathan M. B. Downing. Relativistic binaries in globular clusters. *Living Reviews in Relativity*, 16(4), 2013. doi: 10.1007/lrr-2013-4. URL http://www.livingreviews.org/lrr-2013-4.

[39] Emanuele Berti, Vitor Cardoso, and Andrei O Starinets. Quasinormal modes of black holes and black branes. *Classical and Quantum Gravity*, 26(16):163001, 2009. URL http://stacks.iop.org/0264-9381/26/i=16/a=163001.

[40] Jonathan Blackman, Bela Szilagyi, Chad R. Galley, and Manuel Tiglio. Sparse representations of gravitational waves from precessing compact binaries. *Phys. Rev. Lett.*, 113:021101, Jul 2014. doi: 10.1103/PhysRevLett.113.021101. URL http://link.aps.org/doi/10.1103/PhysRevLett.113.021101.

[41] Jonathan Blackman, Scott E. Field, Chad R. Galley, Béla Szilágyi, Mark A. Scheel, Manuel Tiglio, and Daniel A. Hemberger. Fast and accurate prediction of numerical relativity waveforms from binary black hole coales-

cences using surrogate models. *Phys. Rev. Lett.*, 115:121102, Sep 2015. doi: 10.1103/PhysRevLett.115.121102. URL http://link.aps.org/doi/10.1103/PhysRevLett.115.121102.

[42] Luc Blanchet. Gravitational radiation from post-Newtonian sources and inspiralling compact binaries. *Living Reviews in Relativity*, 17, 2014. ISSN 1433-8351. doi: 10.12942/lrr-2014-2. URL http://dx.doi.org/10.12942/lrr-2014-2.

[43] Alejandro Bohé, Sylvain Marsat, and Luc Blanchet. Next-to-next-to-leading order spin-orbit effects in the gravitational wave flux and orbital phasing of compact binaries. *Class.Quant.Grav.*, 30:135009, 2013. doi: 10.1088/0264-9381/30/13/135009.

[44] Alejandro Bohé, Guillaume Faye, Sylvain Marsat, and Edward K Porter. Quadratic-in-spin effects in the orbital dynamics and gravitational-wave energy flux of compact binaries at the 3PN order. 2015.

[45] Jeffrey M. Bowen and James W. York. Time-asymmetric initial data for black holes and black-hole collisions. *Phys. Rev. D*, 21:2047–2056, Apr 1980. doi: 10.1103/PhysRevD.21.2047. URL http://link.aps.org/doi/10.1103/PhysRevD.21.2047.

[46] Michael Boyle. Uncertainty in hybrid gravitational waveforms: Optimizing initial orbital frequencies for binary black-hole simulations. *Phys. Rev.*, D84:064013, 2011. doi: 10.1103/PhysRevD.84.064013.

[47] Steven Brandt and Bernd Brügmann. A simple construction of initial data for multiple black holes. *Phys. Rev. Lett.*, 78:3606–3609, May 1997. doi: 10.1103/PhysRevLett.78.3606. URL http://link.aps.org/doi/10.1103/PhysRevLett.78.3606.

[48] Dieter R. Brill and Richard W. Lindquist. Interaction energy in geometrostatics. *Phys. Rev.*, 131:471–476, Jul 1963. doi: 10.1103/PhysRev.131.471. URL http://link.aps.org/doi/10.1103/PhysRev.131.471.

[49] Bernd Brügmann, José A. González, Mark Hannam, Sascha Husa, and Ulrich Sperhake. Exploring black hole superkicks. *Phys. Rev. D*, 77:124047, Jun 2008. doi: 10.1103/PhysRevD.77.124047. URL http://link.aps.org/doi/10.1103/PhysRevD.77.124047.

[50] Bernd Brügmann, José A. González, Mark Hannam, Sascha Husa, Ulrich Sperhake, and Wolfgang Tichy. Calibration of moving puncture simulations. *Phys. Rev. D*, 77:024027, Jan 2008. doi: 10.1103/PhysRevD.77.024027. URL http://link.aps.org/doi/10.1103/PhysRevD.77.024027.

[51] A. Buonanno and T. Damour. Effective one-body approach to general relativistic two-body dynamics. *Phys. Rev. D*, 59(8), Mar 1999. ISSN 1089-4918. doi: 10.1103/physrevd.59.084006. URL http://dx.doi.org/10.1103/PhysRevD.59.084006.

[52] Alessandra Buonanno and Thibault Damour. Transition from inspiral to plunge in binary black hole coalescences. *Phys. Rev.*, D62:064015, 2000. doi: 10.1103/PhysRevD.62.064015.

[53] Alessandra Buonanno, Yi Pan, John G. Baker, Joan Centrella, Bernard J. Kelly, Sean T. McWilliams, and James R. van Meter. Toward faithful templates for non-spinning binary black holes using the effective-one-body approach. *Phys. Rev.*, D76:104049, 2007. doi: 10.1103/PhysRevD.76.104049.

[54] Alessandra Buonanno, Bala R. Iyer, Evan Ochsner, Yi Pan, and B. S. Sathyaprakash. Comparison of post-newtonian templates for compact binary inspiral signals in gravitational-wave detectors. *Phys. Rev. D*, 80:084043, Oct 2009. doi: 10.1103/PhysRevD.80.084043. URL http://link.aps.org/doi/10.1103/PhysRevD.80.084043.

[55] Alessandra Buonanno, Yi Pan, Harald P. Pfeiffer, Mark A. Scheel, Luisa T. Buchman, and Lawrence E. Kidder. Effective-one-body waveforms calibrated to numerical relativity simulations: Coalescence of non-spinning, equal-mass black holes. *Phys. Rev.*, D79:124028, 2009. doi: 10.1103/PhysRevD.79.124028.

[56] M. Campanelli, C. O. Lousto, P. Marronetti, and Y. Zlochower. Accurate evolutions of orbiting black-hole binaries without excision. *Phys. Rev. Lett.*, 96:111101, Mar 2006. doi: 10.1103/PhysRevLett.96.111101. URL http://link.aps.org/doi/10.1103/PhysRevLett.96.111101.

[57] Manuela Campanelli, Carlos O. Lousto, Yosef Zlochower, Badri Krishnan, and David Merritt. Spin flips and precession in black-hole-binary mergers. *Phys. Rev. D*, 75:064030, Mar 2007. doi: 10.1103/PhysRevD.75.064030. URL http://link.aps.org/doi/10.1103/PhysRevD.75.064030.

[58] Priscilla Canizares, Scott E. Field, Jonathan Gair, Vivien Raymond, Rory Smith, and Manuel Tiglio. Accelerated gravitational-wave parameter estimation with reduced order modeling. *Phys. Rev. Lett.*, 114(7):071104, 2015. doi: 10.1103/PhysRevLett.114.071104.

[59] Collin Capano, Ian Harry, Stephen Privitera, and Alessandra Buonanno. Implementing a search for gravitational waves from non-precessing, spinning binary black holes. 2016.

[60] Joan Centrella, John G. Baker, Bernard J. Kelly, and James R. van Meter. Black-hole binaries, gravitational waves, and numerical relativity. *Rev. Mod.*

Phys., 82:3069–3119, Nov 2010. doi: 10.1103/RevModPhys.82.3069. URL http://link.aps.org/doi/10.1103/RevModPhys.82.3069.

[61] Michael I. Cohen, Jeffrey D. Kaplan, and Mark A. Scheel. Toroidal horizons in binary black hole inspirals. *Phys. Rev. D*, 85:024031, Jan 2012. doi: 10.1103/PhysRevD.85.024031. URL http://link.aps.org/doi/10.1103/PhysRevD.85.024031.

[62] The LIGO Scientific Collaboration. Advanced ligo. *Classical and Quantum Gravity*, 32(7):074001, 2015. URL http://stacks.iop.org/0264-9381/32/i=7/a=074001.

[63] G. B. Cook. Initial Data for Numerical Relativity. *Living Rev. Rel.*, 3:5, 2000. doi: 10.12942/lrr-2000-5.

[64] Gregory B. Cook and James W. York. Apparent horizons for boosted or spinning black holes. *Phys. Rev. D*, 41:1077–1085, Feb 1990. doi: 10.1103/PhysRevD.41.1077. URL http://link.aps.org/doi/10.1103/PhysRevD.41.1077.

[65] Curt Cutler and Eanna E. Flanagan. Gravitational waves from merging compact binaries: How accurately can one extract the binary's parameters from the inspiral wave form? *Phys.Rev.*, D49:2658–2697, 1994. doi: 10.1103/PhysRevD.49.2658.

[66] Tito Dal Canton, Andrew P. Lundgren, and Alex B. Nielsen. Impact of precession on aligned-spin searches for neutron-star–black-hole binaries. *Phys. Rev.*, D91(6):062010, 2015. doi: 10.1103/PhysRevD.91.062010.

[67] Thibault Damour. Coalescence of two spinning black holes: an effective one-body approach. *Phys. Rev.*, D64:124013, 2001. doi: 10.1103/PhysRevD.64.124013.

[68] Thibault Damour and Alessandro Nagar. An Improved analytical description of inspiralling and coalescing black-hole binaries. *Phys. Rev.*, D79:081503, 2009. doi: 10.1103/PhysRevD.79.081503.

[69] Thibault Damour and Alessandro Nagar. New effective-one-body description of coalescing nonprecessing spinning black-hole binaries. *Phys. Rev. D*, 90 (4), Aug 2014. ISSN 1550-2368. doi: 10.1103/physrevd.90.044018. URL http://dx.doi.org/10.1103/PhysRevD.90.044018.

[70] Thibault Damour and Alessandro Nagar. New effective-one-body description of coalescing nonprecessing spinning black-hole binaries. *Phys. Rev. D*, 90: 044018, Aug 2014. doi: 10.1103/PhysRevD.90.044018. URL http://link.aps.org/doi/10.1103/PhysRevD.90.044018.

[71] Thibault Damour, Bala R. Iyer, and B. S. Sathyaprakash. A Comparison of search templates for gravitational waves from binary inspiral. *Phys. Rev.*, D63:044023, 2001. doi: 10.1103/PhysRevD.63.044023,10.1103/PhysRevD.72.029902. [Erratum: Phys. Rev.D72,029902(2005)].

[72] Thibault Damour, Alessandro Nagar, Ernst Nils Dorband, Denis Pollney, and Luciano Rezzolla. Faithful Effective-One-Body waveforms of equal-mass coalescing black-hole binaries. *Phys. Rev.*, D77:084017, 2008. doi: 10.1103/PhysRevD.77.084017.

[73] Thibault Damour, Alessandro Nagar, Mark Hannam, Sascha Husa, and Bernd Bruegmann. Accurate Effective-One-Body waveforms of inspiralling and coalescing black-hole binaries. *Phys. Rev.*, D78:044039, 2008. doi: 10.1103/PhysRevD.78.044039.

[74] Thibault Damour, Alessandro Nagar, and Miguel Trias. Accuracy and effectualness of closed-form, frequency-domain waveforms for non-spinning black hole binaries. *Phys. Rev.*, D83:024006, 2011. doi: 10.1103/PhysRevD.83.024006.

[75] Thibault Damour, Alessandro Nagar, and Sebastiano Bernuzzi. Improved effective-one-body description of coalescing nonspinning black-hole binaries and its numerical-relativity completion. *Phys.Rev.*, D87(8):084035, 2013. doi: 10.1103/PhysRevD.87.084035.

[76] R.W.P. Drever, F.J. Raab, K.S. Thorne, R. Vogt, and R.Weiss. Laser interferometer gravitational-wave observatory (ligo) technical report, 1989. URL https://dcc.ligo.org/LIGO-M890001/public/main.

[77] Albert Einstein. On the electrodynamics of moving bodies. *Annalen Phys.*, 17: 891–921, 1905. doi: 10.1002/andp.200590006. [Annalen Phys.14,194(2005)].

[78] Albert Einstein. On the General Theory of Relativity. *Sitzungsber. Preuss. Akad. Wiss. Berlin (Math. Phys.)*, 1915:778–786, 1915. [Addendum: Sitzungsber. Preuss. Akad. Wiss. Berlin (Math. Phys.)1915,799(1915)].

[79] Albert Einstein. Näherungsweise integration der feldgleichungen der gravitation. *Sitzungsberichte der Königlich Preußischen Akademie der Wissenschaften (Berlin)*, 1:688–696, 1916.

[80] Albert Einstein. Über gravitationswellen. *Sitzungsberichte der Königlich Preußischen Akademie der Wissenschaften (Berlin)*, 1:154–167, 1918.

[81] Will M. Farr, Niharika Sravan, Andrew Cantrell, Laura Kreidberg, Charles D. Bailyn, Ilya Mandel, and Vicky Kalogera. The mass distribution of stellar-mass black holes. *The Astrophysical Journal*, 741(2):103, 2011. URL http://stacks.iop.org/0004-637X/741/i=2/a=103.

[82] Scott E. Field, Chad R. Galley, and Evan Ochsner. Towards beating the curse of dimensionality for gravitational waves using reduced basis. *Phys. Rev. D*, 86:084046, Oct 2012. doi: 10.1103/PhysRevD.86.084046. URL http://link.aps.org/doi/10.1103/PhysRevD.86.084046.

[83] Scott E. Field, Chad R. Galley, Jan S. Hesthaven, Jason Kaye, and Manuel Tiglio. Fast prediction and evaluation of gravitational waveforms using surrogate models. *Phys. Rev. X*, 4:031006, Jul 2014. doi: 10.1103/PhysRevX.4.031006. URL http://link.aps.org/doi/10.1103/PhysRevX.4.031006.

[84] H Grote and the LIGO Scientific Collaboration. The geo 600 status. *Classical and Quantum Gravity*, 27(8):084003, 2010. URL http://stacks.iop.org/0264-9381/27/i=8/a=084003.

[85] Carsten Gundlach and José M. Martín-García. Well-posedness of formulations of the einstein equations with dynamical lapse and shift conditions. *Phys. Rev. D*, 74:024016, Jul 2006. doi: 10.1103/PhysRevD.74.024016. URL http://link.aps.org/doi/10.1103/PhysRevD.74.024016.

[86] Carsten Gundlach and José M Martín-García. Hyperbolicity of second order in space systems of evolution equations. *Classical and Quantum Gravity*, 23 (16):S387, 2006. URL http://stacks.iop.org/0264-9381/23/i=16/a=S06.

[87] Mark Hannam. Modelling gravitational waves from precessing black-hole binaries: Progress, challenges and prospects. *Gen. Rel. Grav.*, 46:1767, 2014. doi: 10.1007/s10714-014-1767-2.

[88] Mark Hannam, Sascha Husa, Bernd Bruegmann, and Achamveedu Gopakumar. Comparison between numerical-relativity and post-Newtonian waveforms from spinning binaries: The Orbital hang-up case. *Phys. Rev.*, D78:104007, 2008. doi: 10.1103/PhysRevD.78.104007.

[89] Mark Hannam, Sascha Husa, Frank Ohme, and P. Ajith. Length requirements for numerical-relativity waveforms. *Phys. Rev. D*, 82:124052, Dec 2010. doi: 10.1103/PhysRevD.82.124052. URL http://link.aps.org/doi/10.1103/PhysRevD.82.124052.

[90] Mark Hannam, Sascha Husa, Frank Ohme, Doreen Müller, and Bernd Brügmann. Simulations of black-hole binaries with unequal masses or nonprecessing spins: Accuracy, physical properties, and comparison with post-newtonian results. *Phys. Rev. D*, 82:124008, Dec 2010. doi: 10.1103/PhysRevD.82.124008. URL http://link.aps.org/doi/10.1103/PhysRevD.82.124008.

[91] Mark Hannam, Patricia Schmidt, Alejandro Bohé, Leïla Haegel, Sascha Husa, Frank Ohme, Geraint Pratten, and Michael Pürrer. Simple model of complete

precessing black-hole-binary gravitational waveforms. *Phys. Rev. Lett.*, 113: 151101, Oct 2014. doi: 10.1103/PhysRevLett.113.151101. URL http://link.aps.org/doi/10.1103/PhysRevLett.113.151101.

[92] Enno Harms, Sebastiano Bernuzzi, Alessandro Nagar, and An Zenginoglu. A new gravitational wave generation algorithm for particle perturbations of the Kerr spacetime. *Class. Quant. Grav.*, 31(24):245004, 2014. doi: 10.1088/0264-9381/31/24/245004.

[93] Ian Harry, Stephen Privitera, Alejandro Bohé, and Alessandra Buonanno. Searching for Gravitational Waves from Compact Binaries with Precessing Spins. 2016.

[94] I.W. Harry, A.H. Nitz, Duncan A. Brown, A. Lundgren, Evan Ochsner, et al. Investigating the effect of precession on searches for neutron-star-black-hole binaries with Advanced LIGO. *Phys.Rev.*, D89(2):024010, 2014. doi: 10.1103/PhysRevD.89.024010.

[95] Carl-Johan Haster, Zhilu Wang, Christopher P. L. Berry, Simon Stevenson, John Veitch, and Ilya Mandel. Inference on gravitational waves from coalescences of stellar-mass compact objects and intermediate-mass black holes. *Monthly Notices of the Royal Astronomical Society*, 457(4):4499–4506, 2016. doi: 10.1093/mnras/stw233. URL http://mnras.oxfordjournals.org/content/457/4/4499.abstract.

[96] Daniel A. Hemberger, Mark A. Scheel, Lawrence E. Kidder, Béla Szilágyi, Geoffrey Lovelace, Nicholas W. Taylor, and Saul A. Teukolsky. Dynamical Excision Boundaries in Spectral Evolutions of Binary Black Hole Spacetimes. *Class. Quant. Grav.*, 30:115001, 2013. doi: 10.1088/0264-9381/30/11/115001.

[97] Ian Hinder, Frank Herrmann, Pablo Laguna, and Deirdre Shoemaker. Comparisons of eccentric binary black hole simulations with post-newtonian models. *Phys. Rev. D*, 82:024033, Jul 2010. doi: 10.1103/PhysRevD.82.024033. URL http://link.aps.org/doi/10.1103/PhysRevD.82.024033.

[98] Ian Hinder, Alessandra Buonanno, Michael Boyle, Zachariah B Etienne, James Healy, Nathan K Johnson-McDaniel, Alessandro Nagar, Hiroyuki Nakano, Yi Pan, Harald P Pfeiffer, and et al. Error-analysis and comparison to analytical models of numerical waveforms produced by the nrar collaboration. *Class. Quantum Grav.*, 31(2):025012, Jan 2013. ISSN 1361-6382. doi: 10.1088/0264-9381/31/2/025012. URL http://dx.doi.org/10.1088/0264-9381/31/2/025012.

[99] Sascha Husa, José A González, Mark Hannam, Bernd Brügmann, and Ulrich Sperhake. Reducing phase error in long numerical binary black hole evo-

lutions with sixth-order finite differencing. *Classical and Quantum Gravity*, 25(10):105006, 2008. URL http://stacks.iop.org/0264-9381/25/i=10/a=105006.

[100] Sascha Husa, Sebastian Khan, Mark Hannam, Michael Pürrer, Frank Ohme, Xisco Jiménez Forteza, and Alejandro Bohé. Frequency-domain gravitational waves from nonprecessing black-hole binaries. i. new numerical waveforms and anatomy of the signal. *Phys. Rev. D*, 93:044006, Feb 2016. doi: 10.1103/PhysRevD.93.044006. URL http://link.aps.org/doi/10.1103/PhysRevD.93.044006.

[101] Werner Israel. Event horizons in static vacuum space-times. *Phys. Rev.*, 164: 1776–1779, Dec 1967. doi: 10.1103/PhysRev.164.1776. URL http://link.aps.org/doi/10.1103/PhysRev.164.1776.

[102] Bala Iyer et al. Ligo-india technical report, 2011. URL https://dcc.ligo.org/LIGO-M1100296-v2/public.

[103] Chinmay Kalaghatgi, Parameswaran Ajith, and K. G. Arun. Template-space metric for searches for gravitational waves from the inspiral, merger, and ringdown of binary black holes. *Phys. Rev. D*, 91:124042, Jun 2015. doi: 10.1103/PhysRevD.91.124042. URL http://link.aps.org/doi/10.1103/PhysRevD.91.124042.

[104] Ioannis Kamaretsos, Mark Hannam, Sascha Husa, and B. S. Sathyaprakash. Black-hole hair loss: Learning about binary progenitors from ringdown signals. *Phys. Rev. D*, 85:024018, Jan 2012. doi: 10.1103/PhysRevD.85.024018. URL http://link.aps.org/doi/10.1103/PhysRevD.85.024018.

[105] Roy P. Kerr. Gravitational field of a spinning mass as an example of algebraically special metrics. *Phys. Rev. Lett.*, 11:237–238, Sep 1963. doi: 10.1103/PhysRevLett.11.237. URL http://link.aps.org/doi/10.1103/PhysRevLett.11.237.

[106] Sebastian Khan, Sascha Husa, Mark Hannam, Frank Ohme, Michael Pürrer, Xisco Jiménez Forteza, and Alejandro Bohé. Frequency-domain gravitational waves from nonprecessing black-hole binaries. ii. a phenomenological model for the advanced detector era. *Phys. Rev. D*, 93:044007, Feb 2016. doi: 10.1103/PhysRevD.93.044007. URL http://link.aps.org/doi/10.1103/PhysRevD.93.044007.

[107] Lawrence E. Kidder. Coalescing binary systems of compact objects to $(\text{post})^{5/2}$-newtonian order. v. spin effects. *Phys. Rev. D*, 52:821–847, Jul 1995. doi: 10.1103/PhysRevD.52.821. URL http://link.aps.org/doi/10.1103/PhysRevD.52.821.

[108] Lawrence E. Kidder. Using full information when computing modes of post-newtonian waveforms from inspiralling compact binaries in circular orbit. *Phys. Rev. D*, 77:044016, Feb 2008. doi: 10.1103/PhysRevD.77.044016. URL http://link.aps.org/doi/10.1103/PhysRevD.77.044016.

[109] Kostas D. Kokkotas and Bernd G. Schmidt. Quasinormal modes of stars and black holes. *Living Rev. Rel.*, 2:2, 1999. doi: 10.12942/lrr-1999-2.

[110] Prayush Kumar, Kevin Barkett, Swetha Bhagwat, Nousha Afshari, Duncan A. Brown, Geoffrey Lovelace, Mark A. Scheel, and Béla Szilágyi. Accuracy and precision of gravitational-wave models of inspiraling neutron star – black hole binaries with spin: comparison with numerical relativity in the low-frequency regime. 2015.

[111] Prayush Kumar, Kevin Barkett, Swetha Bhagwat, Nousha Afshari, Duncan A. Brown, Geoffrey Lovelace, Mark A. Scheel, and Béla Szilágyi. Accuracy and precision of gravitational-wave models of inspiraling neutron star-black hole binaries with spin: Comparison with matter-free numerical relativity in the low-frequency regime. *Phys. Rev. D*, 92:102001, Nov 2015. doi: 10.1103/PhysRevD.92.102001. URL http://link.aps.org/doi/10.1103/PhysRevD.92.102001.

[112] Prayush Kumar, Tony Chu, Heather Fong, Harald P. Pfeiffer, Michael Boyle, Daniel A. Hemberger, Lawrence E. Kidder, Mark A. Scheel, and Bela Szilagyi. Accuracy of binary black hole waveform models for aligned-spin binaries. 2016.

[113] Norbert Lages. *Apparent Horizons and Marginally Trapped Surfaces in Numerical General Relativity*. PhD thesis, Friedrich-Schiller-Universität Jena, 2010.

[114] Lee Lindblom, Mark A Scheel, Lawrence E Kidder, Robert Owen, and Oliver Rinne. A new generalized harmonic evolution system. *Classical and Quantum Gravity*, 23(16):S447, 2006. URL http://stacks.iop.org/0264-9381/23/i=16/a=S09.

[115] Tyson B. Littenberg, Ben Farr, Scott Coughlin, Vicky Kalogera, and Daniel E. Holz. Neutron stars versus black holes: Probing the mass gap with ligo/virgo. *The Astrophysical Journal Letters*, 807(2):L24, 2015. URL http://stacks.iop.org/2041-8205/807/i=2/a=L24.

[116] Lionel London, Deirdre Shoemaker, and James Healy. Modeling ringdown: Beyond the fundamental quasinormal modes. *Phys. Rev. D*, 90:124032, Dec 2014. doi: 10.1103/PhysRevD.90.124032. URL http://link.aps.org/doi/10.1103/PhysRevD.90.124032.

[117] Carlos O. Lousto and James Healy. Flip-flopping binary black holes. *Phys. Rev. Lett.*, 114:141101, Apr 2015. doi: 10.1103/PhysRevLett.114.141101. URL http://link.aps.org/doi/10.1103/PhysRevLett.114.141101.

[118] Geoffrey Lovelace, Robert Owen, Harald P. Pfeiffer, and Tony Chu. Binary-black-hole initial data with nearly extremal spins. *Phys. Rev. D*, 78:084017, Oct 2008. doi: 10.1103/PhysRevD.78.084017. URL http://link.aps.org/doi/10.1103/PhysRevD.78.084017.

[119] Geoffrey Lovelace, Mark A. Scheel, and Béla Szilágyi. Simulating merging binary black holes with nearly extremal spins. *Phys. Rev. D*, 83:024010, Jan 2011. doi: 10.1103/PhysRevD.83.024010. URL http://link.aps.org/doi/10.1103/PhysRevD.83.024010.

[120] Ilana MacDonald, Samaya Nissanke, and Harald P. Pfeiffer. Suitability of post-Newtonian/numerical-relativity hybrid waveforms for gravitational wave detectors. *Class. Quant. Grav.*, 28:134002, 2011. doi: 10.1088/0264-9381/28/13/134002.

[121] Ilana MacDonald, Abdul H. Mroué, Harald P. Pfeiffer, Michael Boyle, Lawrence E. Kidder, et al. Suitability of hybrid gravitational waveforms for unequal-mass binaries. *Phys.Rev.*, D87:024009, 2013. doi: 10.1103/PhysRevD.87.024009.

[122] M. Maggiore. *Gravitational Waves: Volume 1: Theory and Experiments*. OUP Oxford, 2007. ISBN 9780198570745. URL https://books.google.it/books?id=AqVpQgAACAAJ.

[123] Sylvain Marsat. Cubic order spin effects in the dynamics and gravitational wave energy flux of compact object binaries. *Class. Quant. Grav.*, 32(8):085008, 2015. doi: 10.1088/0264-9381/32/8/085008.

[124] D. J. A. McKechan. *On the use of higher order waveforms in the search for gravitational waves emitted by compact binary coalescences*. PhD thesis, Cardiff U., 2010. URL https://inspirehep.net/record/889087/files/arXiv:1102.1749.pdf.

[125] D J A McKechan, C Robinson, and B S Sathyaprakash. A tapering window for time-domain templates and simulated signals in the detection of gravitational waves from coalescing compact binaries. *Classical and Quantum Gravity*, 27(8):084020, 2010. URL http://stacks.iop.org/0264-9381/27/i=8/a=084020.

[126] Balazs Mikoczi, Matyas Vasuth, and Laszlo A. Gergely. Self-interaction spin effects in inspiralling compact binaries. *Phys. Rev.*, D71:124043, 2005. doi: 10.1103/PhysRevD.71.124043.

[127] Abdul H. Mroué, Mark A. Scheel, Bela Szilagyi, Harald P. Pfeiffer, Michael Boyle, et al. A catalog of 174 binary black-hole simulations for gravitational-wave astronomy. *Phys.Rev.Lett.*, 111:241104, 2013. doi: 10.1103/PhysRevLett.111.241104.

[128] Alessandro Nagar, Thibault Damour, Christian Reisswig, and Denis Pollney. Energetics and phasing of nonprecessing spinning coalescing black hole binaries. 2015.

[129] Ramesh Narayan and Jeffrey E. McClintock. Observational Evidence for Black Holes. 2013.

[130] E. Newman and R. Penrose. An Approach to Gravitational Radiation by a Method of Spin Coefficients. *Journal of Mathematical Physics*, 3:566–578, May 1962. doi: 10.1063/1.1724257.

[131] Alexander H. Nitz, Andrew Lundgren, Duncan A. Brown, Evan Ochsner, Drew Keppel, et al. Accuracy of gravitational waveform models for observing neutron-star–black-hole binaries in Advanced LIGO. *Phys.Rev.*, D88(12): 124039, 2013. doi: 10.1103/PhysRevD.88.124039.

[132] Frank Ohme, Mark Hannam, and Sascha Husa. Reliability of complete gravitational waveform models for compact binary coalescences. *Phys. Rev. D*, 84:064029, Sep 2011. doi: 10.1103/PhysRevD.84.064029. URL http://link.aps.org/doi/10.1103/PhysRevD.84.064029.

[133] Yi Pan, Alessandra Buonanno, Luisa T. Buchman, Tony Chu, Lawrence E. Kidder, Harald P. Pfeiffer, and Mark A. Scheel. Effective-one-body waveforms calibrated to numerical relativity simulations: coalescence of non-precessing, spinning, equal-mass black holes. *Phys. Rev.*, D81:084041, 2010. doi: 10.1103/PhysRevD.81.084041.

[134] Yi Pan, Alessandra Buonanno, Michael Boyle, Luisa T. Buchman, Lawrence E. Kidder, Harald P. Pfeiffer, and Mark A. Scheel. Inspiral-merger-ringdown multipolar waveforms of nonspinning black-hole binaries using the effective-one-body formalism. *Phys. Rev.*, D84:124052, 2011. doi: 10.1103/PhysRevD.84.124052.

[135] Yi Pan, Alessandra Buonanno, Michael Boyle, Luisa T. Buchman, Lawrence E. Kidder, Harald P. Pfeiffer, and Mark A. Scheel. Inspiral-merger-ringdown multipolar waveforms of nonspinning black-hole binaries using the effective-one-body formalism. *Phys. Rev. D*, 84:124052, Dec 2011. doi: 10.1103/PhysRevD.84.124052. URL http://link.aps.org/doi/10.1103/PhysRevD.84.124052.

[136] Yi Pan, Alessandra Buonanno, Andrea Taracchini, Lawrence E. Kidder, Abdul H. Mroué, Harald P. Pfeiffer, Mark A. Scheel, and Béla Szilágyi. Inspiral-merger-ringdown waveforms of spinning, precessing black-hole binaries in the effective-one-body formalism. *Phys. Rev. D*, 89(8), Apr 2014. ISSN 1550-2368. doi: 10.1103/physrevd.89.084006. URL http://dx.doi.org/10.1103/PhysRevD.89.084006.

[137] Yi Pan, Alessandra Buonanno, Andrea Taracchini, Lawrence E. Kidder, Abdul H. Mroué, Harald P. Pfeiffer, Mark A. Scheel, and Béla Szilágyi. Inspiral-merger-ringdown waveforms of spinning, precessing black-hole binaries in the effective-one-body formalism. *Phys. Rev. D*, 89:084006, Apr 2014. doi: 10.1103/PhysRevD.89.084006. URL http://link.aps.org/doi/10.1103/PhysRevD.89.084006.

[138] Roger Penrose. Asymptotic properties of fields and space-times. *Phys. Rev. Lett.*, 10:66–68, Jan 1963. doi: 10.1103/PhysRevLett.10.66. URL http://link.aps.org/doi/10.1103/PhysRevLett.10.66.

[139] P. C. Peters. Gravitational radiation and the motion of two point masses. *Phys. Rev.*, 136:B1224–B1232, Nov 1964. doi: 10.1103/PhysRev.136.B1224. URL http://link.aps.org/doi/10.1103/PhysRev.136.B1224.

[140] Eric Poisson. Gravitational waves from inspiraling compact binaries: The Quadrupole moment term. *Phys. Rev.*, D57:5287–5290, 1998. doi: 10.1103/PhysRevD.57.5287.

[141] Eric Poisson and Clifford M. Will. Gravitational waves from inspiraling compact binaries: Parameter estimation using second postNewtonian wave forms. *Phys.Rev.*, D52:848–855, 1995. doi: 10.1103/PhysRevD.52.848.

[142] Frans Pretorius. Evolution of binary black-hole spacetimes. *Phys. Rev. Lett.*, 95:121101, Sep 2005. doi: 10.1103/PhysRevLett.95.121101. URL http://link.aps.org/doi/10.1103/PhysRevLett.95.121101.

[143] Michael Pürrer. Frequency-domain reduced order models for gravitational waves from aligned-spin compact binaries. *Class. Quantum Grav.*, 31(19): 195010, Sep 2014. ISSN 1361-6382. doi: 10.1088/0264-9381/31/19/195010. URL http://dx.doi.org/10.1088/0264-9381/31/19/195010.

[144] Michael Pürrer, Sascha Husa, and Mark Hannam. An efficient iterative method to reduce eccentricity in numerical-relativity simulations of compact binary inspiral. *Phys. Rev. D*, 85:124051, Jun 2012. doi: 10.1103/PhysRevD.85.124051. URL http://link.aps.org/doi/10.1103/PhysRevD.85.124051.

[145] Michael Pürrer, Mark Hannam, P. Ajith, and Sascha Husa. Testing the validity of the single-spin approximation in inspiral-merger-ringdown waveforms. *Phys.*

Rev. D, 88:064007, Sep 2013. doi: 10.1103/PhysRevD.88.064007. URL http://link.aps.org/doi/10.1103/PhysRevD.88.064007.

[146] Michael Pürrer. Frequency domain reduced order model of aligned-spin effective-one-body waveforms with generic mass-ratios and spins. 2015.

[147] Michael Pürrer, Mark Hannam, and Frank Ohme. Can we measure individual black-hole spins from gravitational-wave observations? 2015.

[148] C. Reisswig, N. T. Bishop, D. Pollney, and B. Szilágyi. Unambiguous determination of gravitational waveforms from binary black hole mergers. *Phys. Rev. Lett.*, 103:221101, Nov 2009. doi: 10.1103/PhysRevLett.103.221101. URL http://link.aps.org/doi/10.1103/PhysRevLett.103.221101.

[149] Christian Reisswig and Denis Pollney. Notes on the integration of numerical relativity waveforms. *Classical and Quantum Gravity*, 28(19):195015, 2011. URL http://stacks.iop.org/0264-9381/28/i=19/a=195015.

[150] Milton Ruiz, Miguel Alcubierre, Darío Núñez, and Ryoji Takahashi. Multiple expansions for energy and momenta carried by gravitational waves. *General Relativity and Gravitation*, 40(8):1705–1729, 2007. ISSN 1572-9532. doi: 10.1007/s10714-007-0570-8. URL http://dx.doi.org/10.1007/s10714-007-0570-8.

[151] L. Santamaría, F. Ohme, P. Ajith, B. Brügmann, N. Dorband, M. Hannam, S. Husa, P. Mösta, D. Pollney, C. Reisswig, E. L. Robinson, J. Seiler, and B. Krishnan. Matching post-newtonian and numerical relativity waveforms: Systematic errors and a new phenomenological model for nonprecessing black hole binaries. *Phys. Rev. D*, 82:064016, Sep 2010. doi: 10.1103/PhysRevD.82.064016. URL http://link.aps.org/doi/10.1103/PhysRevD.82.064016.

[152] Olivier Sarbach, Gioel Calabrese, Jorge Pullin, and Manuel Tiglio. Hyperbolicity of the baumgarte-shapiro-shibata-nakamura system of einstein evolution equations. *Phys. Rev. D*, 66:064002, Sep 2002. doi: 10.1103/PhysRevD.66.064002. URL http://link.aps.org/doi/10.1103/PhysRevD.66.064002.

[153] B. S. Sathyaprakash and B. F. Schutz. Physics, Astrophysics and Cosmology with Gravitational Waves. *Living Rev. Rel.*, 12:2, 2009. doi: 10.12942/lrr-2009-2.

[154] Peter R. Saulson. Josh goldberg and the physical reality of gravitational waves. *Gen. Relat. Gravit.*, 43(12):3289–3299, 2011. doi: 10.1007/s10714-011-1237-z. URL http://dx.doi.org/10.1007/s10714-011-1237-z.

[155] Mark A Scheel, Matthew Giesler, Daniel A Hemberger, Geoffrey Lovelace, Kevin Kuper, Michael Boyle, Béla Szilágyi, and Lawrence E Kidder. Improved methods for simulating nearly extremal binary black holes. *Classical and Quantum Gravity*, 32(10):105009, 2015. URL http://stacks.iop.org/0264-9381/32/i=10/a=105009.

[156] Patricia Schmidt. *Studying and Modelling the Complete Gravitational-Wave Signal from Precessing Black Hole Binaries*. PhD thesis, Cardiff School of Physics and Astronomy, 2014.

[157] Patricia Schmidt, Mark Hannam, Sascha Husa, and P. Ajith. Tracking the precession of compact binaries from their gravitational-wave signal. *Phys. Rev. D*, 84:024046, Jul 2011. doi: 10.1103/PhysRevD.84.024046. URL http://link.aps.org/doi/10.1103/PhysRevD.84.024046.

[158] Patricia Schmidt, Mark Hannam, and Sascha Husa. Towards models of gravitational waveforms from generic binaries: A simple approximate mapping between precessing and nonprecessing inspiral signals. *Phys. Rev. D*, 86:104063, Nov 2012. doi: 10.1103/PhysRevD.86.104063. URL http://link.aps.org/doi/10.1103/PhysRevD.86.104063.

[159] Patricia Schmidt, Frank Ohme, and Mark Hannam. Towards models of gravitational waveforms from generic binaries: Ii. modelling precession effects with a single effective precession parameter. *Phys. Rev. D*, 91:024043, Jan 2015. doi: 10.1103/PhysRevD.91.024043. URL http://link.aps.org/doi/10.1103/PhysRevD.91.024043.

[160] Karl Schwarzschild. On the gravitational field of a mass point according to Einstein's theory. *Sitzungsber. Preuss. Akad. Wiss. Berlin (Math. Phys.)*, 1916:189–196, 1916.

[161] Masaru Shibata and Takashi Nakamura. Evolution of three-dimensional gravitational waves: Harmonic slicing case. *Phys. Rev. D*, 52:5428–5444, Nov 1995. doi: 10.1103/PhysRevD.52.5428. URL http://link.aps.org/doi/10.1103/PhysRevD.52.5428.

[162] D. Shoemaker et al. Advanced ligo anticipated sensitivity curves. *LIGO-T0900288, https://dcc.ligo.org/cgi-bin/DocDB/ShowDocument?docid=2974*, 2010.

[163] Béla Szilágyi, Jonathan Blackman, Alessandra Buonanno, Andrea Taracchini, Harald P. Pfeiffer, Mark A. Scheel, Tony Chu, Lawrence E. Kidder, and Yi Pan. Approaching the Post-Newtonian Regime with Numerical Relativity: A Compact-Object Binary Simulation Spanning 350 Gravitational-Wave Cycles. *Phys. Rev. Lett.*, 115(3):031102, 2015. doi: 10.1103/PhysRevLett.115.031102.

[164] Andrea Taracchini, Yi Pan, Alessandra Buonanno, Enrico Barausse, Michael Boyle, Tony Chu, Geoffrey Lovelace, Harald P. Pfeiffer, and Mark A. Scheel. Prototype effective-one-body model for nonprecessing spinning inspiral-merger-ringdown waveforms. *Phys. Rev.*, D86:024011, 2012. doi: 10.1103/PhysRevD.86.024011.

[165] Andrea Taracchini, Alessandra Buonanno, Gaurav Khanna, and Scott A. Hughes. Small mass plunging into a Kerr black hole: Anatomy of the inspiral-merger-ringdown waveforms. *Phys. Rev.*, D90(8):084025, 2014. doi: 10.1103/PhysRevD.90.084025.

[166] Andrea Taracchini, Alessandra Buonanno, Yi Pan, Tanja Hinderer, Michael Boyle, Daniel A. Hemberger, Lawrence E. Kidder, Geoffrey Lovelace, Abdul H. Mroué, Harald P. Pfeiffer, Mark A. Scheel, Béla Szilágyi, Nicholas W. Taylor, and Anil Zenginoglu. Effective-one-body model for black-hole binaries with generic mass ratios and spins. *Phys. Rev. D*, 89:061502, Mar 2014. doi: 10.1103/PhysRevD.89.061502. URL http://link.aps.org/doi/10.1103/PhysRevD.89.061502.

[167] The LIGO Scientific Collaboration. LALSuite: LSC Algorithm Library Suite. https://www.lsc-group.phys.uwm.edu/daswg/projects/lalsuite.html, 2015.

[168] J Thornburg. *Numerical Relativity in Black Hole Spacetimes*. PhD thesis, University of British Columbia, Vancouver, British Columbia, 1993.

[169] Samantha A. Usman et al. An improved pipeline to search for gravitational waves from compact binary coalescence. 2015.

[170] Alex Vañó-Viñuales. *Free evolution of the hyperboloidal initial value problem in spherical symmetry*. PhD thesis, U. Iles Balears, Palma, 2015. URL https://inspirehep.net/record/1407828/files/arXiv:1512.00776.pdf.

[171] J. Veitch and A. Vecchio. Bayesian coherent analysis of in-spiral gravitational wave signals with a detector network. *Phys. Rev. D*, 81:062003, Mar 2010. doi: 10.1103/PhysRevD.81.062003. URL http://link.aps.org/doi/10.1103/PhysRevD.81.062003.

[172] J. Veitch, V. Raymond, B. Farr, W. Farr, P. Graff, S. Vitale, B. Aylott, K. Blackburn, N. Christensen, M. Coughlin, W. Del Pozzo, F. Feroz, J. Gair, C.-J. Haster, V. Kalogera, T. Littenberg, I. Mandel, R. O'Shaughnessy, M. Pitkin, C. Rodriguez, C. Röver, T. Sidery, R. Smith, M. Van Der Sluys, A. Vecchio, W. Vousden, and L. Wade. Parameter estimation for compact binaries with ground-based gravitational-wave observations using the lalinference software library. *Phys. Rev. D*, 91:042003, Feb 2015. doi:

10.1103/PhysRevD.91.042003. URL http://link.aps.org/doi/10.1103/PhysRevD.91.042003.

[173] J.A. Wheeler and K. Ford. *Geons, Black Holes, and Quantum Foam: A Life in Physics*. W. W. Norton, 2010. ISBN 9780393079487. URL https://books.google.co.uk/books?id=zGFkK2tTXPsC.

[174] J. W. York, Jr. Kinematics and dynamics of general relativity. In L. L. Smarr, editor, *Sources of Gravitational Radiation*, pages 83–126, 1979.

[175] James W. York. Role of conformal three-geometry in the dynamics of gravitation. *Phys. Rev. Lett.*, 28:1082–1085, Apr 1972. doi: 10.1103/PhysRevLett.28.1082. URL http://link.aps.org/doi/10.1103/PhysRevLett.28.1082.

[176] Nicolas Yunes, Alessandra Buonanno, Scott A. Hughes, M. Coleman Miller, and Yi Pan. Modeling Extreme Mass Ratio Inspirals within the Effective-One-Body Approach. *Phys. Rev. Lett.*, 104:091102, 2010. doi: 10.1103/PhysRevLett.104.091102.